Late evolution, death, and afterlife of stars stripped in binaries

Laplace, E.C.

Publication date
2022
Document Version
Final published version

Late evolution, death, and afterlifeof stars stripped in binaries

Eva Laplace

Late evolution, death, and afterlife of stars stripped in binaries

Eva Laplace

Late evolution, death, and afterlife of stars stripped in binaries

ACADEMISCH PROEFSCHRIFT

ter verkrijging van de graad van doctor
aan de Universiteit van Amsterdam
op gezag van de Rector Magnificus
prof. dr. ir. K. I. J. Maex
ten overstaan van een door het College voor Promoties ingestelde
commissie, in het openbaar te verdedigen in de Aula der Universiteit
op vrijdag 14 januari 2022, te 14:00 uur

door

Eva Cecilia Laplace

geboren te Strasbourg

Promotiecommissie

Promotores:	dr. S. E. de Mink	Universiteit van Amsterdam
	prof. dr. L. Kaper	Universiteit van Amsterdam
Copromotores:	prof. dr. S. Justham	University of Chinese Academy of Sciences
Overige leden:	prof. dr. E. P. J. van den Heuvel	Universiteit van Amsterdam
	prof. dr. H. J. G. L. M. Lamers	Universiteit van Amsterdam
	prof. dr. H. A. A. Sana	KU Leuven
	prof. dr. G. A. Nelemans	Radboud Universiteit
	dr. P. Moesta	Universiteit van Amsterdam
	dr. M. Modjaz	New York University
	dr. T. Moriya	National Astronomical Observatory of Japan

Faculteit der Natuurwetenschappen, Wiskunde en Informatica

UNIVERSITY OF AMSTERDAM

ANTON PANNEKOEK
INSTITUTE

The research reported in this thesis was carried out at the Anton Pannekoek Institute for Astronomy (API), University of Amsterdam. It was supported by funding from the European Union's Horizon 2020 research and innovation program from the European Research Council (ERC, grant agreement No.715063) and the Netherlands Organisation for Scientific Research (NWO) as part of the Vidi research program BinWaves with project number 639.042.728. The Leids Kerkhoven-Bosscha Fonds (LKBF) provided occasional travel funding, and additional travels were partially supported by the Space Telescope Science Institute, (Baltimore, USA), and the Yukawa Institute (Kyoto, Japan). The ET Outreach fund of the Royal Holland Society of Sciences and Humanities provided support for the TULIPS project that is part of this thesis.

To my family

Contents

Chapter

1

Introduction

Perhaps one of the most fascinating discoveries of the last century is that most types of atom in the Universe are created in the cores of stars (Burbidge et al. 1957). To paraphrase the American astrophysicist and science communicator Carl Sagan[1]: the carbon we are made of, the oxygen we breathe, the calcium in our teeth, have all once been created during the collision of atomic nuclei under extreme pressure and density conditions in the center of a star.

During their lives, stars produce new elements and their isotopes through nuclear fusion or neutron and electron capture processes. Stars can eject some of these products into their surroundings through their stellar winds and outflows, which also significantly contribute to the energy and momentum budget of the inter-stellar medium (Woosley & Weaver 1995). Yet it is through their explosions that stars about ten times more massive than the Sun eject most of the heavy elements in the Universe. These elements chemically enrich interstellar matter, which, in time, forms the gas clouds from which new generations of stars will be born.

Thus understanding the explosions of stars is crucial for apprehending the chemical evolution of the Universe. But that is not all. For stars, death is not the end of their story, for they have afterlives. The core of a star typically lives on beyond the death of its progenitor star as an extremely compact object, such as a white dwarf, a neutron star, or a black hole (Heger et al. 2003). In turn, when these compact objects merge with each other or accrete matter, they can create rare elements, such as titanium and lead in the case of a neutron star merger (Abbott et al. 2017b), and eject these into their surroundings.

Thanks to progress made in both theoretical an observational astrophysics, our understanding of single stellar evolution has advanced enormously over the past century, though many uncertainties remain. These uncertainties primarily concern massive stars, namely their winds, outflows, mixing processes, rotation, and magnetic fields.

In the last decade, a major shift has occurred in our thinking. It is now well established that stars - especially massive stars that undergo supernova explosions - prefer to live their lives not as single stars, but with close companion stars (e.g., Sana et al. 2012). The role of binaries on the evolution and final fate of stars and how this impacts our understanding of the chemical evolution of the Universe has thus become a pressing question.

The field of stellar astrophysics is entering a new age. With the rise of fast cadence and deep, fully automated robotic transient surveys, the number of observed transients is

[1] Origial quote: "All of the rocky and metallic material we stand on, the iron in our blood, the calcium in our teeth, the carbon in our genes were produced billions of years ago in the interior of a red giant star. " - Sagan (1973)

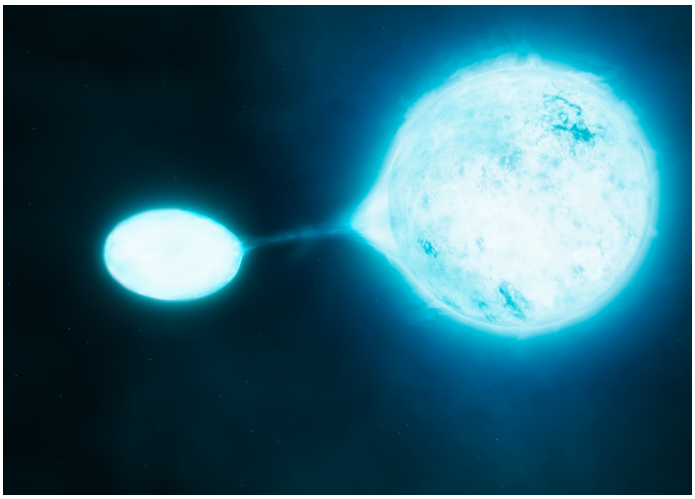

Fig. 1.1: Artist's impression of a star (on the right) that transfers its outer layers to a companion star (on the left), becoming a binary-stripped star. Credit: ESO/M. Kornmesser/S.E. de Mink

expected to reach unprecedented scales in the near future (e.g., the Vera Rubin telescope is expected to discover more than 1000 SNe per night, Ivezic et al. 2008) and with it, the diversity of observed events, especially in the fast and faint discovery space (as revealed by ZTF, Kulkarni 2012; Bellm et al. 2019 and ASSA-SN, Shappee et al. 2014). Almost the entire electromagnetic spectrum is being monitored by both ground and space-based telescopes, allowing unprecedented insights (as seen from the multi-wavelength follow up of the first detected double-neutron star merger, Abbott et al. 2017c). In fact, so much data is being accumulated that we have to rely on machine-learning techniques to analyze it all (Hassan & Fluke 2011). In addition, a revolution has been brought by the detection of gravitational waves from compact object mergers (Abbott et al. 2016, 2017a). This new messenger of the Universe is now bringing us independent insights and a new perspective onto the properties of stellar remnants.

On the theoretical side, multi-dimensional hydrodynamic simulations have recently reached a new level by achieving successful simulations of core-collapse explosions in three dimensions by independent groups (including Takiwaki et al. 2012; Lentz et al. 2015; Melson et al. 2015; Müller 2015; Kuroda et al. 2018; Vartanyan et al. 2019b; Burrows et al. 2019a).

The interactions in binary star systems are complex and can affect the stars in multiple ways. In this thesis, we focus on the properties of stars that begin their lives with masses between about 8 and 20 times the mass of our Sun and transfer their outer layers to their companion, see Fig. 1.1 for an artist's impression of this process. Once they have lost most of their outer envelope, these objects are called binary-stripped stars. How does binary stripping affect the late evolution, death, and afterlife of massive stars? This is the central question the present thesis aims to address.

1.1 The life cycle of stars

1.1.1 Historical context

Astronomy is perhaps the oldest scientific discipline there is. Virtually every single human civilization that we know of has sought to comprehend the stellar objects that illuminate the Earth's night sky (Hamacher 2014). The most extensive written record of astronomical observations known are the accounts from Chinese astronomers, which span over 4000 years of human history and contain precious information about historical astronomical events that occurred at the time (Hsi 1957; Xi & Bo 1965; Shi 2015; Bonnet-Bidaud et al. 2009; Zhou et al. 2018). Yet the exact nature of stars has been known for less than a hundred years. It appears that this late development is related to the nature of astronomical research. Understanding stellar objects requires to observe them carefully, to correctly interpret the light they radiate, and to understand the source of this radiation. Thus, to understand the nature of stellar objects, it was necessary to invent better means to observe them. It also required a theory connecting the smallest, nuclear scales and the largest, cosmic scales that could explain both the properties of electromagnetic radiation and its sources.

The idea that stars could be "other Suns" is ancient. The first written record of this idea comes from Anaxagoras in 450 BC. The 16th century, with the invention of the telescope and the advent of a mathematical model describing the motion of planets and the place of our Sun in our Solar System, marked a major advance in astronomy. Further progress in astronomy was achieved in the 17th century with, among other findings, the formulation of the laws of motion by Isaac Newton. Nevertheless, what stars are composed of, why they appear different from another, and why they display distinct colors, brightness, and brightness variations, remained a mystery before the mid-19th century. It was only after major technological and theoretical advances in (astro)physics that the modern theory of stellar evolution could be born.

The mid-19th century allowed such advances with the invention of the spectrometer, the development of a theory of thermodynamics, and first steps in heat and radiation transport. In the beginning of the 19th century, Joseph Fraunhofer noticed that the Sun's spectrum contained black lines. In the 1860s, Margaret and William Huggins then made the fundamental connection between spectral lines of elements measured on Earth and the ones observed in stars that gave birth to a new window into the properties of stars. Efforts by Williamina Fleming led to the first spectral classification of stars based on their hydrogen absorption lines, which was then revised by Annie Jump Cannon, and reordered as a function of (decreasing) temperature.

A few years later, Antonia Maury developed her own system for the classification of stars that relied on the width and strength of spectral lines to distinguish between stellar types. She realized that the differences between the width of spectral lines could be indications for the size of these stars (Maury & Pickering 1897). Ten years later, the value of this work was recognized by Ejnar Hertzsprung, who used Maury's classification to identify bright red giant stars among stars of the same spectral class (Hertzsprung 1909). It was then that the

astronomical community realized that stars have different sizes and that the expansion of stars is an important indicator of their evolutionary state. By ordering the stars by spectral type and magnitude in a 2D diagram (known as the Hertzsprung-Russell diagram, HRD, Hertzsprung 1911; Russell 1914), it became clear that the stars occupy certain regions such as a diagonal band, which we now call the main sequence. Other stars, such as red giants and white dwarfs deviate. This diagram and the attempts by theorists to understand the origin of these structures has been crucial for understanding how stars evolve.

In parallel to this development, advances in quantum mechanics led to the realization that stars can be powered by nuclear fusion. The invention of electronic computers brought a revolution in stellar physics by enabling calculations of numerical stellar models.

1.1.2 Single-star evolution

The technical development of astronomical observations and the progress in the theoretical understanding of electromagnetic radiation and nuclear physics brought forth a theory of the structure and evolution of stars. With it, the life of single stars is now understood reasonably well. It has been reviewed by many (see e.g., Eddington 1926; Schwarzschild 1958; Maeder & Meynet 2000; Woosley et al. 2002; Kippenhahn et al. 2012; Langer 2012; Prialnik 2009; Lamers & Levesque 2017; Eldridge & Tout 2019) and we refer to these works for detailed explanations. Here we give a brief overview.

The evolution of stars is mainly determined by their initial mass and, to a smaller degree, by their initial composition and initial rotation. In this thesis, we consider massive stars with initial masses ranging from about 8 to 20 $M_\odot$ that are progenitors of core-collapse explosions (e.g., Woosley et al. 2002, for standard assumptions). Stars spend their lives on a balance between their own gravity that seeks to crush the star inwards, and internal heat that creates pressure from gas and radiation, which strives to burst the star apart. This is called hydrostatic equilibrium. Part of the internal heat is radiated outwards and causes stars to shine. Without another energy source to compensate for this loss of energy, stars would continue to contract, heat up, and shine, and live short lives. Fortunately, the enormous pressures and temperatures reached in the interiors of stars allow for nuclear fusion reactions to take place, which provide the energy necessary to (temporarily) compensate for this heat loss. This energetic balance, the stellar structure, and the transport of energy in stars can be approximated mathematically by a set of coupled, non-linear, differential equations, known as the stellar structure equations. Numerical solution of these have provided key insight into how stars evolve. Below we briefly summarize the main findings.

Stars spend the majority of their lives fusing hydrogen into helium. More massive stars have a deeper gravitational potential, use their "fuel" faster, and as a result lead shorter lives than less massive stars. After most of the hydrogen has been consumed in the central region of a star, where the conditions for nuclear fusion are met, insufficient energy is produced there by nuclear fusion. As a result, the star temporarily contracts and heats up until nuclear fusion of hydrogen begins once again in a small shell around the newly formed helium core. The core

continues to contract while the stellar envelope expands until the pressure and temperature conditions are right for helium fusion to occur in the stellar center.

In this manner, stars experience successive nuclear fusion and contraction phases, typically followed by expansion. These nuclear fusion reactions accelerate after the onset of core carbon fusion because of the production of large amounts of neutrinos. These have such small cross sections that they escape the star, inducing an additional energy loss that needs to be compensated by yet more intense nuclear fusion reactions in a smaller mass region in the core. As a result, massive stars only have less than a few thousand years left to live after the onset of core carbon burning. The successive nuclear reactions in the core lead to the formation of a peculiar concentric internal composition structure at the end of the life of massive stars, which is depicted in Fig. 1.2, in a diagram that was developed as part of this thesis. The evolution ends once no more energy can be produced from nuclear reactions in the core, after which the core becomes dynamically unstable, and collapses (see also Section 1.2.2).

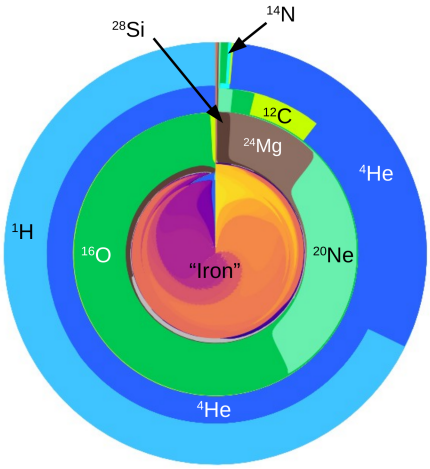

Fig. 1.2: Interior composition of a single star with an initial mass of 16 $M_\odot$ at the onset of core collapse. The diagram contains nested pie charts that show the mass fraction of isotopes in every layer of the star, where each isotope is represented by a specific color. For example, in the outer layers or "envelope", the star is composed mainly of hydrogen (~ 72%) and helium (~ 27%). In the layer below, the star is mainly composed of helium, then of oxygen, neon, and magnesium. In the inner-most layer, a region commonly referred to as the "iron core", the star is composed of several iron-group isotopes. The radius of each pie chart is given by the square root of the mass coordinate, which means the surface area of a given isotope is proportional to the mass of the isotope in the star.

1.1.3 Binary evolution

During the last decades, it has been widely accepted that most massive stars are born with companions (Abt 1983; Mason et al. 2009; Sana & Evans 2011; Chini et al. 2012; Kobulnicky et al. 2014; Almeida et al. 2017). In fact, the more massive a star is, the more likely it is to have one or more companions (e.g., Eggleton & Tokovinin 2008; Sana et al. 2014; Moe

& Di Stefano 2017). The origin of this multiplicity relates to the formation mechanism of massive stars and is a subject of active research (Zinnecker & Yorke 2007; Sana et al. 2017; Ramírez-Tannus et al. 2021). Moreover, the majority of massive multiple systems are born with such short separations that they will attempt to exchange matter during their lifetime (Sana et al. 2012).

Binary systems consist of two stars that attract one another with their gravitational potentials, influencing each other's lives. The initially more massive component is referred to as the primary in this thesis, while the less massive one is called the secondary or companion. Common binary interactions include tides (e.g., Hut 1981) and binary mass transfer (Kippenhahn & Weigert 1967).

Mass transfer can occur at different moments in the evolution of binary systems. In general, it is triggered by the radius expansion of one of the binary components, until a critical radius is reached (called the effective Roche-lobe radius) at which matter feels the gravitational attraction from both stars equally after accounting for the centrifugal effects (Kopal 1956; Eggleton 1983)[2]. Mass transfer can be dynamically stable or unstable, and generally leads to mass gain/loss (where one of the stars is the mass donor and the other the mass accretor/gainer), or mergers (where two stars merge to form one star, typically by first forming a system sharing a common envelope).

In this thesis, we focus on stable mass transfer from stars that are initially more massive than their binary companion and experience a rapid radius expansion after leaving the main sequence, while their companion is typically still on the main sequence (also known as case B systems). This interaction is particularly important because it is the most common type of stable mass transfer for a typical massive star (Webbink 1979) and thus affects a great number of systems.

Evolution of binary-stripped stars

The evolution of all case B donor stars in binary systems that undergo stable mass transfer we study in this thesis is remarkably similar, independently of their initial masses and orbital periods. For low metallicities and/or low wind mass loss rates, only the very last stages of the evolution are somewhat different because the stars retain a hydrogen-rich envelope after mass transfer (see Chapter 2 for a detailed discussion). In Fig. 1.3, we present the typical evolutionary track of a donor star in one of the binary systems we study on the HRD (blue line). This star begins its life with the exact same initial conditions (initial mass of 11 $M_\odot$, solar metallicity Z=0.014, Asplund et al. 2009) as the single star discussed in the previous section, except for the presence of binary companion with a mass of 8.8 $M_\odot$ on a circular orbit of 25 d. Inset pictograms illustrate the main evolutionary stages that will be discussed below.

At the beginning of its evolution (labeled as phase 1 in Fig. 1.3), the primary star in a binary system follows the exact same evolutionary track as the single star (shown in gray in Fig. 1.3).

[2] Mass transfer can also be triggered by the loss of angular momentum induced, e.g., for lower-mass binaries, by magnetic braking (Verbunt & Zwaan 1981).

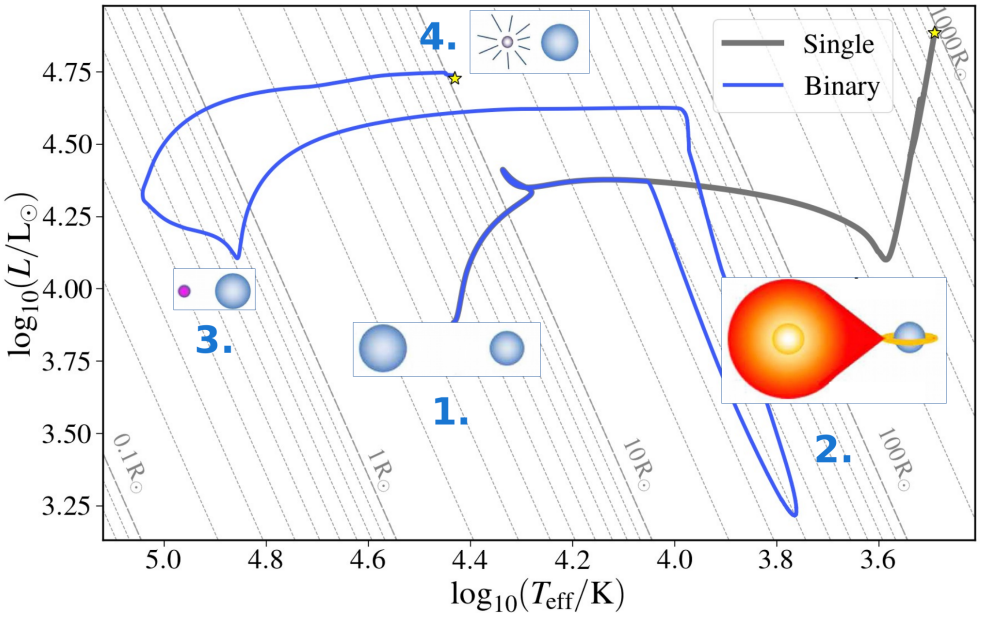

Fig. 1.3: Example evolution of a single massive star of 11 $M_\odot$ (in gray) compared to the evolution of a star with the same initial mass that transfers its outer layers to an initially less massive companion star, becoming a binary-stripped star (in blue). Numbers and pictograms mark key evolutionary moments in the evolution of the binary-stripped star and are adapted from Fig. 1 of Tauris et al. (2017), with permission.

It evolves on the main sequence, becoming more luminous and increasing in size while it fuses hydrogen into helium in its core. After all the hydrogen in the core has been fused, the star leaves the main sequence and expands rapidly while undergoing hydrogen shell burning. At the point where the single star evolutionary track and the donor star track diverge, the primary in the binary system exceeds the critical radius that allows matter to flow to the companion star. This marks the beginning of phase 2, during which the donor star transfers matter stably to its companion on a thermal time scale. This phase is clearly distinguishable on the diagram with a dramatic change in the luminosity and effective temperature evolution. During this phase, the star transfers the majority of its hydrogen-rich outer layers to its companion, and becomes a binary-stripped star. After the end of mass transfer (phase 2), the donor star becomes small (radius of less than 0.8 $R_\odot$) and extremely hot, with an effective temperature exceeding 56,000 K. Phase 3 is the longest-lived part of the binary-stripped star's life, during which it fuses helium in its core into carbon and oxygen. During this phase the binary-stripped star reaches maximum effective temperatures that exceed 100,000 K. This extreme temperature and the properties of its surface layers result in the production of ionizing photons that have been shown to be of interest for the reionization of the Universe (Götberg et al. 2017, 2018, 2019, 2020a). Once helium fusion is no longer dominant in the core, the last phase of the evolution begins (phase 4 in Fig.1.3), which is the main focus of this thesis. During this phase, the radius

of the star increases. Carbon, neon, oxygen, and silicon are successively fused in the stellar core until an iron core is formed and the core begins to collapse.

Thus binary stripping can lead to a completely different life for donor stars in binary systems compared to stars that remain single. It also leads to a different stellar structure at the end of its evolution. At the moment of core collapse, single stars and binary-stripped stars (at solar metallicity) have vastly different properties.

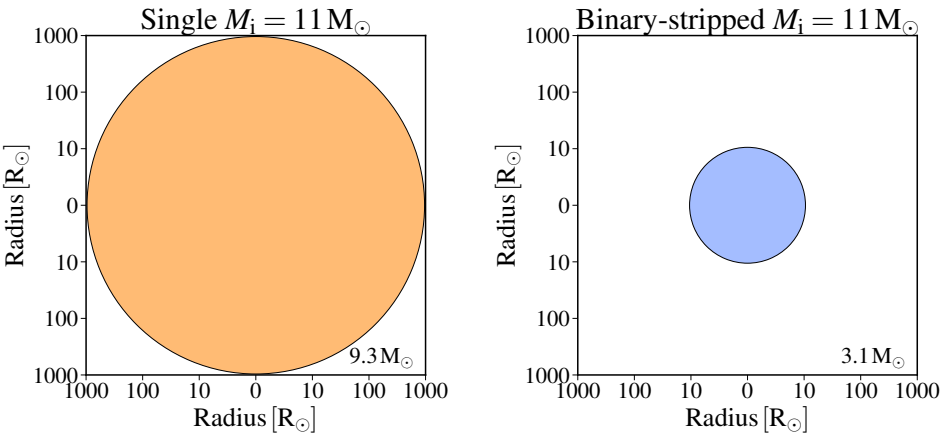

Fig. 1.4: Example visualization of the final aspect of a single and a binary-stripped star that begin their lives with the same initial mass of 11 $M_\odot$, whose evolutionary track on the HRD is shown in Fig. 1.3. **Left:** a single star that ends its life as a red supergiant with a radius of 1000 $R_\odot$. **Right:** Donor star in a binary system with an initially 8.8 $M_\odot$ companion with an initial orbital period of 25d. This star becomes binary-stripped and ends its life as a blue 15 $R_\odot$ star with no hydrogen envelope. These diagrams were created with the `TULIPS` software (see Chapter 6.

In Fig. 1.4, we visualize the two stars whose evolution on the HRD is shown in Fig. 1.3 at the onset of core collapse. The star on the left panel of Fig. 1.4 is single, while the right panel of Fig. 1.4 is binary-stripped. At the moment of death, the single star is a red supergiant, with a radius of approximately 1000 $R_\odot$, and appears red to the human eye. In contrast, the binary-stripped star is significantly smaller, with a radius of about 50 $R_\odot$ (note the logarithmic scale), and appears blue to the human eye. It is not surprising that the resulting explosions from such distinct stellar structures are also different.

1.2 Stellar explosions

1.2.1 Historical development

Supernovae (SNe) have been observed and recorded by humanity since antiquity (e.g., Hamacher 2014). The oldest written account of supernovae known comes from Chinese

astronomers, who called them "guest stars" (Xi & Bo 1965; Hsi 1957; Zhou et al. 2018). Several supernovae were observed by astronomers in different regions of the Earth, but it is not before 1930s that supernovae were distinguished as a separate type of phenomenon from the less luminous novae events that were observed more frequently (Baade & Zwicky 1934b). They were known to occur in the spiral arms and centers of galaxies and to reach luminosities as high as the centers of galaxies. From their luminosity alone, Baade & Zwicky (1934b) hypothesized that, quote: "the phenomenon of a super-nova represents the transition of an ordinary star into a body of considerably smaller mass". Following the discovery of the neutron by James Chadwick in 1932, the same authors argued that supernovae could be powered by gravitational collapse of a star into a "neutron star" (Baade & Zwicky 1934a), decades before Jocelyn Bell observed the first pulsar (Hewish et al. 1968).

By the 1940s, a spectral classification of supernovae emerged that "provisionally" divided supernovae into a hydrogen-poor (I) and hydrogen-rich (II) class (Minkowski 1941) based on their spectra. On the theoretical side, the model of an accreting CO white dwarf undergoing a thermonuclear runaway explosion was proposed, which could successfully reproduce the spectral properties of classical type I supernovae, now known as type Ia SNe (Nomoto 1982a,b; Nomoto et al. 1984; Sutherland & Wheeler 1984; Woosley & Weaver 1986).

Improvements in observational capabilities led to the discovery of multiple sub-types of SNe (II-P, II-L, II-b, Ia, Ib, Ic). At the end of the 1980s, it was established that the type Ia SNe (featuring strong Si II absorption lines) was a distinct type of object from the sub-types Ib (featuring strong He I lines) and Ic (neither He I nor Si II) SNe (Filippenko 1997). Type Ib and Ic SNe were quickly understood to originate from massive stars that lost their outer layers based on their observational properties and on their host environment (Wheeler & Levreault 1985). Type II supernovae and their subtypes (II-P, for the "plateau" observed in their light-curves, II-L, with a linear drop of the light-curve at late times) could be explained by core-collapse explosions of massive single stars that retained their envelope until the moment of death. This was later confirmed when direct progenitors of SNe were found. Looking at archival images at the location of observed type II-P SNe, researchers were able to find several progenitor stars, which were all red supergiants (Smartt et al. 2009, and references therein).

Over time, a large number of supernova sub-classes has emerged. These sub-classes include type IIn and Ibn (e.g., Pastorello et al. 2008) supernovae (where n stands for narrow lines), which show signs of interactions with circumstellar material. Super-luminous SNe (SLSNe) are another recent class of SN, which have a larger luminosity than the average SN classes (Quimby et al. 2011; Nicholl et al. 2015, e.g.,). The discovery of an association between the supernova SN1998bw and a long gamma-ray burst (LGRB) provided evidence for a link between two astrophysical explosions: LGRB and Ic-BL supernovae, which show broad lines in their spectra, indicating high expansion velocities (e.g., Woosley & Bloom 2006; Cano et al. 2017). The difference between Ic SNe, Ic-BL SNe with observed GRBs and Ic-BL SNe without GRBs, and their progenitors is still actively researched to this day (see, e.g., Modjaz et al. 2016, 2020). Recently, an ultra-long GRB was found to be associated with a SLSN (Greiner et al. 2015).

With the rise of robotic transient surveys that are exploring the fast and faint discovery space for the first time, new classes of transients are being discovered, such as Ca-rich gap transients (Perets et al. 2010) or Fast Blue Optical Transients (e.g. Inserra 2019, and references therein). These are probably associated with the explosions of rarer products of stellar evolution (e.g., Eldridge et al. 2018).

1.2.2 The core-collapse mechanism

Which stars explode and how remains one of the main open question in astrophysics (e.g., Janka et al. 2007; Janka 2012; Burrows & Vartanyan 2021). Below we provide a general description.

At the end of the life of a massive star, there comes a moment when the core cannot produce energy from nuclear reactions any longer. This can occur when the core cannot provide adequate conditions for the fusion of heavier elements, in which case the core density increases and electron-capture processes become important. Heavy nuclei (mainly ^{20}Ne and ^{24}Mg) capture electrons, and the internal pressure provided by these electrons disappears, triggering the collapse of the core and leading to the formation of a so-called electron-capture supernova (Nomoto 1984). Just a few months before writing this text, the most convincing observational evidence to date for a supernova of this type was reported (Hiramatsu et al. 2021).

The other, better-known condition that can trigger core collapse arises for stars whose core is massive enough to produce a partially degenerate iron-rich inner region. Once a large quantity of nature's most tightly bound nuclei (^{62}Ni and ^{56}Fe) has been produced, nuclear fusion no longer produces energy. The core contracts and reaches high enough energies for photodisintegration of iron to occur, i.e., the destruction of iron nuclei into alpha particle, which reduce the internal energy of the core. The colossal density of the inner core ($\rho \geq 10^{10}\,\mathrm{g\,cm^{-3}}$, e.g., Woosley et al. 2002) also enables electron captures onto iron-rich nuclei, which play a crucial role in further accelerating the collapse by removing internal pressure from electrons. This process replaces protons by neutrons, producing a degenerate neutron gas, and creates an enormous neutrino flux that carries away 99.9% of the energy released in a supernova (e.g., Janka et al. 2007). Evidence for such a neutrino flux was obtained for the first time when a total of 25 neutrinos where detected (Hirata et al. 1987; Bionta et al. 1987; Burrows & Lattimer 1987; Bruenn 1987; Sato & Suzuki 1987) shortly before the appearance of the well-known supernova SN1987a (Kunkel et al. 1987; Phillips et al. 1987; Herald et al. 1987), which is the closest supernova to Earth to have occurred in recent history (e.g., Podsiadlowski 1992).

When the density of the inner core exceeds nuclear density ($\rho \geq 10^{14}\,\mathrm{g\,cm^{-3}}$), the pressure of the neutron gas becomes large enough to halt the collapse. As described by Woosley et al. (2002), the inner-most core has become, quote: "[...] essentially one gigantic stellar mass nucleus [sic]. Here the repulsive hard-core potential of the nucleus acts as a stiff spring storing up energy in the compressive phase, then rebounding as the compression phase ends". The

rebounding nucleus encounters infalling matter and this collision creates a shock.

The shock wave does not immediately accelerate through the entire stellar structure and destroy the star. On the contrary, it loses copious amounts of energy by traveling through the material infalling from the outer core, heating it up and breaking it up into protons and neutrons through photodisintegration. For every 0.1 $M_\odot$ of material, roughly 10^{51} erg = 1B of energy is lost in this process (Woosley et al. 2002). When the shock reaches the lower-density region of the outer iron core, a neutrino "burst" occurs, produced by escaping neutrinos that were trapped behind the shock in an opaque "neutrinosphere" region with a radius of about 30-60 km (Janka 2012). Parts of the escaping neutrinos overtake the shock and scatter with electrons, which allows some of them to escape, carrying away yet more of the shock energy. The shock stalls at 100-200 km (Janka 2017), still trapped inside the iron-rich core, and another mechanism is needed to help its progression through the stellar structure.

The neutrino-driven explosion paradigm is probably the most promising shock revival mechanism, developed from the pioneering work by Colgate & White (1966). As proposed by Wilson (1985) and Bethe & Wilson (1985) this mechanism explains the revival of the stalled supernova shock by heat deposition through neutrinos provided by the contraction of the innermost core, which is now a neutron star. Under these extreme conditions, neutrinos of all flavors can interact with the post-shock region and deposit energy that can help revive the shock (Burrows & Goshy 1993). However, this mechanism did not prove successful in simulations assuming spherical symmetry. With the help of both numerical and observational developments, it is now established that supernovae are intrinsically asymmetric and that these asymmetries have important consequences beyond the revival of the stalled supernova shock (Janka et al. 2007). Asymmetries also explain pulsar kicks, the highly non-spherical shape of supernova ejecta, and predict gravitational-wave emission from supernovae. Beyond asymmetries, there is now a consensus that the internal core structure of stars itself, and the development of convective turbulence are all important to achieve a successful explosion (for a recent review, see, e.g., Burrows & Vartanyan 2021).

Alternative shock revival mechanisms also exist, notably magnetohydrodynamic explosions, in which strong magnetic fields coupled to a fast rotating neutron star help revive the supernova shock (Akiyama et al. 2003; Bisnovatyi-Kogan et al. 1976; LeBlanc & Wilson 1970; Meier et al. 1976; Mösta et al. 2015, 2014). Other (debated) core-collapse explosion mechanism are explosions powered by accretion of nuclear burning shells (Hoyle & Fowler 1960; Fowler & Hoyle 1964; Kushnir & Katz 2015; Kushnir 2015), and jet-driven explosions (Wheeler et al. 2000, 2002; Soker et al. 2019). Further studies are needed to explain exactly how explosions are triggered when stellar cores collapse.

Not every massive star is expected to successfully explode. The initial mass and metallicity of single stars alone already create a complex "landscape of explodability" (Heger et al. 2003). The question of which stellar structures produce a successful supernova explosion is a field of active research (e.g., Sukhbold et al. 2016; Müller et al. 2018; Patton & Sukhbold 2020). Several efforts have been made to determine predictors of successful explosion, or "explodability". Notable examples include the so-called compactness parameter (O'Connor &

Ott 2013) and the two-parameter criterion of Ertl et al. (2016), which relate explodability to stellar parameters.

1.2.3 Supernova light curves

When a star explodes, the resulting event can be so bright that it outshines the center of galaxies. If a galactic supernova were to occur tomorrow, there is a fair chance it could be observable with the naked eye, perhaps even during daytime (Adams et al. 2013; Murphey et al. 2021). Even without any knowledge of the spectrum, it is possible to infer several properties of the explosion from the so-called *light curve* of the supernova alone, i.e., by observing how radiation changes over time. This remarkable feat is possible because the general physics of how exploding stars emit radiation is well understood. We summarize the basic principles below, and refer to Falk & Arnett (1973, 1977); Arnett (1979, 1987); Bersten et al. (2012); Piro & Nakar (2013) for further details.

The successful collapse of a stellar core produces a shock wave that transports a large amount of energy through the stellar structure from the core to the surface. As the shock wave travels through the stellar structure, it heats and accelerates the matter it encounters. How much a stellar layer is accelerated depends on the local density profile. As a result, the outer layers are accelerated most (e.g., Falk & Arnett 1977; Bersten et al. 2012).

As the shock wave approaches the surface, a fraction of photons are scattered ahead of the shock and reach the surface, producing an intense flash of radiation ("shock breakout") with typical temperatures in the range of $10^5 - 10^7$ K (UV to soft X-rays, higher for SESNe, Chevalier 1976; Nakar & Sari 2010; Schawinski et al. 2008; Piro & Nakar 2013; Nakar & Piro 2014). Because the main emission lies in the UV range and is typically short (a few hours for red supergiants), it is difficult to detect with optical telescopes. Several such detections have now been claimed with reasonable credibility (Soderberg et al. 2008; Schawinski et al. 2008; Modjaz et al. 2009; Moriya & Maeda 2012; Gezari et al. 2015; Huang et al. 2018; Bersten et al. 2018).

When the shock reaches the surface of the star, it leaves the ejecta completely ionized, leaving a large fraction of photons trapped inside the ejecta and preventing significant cooling through photon diffusion. The main cooling mechanism becomes the expansion of the envelope, and the (bolometric) luminosity drops rapidly, along with the temperature. It is then, a few days after the explosion, that additional energy sources become important contributors to the luminosity of the supernova.

A mechanism that contributes significantly to the supernova luminosity is the radioactive decay of ^{56}Ni, which is synthesized during the explosion and has a half-life of 6.1 d. This isotope is radioactive and decays to ^{56}Co, which then decays to ^{56}Fe. At late times, most supernova light-curves show an exponential decrease on a time-scale of 50-100d that corresponds to the decay of ^{56}Co, which has a half-life of 77 d.

In hydrogen-poor supernovae progenitors, such as stripped-envelope stars or white dwarfs, ^{56}Ni decay is the main source of luminosity after the initial peak. By making only few

assumptions on the supernova properties, it is possible to define a scaling relation that connects the kinetic energy of the explosion E, the mass of the ejecta $M_{\rm ej}$, and the total mass of synthesized ^{56}Ni, $M_{\rm Ni}$, to features of the supernova light-curve (Arnett's rule, Arnett 1979, 1982, 1987). To this day, these scaling relation remain one of the main tools to characterize the explosion properties of hydrogen-poor supernovae (Cano 2013).

Observations of SN1987a demonstrated that the ^{56}Ni *distribution* or "mixing" is important to explain its light-curve (Pinto & Woosley 1988; Shibazaki & Ebisuzaki 1988; Itoh et al. 1987). Recent studies of SN light-curve also underline the effect of the ^{56}Ni in determining the shape of the resulting supernova light-curve (Bersten et al. 2012; Ugliano et al. 2012; Moriya et al. 2020). In addition, important deviations of Arnett's rule for SESNe have been pointed out in recent years (e.g., Dessart et al. 2015, 2016; Khatami & Kasen 2019). Arnett et al. (2017) argue that these deviations do not stem from the rule itself but from oversimplified applications.

In hydrogen-rich supernovae, the other important source of photons that power the light-curve after the initial shock cooling emission comes from the secondary effects of the recombination of hydrogen atoms. When the temperature has cooled down to 5000-6000K, electrons can recombine with protons, leading to a sudden drop in the opacity. This allows trapped photons to escape and to release the energy that had been deposited when the shock traveled through these layers. The rate at which the temperature was dropping decreases. Depending on the density profile of the progenitor, the envelope mass, and the helium content, this can lead to the formation of a so-called "plateau" phase, during which the luminosity remains nearly constants for about 100d (e.g., Imshenik & Nadezhin 1965; Grassberg et al. 1971; Popov 1993; Kasen & Woosley 2009; Faran et al. 2019).

Additional effects can also affect the shape and aspect of supernova light-curves, such as the presence of low-density circumstellar material, which can originate from the wind of the progenitor (e.g., Moriya et al. 2018), an additional power source that increases the luminosity of supernovae (e.g., the "magnetar model", Thompson et al. 2004; Burrows et al. 2007; Kasen & Bildsten 2010; Metzger et al. 2011; Inserra et al. 2013; Metzger et al. 2015), or strong asymmetries (Matzner et al. 2013; Afsariardchi & Matzner 2018).

1.2.4 Stellar remnants and population studies

We have described how *individual* single stars and the binary-stripped stars studied in this thesis evolve and end their lives. Thinking of the evolution of these stellar objects as a *population* instead can give precious insights, in particular for comparing to observations. For example, one can predict the population of X-ray binaries based on physical assumptions and compare it to the observed distribution, and ideally, set constraints on these assumed quantities (see, e.g., Fragos et al. 2013).

So-called (binary/multiple) population synthesis calculations are able to simulate the evolution of millions of stellar systems and make predictions for stellar populations and their remnants. These calculations are becoming ever more popular, sophisticated, and widespread,

thanks to their improving predictive power and to ever enhanced computational capabilities. Common population synthesis calculations include BSE (Hurley et al. 2002), Binary_c (Izzard et al. 2004, 2006), COMPAS (Stevenson et al. 2017; Vigna-Gómez et al. 2018), COSMIC (Breivik et al. 2019), SeBa (Toonen et al. 2012), and StarTrack (Belczynski et al. 2008). To achieve the feat of predicting the outcome of the evolution of millions of stellar systems, population synthesis calculations need to approximate the evolution of stellar systems. Typically they utilize fits to trends observed for specific phases of the evolution in detailed stellar models, such as the ones described in Hurley et al. (2000), or (increasingly) rely on the interpolation of pre-computed, detailed stellar evolution calculations (Eldridge & Stanway 2016; Eldridge et al. 2017). It is crucial to understand the main underlying uncertainties of the stellar models these calculations are based on.

One of the most pressing questions in astrophysics, which can now be confronted to observations, is how many of the compact objects that remain after stars end their lives will merge while emitting a gravitational-wave signal that can be detected on Earth or from future space missions such as LISA The Laser Interferometer Space Antenna (LISA, Amaro-Seoane et al. 2017; Colpi et al. 2019). Interestingly, it appears that most predictions of the distribution of gravitational-wave sources underestimated the rate and mass distribution of double neutron-star (DNS), black-hole neutron star (BHNS), and double black hole mergers (DBH) before they were observed for the first time (Abbott et al. 2019, 2017a). This reveals the large number of assumptions and uncertainties that remain part of the simplified population synthesis prescriptions.

To understand the formation of double compact objects from binary systems, it is crucial to understand the evolutionary "channels", i.e., the pathways that can lead to the formation of such merging compact objects, and to compare these to observed systems. Assuming that binary systems will not encounter other stars that may influence their evolution during their lifetime, a few main paths are possible based on the initial system configuration (e.g., the initial separation, masses, and metallicity). A typical evolutionary path that will lead to the formation of a DNS merger is shown in Fig. 1.5. This formation channel contains two SN events, both of which are stripped-envelope SNe.

1.2.5 The progenitors of stripped-envelope supernovae

Stripped-envelope supernovae (SESNe) were first discovered as a subclass of classical hydrogen-poor supernovae (now known as type Ia SNe). The so-called "peculiar" type I (now known as type Ib SNe) were fainter than classical type I SNe, and did not display prominent Si II absorption lines, while having similar ejecta velocities and light-curve peaks with similar widths (Bertola 1964; Bertola et al. 1965). Wheeler & Levreault (1985) argued that these peculiar SNe could be explained by the explosion of the bare core of a massive star that could have lost its outer envelope either due to wind mass loss or due to binary mass transfer. Decades of searches for the most likely progenitor scenario ensued.

Massive single stars that end their lives as Wolf-Rayet stars and experience strong wind

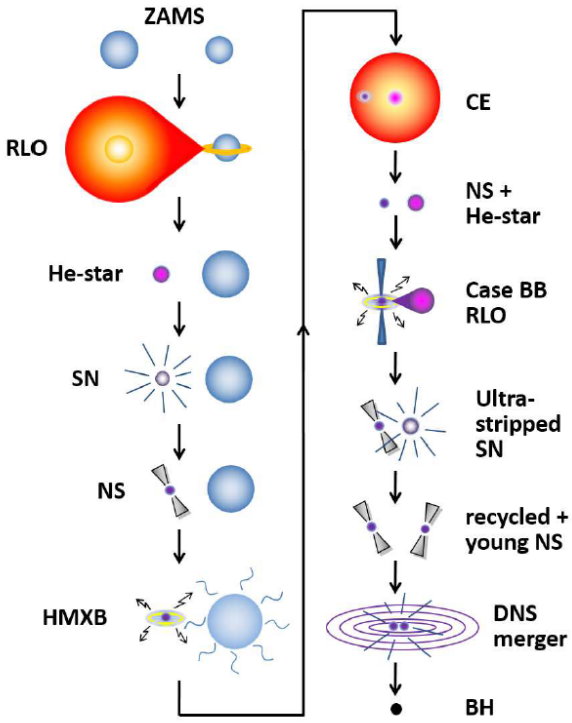

Fig. 1.5: A typical evolution of an isolated massive binary system leading to the creation of two double compact objects that merge due to the emission of gravitational waves (courtesy of Tauris et al. 2017, with permission). Abbreviations: ZAMS: Zero-age main-sequence (begin of the evolution); RLO: Roche lobe overflow (stable mass transfer); He star: helium star (binary-stripped star); SN: supernova explosion; NS: formation of a neutron star; HMXB: High-mass X-ray binary (observed binary systems that emit X-rays and contain a massive star in orbit with a compact object); CE: Common envelope evolution (The compact object becomes engulfed in the envelope of the companion star); Case BB RLOF: mass transfer while the donor star (here, the He star) is undergoing helium shell burning; DNS merger: double neutron star merger; BH: black hole.

mass loss were thought to be plausible progenitors of type Ic SNe (Woosley et al. 1993a, and references therein). For several years, this explanation remained the favored model for explaining the progenitors of the majority of type Ib/c SNe.

Podsiadlowski et al. (1992) pointed out the importance of binary mass transfer for explaining the observed diversity of SNe. These authors also argued that type II-L SNe may also be stripped-envelope SNe whose progenitors lost only parts of their hydrogen-rich envelopes due to binary mass transfer. To this day, whether the SNe sub-types II-L, IIb, Ib, Ic, Ic-BL form a continuum of increased stripping of the progenitor's envelope remains one of the main unsolved questions in the field (Modjaz et al. 2019).

In recent years, with the advent of large-scale surveys that could characterize large numbers of SNe, and improved and corrected classifications (e.g., Williamson et al. 2019), a statistical

understanding of the population of SESNe has begun to emerge (Shivvers et al. 2017). Several works, based on various methods, have shown that single star progenitors alone cannot account for all SESNe (Eldridge et al. 2008; Smith et al. 2011; Lyman et al. 2016; Taddia et al. 2018; Prentice et al. 2019; Graur et al. 2017b). In particular the distribution of ejecta masses of SESNe, peaked at low masses of 2-3 $M_\odot$,indicates that binary-stripped stars with initial masses between 8-20 $M_\odot$ are the most likely progenitors of the majority of SESNe (Eldridge et al. 2013; Lyman et al. 2016; Taddia et al. 2018). This is also supported by direct observations of SESNe progenitors from archival data, the majority of which are compatible with a binary-stripped progenitor (e.g., Eldridge et al. 2013, 2017). Recently, indications for surviving companions of SNe were found that further strengthened this finding (Maund et al. 2004; Ryder et al. 2018; Zapartas et al. 2017).

Further evidence for the binary origin of the majority of SESNe comes from the large intrinsic rate of SESNe (about one third of all core-collapse SNe, Li et al. 2011; Shivvers et al. 2017, 2019; Graur et al. 2017a,b). This rate is difficult to reproduce with single-star evolution, but can be well reproduced by binary population synthesis calculations (Podsiadlowski et al. 1992; Eldridge et al. 2008; Yoon et al. 2010; Claeys et al. 2011; Zapartas et al. 2017). In fact, a recent study by Zapartas et al. (2021b) argues that no single stars that have been stripped of their entire hydrogen envelope explode, reducing the contribution of single-star channels to SESNe progenitors even further.

Larger samples, together with better progenitor models and improved classification methods, are needed to further constrain and understand the progenitors of SESNe and the role of binary interactions.

1.3 Thesis summary

This thesis, entitled "Late evolution, death, and afterlife of stars stripped in binaries" aims to address how mass loss due to binary mass transfer impacts the evolution and explosions of massive stars.

Throughout this thesis, we use numerical calculations to investigate the structure and evolution of massive stars that transfer their outer layers to a binary companion. We employ the one-dimensional, open-source stellar evolution code Modules for Experiments in Stellar Astrophysics (`MESA` Paxton et al. 2011, 2013, 2015, 2018, 2019). This code calculates numerical solutions of the stellar structure equations and contains a module that computes the interactions between two gravitationally-bound stars. In Chapter 4, we use the multi-dimensional radiation hydrodynamics code FORNAX (Skinner et al. 2019) to self-consistently follow the core collapse at the end of the life of massive stars and the creation and propagation of a supernova shock wave. In Chapter 7, we present preliminary calculations of supernova light-curves with the one-dimensional hydrodynamic code `SNEC` (Morozova et al. 2015, 2016).

In Chapter 2, we investigate the late evolution of binary-stripped stars at solar and low metallicity, focusing on their expansion, which is crucial for determining whether they will

interact again with their binary companion. At solar metallicity (Z=0.0142, Asplund et al. 2009), our final models reach radii of up to 100 $R_\odot$ for models with initial masses below 10 $M_\odot$, and 4 $R_\odot$ for models with initial masses of 15 $M_\odot$, and are hydrogen-poor. At low metallicity (Z=0.001), all our models retain a hydrogen-rich envelope, which allows the stars to expand to giant sizes, reaching radii of 400 and 600 $R_\odot$. This means all of them will interact again with their binary companion. In fact, we find that all binary-stripped stars we model at low metallicity will fill their Roche lobe before the moment of explosion, which may have interesting consequences for the observed supernovae. We show that the expansion of binary-stripped stars is underestimated by up to two orders of magnitude in population synthesis models that approximate the evolution of binary-stripped stars as pure helium stars. We discuss the implications of our findings for the rate of gravitational-wave sources from DNS mergers and its metallicity dependence.

Due to this less massive – or nonexistent – hydrogen-rich envelope, binary-stripped stars that explode naturally have very different characteristics from stars that retained their envelope. The supernovae they produce lack the prominent hydrogen lines that are the signature of the large hydrogen-rich envelope of single stars. Furthermore, the shape of their light-curves is affected by this less massive, or even non-existent envelope (see Section 1.2.3). Are only the outer layers of stars affected by binary stripping? Is the core affected at all by mass loss from the envelope? Are there systematic differences between the core structures of single and binary-stripped stars?

These are the questions we address in Chapter 3, where we present a systematic comparison of the core structures of single and binary-stripped stars with the same initial mass. In this chapter, we show that the binary-stripped stars we study in this thesis indeed produce different core structures from single stars. For the same initial mass, the helium cores of binary-stripped stars have smaller masses and are more compact than cores of single stars. This is due to two effects (1) binary-stripped stars cannot grow a larger helium core due to hydrogen shell burning while single stars do (2) binary-stripped stars lose some of their helium layers to winds. Interestingly, even with the same core mass, single and binary-stripped stars develop different core structures. Their density profiles are different, and their composition as well. Binary-stripped stars develop a carbon-rich layer around the oxygen-rich core that does not exist in single-star structures. This is due to differences during helium core burning. We show that this difference persists until the onset of core collapse and leads to different initial conditions for the explosion of single star and binary-stripped star cores.

In Chapter 4, we build upon this work to investigate how this difference between single and binary-stripped star cores impacts the supernovae explosions. To this end, we compute the core collapse of these stars in two dimensions with the `FORNAX` code. In general, we find that binary-stripped stars are more explodable than single stars. We show that no single parameter can predict the explosion outcome, but that a combination of factors lead to successful explosion.

The most prominent difference in composition we found in Chapter 3 was for the ^{12}C content of single and binary-stripped massive stars. For the models we computed, we found that binary-stripped stars contain a factor two more ^{12}C in their interiors than single stars.

This is particularly interesting because of the role of ^{12}C as a building block for life. Is this ^{12}C eventually ejected during the supernova explosion or is it transformed into other isotopes during supernova nucleosythesis? Are massive binary-stripped stars a major source of ^{12}C in the Universe? Could ^{12}C be an additional signature of binary-stripped star explosions, potentially observable in supernova remnants? We address these questions in Chapter 5, and find that, indeed, the binary-stripped stars that we simulate produce overall twice as much ^{12}C in the Universe than single stars through their winds and supernova explosions. We find that the ^{12}C ejected during supernovae is barely affected by the supernova shock wave and the nucleosynthesis it leaves in its path, for the range of SN energies we model. This is because this shock wave cools down drastically before it reaches the carbon-rich layers, and is unable to destroy large amounts of ^{12}C.

Chapter 6 introduces `TULIPS`, an open-source and free software tool that enables supporting analysis and (dynamic) visualization of the structure and evolution of stars. `TULIPS` was developed and applied for the research presented in this thesis (see, e.g., the composition diagrams of Chapter 3). It is based on the simulation results of one-dimensional stellar evolution simulations and is optimized for use with MESA. `TULIPS` makes use of the intrinsic spherical symmetry of these simulations to visualize the properties of stars as the properties of circles. Several example applications of TULIPS are shown, including a Sun-like star, a 16 $M_\odot$ massive star, and a white dwarf accreting hydrogen-rich material. Chapter 6 compares `TULIPS` to traditional diagrams, such as the Hertzsprung-Russell diagram and discuss the differences. `TULIPS` is not meant as a replacement of traditional depictions of the stellar structure. It rather provides a change of perspective which has the potential to allow a more intuitive understanding of the physical processes investigated. `TULIPS` was created with the intention to transmit the beauty of the physics that determines the lives and interiors of stars to a broad community, and can also be applied for educational and public outreach purposes.

Finally, in Chapter 7 we give an outlook on future research on the topic of binary-stripped stars, their explosions, and afterlives. We present a preliminary investigation on a method to constrain the explosion properties of observed stripped-envelope supernovae based on a large collection of pre-computed supernova light-curve models. We discuss the implications of our preliminary findings and conclude with an outlook on avenues for which observations have the potential to provide constraints on binary-stripped stars.

Chapter 2

The expansion of stripped-envelope stars: Consequences for supernovae and gravitational-wave progenitors

E. Laplace, Y. Götberg, S. E. de Mink, S. Justham, and R. Farmer

The content of this chapter was published in Astronomy & Astrophysics, 2020, 637, A6[1]

Abstract

Massive binaries that merge as compact objects are the progenitors of gravitational-wave sources. Most of these binaries experience one or more phases of mass transfer, during which one of the stars loses all or part of its outer envelope and becomes a stripped-envelope star. The evolution of the size of these stripped stars is crucial in determining whether they experience further interactions and understanding their ultimate fate. We present new calculations of stripped-envelope stars based on binary evolution models computed with MESA. We use these to investigate their radius evolution as a function of mass and metallicity. We further discuss their pre-supernova observable characteristics and potential consequences of their evolution on the properties of supernovae from stripped stars. At high metallicity, we find that practically all of the hydrogen-rich envelope is removed, which is in agreement with earlier findings. Only progenitors with initial masses below $10\,M_\odot$ expand to large radii (up to $100\,R_\odot$), while more massive progenitors remain compact. At low metallicity, a substantial amount of hydrogen remains and the progenitors can, in principle, expand to giant sizes ($> 400\,R_\odot$) for all masses we consider. This implies that they can fill their Roche lobe anew. We show that the prescriptions commonly used in population synthesis models underestimate the stellar radii by up to two orders of magnitude. We expect that this has consequences for the predictions for gravitational-wave sources from double neutron star mergers, particularly with regard to their metallicity dependence.

[1] The models are available in electronic form at the CDS via anonymous ftp to cdsarc.u-strasbg.fr (130.79.128.5) or via http://cdsarc.u-strasbg.fr/viz-bin/qcat?J/A+A/

2.1 Introduction

The formation of gravitational-wave (GWs) sources is a key problem that is becoming increasingly relevant for discussion in the new era of gravitational-wave detections (Abbott et al. 2016, 2017b; LIGO Scientific Collaboration and Virgo Collaboration et al. 2019). The compact objects, neutron stars (NSs), or black holes (BHs), whose mergers give rise to the gravitational wave chirp, represent the end products of massive stars (above about $8\,M_\odot$).

The way in which remnants of two stars can eventually end up in an orbit that is close enough for them to merge through the emission of gravitational waves within a Hubble time is a process that includes many aspects which are still poorly understood. Not only does it require a detailed understanding of the evolution and fate of massive stars, but also of their binary interaction. Moreover, with the reach of present-day GW detectors, we can probe nearby mergers of compact objects, but we expect their progenitors to have formed at appreciable or even large redshifts. This is because of the time delay between the formation of a double compact objects and the final merger. Thus, we expect that many of the progenitors formed out of more pristine gas, that is, gas that is less enriched by heavy elements that have been contributed by previous generations of stars. This means we must carefully understand the effect that metallicity has on the evolution of massive stars in binaries.

Several scenarios for the formation of gravitational-wave sources have been proposed. Many of these involve the interaction between two stars in a close binary system through one or multiple phases of Roche-lobe overflow (e.g., Kippenhahn & Weigert 1967; Tutukov et al. 1973; Tauris et al. 2017, and references therein) that end up stripping one star, or eventually both stars, of most of the hydrogen-rich envelope, which is about two thirds of the initial mass. The star that results from this process is what we refer to as a stripped star, hereafter.

Stripped stars are largely composed of helium and, eventually, heavier elements. As a result, one may naively expect these stars to be very compact. This is largely the case, at least during the long-lived phase of core helium fusion. However, it has been shown that stripped stars can swell and reach giant dimensions in the late stages of their evolution, depending on their mass. Some of the early numerical calculations already demonstrated this phenomenon, approximating stripped stars as pure helium stars (e.g., Divine 1965; Habets 1986b). More recent calculations confirmed this either by considering pure helium stars (Dewi et al. 2002; Dewi & Pols 2003; Ivanova et al. 2003) or by fully following the evolution of the massive star progenitor through the stripping process in a binary system (e.g., Yoon et al. 2010; Eldridge et al. 2013; Sravan et al. 2019)

Whether or not a stripped star expands and by how much is relevant for understanding their fate as the progenitors of core-collapse supernovae and possibly gravitational-wave sources. The large size of stripped stars implies that they can fill their Roche lobe anew and undergo an additional phase of mass transfer (Dewi et al. 2002; Dewi & Pols 2003; Ivanova et al. 2003). Additional phases of mass transfer can produce stars with even lower envelope masses, known as ultra-stripped stars (Tauris et al. 2015). When these stars end their lives, it is believed that the resulting low ejecta masses lead to very small supernova kicks (e.g., Podsiadlowski

et al. 2004), which can prevent disruption of the binary system at the moment of explosion. This favors the formation of close NS binaries, some of which will be tight enough to merge as a result of GWs within a Hubble time (Tauris et al. 2017). The occurrence and outcome of additional phases of mass transfer thus directly impact predictions for the formation of gravitational-wave sources, particularly double neutron star mergers.

Improving our understanding of the expansion of stripped stars is also relevant in the light of upcoming electromagnetic transient surveys because they are responsible for about a third of all core-collapse supernovae (Graur et al. 2017a,b; Modjaz et al. 2019). The radius and the mass of their envelopes impact the light-curves predicted for stripped-envelope supernovae (Kleiser & Kasen 2014; Dessart et al. 2018; Kleiser et al. 2018), together with the mass-loss rate expected at late times and, thus, the circumstellar material around the progenitor at the moment of explosion (Ouchi & Maeda 2017). The case of type Ib supernova iPTF13bvn (Cao et al. 2013) is of particular interest as it appears to provide the most direct evidence we have that stripped stars can end their lives as helium giants (e.g., Fremling et al. 2014; Bersten et al. 2014; Eldridge & Maund 2016)

Recently, several studies have drawn attention to the fact that metallicity can have a large impact on the properties of stripped stars. Götberg et al. (2017) and Yoon et al. (2017) find that metallicity strongly affects the radial extent of the hydrogen layer that is left at the surface of the star after stripping. At low metallicity the reduced internal opacity makes it possible for stars to retract within their Roche lobe before the hydrogen envelope has been fully removed; see also Götberg et al. (2017). In addition, metallicity affects the stellar winds, which can strip the stars even further (see also Vink et al. 2001; Gilkis et al. 2019).

Calculations of the formation of gravitational-wave progenitors are typically made with binary population synthesis simulations, which rely on simplified assumptions for the stellar structure and interaction phases. Such simplifications are necessary because the simulations typically involve following the evolution of millions of stars in binary systems through complex phases of interaction. In the vast majority of binary population synthesis codes stars are treated with analytic fits by Hurley et al. (2000) against evolutionary models by Pols et al. (1998). A list of examples is given in Section 2.5.1. An alternative is to interpolate in pre-computed grids of models. Two examples of recent studies that use grids of pre-computed single-star models are Kruckow et al. (2018) and Giacobbo & Mapelli (2018); see also Section 2.5.2. A third alternative is to post-process extended grids of binary evolutionary models. The most prominent example of this is the BPASS code (Eldridge & Stanway 2016; Eldridge et al. 2017).

For the treatment of stripped stars, all population synthesis studies listed above (with the exception of BPASS) use interpolation in grids of models, or fits against them, of single helium stars computed at solar metallicity. They do not make use of models where the stripped star has been computed self-consistently through the Roche stripping process. This has two drawbacks: (1) they do not account for the effect that a leftover layer of hydrogen on the surface may have on the properties of stripped stars; (2) they do not fully account for the effect that metallicity may have on the properties of stripped stars.

In this paper, we present a study of the radius evolution of stars stripped in massive binaries considering solar and low metallicity. For this purpose, we compute a grid of representative progenitor models for different masses that are relevant as supernova and possible neutron star progenitors. We follow their evolution through Roche-lobe overflow with a detailed binary evolution code. We focus on the expansion phases after central helium depletion and discuss how this is linked with their interior evolution and in particular the burning phases. We then show how the radii compare to sizes usually assumed in binary population synthesis models and estimate how the differences impact the number of systems that can interact a second time through Roche-lobe overflow. We estimate and discuss the implications for core-collapse supernovae and gravitational-wave progenitors.

This paper can be considered as a companion of the paper by Götberg et al. (2017), which presents an extensive discussion of the effect of metallicity on the long-lived phase of central helium burning. In this work, we extend this study to the later evolutionary phases. The paper is structured as follows: we summarize our model assumptions in Section 2.2 and we discuss the effect of metallicity using two representative stellar models in Section 2.3. In Section 2.4, we present our full grids of evolutionary stellar models. We compare the radii obtained to those commonly used in population synthesis models in Section 2.5. We then discuss the impact of these large radii on the progenitors of supernova and GW sources in Section 2.6 together with a discussion of the uncertainties. A summary with our conclusions is provided in Section 2.7.

2.2 Binary evolution models

For our calculations of the interacting binary stars, we used the open-source 1D stellar evolution code *MESA* (version 10398, Paxton et al. 2011, 2013, 2015, 2018, 2019). The models are computed at solar metallicity (initial metal fraction of $Z_\odot \equiv 0.0142$, based on values from Asplund et al. (2009) and sub-solar metallicity ($Z = 0.001$, representative of nearby low-metallicity environments, such as the Small Magellanic Cloud, $Z_{\rm SMC} \cong Z_\odot/5$). Our zero age main sequence (ZAMS) models were computed by following their pre-main sequence evolution until the central helium abundance has increased by 5%. Following Tout et al. (1996), which is also consistent with Pols et al. (1998), we assumed an initial hydrogen mass fraction of $X = 1 - Z - Y$, where $Y = 0.24 + 2Z$ is the helium mass fraction. Strictly speaking, given the updated abundances from Asplund et al. (2009), the helium abundances should be adapted, even though the difference is small. We computed the evolution of the stars until core carbon depletion (defined as the moment when the core carbon abundance decreases below 10^{-4}). This is sufficient for the purpose of this work since the remaining evolutionary time is so short (less than 100 yr in these models) that the outer layers do not have time to react to quasi-hydrostatic changes in the core.

We used a nuclear network comprising 21 isotopes which follows the most prominent nuclear processes that influence the life of massive stars from hydrogen burning through the

CNO cycle until silicon burning with sufficient accuracy (approx21, Paxton et al. 2011). It has the advantage of enabling fast calculations while containing the most important isotopes relevant for our study. We used the default opacity tables of *MESA* (Iglesias & Rogers 1993, 1996; Buchler & Yueh 1976; Cassisi et al. 2007).
Convective mixing was accounted for by using mixing-length theory (Böhm-Vitense 1958) with a mixing length parameter of $\alpha = 1.5$ commonly used in stellar evolution models (e.g., Pols et al. 1998). We employed values for step overshooting above convective regions of 0.335 pressure scale heights, based on the calibration of stellar models for early B-type stars against observations valid in a comparable mass range as our models, ($10 - 20\,M_\odot$; Brott et al. 2011). We also took into account rotational mixing (Paxton et al. 2013), semi-convection, and thermohaline mixing (Kippenhahn et al. 1980) until the end of core helium burning, even though earlier studies have shown that these have little impact on the stellar structures of stripped stars (Yoon et al. 2010; Götberg et al. 2017).

We used the theoretical wind mass-loss algorithm from Vink et al. (2001) for the main sequence evolution and the de Jager et al. (1988) prescription for stars with hydrogen mass fractions lower than $X_{\mathrm{H,\,s}} = 0.4$ and effective temperatures lower than 10^4K. Because of the scarcity of observational constraints for the wind mass-loss from stripped stars, we employ the empirically derived wind mass-loss prescription from Nugis & Lamers (2000) based on the winds of Wolf-Rayet (WR) stars. This mass-loss rate is very close to the value derived for the observed intermediate mass stripped star (the qWR star HD 45166, Groh et al. 2008). It is possible that stripped stars have lower wind mass-loss rates than what is predicted from the extrapolated wind mass-loss scheme of Nugis & Lamers (2000) since they are not close to the Eddington limit (Bestenlehner et al. 2014). Indeed, Vink (2017) suggests that the wind mass loss rate from stripped stars is about ten times lower than what is predicted from the Nugis & Lamers (2000) prescription. However, the models from Vink (2017) assume an effective temperature for stripped stars of $T_{\mathrm{eff}} = 50,000$ K, which is much lower than what is implied by our models for the long-lived phase of central helium burning. If stripped stars have lower wind mass-loss rates than the amount we employ in this study, they may expand more because less of the hydrogen is removed from the surface (cf. Gilkis et al. 2019).
We computed our models by employing the default spatial and temporal resolution of *MESA* (`varcontrol_target` = 10^{-4} and `mesh_delta_coeff` = `1.0`). We increased the temporal resolution for phases involving the depletion of fuel in the core (e.g., core hydrogen depletion). Due to numerical issues, we lowered the temporal resolution to a maximum of 10^{-3} after core helium depletion and lower the sensitivity of the models to changes in abundances of elements in the core after the formation of an oxygen core.
We computed the interaction with a binary companion using the approach described in Paxton et al. (2015). We took the effect of tides into account using Hut (1981) and use the implicit mass-transfer scheme of Ritter (1988) for the Roche-lobe overflow. As a representative case for stable mass transfer, we treated the secondary component of the binary system as a point mass that has 80% of the primary's mass. We assumed a conservative mass transfer. We only

considered stripped-envelope stars created by the transfer of mass from stars that fill their Roche lobe due to a rapid expansion during their hydrogen shell burning phase after leaving the main sequence (case B mass-transfer, see Kippenhahn & Weigert 1967; Podsiadlowski et al. 1992). To this end, we adopted an initial orbital period of 25 d for all models. Stripped stars created through this channel at solar metallicity have very similar properties regardless of the exact choice of the initial orbital period and companion mass (Götberg et al. 2017). At low metallicity, the efficiency of stripping of the envelope is dependent on the initial orbital period (see Yoon et al. 2017; Ouchi & Maeda 2017). Therefore, at low metallicity, our results should be regarded as a representative approximation.

Stars may, alternatively, be stripped by common-envelope evolution. It is currently not known whether stars which have their envelopes ejected in this manner have different post-envelope-ejection properties than stars which are stripped by stable mass transfer (see, e.g., Ivanova et al. 2013) or even whether there is a metallicity dependence at all.

Stripped stars have relatively small radii during central helium burning (around $1\,R_\odot$ Habets 1986b; Götberg et al. 2017; Yoon et al. 2010) but they are expected to swell up once helium is depleted in the core. In this paper, we investigate the impact of the radius expansion at the end of core helium burning. If models expand enough to fill their Roche lobe anew, they are expected to start an additional mass-transfer phase (sometimes referred to as case BB and BC mass-transfer, see e.g., Dewi et al. 2002). The size of the Roche lobe varies depending on the size of the orbit, which, in turn depends on how angular momentum and mass is transferred. This is still a major uncertainty in binary evolution (e.g., de Mink et al. 2007). To avoid these complications and derive results that are of more generic use, we followed the late evolution of stripped stars by letting them expand as much as their internal structure dictates, ignoring any limitation imposed by the finite but highly uncertain size of the Roche lobe at this stage. In other words, we effectively treat the stripped stars as single stars during their late evolutionary phases. This allows us to investigate their full expansion and simplifies the interpretation of the physical processes involved in the radial expansion. It also makes the results of our simulations more suitable for inclusion in future populations synthesis simulations.

For the analysis, we used the following software: `mesaPlot` (Farmer 2020), `matplotlib` (Hunter 2007), `numpy` (van der Walt et al. 2011), `ipython/jupyter` (Perez & Granger 2007), and `ColorPy`[2].

2.3 Evolution of two representative models

Before presenting our full grid of models, we first describe the evolution and properties of two representative stellar models with identical initial component masses and orbital periods at solar ($Z = 0.0142$) and low metallicity ($Z = 0.001$). The initial mass of the hydrogen-rich primary star in these models is $10.5\,M_\odot$, corresponding to the mean initial mass in our grid. Following the method described in the previous section, we place this star in an orbit with an

[2] © Mark Kness http://markkness.net/colorpy/ColorPy.html

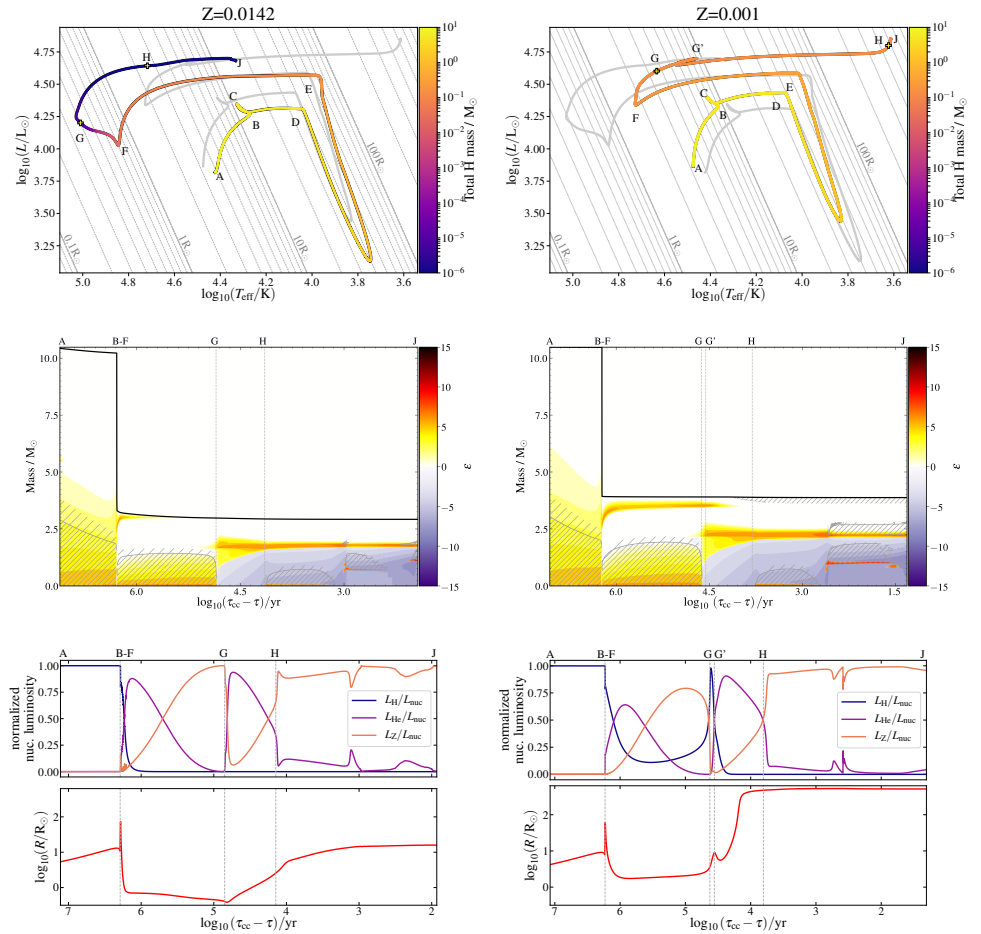

Fig. 2.1: Evolution of a high (left) and low (right) metallicity star of initially 10.5 $M_\odot$ that is stripped due to binary interaction. Letters A to J mark evolutionary points discussed in section 2.3. **Top:** evolutionary tracks on the Hertzsprung-Russell diagram. The color indicates the total mass of hydrogen present at a given moment. For comparison, we show lines of constant radii as well as the evolution of the alternate-metallicity model in gray. **Middle:** evolution of the stellar structure of the stars in mass coordinate (Kippenhahn diagrams), given as a function of time until core collapse (τ_{cc}). Convective and overshooting regions are marked with double- and single-hatched regions, respectively. Colors indicate zones dominated by nuclear burning (yellow) or neutrino cooling (purple) where $\epsilon = \mathrm{sign}\,(\epsilon_{nuc} - \epsilon_\nu)\log_{10}\left(\max\left(1.0, |\epsilon_{nuc} - \epsilon_\nu|\right)/[\mathrm{erg\,g^{-1}\,s^{-1}}]\right)$. Here ϵ_{nuc} is the nuclear energy generation rate and ϵ_ν the neutrino energy. The black line indicates the location of the stellar surface. **Bottom:** luminosity produced by hydrogen-, helium- and metal-burning as a fraction of the total luminosity produced by nuclear reactions (upper) and stellar radius (lower) as a function of time until core-collapse.

initial period of 25 d, with an 8.4 $M_\odot$ companion. For the purposes of our investigation, the companion is removed after the mass-transfer phase, when the primary star that has become a stripped star has reached core helium depletion.

Figure 2.1 compares the evolution of these primary-star models (left panels: solar metal-

licity, right panels: low metallicity). The top pair of panels presents their evolution in Hertzsprung-Russell diagrams (HRDs). The middle panels present their Lagrangian internal structures as a function of time, known as Kippenhahn diagrams. The lower sets of plots give the time evolution of the stellar radii, along with the fractional contributions of different forms of nuclear luminosity. Key points are labelled with letters in each panel, and is discussed in the following subsections.

2.3.1 Evolution until core helium burning (A–F)

The early evolution of the primary star in the binary is effectively the same as that of a single star. While we include the effects of rotation and tides, they have a negligible impact on the evolution. During their main-sequence evolution (labeled as A–B in Fig. 2.1) the stars burn hydrogen into helium in a convective core. As they do so, they increase in luminosity. The higher-metallicity star is cooler and larger due to a higher opacity in the outer layers (due to increased bound-free and bound-bound absorption, e.g., Maeder 1990; Schaller et al. 1992). After leaving the main sequence (B), the stars contract (see also the middle and lower panel of Fig. 2.1) until hydrogen is ignited in a shell (C). They then expand on their thermal time-scale until they fill their Roche lobe, which leads to transfer of matter to their companion.
During mass transfer (D–E), the stars lose the majority of their hydrogen-rich envelopes on a thermal time-scale (see, e.g., Kippenhahn & Weigert 1967, for more details). The mass-transfer phase occurs at similar effective temperatures in both models presented here since the size of the Roche lobe is the same, although the lower metallicity model has expanded slightly more relative to the higher metallicity model as of the end of the main sequence. More hydrogen is retained after the end of the Roche lobe overflow phase (B–F) in the lower metallicity model ($0.27\,M_\odot$, compared to $0.12\,M_\odot$ at solar metallicity; see also the upper panels of Fig. 2.1). This is because the stripping process becomes less effective at low metallicity due to the lower opacity in the outermost layers (see, especially Götberg et al. 2017 and references therein; also Klencki & Nelemans 2018). With a lower opacity, more of the hydrogen-rich envelope remains within the Roche lobe once the stars detach, leaving a thicker layer of hydrogen on top of the metal-poor stripped star. This is clearest in the Kippenhahn diagrams in Fig. 2.1, where the lower metallicity model has more mass outside the hydrogen-burning shell. After the end of the mass-transfer phase the stripped star shrinks towards a new gravothermal equilibrium structure. Meanwhile, convective helium burning has already started in the core. From the luminosity minimum (F), the dominant driver of structural change is, once more, nuclear burning.

2.3.2 Core helium burning phase (F–G)

Point F in Fig. 2.1 marks the longest-lived phase of these stripped stars (about 10% of the stellar lifetime), with helium burning in a convective core. The metal-rich model is hotter and more compact than the metal-poor model because the metal-poor model retains

more hydrogen in its envelope, which allows it to be larger (Cox & Giuli 1961). From here onwards, the evolution varies considerably between the two models. The metal-rich star shrinks monotonically during the core helium burning phase, while the metal-poor model first shrinks, then stays approximately constant, before starting to expand again (e.g., Götberg et al. 2017).

2.3.3 Expansion phase after core helium depletion (G–J)

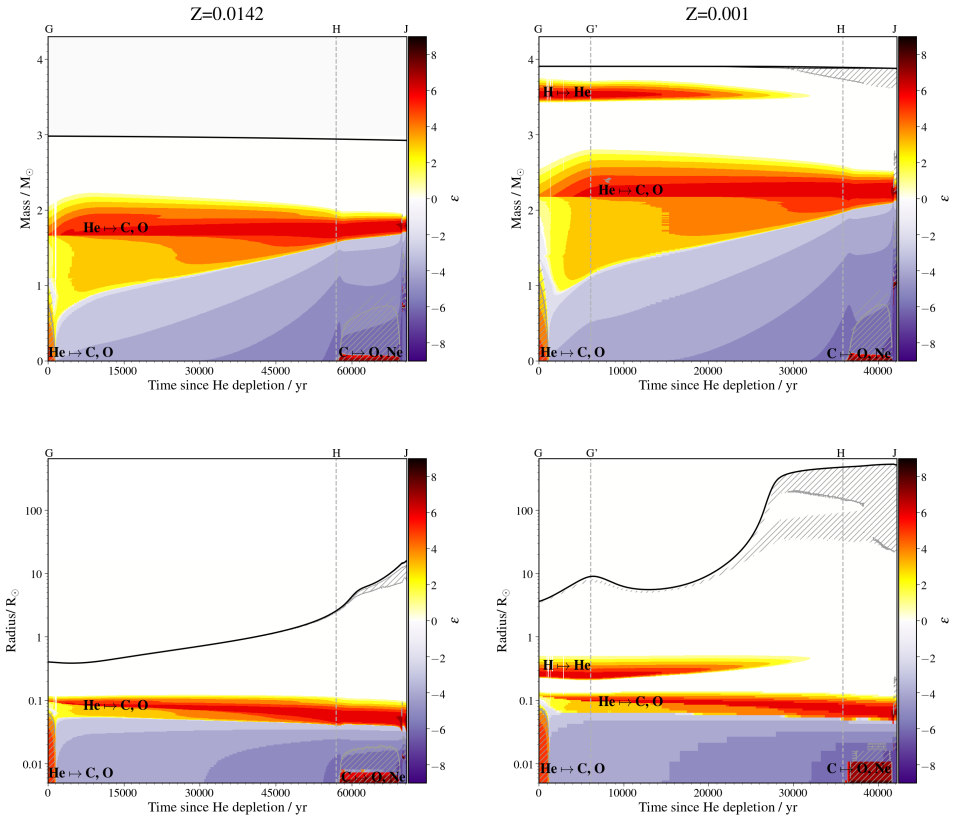

Fig. 2.2: Kippenhahn diagrams showing the evolution of the stellar structure for our two example models at solar (left panels) and low (right panels) metallicity. They are shown using mass coordinate as the vertical axis (top panels) and radius coordinate (bottom panels). The horizontal axis indicates the time since helium depletion up to core carbon depletion. The black line represents the surface of the star. Regions of mixing by convection and overshooting are marked with double- and single-hatches, respectively. Colors indicate zones dominated by nuclear burning or neutrino cooling. See Fig. 2.1 and Section 2.3 for details and a discussion.

After core helium depletion, the stars begin the short last phase of their lives, which lasts for less than 1% of their total stellar lifetime. Points labelled G in Fig. 2.1 represent

the moment at which the central helium mass fraction drops below 10^{-4}. At this point, the metal-rich model has a total mass of $2.98\,M_\odot$ and has lost all its remaining hydrogen due to stellar winds, whereas the metal-poor model has a total mass of $3.90\,M_\odot$ and a total mass of hydrogen of $0.14\,M_\odot$. The structures during the post-core-helium-burning phase are presented in more detail in Fig. 2.2, using both mass and radius coordinate systems (the top and bottom panels, respectively).
We see large differences between the high- and low-metallicity models in this last evolutionary phase. The radius evolution becomes very distinct, with a monotonic increase of the radius for the metal-rich model until a maximum of $15\,R_\odot$ is reached, and a non-monotonic increase of the radius for the metal-poor model until a maximum of $530\,R_\odot$ (see the upper and lower panels of Fig. 2.1). We further find that while the burning processes in the inner core are fairly similar, the metal-poor model develops prominent convection zones in the outer envelope and around the helium burning shell, and still experiences hydrogen shell-burning, while the metal-rich model has lost all its remaining hydrogen layer by this point due to winds (see Fig. 2.2 and the middle panels of Fig. 2.1).

Some general features are common to the evolution at both metallicities, for example, the narrowing of the helium-burning shell (in mass extent, see upper panels of Fig. 2.2) as the size of the carbon-oxygen (CO) core decreases (in radial extent, see lower panels of Fig. 2.2), and the increasing rate of neutrino cooling from the CO core as it contracts. During this phase of core contraction, both models expand overall. Since the mass of the CO core is somewhat higher in the less-stripped low-metallicity model, the evolution occurs more rapidly here.

Figure 2.2 shows that the low-metallicity model also retains a significant hydrogen layer which can sustain a burning shell, unlike the high-metallicity model that loses its hydrogen-rich envelope due to stellar winds. For the low-metallicity model hydrogen shell burning dominates the nuclear luminosity around the time of core helium exhaustion, and there is a local maximum in the radius evolution (G'), as shown in the lower-right panels of Figs. 2.1 and 2.2. In contrast, by point G, hydrogen burning is not relevant for the higher metallicity model and soon a shallow minimum in the radius evolution is apparent.

The radius expansion during the shell-burning phases, including the non-monotonic expansion of the low-metallicity model, might be interpreted in terms of the "mirror principle" (see, e.g., Kippenhahn et al. 2012). In examining the middle and lower panels of Fig. 2.1 and Fig. 2.2, respectively, the phases of radius expansion occur when one shell-burning source dominates the nuclear luminosity. The lower-right panels of Fig. 2.1 show that the first peak in the radius expansion of the low-metallicity model occurs when two shell sources are releasing roughly equivalent luminosities, analogous to the blue loop observed in some models for intermediate mass stars (see e.g., Kippenhahn et al. 2012). The layer above the helium-burning shell expands, as seen in Fig. 2.2, which leads to the cooling of the hydrogen burning shell. Eventually the temperature and density of the hydrogen-rich material are too low to sustain hydrogen burning and the shell is extinguished.

Carbon is later ignited in the center, leading to the development of a new convective

core (point H indicates this, showing the moment when the core carbon abundance drops by 2% from the post-core-helium-burning value). This is associated with a sharp rise in the burning luminosity of elements heavier than helium, as seen in the lower panels of Fig. 2.1. By this time, both stars, of 2.98 $M_\odot$ and 3.90 $M_\odot$ for the metal-rich and the metal-poor model, respectively, have only one shell source, helium. The hydrogen-rich envelope of the low-metallicity model still means that the star is more than an order of magnitude larger than the solar-metallicity model.

At the end of the evolution, more than 90% of the envelope has become convective and extends over 400 $R_\odot$, while only containing a few tenths of a solar mass of material. In reality, we do not expect the stripped star to be able to expand this much. It will likely interact again with its companion, which is still expected to be present. This would lead to another phase of mass transfer, with potentially important consequences for the type of supernova (see, e.g. Yoon et al. 2010, 2017; Dessart et al. 2018). After core carbon depletion is reached (as marked with letter J), less than 100 yr remains before these models reach core collapse. Since the thermal timescale of the stars are much longer than 100 yrs, their radii, masses, and surface composition are not significantly affected after central carbon depletion. We can, therefore, regard the properties the stripped stars have at point J as the properties the stripped stars exhibit at the moment of explosion.

2.4 Comparing the metal-poor and metal-rich grids

Here we present results from two grids of evolutionary models of stars that are stripped through binary mass transfer. The grids are computed at two different metallicities (solar and $Z = 0.001$) and each consists of twenty-three models with different initial masses for the primary star, ranging from 8.8 to 15 $M_\odot$. Tables A.2 and A.3 provide an overview of the key parameters.

2.4.1 Evolutionary tracks in the Hertzsprung-Russell diagram

The evolutionary tracks are presented in Fig. 2.3, with the top panel showing the results for solar metallicity and the bottom panel the results for low metallicity. The tracks show the evolution from the onset of hydrogen burning up to the completion of helium burning in light grey; for a detailed description, see Section 2.3.1 and 2.3.2. Here we highlight in color the last phases of the evolution from the completion of central helium burning until central carbon depletion, where the color indicates the initial mass of the progenitor.

The most striking feature in these plots is how far the evolutionary tracks extend to the right during the late stages of their evolution, that is, how much their effective temperature decreases and their radius expands before carbon is depleted in the core (which is marked with a yellow star symbol). In our solar-metallicity models, shown in the top panel, there is a wide range of final effective temperatures and thus final radii, which is in general agreement with earlier studies (cf. Habets 1986a; Dewi & Pols 2003; Yoon et al. 2010, 2017). The lowest mass

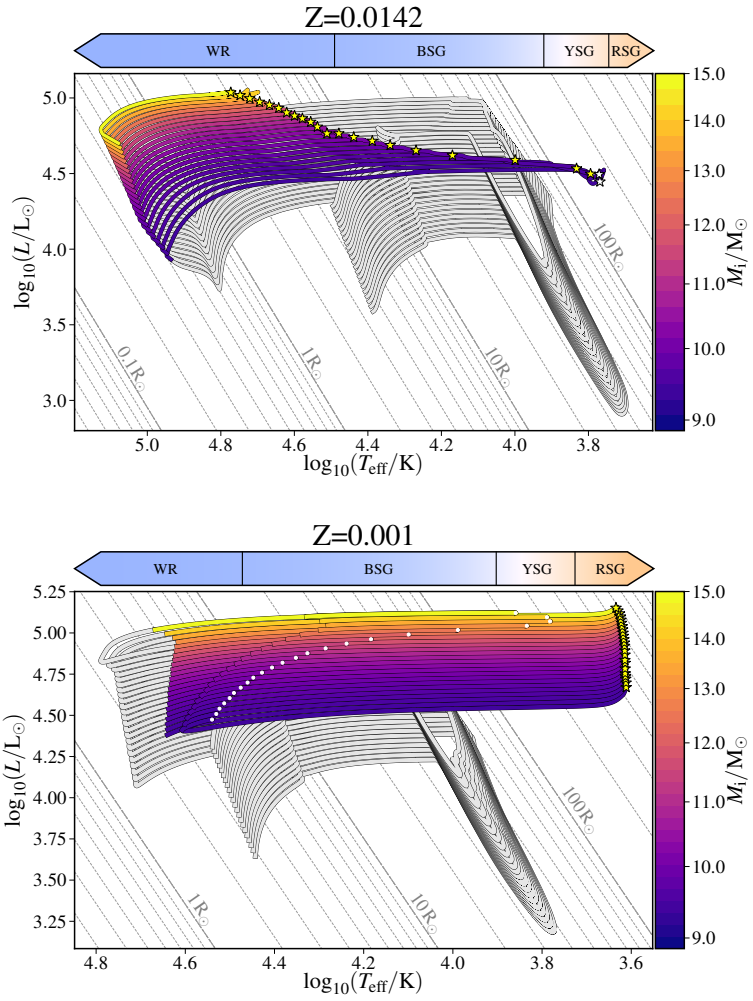

Fig. 2.3: Evolutionary tracks of stars at solar (top) and sub-solar metallicity (bottom) showing their luminosity, L as a function of effective temperature, $T_{\rm eff}$. Lines of constant radius are provided for reference. We highlight the evolution after core helium depletion in color, where the color refers to the initial mass. Yellow star symbols indicate core carbon exhaustion, and white star symbols denote the final time step calculated for models that did not reach core carbon exhaustion. The white circles in the lower panel indicate when the radius reaches a first maximum after core helium depletion. Above each panel, we indicate approximate ranges of effective temperatures typical for Wolf Rayet stars (WR), blue, yellow, and red supergiants (BSG, YSG and RSG respectively). The horizontal color scale above each panel indicates, for each effective temperature, the color as perceived by the human eye.

models in our grid ($M_{\rm ZAMS} < 9.5\,{\rm M}_\odot$) reach the lowest final effective temperatures and largest final radii of $\log_{10} T_{\rm eff}/{\rm K} \approx 3.8$ and $R \approx 150\,{\rm R}_\odot$, respectively. These temperatures are typical for yellow supergiants (YSG, e.g., Drout et al. 2009). For the intermediate-mass models in our

grid, we find final temperatures and radii that are more typical for blue supergiants (BSG, e.g., Fitzpatrick 1988). The highest mass models in the grid reach final effective temperatures and radii of up to $\log_{10} T_{\rm eff}/{\rm K} \approx 4.7$ and as low as $R \approx 3.5\,{\rm R}_\odot$, respectively. Their wind mass-loss rate is of the order of $10^{-6}\,{\rm M}_\odot/{\rm yr}$ or more. These properties are characteristic for classic Wolf-Rayet stars (WR, e.g., Crowther 2007). All the models in our low-metallicity grid end their lives as cool ($\log_{10} T_{\rm eff}/{\rm K} \cong 3.55$) and large ($R > 400 - 700\,R_\odot$) stars that are typical for red giants or red supergiants (RSG, e.g., Groh et al. 2013).

2.4.2 Evolution of the radius and its connection to the nuclear burning shells

The evolution of the radii is shown in the panels in Fig. 2.4 as a function of time since helium depletion. The solar-metallicity models are shown on the left and low-metallicity models on the right. The color bars indicate the relevant physical quantities, which are different for each row; this is discussed in more detail further on in this paper. Each panel show a sequence of twenty-three tracks which correspond to our models for different initial masses. The tracks for the massive models can be readily identified as they evolve faster and complete their final phases of evolution in about 20 kyr. The lower mass models in our grid take 125 kyr at solar metallicity and about 80 kyr at low metallicity.

We see that the solar-metallicity models expand from about $0.5\,{\rm R}_\odot$ up to final radii of $3\,{\rm R}_\odot$ for the more massive models, while the lower mass models expand to radii of $180\,{\rm R}_\odot$. In contrast, the low-metallicity models start at radii of 3 to $5\,{\rm R}_\odot$ and reach their final radii of 400-700 $\rm R_\odot$. For an overview, see also Tables A.2 and A.3.

For the low-metallicity models, the post-core-helium-burning radius expansion is clearly not monotonic with time, as we discuss in Section 2.3. The stars expand to a first maximum around 8 kyr after helium depletion for all models, followed by a contraction and re-expansion phase. The first expansion phase is most significant for the most massive models, which reach radii of up to $300\,{\rm R}_\odot$. The total radius expansion for the low-metallicity models is very significant (two orders of magnitude). The implication of this is that these stars are expected to exceed the size of their Roche lobe and, at low metallicity, they may already do so during the first expansion phase. This would trigger at least one additional phase of mass transfer shortly after core helium depletion; those are not modeled here. Moreover, they may well fill their Roche lobe shortly before or at the moment of explosion.

To understand the origin of the difference in behavior between solar- and low-metallicity models, it is helpful to inspect subsequent physical parameters. The main difference between the solar- and low-metallicity models is the remaining hydrogen mass, which is indicated in color in the panels in the top row of Fig. 2.4. The solar-metallicity models contain almost no hydrogen, that is, less than about $0.05\,{\rm M}_\odot$ after the mass transfer ceases and even less at the end their evolution (see $M_{\rm H}^{\rm postMT}$ and $M_{\rm H}^{\rm f}$ in Table A.2). In contrast, the low-metallicity models contain about $0.2\,{\rm M}_\odot$ of hydrogen after the mass transfer ceases and the stellar winds are too weak to substantially reduce this afterwards.

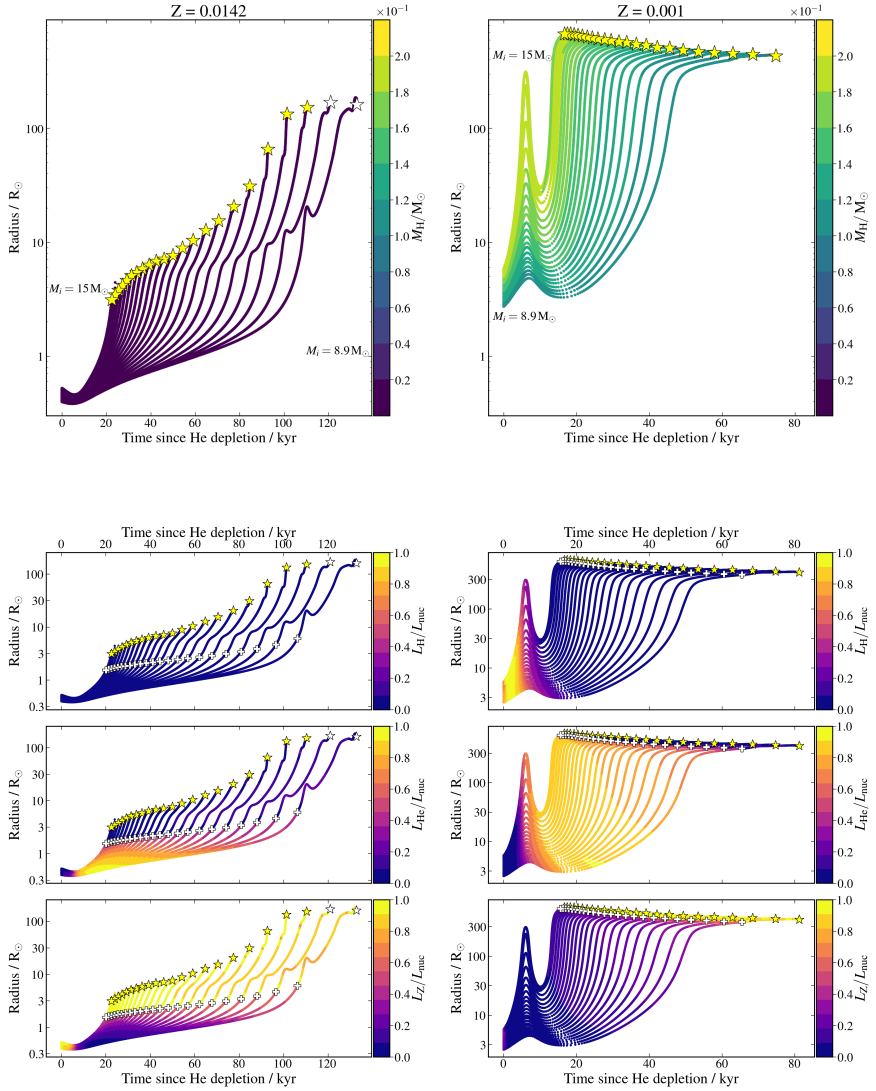

Fig. 2.4: Evolution of the radius as a function of time after core helium depletion for the stars in our model grids at solar (left) and lower (right) metallicity. From top to bottom, colors indicate the remaining mass of hydrogen and the normalized luminosity from nuclear burning of hydrogen, helium, and heavier elements; see text for details. More massive stars evolve faster and are thus located towards the left of the figures. White crosses indicate the moment of core carbon ignition. Yellow star symbols indicate core carbon exhaustion, and white star symbols denote the final time step calculated for models that did not reach core carbon exhaustion.

We can gain further insights in considering the nuclear burning processes that contribute to the total luminosity by nuclear burning ($L_{\rm nuc}$). Colors in the lower panels of rows 2, 3, and 4 of Fig. 2.4 show the relative contribution to the total nuclear luminosity resulting from the burning of hydrogen ($L_{\rm H}$), burning of helium through the triple-alpha reaction ($L_{\rm He}$), and the collective burning of heavier elements ($L_{\rm Z}$), including helium burning by alpha captures onto carbon.

During the first 10,000 years after helium depletion, the radii of the solar-metallicity models change slowly, while the low-metallicity models expand rapidly. At solar metallicity, the thin hydrogen-rich layer that is left after Roche-lobe stripping, if any, is not sufficient to support hydrogen shell burning. By contrast, in the low-metallicity models enough hydrogen is retained to sustain hydrogen shell burning. Hydrogen burning dominates the nuclear luminosity during the first expansion phase, as can be seen on the second row of Fig. 2.4. At the peak of the first stellar expansion hydrogen burning contributes about half of the total nuclear luminosity. At that time, the contribution from the helium-burning shell is increasing, as can be seen in the panel on the third row of Fig. 2.4. The turning point in radial expansion occurs when the stars have roughly equivalent luminosity contributions from two shell sources. The first expansion in the low-metallicity models is thus associated with hydrogen shell-burning, and the subsequent contraction is consistent with the "double mirror effect" (see also Sect. 2.3.3).

Thereafter, both high- and low-metallicity models show radius expansion when helium-shell burning dominates the nuclear luminosity. The low-metallicity models reach much larger radii, and most of their expansion is during this burning phase. The plus symbols in Fig. 2.4 indicate the start of core carbon burning, which we define as the moment when the core carbon abundance drops by 2% below its post-core-helium-burning value. The solar-metallicity models show significant further expansion after this time, for the lowest mass models by more than an order of magnitude in radius, as a result of to the left-over hydrogen layer. The low-metallicity models have completed most of their expansion by the onset of core carbon burning.

2.4.3 Binding energy

In the previous sections, we discuss the expansion of stripped stars in their final evolutionary phases. As a result of this expansion, stripped stars can fill their Roche lobe again, initiating a subsequent phase of mass transfer. In the case of unstable mass transfer, the system is expected to enter a common-envelope phase. This would shrink the orbit and, thus, carry significant potential consequences for the final fate of the binary, possibly as source of gravitational waves. We briefly discuss the most important stellar property affecting the outcome of a common envelope phase that we can compute, namely, the binding energy of the envelope (e.g., Webbink 1984).

We define the binding energy $E_{\rm B}$ of the (hydrogen or helium) envelope as:

$$E_{\rm B} = -\int_{\rm core}^{\rm surface} \left(-\frac{Gm}{r} + \epsilon(m)\right) dm, \tag{2.1}$$

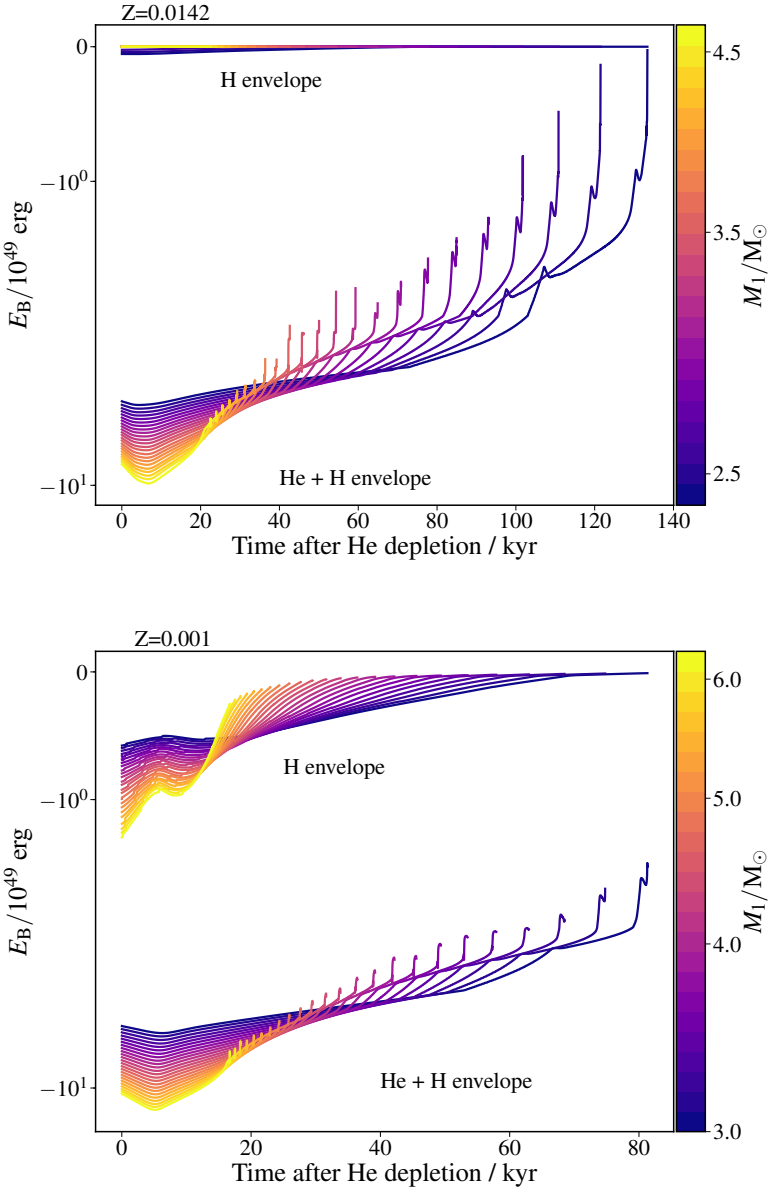

Fig. 2.5: Binding energy of the envelope as a function of radius after core helium depletion at solar (top panel) and low (bottom panel) metallicity. We show values for the hydrogen-rich envelope alone, as well as the hydrogen and helium envelope combined, as labelled. Colors indicate the mass of the stripped star.

where G is the gravitational constant, m the mass coordinate, and r the radius coordinate of the star, and ϵ the specific internal energy. This internal energy includes not only the thermal energy terms, but also the potential energy stored in ionised species and dissociated molecules (see, e.g., Han et al. 1994; Ivanova et al. 2013). We define the relevant core-envelope boundary as the point at which the abundance of the dominant element in the envelope drops below 10%. The chosen definition is somewhat arbitrary, but we consider it reasonable for our current purposes (see also Appendix A.5).

The results for our solar-metallicity models are shown in the top panel of Fig. 2.5. The binding energy of the H envelope is negligible, as expected, since most hydrogen has been removed efficiently during Roche-lobe overflow and subsequently by the stellar wind. Shortly after helium depletion, the He+H envelope has a binding energy of the order of about -5 to -10×10^{49} erg, where the more massive stars in our grid are more tightly bound (i.e., their binding energies are more negative). As time proceeds, the stars evolve and expand. Their envelopes loosen to reach values of the binding energy of about -2 to -6×10^{49} erg at the end of their evolution, when the envelope starts to become convective.

For our low-metallicity models, shown in the bottom panel, we find the same qualitative trend with mass and time. However, the binding energies are about -1×10^{49} erg for the H envelope and about ten times more than that for the H+He envelope. All these models develop a convective envelope when their radius reaches 200–300 $R_\odot$. We discuss the consequences for the stability of mass-transfer and gravitational-wave progenitors in Section 2.6.2.

2.5 Comparison with radii for helium stars adopted in population synthesis simulations

Having accurate estimates for the minimum and maximum radii of stars is crucial in the context of binary systems. For an individual binary system, the radial expansion determines whether a star can swell to fill its Roche lobe and start a (new) phase of mass transfer. For a full population of binary systems, the radial expansion is an essential factor in determining what fraction of this population interacts.

To simulate large populations of binary systems and their exotic end products as X-ray binaries and gravitational wave progenitors, prescriptions are needed that can be evaluated quickly. Generally, two approaches are commonly adopted. Many population synthesis codes make use of the analytic formulae by Hurley et al. (2000). We compare our results with these prescriptions in Section 2.5.1. Alternatively, one can make use of interpolation in grids of pre-computed stellar evolution models. One example of this is the SEVN code, with which we compare in Section 2.5.2.

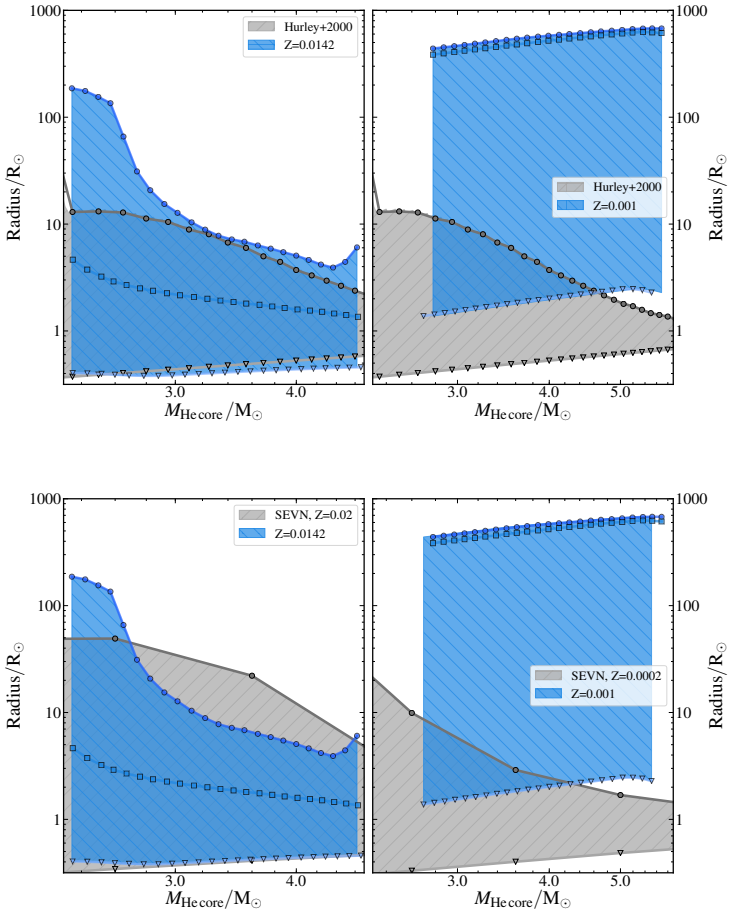

Fig. 2.6: Comparison of our results (shown in blue in each panel) with (1) the widely-used prescriptions by Hurley et al. (2000) (shown in grey in the panels on the top rown) and (2) the PARSEC models (Bressan et al. 2012) used in the SEVN code (Spera et al. 2019) (shown in grey in the panels on the bottom row). Panels on the left show a comparison at solar metallicity (or its closest available equivalent, i.e. Z= 0.02 for SEVN) and panels on the right show a comparison for low metallicity (Z= 0.0002 for SEVN). We show the maximum radius (circles) and the minimum radius (triangles). For our models, we also mark the radius at core carbon ignition (squares).

2.5.1 Analytic prescriptions by Hurley et al. (2000)

The Hurley fitting formulae are adopted in many population synthesis codes that are in active use. These include, but are not limited to, `BSE` (Hurley et al. 2002), `StarTrack` (Belczynski et al. 2008), `Binary_c` (Izzard et al. 2004, 2006), `COMPAS` (Stevenson et al. 2017; Vigna-Gómez et al. 2018), and the latest arrival `COSMIC` (Breivik et al. 2019). The discussion below thus applies to these studies and others that make use of these prescriptions.

The Hurley fitting formulae are based on evolutionary models by Pols et al. (1998) which solve for the full set of stellar structure equations using the Eggleton code (Eggleton 1971, 1972; Eggleton et al. 1973) with updates to the equation of state by Pols et al. (1995). Specifically, the fitting formulae for helium stars (provided in Section 6.1 of Hurley et al. 2002) are based on detailed models for single stars computed with the same input physics as the grid presented in Pols et al. (1998). These models assume a homogeneous initial composition with a helium mass fraction of $Y = 0.98$, a mass fraction of heavier elements of $Z = 0.02$ and no hydrogen, $X = 0$, (see Dewi et al. 2002; Dewi & Pols 2003, for a discussion).

The main disparity from our models is that we self-consistently account for the stripping process due to a binary companion, assuming a representative initial orbital period. In our models, the resulting stripped star can still contain a remaining layer of hydrogen at the surface. The effect of such a remaining layer of hydrogen is thus not accounted for in the Hurley prescriptions. A further difference is that the original stellar models behind the Hurley prescriptions were provided for only one fixed value of the metallicity. In our calculations we find large differences between stripped stars at solar and at low metallicity, which are not accounted for in the Hurley prescriptions.

The top row of Fig. 2.6 compares our results (in blue) with the Hurley prescriptions (in grey). For solar metallicity, shown in the top left panel, we find that minimum radii given by the Hurley prescription are comparable to the minimum radii we find in our detailed models. The maximum radii from Hurley et al. (2000) show a similar trend with mass as we find in our models, but we also observe significant and meaningful differences, in particular at the low-mass end (helium core masses of 2–2.5 $M_\odot$). Our models reach maximum radii of about 200 $R_\odot$, an order of magnitude larger than the maximum radii for the Hurley prescriptions, which reach only about 20 $R_\odot$.

At low metallicity, shown in the top right panel of Fig. 2.6, we find that the Hurley prescription under-estimates the minimum radii by about a factor of three. The differences are much larger for the maximum radii. The maximum radii in our models increase with increasing mass and reach radii of 400–600 $R_\odot$, which is two to three orders of magnitude larger than the maximum radii from the Hurley prescriptions. We find the largest differences in radii at the high-mass end, where our models have radii that are 500 times larger than the Hurley maximum radii. These differences are due to the presence of the remaining hydrogen layer in our stripped models, which is not accounted for in the Hurley prescriptions.

2.5.2 Example of grid based interpolations: SEVN code

An example of a code that uses interpolation within a pre-computed stellar model grid is SEVN, a grid-based population synthesis code (Spera et al. 2019) which has also been used to make predictions for gravitational wave progenitors. The stellar models behind this code are single stellar models computed with the PARSEC stellar evolution code (Bressan et al. 2012).

The bottom panels of Fig. 2.6 compare our results to those of SEVN that are closest in metallicity. In the lower left panel, we compare our solar-metallicity models (Z=0.0142) to

their models (those which assume a slightly higher value for the solar metallicity, $Z = 0.02$, which is the old canonical value for solar metallicity). In the lower right panel, we show the PARSEC models for $Z = 0.0002$, which is closest to the metallicity of Z=0.001 that we adopted for our low-metallicity grid.

We find similar general differences as described above when making comparisons with the Hurley prescriptions. For solar metallicity, we find, again, that the minimum radii are in fairly good agreement. For the maximum radii, again we note significant differences depending on the mass. We find significantly larger maximum radii of about $200\,R_\odot$, compared to about $60\,R_\odot$, for the PARSEC models at the lower mass end (for masses below about $2.7\,M_\odot$). For larger masses, the models used in SEVN reach maximum radii of 10 to 50 $R_\odot$, which is substantially larger than the maximum radii we find (of 5 to $30\,R_\odot$) in our models. Understanding the origin of these differences would require further investigation. It may be due in part to the difference in metallicity, but differences in the micro-physics or treatment of convection may also play a role. At low metallicity, we again find very large differences, similar to – but even more pronounced – than the differences we find with the Hurley prescription, as shown in the lower right panel of Fig. 2.6. We provide new analytic fits to our models for use in population synthesis calculations in Appendix A.4.

2.6 Discussion

As shown in Section 2.5, we find systematically larger radii for stripped stars than those commonly used in population synthesis calculations. The large radii can trigger additional phases of mass and angular momentum transfer (traditionally referred to as Case BB or Case BC mass transfer, Dewi et al. 2002, and references therein).

Such additional interaction can impact the final masses and orbital separation and they are, thus, important for modeling the populations of binaries. Specifically, these later phases of interaction are thought to be very important in the formation of peculiar supernovae and gravitational wave progenitors (Ivanova et al. 2003; Dewi & Pols 2003; Tauris et al. 2013). Moreover, Zevin et al. (2019) argue that these additional mass-transfer phases are necessary to explain enrichment in globular clusters, assuming that r-process enrichment primarily originates from double-neutron star systems.

A full assessment of the implications would require extended grids of models that follow these additional phases of mass transfer self-consistently. We provide a first estimate of the additional number of systems affected compared to the widely used prescriptions in Section 2.6.1. In Section 2.6.2, we discuss the question of whether the late phase of mass transfer would be stable or would lead to a common envelope phase involving a neutron star. We examine the implications for the observability of these stars in Section 2.6.3 and for supernova progenitors in Section 2.6.4. In Section 2.6.5 we discuss the main uncertainties that affect the results presented in this work.

2.6.1 Expected increase in the number of binary systems that interact with a helium donor

Whether or not the stripped star will fill its Roche lobe anew depends on the size of the Roche lobe, which scales linearly with the separation a for a given mass ratio (e.g., Eggleton 1983). The separation of a particular binary system depends on its initial separation, the amount of mass that is transferred, and the amount of angular momentum that is lost from the system during the first mass transfer. Given the large uncertainties in the mass-transfer process, the distribution of separations is not well known.

In order to make a simple estimate, we make the agnostic assumption that the separations (or, more precisely, the Roche-lobe radii) are distributed according to the standard Öpik (1924) law, which is a distribution that is flat in the logarithm. We further assume that the separations span the full "range of interest", meaning they are such that the Roche radii span from $R_{\rm min}$ to at least $R_{\rm max}$, where,

$$R_{\rm min} \equiv \min(R_{\rm min}^{\rm this\ study}, R_{\rm min}^{\rm Hurley}) \text{ and } R_{\rm max} \equiv \max(R_{\rm max}^{\rm this\ study}, R_{\rm max}^{\rm Hurley}).$$

Here we use the superscripts to indicate the origin of the minimum and maximum radii.

Assuming Öpik's law leads to the following expression for the relative number of systems that interact with our new estimates for the radial expansion, compared to what would have been obtained with the Hurley prescriptions:

$$f \approx \frac{\log R_{\rm max}^{\rm this\ study} - \log R_{\rm min}}{\log R_{\rm max}^{\rm Hurley} - \log R_{\rm min}}. \tag{2.2}$$

With this, we find that a stripped star is about twice as likely to interact relative to Hurley et al. (2000) if we consider solar metallicity progenitors in the stripped-star mass range $2 - 2.5\,{\rm M}_\odot$. At low metallicity, this fraction grows even larger due to the larger increases in radius. With this simple estimate, we find that stripped stars between 2 and $6\,{\rm M}_\odot$ are 2-30 times more likely to interact relative to the Hurley et al. (2000) prescriptions.

The numbers quoted here should be taken with a grain of salt. We have little reason to expect a logarithmically flat separation distribution to be realistic for systems that have already gone through a phase of interaction. Moreover, this simple estimate does not take into account the dependence of the low-metallicity models on the initial orbital parameters. For short enough orbits, stars at lower metallicity would lose their hydrogen-rich envelopes after the first binary interaction, leading to a smaller increase in radius (see, e.g., low-metallicity models with short orbital periods of Yoon et al. 2017). However, it is noteworthy that at low metallicity, 100% of all stripped stars computed with these initial orbital parameters will fill their Roche lobe anew (see Fig. 2.3). This is in stark contrast with what follows from the Hurley prescription that predicts no stripped stars in this mass range to fill their Roche lobe again.

2.6.2 Unstable mass transfer in systems with neutron star companions

The large radii of stripped stars may allow them to fill their Roche lobe anew and start to transfer mass to their companion. The case where the companion is already a neutron star is of particular interest since such a system is a possible immediate progenitor of a double neutron star system (e.g., Fragos et al. 2019).

When the stripped star fills its Roche lobe, its mass is still expected to exceed that of a typical neutron star of $1.4\,M_\odot$. If the mass transfer is stable, the orbit is expected to shrink because mass is transferred from a more massive star to a less massive companion (Paczyński 1971). Secondly, mass lost from the system is likely to be emitted primarily from the vicinity of the less massive neutron star. The mass lost thus likely carries a specific angular momentum that is similar to or larger than the specific orbital angular momentum of the neutron star. This is larger than the average specific orbital angular momentum and, thus, we expect the orbital separation to shrink (van den Heuvel et al. 2017).

A more dramatic shrinking of the orbit is expected when mass transfer is unstable. In this case, the neutron star becomes engulfed in the envelope of the donor (known as common envelope (CE) evolution, for a review see Ivanova et al. 2013) and the orbital separation can be shortened drastically, depending on the binding energy of the envelope and the efficiency with which it is ejected.

To know whether or not a mass transfer is unstable would require further detailed calculations. For a first estimate, we assume that unstable mass transfer occurs in these systems only if the donor star has a convective envelope. The stripped stars we consider have masses in the range of 2-6 $M_\odot$, hence, if the companion is a $1.4\,M_\odot$ neutron star, only the highest-mass of these stripped stars would canonically be expected to undergo unstable mass transfer when they have radiative envelopes.

In Fig. 2.7, we show various tracks for our stripped stars where we highlight systems with convective envelopes at the onset of mass-transfer with colors. Stripped stars with radii larger than about $200\,R_\odot$ have convective envelopes. Assuming again that these systems are distributed flat in $\log a$ implies that about a fifth of the systems would begin mass transfer with a convective envelope. However, as a caveat, we note that these stars do not develop very massive convective envelopes (see for example Fig. 2.2). We also note that if the remaining nuclear-burning lifetime is very short; Tauris et al. (2015) argue that there may not be sufficient time to complete the common-envelope inspiral before core collapse.

The top panels of Fig. 2.7 show the binding energy as a function of radius and, for reference, the corresponding separation if the companion were a neutron star. In the bottom panels of Fig. 2.7, we present the predicted post-CE separation as a function of the pre-CE separation if the mass transfer was to be unstable. For this calculation, we take the standard assumption that the orbital energy is completely converted into the binding energy of the envelope (common envelope efficiency parameter $\alpha_{\rm CE} = 1$, Webbink 1984) and that the envelope is ejected with exactly the necessary escape velocity. We compute the envelope structure parameter λ calculations in the appendix A.5.

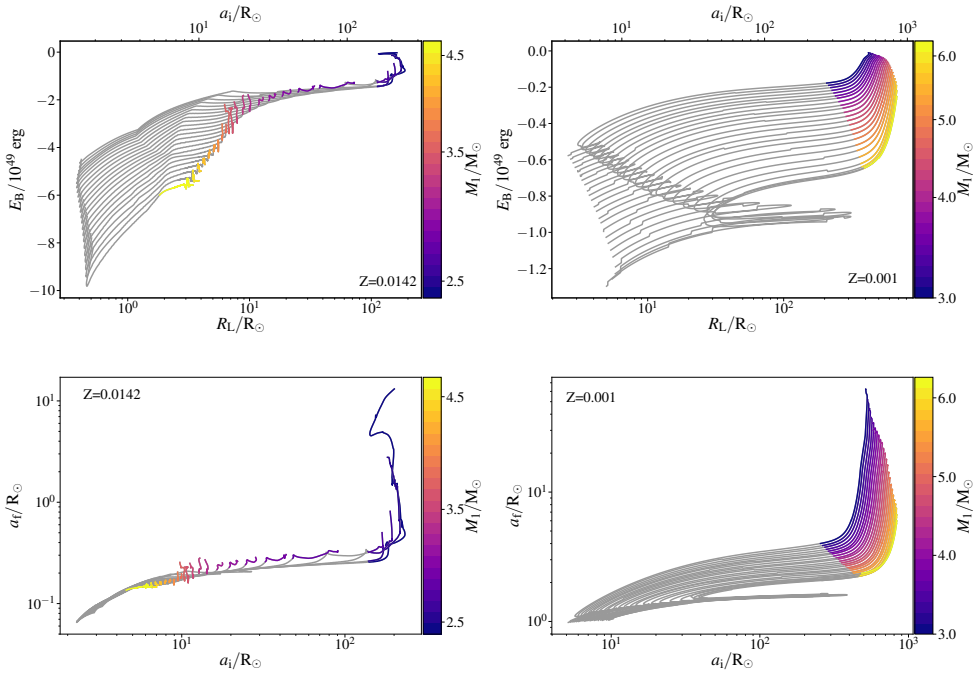

Fig. 2.7: Top: Binding energy of the envelope plotted as a function of radius. On the top x-axis we have indicated the orbital separation assuming a neutron star companion with a canonical mass of 1.4 $M_\odot$, for reference. Our solar models are shown in the top left panel where we show the binding energy of the helium envelope. Our low-metallicity models are shown in the top-right panel, where we show the binding energy of the hydrogen envelope (cf. Section 2.3.3 and Fig. 2.5). Bottom: final separation after the common envelope evolution of stripped stars with neutron star companions as a function of the initial separation at solar (left) and low (right) metallicity. Stars with a pre-CE convective envelope are marked with colors, which indicate the mass of the stripped star, assuming a common envelope efficiency parameter $\alpha_{CE} = 1$.

At low metallicity, we find that the final separation is between 2 and 3 $R_\odot$ for initial separations smaller than 300 $R_\odot$ through stable mass-transfer. This is of potential interest for studies of gravitational wave progenitors. Above these initial separations, the envelope becomes convective and the final separations reach values between 3 and 100 $R_\odot$ for the lowest mass models. These systems could become gravitational-wave sources if the final explosion marking the formation of the second neutron star results in a tighter orbit.

Our detailed simulations show strong metallicity effects which might affect the formation of double neutron stars. These effects are currently not included in the vast majority of binary population synthesis codes and may alter the rates and distributions of compact object mergers. Population synthesis simulations typically predict that double-neutron star merger rates are only very weakly metallicity-dependent (e.g., Neijssel et al. 2019).

2.6.3 Observability

Stars stripped in binaries are notoriously difficult to detect during their longest-lived phase of core helium burning with current instruments. Not only are they compact, with typical sizes of about $1\,R_\odot$, but most of their radiation is emitted in the extreme ultraviolet. Their companions typically outshine them in optical wavelengths (Götberg et al. 2017, 2018). However, this is no longer the case for the later evolutionary phases on which this work focuses. Their radius and luminosity increase until they reach giant sizes, a finding which is in agreement with previous studies (e.g., Habets 1986b; Yoon et al. 2010, 2012). Schootemeijer et al. (2018) discuss several systems which probably contain a helium-shell burning stripped star. Of those, the closest to the models we present is υ Sgr, with an inferred stripped-star mass of $2.5\,M_\odot$ (Dudley & Jeffery 1990).

All our model stars reach effective temperatures ranging from $4,000$ to $10,000\,K$, which spans typical ranges for WR stars and YSGs, while reaching the high end of the temperature range for RSGs (see Fig. 2.3). We can estimate their observational characteristics based on their composition, luminosity, and effective temperature. At high metallicity, typical spectra should be helium and nitrogen-rich, and hydrogen-poor. We expect surface gravity values ranging from $0.3 < \log_{10}\left(g/[\mathrm{cm\,s^{-2}}]\right) < 4$ (see Table A.2). As helium lines can be challenging to measure, these spectra could be confused with those from nitrogen-enhanced B-stars.

At low metallicity, typical spectra should be similar, but the amount of hydrogen varies depending on the mass-transfer history and the orbital separation. We find extremely low surface gravity values of $\log_{10}\left(g/[\mathrm{cm\,s^{-2}}]\right) \approxeq -0.4$ (see Table A.3) and expect narrow absorption features in their spectra, provided they do not experience strong mass-loss episodes. Given the lack of resolved stellar populations at such low metallicity, it may be challenging to measure spectra of systems containing such giant stripped stars with the present facilities. The Magellanic Clouds may provide examples that are sufficiently varied in composition from those of the Galaxy so that we may test the metallicity trends we describe here.

Stripped stars with the lowest effective temperatures and highest luminosities are expected to be easiest to detect at optical wavelengths. These may well dominate the total emission of their binary system. These may be observed as helium red giants (Trimble & Paczynski 1973; Yoon et al. 2012). The most promising way to detect these systems is by detecting sources that are overluminous for their (Keplerian) masses, just like the system ϕ Persei, discussed by Schootemeijer et al. (2018). These may be identified by searching for discrepancies between spectroscopic, evolutionary, and Keplerian masses, if available.

2.6.4 Supernova progenitors

Our findings are relevant for understanding the properties of core-collapse supernovae, in particular stripped-envelope supernovae of type Ibc and type IIb (for a pioneering work on the subject, see Podsiadlowski et al. 1992; for interpretations of the class-defining Type IIb SN 1993J, see Podsiadlowski et al. 1993; Nomoto et al. 1993; for recent studies see, e.g., Bersten

et al. 2012; Eldridge et al. 2015; Dessart et al. 2018; Sravan et al. 2019).

At the moment of explosion, the supernovae from our progenitor models may be classified as type Ibc or type IIb supernovae, depending on the amount of hydrogen and helium retained (see also Yoon et al. 2017). The large radii of many of our models can be identified through shock cooling signatures in early light-curves (e.g., Schawinski et al. 2008; Yoon et al. 2010; Piro & Nakar 2013). Next we discuss two potential consequences for the evolution of these stars that, at least to our knowledge, have not been previously pointed out.

Circumstellar material prior to explosion

At low metallicity, we find that the stars experience two phases of expansion. The first occurs shortly after helium depletion and is associated with hydrogen shell burning. The expansion is most significant in our models for higher mass stars, which expand by more than an order of magnitude. After this phase, the stars contract until they expand again at the end of their life. The first phase of expansion is so severe for the more massive progenitors that we expect them to briefly fill their Roche lobe. If the resulting mass-transfer event is non-conservative, we would expect an ejection of mass prior to the explosion. For the most massive progenitors, this occurs about 10,000 years before their terminal explosion. This is short enough that the ejected material may still be close enough to the star at the moment of explosion to interact with the supernova shock. If so, these systems might be progenitors of at least some type Ibn supernovae (see, e.g., Foley et al. 2007; Pastorello et al. 2007, 2008; Hosseinzadeh et al. 2019).

Asymmetric supernova progenitors

Due to the large radial expansion, we expect many stripped stars to fill their Roche lobe again shortly before their death or even at the moment they explode. This implies that the supernova progenitor is not spherical, but instead has a non-axisymmetric, "pear-like" shape as imposed by the shape of the Roche lobe. We expect this to have implications for the explosion, in particular, when the supernova shock reaches the outer layers where the deformation is strongest.

Afsariardchi & Matzner (2018) study explosions in non-spherical progenitors. They find that aspherical progenitors may have different shock-breakout signatures that are viewing angle-dependent. They further find that asphericity leads to collisions that would otherwise not have occurred and affect the observables. The case of a non-axisymmetric progenitor has not been modeled in their study. Although they argue the effects of asphericity in extended progenitors would be weak, they do not model Roche-lobe filling stars at explosion. Given that these configurations may be common, we encourage further detailed studies of these effects to be carried out.

2.6.5 Uncertainties

The evolutionary models presented in this work are affected by several uncertainties. We have considered a fixed typical initial orbital period and mass ratio. For our high-metallicity models we have verified that the exact choice of the initial orbital period and companion mass has very little effect on the maximum radius of stripped stars if varied within reasonable limits (cf. Götberg et al. 2017, 2018). At low metallicity, Yoon et al. (2010, 2017), Claeys et al. (2011), and Ouchi & Maeda (2017) show that the amount of hydrogen left at the surface of the donor star is a function of the initial orbital separation. In appendix A.3, we demonstrate that for case B mass transfer, our general findings are robust against variations of the orbital period at low metallicity.

We further emphasize that we have modeled the late evolution of stripped stars by allowing them to fully expand, since our objective was to determine their maximum radii. In reality, we expect these stars to still be in orbit around a companion star. This would truncate their expansion and initiate a new phase of Roche-lobe overflow.

We consider the effects of internal mixing by convection and overshooting. Internal mixing is one of the main uncertainties in stellar evolution and also affects our results. Yoon et al. (2017) have pointed out the importance of mixing in the region above the retreating convective core of the donor star while it is on the main sequence. The choice of overshooting, efficiency of semi-convection, and other potential mixing processes affects the details of the chemical profile. This, in turn, modifies the response of the donor star to stripping process and determines the mass of the hydrogen-rich layer that is left after the stripping process. Observations of stripped stars, for example, as proposed by Götberg et al. (2018), may help to constrain these uncertainties in the future. The presence or absence of the expansion described in Section 2.6.4, which is equivalent to a blue loop, probably depends on the treatment of internal mixing (although similar additional expansion phases can be also seen in models from Yoon et al. 2017).

When estimating the number of systems that interact anew we assume a uniform distribution of orbital separations in log space. The actual distribution of separations is uncertain and depends on both the distribution of initial separations and the amount of orbital shrinking and widening during the first phase of interaction. A more advanced assumption would be to use the output of population synthesis simulations (Dewi & Pols 2003; Ivanova et al. 2003). We include estimates for the binding energy of the envelope. These depend on the chosen definition of the core-envelope boundary (e.g., Tauris & Dewi 2001) and on the energy terms that are given (e.g., Ivanova et al. 2013). This is discussed further in Appendix A.5.

Stellar wind mass loss is also an important uncertainty for the evolution of massive stars (Smith 2014; Renzo et al. 2017). In the cases studied here, mass is primarily removed by Roche-lobe overflow and not by the stellar winds, so we do not expect a large impact on our results. However, we stress that the mass-loss rates for stripped stars are uncertain (Götberg et al. 2017, 2018; Vink 2017; Gilkis et al. 2019). This should not have a large effect on our solar-metallicity models, except perhaps for the highest mass models in our grid. The effect of

wind mass loss at low metallicity is negligible, as we demonstrate in appendix A.2.

The spatial and temporal resolutions, along with the nuclear network that we have adopted, should be sufficient for our purposes. We note that these models have not been optimized as input for supernova simulations, as this requires higher resolution, a more extended nuclear network, and calculations of the final evolutionary steps (e.g., Farmer et al. 2016). However, we will present and discuss such models in a subsequent paper (Laplace et al. in prep).

2.7 Summary and conclusion

In this paper, we study the radius evolution of stars that have lost most of their hydrogen-rich envelope due to an interaction with a companion. We consider stars with initial masses of 8–15 $M_\odot$ at solar and low metallicity. We investigate how the internal composition profile, and changes in the nuclear burning phases, are linked with the radial evolution of the star. Our results are in general agreement with previous studies. Our findings can be summarized as follows:

1. Stars stripped in binaries can swell up to giant sizes, despite having lost most of their envelope, as has also been shown in earlier studies. This implies they can fill their Roche lobe again (sometimes referred to as Case BB or BC mass transfer).

2. The maximum radius achieved strongly depends on whether or not these stars retain a hydrogen layer. At solar metallicity, mass stripping by Roche-lobe overflow is effective in removing most of the hydrogen envelope. Winds play a minor role, but they are strong enough to remove the remaining hydrogen layer. At low metallicity, all our models retain a significant hydrogen-rich envelope until the end of their evolution, which is in agreement with earlier findings.

3. At high metallicity, we find that the maximum radius (10–100 $R_\odot$) is inversely proportional to the stellar mass. It is only for the low-mass end (progenitors with initial masses between 8 and 9 $M_\odot$) that we expect stripped stars to swell enough to interact anew with their companion, which is in agreement with earlier studies.

4. At low metallicity, for case B mass transfer, stripped stars can reach sizes of up to 400-700 $R_\odot$, unless they fill their Roche-lobe anew. This maximum expansion is robust against variations of the wind mass loss and of the orbital period.

5. Population synthesis studies that rely on the Hurley et al. (2000) predictions or on interpolation of grids of detailed single stellar models do not properly account for the structure of stripped stars, in particular, the effect of a remaining hydrogen layer. We find large discrepancies at solar metallicity in the mass range important for neutron star progenitors. At low metallicity we find discrepancies for the full mass range and we expect progenitors of both neutron stars and black holes to be affected.

6. We estimate, with simple assumptions, that population synthesis studies under-predict the number of systems that interact by a factor of two at solar metallicity (for stripped stars of about 2–3 $M_\odot$). For low metallicity the discrepancy is much worse. The fraction of systems that re-interact is underestimated by a factor of 10–30 (for stripped stars of about 2–6 $M_\odot$).

7. We draw attention to an additional expansion phase that occurs exclusively in low-metallicity models shortly after central helium exhaustion. This phase is associated with hydrogen shell burning and only lasts a few thousand years. The star shrinks again briefly once helium shell-burning dominates, followed by the final expansion phase.

8. The first radius expansion we find at low metallicity may also have important consequences. The low binding energy of the hydrogen envelope suggests that mass may be ejected only a few tens of thousands of years prior to the final explosion, giving rise to a hydrogen-rich shell around the progenitor. This could impact the observable properties of the resulting supernova.

9. Many stripped stars are expected to be filling their Roche lobe at the moment their core collapses. This means that they would not be spherical at the moment they explode but instead they would have a "pear shape" enforced by their Roche lobe. This may carry interesting consequences for the observable characteristics of the final explosion.

10. Our results pose important concerns about the validity of rapid simulations of gravitational-wave sources. Our detailed simulations show metallicity effects that are not accounted for in rapid population synthesis simulations. Specifically, we expect the rates and channels for the formation of double neutron stars to be dependent on metallicity, in contrast to recent claims.

We anticipate further progress in this area as new observational constraints become available for core-collapse supernovae from transient surveys and for double compact-object mergers from gravitational-wave detectors. Robust model predictions will be needed to interpret these observations and learn about the physics of their binary progenitors. Our findings call for detailed investigations to better understand the outcome of additional mass-transfer phases in binary systems that have already experienced previous interactions.

We thank the referee Christopher Tout for detailed comments. This work has benefited from helpful input by M. Renzo and E. Zapartas. The authors further acknowledge N. Afsariardchi, J. J. Eldridge, A. Gilkis, J. Klencki, C. Matzner, T. Moriya, A. Piro, O. R. Pols, T. Tauris, J. Yongje, and S.-Ch. Yoon for useful discussions. The authors acknowledge funding by the European Union's Horizon 2020 research and innovation program from the European Research Council (ERC, grant agreement No. 715063), and by the Netherlands Organisation for Scientific Research (NWO) as part of the Vidi research program BinWaves with project number 639.042.728. YG acknowledges the funding from the Alvin E. Nashman fellowship for Theoretical Astrophysics. RF is supported by the Netherlands Organisation for Scientific Research (NWO) through a top module 2 grant with project number 614.001.501 (PI de Mink). The simulations were computed on the Dutch national e-infrastructure (Cartesius, project number 17234) with the support of the SURF Cooperative.

Chapter 3

Different to the core: the pre-supernova structures of massive single and binary-stripped stars

E. Laplace, S. Justham, M. Renzo, Y. Götberg, R. Farmer, D. Vartanyan, and S. E. de Mink

The content of this chapter has been submitted to Astronomy & Astrophysics

Abstract

The majority of massive stars live in binary or multiple systems and will interact during their lifetimes, which helps to explain the observed diversity of core-collapse supernovae. Donor stars in binary systems can lose most of their hydrogen-rich envelopes through mass transfer. As a result, not only are the surface properties affected, but also the core structure. However, most calculations of the core-collapse properties of massive stars rely on single-star models. We present a systematic study of the difference between the pre-supernova structures of single stars and stars of the same initial mass ($11 - 21\,M_\odot$) that have been stripped due to stable post-main sequence mass transfer at solar metallicity. We present the pre-supernova core composition with novel diagrams that give an intuitive representation of the isotope distribution. As shown in previous studies, at the edge of the carbon-oxygen core, the binary-stripped star models contain an extended gradient of carbon, oxygen, and neon. This layer remains until core collapse and is more extended in mass for higher initial stellar masses. It originates from the receding of the convective helium core during core helium burning in binary-stripped star, which does not occur in single-star models. We find that this same evolutionary phase leads to systematic differences in the final density and nuclear energy generation profiles. Binary-stripped star models have systematically higher total masses of carbon at the moment of core collapse compared to single star models, which likely results in systematically different supernova yields. In about half of our models, the silicon-burning and oxygen-rich layers merge after core silicon burning. We discuss the implications of our findings for the explodability, supernova observations, and nucleosynthesis from these stars. Our models are publicly available and can be readily used as input for detailed supernova simulations.

3.1 Introduction

The question of how massive stars end their lives is one of the most important in stellar astrophysics. Recent developments in supernova simulations, through the inclusion of more sophisticated physics and advancements in computational capabilities, have produced the first successful three-dimensional explosions of stars by independent groups (e.g., Takiwaki et al. 2012; Lentz et al. 2015; Melson et al. 2015; Müller 2015; Roberts et al. 2016; Kuroda et al. 2018; Ott et al. 2018; Summa et al. 2018; Müller et al. 2019; Vartanyan et al. 2019b; Burrows et al. 2019b), though the debate is still open regarding which components are essential (for a recent review, see Burrows & Vartanyan 2021). On the observational side, the rise of robotic transient surveys that are revealing an unprecedented number and diversity of supernovae, is giving us exceptional samples to compare with theoretical predictions. Examples of these facilities include ZTF (Bellm et al. 2019), LSST (Ivezic et al. 2008), DLT40 (Tartaglia et al. 2018), and ASAS-SN (Kochanek et al. 2017). For both stellar explosion models and the interpretation of supernova data, robust stellar models are required that accurately reflect our current understanding of massive star evolution.

Most massive stars live in multiple systems, and will interact with a companion during their lifetime (e.g., Sana et al. 2012). As a result of these interactions, stars can transfer their hydrogen-rich envelope to a companion star before core collapse, leading to supernovae which appear different to those which would be produced if all massive stars were single (Wheeler & Levreault 1985; Podsiadlowski et al. 1992). Transient observations have revealed a diverse population of explosions that resemble the supernovae expected from such binary-stripped stars (for a review see, e.g., Modjaz et al. 2019).

Stars which are stripped by binary interactions before they reach core collapse are also important in forming the observed population of compact-object binaries from isolated binaries (see, e.g., Bhattacharya & van den Heuvel 1991; Dewi & Pols 2003; Podsiadlowski et al. 2004; Dewi et al. 2006). Therefore understanding stripped-envelope stars, and the outcomes of their supernovae, is crucial for understanding the formation of stellar-mass gravitational-wave merger sources (for which see, eg., Abbott et al. 2016, 2017b).

Pioneering work revealed differences between single and binary-stripped stellar structures, namely, systematically less massive final cores (Kippenhahn & Weigert 1967; Habets 1986b), except for the mass range in which a second dredge-up decreases the mass of the helium core in single stars (Podsiadlowski et al. 2004; Poelarends et al. 2008). Langer (1989b, 1991b) and Woosley et al. (1993a) found that wind mass loss in pure helium stars leads to a shrinking convective core that affects the final core mass and composition. Subsequent work investigated the conditions for which envelope loss alters the final core structure enough to change whether a massive star of a given initial mass would form a neutron-star or black hole at core collapse (for early studies see, e.g., Brown et al. 1996, 2001; Wellstein & Langer 1999; Pols & Dewi 2002).

However, despite the importance of massive stripped-envelope stars and the potential effects of envelope loss on the evolution and structure of the core, the majority of detailed

stellar structures at the onset of core collapse are computed for single stars. Studies that follow the binary interaction in detail are rare. A common assumption is that the structures of binary progenitors can be adequately approximated with pure helium star models (e.g., Woosley 2019). An alternative simplifying approximation is that the outcomes following mass transfer in a binary system are equivalent to mass loss over an assumed timescale until a certain surface composition has been reached (e.g., Schneider et al. 2021).

Few calculations of binary stellar models self-consistently capture changes in the composition and interior structure through the final hydrostatic burning phases of massive stars. Instead, stellar evolution calculation of binaries are commonly stopped at earlier stages, such as the end of core carbon burning (e.g., Eldridge & Vink 2006; Yoon et al. 2010, 2017; Eldridge et al. 2018; Gilkis et al. 2019). Models of core-collapse progenitors often use a small nuclear reaction network that only approximately capture the late phases of nuclear burning (Timmes 1999; Timmes et al. 2000; recent examples include Aguilera-Dena et al. 2020; Schneider et al. 2021). In reality, after a silicon-rich core has been formed in massive stars, leptonic losses due to electron-capture processes significantly change the interior stellar structure and composition (Hix & Thielemann 1996). Such electron-capture processes can also be important in earlier phases, notably for massive stars which develop a partially degenerate core before the end of oxygen burning (Thielemann & Arnett 1985; Jones et al. 2013). Farmer et al. (2016) demonstrated the potential impact of the size of the nuclear reaction network and of the numerical resolution on the structure of pre-core-collapse models. However, appropriately extensive nuclear reaction networks are time- and memory-intensive, and thus relatively computationally expensive, therefore few suitably detailed models are available (Woosley et al. 2002; Woosley & Heger 2007; Renzo et al. 2017). This lack of detailed progenitor models matters because even small differences in stellar structure can have large consequences for the outcomes of simulations of stellar core collapse (e.g. the location of the silicon/oxygen interface, for which see Vartanyan et al. 2018).

To better understand the impact of binary interaction on the stellar structure at core collapse, a systematic comparison between the pre-supernova core structures of single stars and of stars stripped in binary systems is needed. Recent studies have presented pre-core-collapse models of stars that have lost their hydrogen-rich envelopes (Marchant et al. 2019; Woosley 2019; Schneider et al. 2021) and even their helium-rich layers (Tauris et al. 2015; Kruckow et al. 2018).

Independent groups have also explored the explodability of stars, and the distribution of remnant compact object masses, using the evolution of carbon/oxygen cores with varying carbon to oxygen mass fractions (e.g. Patton & Sukhbold 2020), or prescriptions based on the masses of carbon-oxygen cores and helium shells (Fryer et al. 2012; Ertl et al. 2016, 2020; Mandel & Müller 2020; Mandel et al. 2020). A limitation of these studies is their assumed homogeneous composition distributions, at either the start or end of core helium burning, which may not accurately capture the complex structure revealed by more detailed stellar evolution models.

In this study, we systematically compare the evolution and pre-supernova structures of

single stars and donor stars in binary systems. We present models of stars at solar metallicity with initial masses of 11 to 21 $M_\odot$ that are representative of neutron star progenitors. After core oxygen depletion we solve the stellar structure simultaneously with a nuclear network of 128 isotopes, so as to self-consistently model the burning including the evolution of the electron fraction during that phase. Following Farmer et al. (2016), we employ a sufficiently high spatial and temporal resolution to ensure a converged final helium core mass. We compare the composition structures using novel diagrams that represent the stellar structure on a two-dimensional surface and enable the visualization of the full isotope distribution. We investigate the origin of the systematic differences in structure and composition by studying details of the late-time evolution. We first review the general effect of stable mass transfer in a binary system and the differences that arise compared to the evolution of single star models of the same initial mass in Section 3.3. We present our main findings on the systematic differences in the pre-supernova density and composition structure of single and binary-stripped star models with the same core mass in Section 3.4. In Section 3.5, we investigate the origin of these differences. We discuss the implications and limitations of our findings in Section 3.6, and conclude in Section 3.7.

3.2 Method

We employed the MESA stellar evolution code (version 10398, Paxton et al. 2011, 2013, 2015, 2018, 2019) to compute stellar structure of massive stars from the beginning of core hydrogen burning until the onset of core collapse. We calculated two sets of 11 stellar models with the same initial masses of 11 – 21 $M_\odot$. The first set follows the evolution of single massive stars, while the second models the evolution of stars with the same initial masses but in a close binary system.

For the binary models, we used the same setup as in Laplace et al. (2020), in which we simplified the computation of the binary interaction by approximating the initially less massive companion star (the secondary) as a point mass with initially 80% of the mass of the primary star. We assumed mass transfer occurs conservatively such that no mass is lost during Roche-lobe overflow. We followed the time-dependent mass transfer evolution, which depends on the radial and orbital evolution of our models, computed self-consistently. We focused on binary systems undergoing the most common type of mass transfer, known as stable case B mass transfer (de Mink et al. 2008). This term designates mass exchange initiated by the primary star filling its Roche lobe after expanding during the hydrogen shell-burning phase that follows the end of core-hydrogen burning (Kippenhahn & Weigert 1967; Tutukov et al. 1973). We chose initial orbital periods between 25 and 35 d. This is not done systematically, but we believe the evolutionary stage at the beginning of mass transfer is sufficiently similar so as to not significantly affect our results (Götberg et al. 2017; Laplace et al. 2020). For these choices of binary parameters at solar metallicity, stars of 11 $M_\odot$ and above do not interact again with their companion after the first phase of mass transfer for these choices of physics

and binary parameters (Yoon et al. 2017; Laplace et al. 2020). Thus, after the primary star reached core helium depletion (defined as the moment when the central helium mass fraction in the core decreases below 10^{-4}), we only followed the evolution of the primary star.

For both the single stars and the primary stars in binary systems, we used the same choice of physical assumptions, explained in detail below.

Starting and stopping conditions – We defined the starting point of the evolution as the moment when the abundance of helium in the center increases by 5%. From this point on, we evolved the models until the onset of core collapse, which we defined as the moment when the in-fall velocity of any point within the boundary of the "iron"-rich core reaches 1000 km s^{-1} (Woosley et al. 2002). Here, "iron" includes all species for which the mass number is higher than 46. Throughout this work, we define the core boundaries as the mass coordinate where the mass fraction of the depleted element (for example ^{28}Si in the case of the "iron" core) decreases below 0.01 and the mass fraction of the most abundant element (for example "iron") increases above 0.1. We did not take rotation into account for the evolution of single stars nor the binary stars.

Metallicity and opacities – The models were computed at solar metallicity, (Z = 0.0142, Asplund et al. 2009, where Z is the mass fraction of elements heavier than helium) and we employed the opacity tables from Ferguson et al. (2005) and from OPAL (Iglesias & Rogers 1993, 1996). We assumed an initial helium mass fraction of $Y = 2Z + 0.24$ and an initial hydrogen mass fraction of $X = 1 - Y - Z$, following Tout et al. (1996) and Pols et al. (1998).

Nuclear reaction network – To obtain accurate information for the interior composition profile at the onset of core collapse, a large nuclear reaction network is needed. It allows to follow all electron-capture processes that become significant after core-oxygen depletion and that affect the core structure through lepton losses. Farmer et al. (2016) showed that only models computed with nuclear reaction networks containing at least 127 isotopes do not exhibit significant variations in their pre-supernova structure (e.g., the mass of the iron core) compared to models with larger networks. Therefore, after core-oxygen depletion, we employed a nuclear reaction network consisting of 128 isotopes (`mesa128`, Timmes 1999; Timmes et al. 2000; Paxton et al. 2011).

MESA solves the fully coupled stellar structure and composition equations simultaneously using a single reaction network (Paxton et al. 2011, 2015). This enables a self-consistent calculation of all quantities, including but not limited to the energy generation rate, the electron fraction, and the composition. We computed nuclear reactions in the stellar interior until the end of core oxygen burning with an alpha-chain network containing the 21 most important isotopes for these evolutionary phases (`approx21`, Timmes et al. 2000; Paxton et al. 2011). We note two imperfections introduced by our use of the approximate alpha-chain network in these early burning phases. The first is a consequence of `approx21` not containing any isotopes of neon aside from ^{20}Ne. In order to approximate the burning of ^{14}N to ^{22}Ne, the network adopts the construction $^{14}\mathrm{N}(\frac{3}{2}\alpha,\gamma)^{20}\mathrm{Ne}$ (for which, see Pols et al. 1995). This inevitably leads to a small systematic error in the electron fraction (Y_e) after helium burning, and also affects the later isotope distribution. This applies to all our models, but we consider that the eventual

overall effect is small. We demonstrate the size of the effect in Appendix B.1, in which we compare representative models which use our standard method to more computationally expensive models which use the full network for the whole evolution (see also, e.g., the comparisons in Sukhbold et al. 2018). We have indicated in figure captions where regions labeled as ^{20}Ne are substituting for ^{22}Ne, which occurs when the neon formed in helium-rich zones. The second issue is potentially more significant, but only for the lower-mass models in our grid. The alpha-chain network `approx21` neglects some electron-capture reactions which become important at high densities, including before the end of oxygen burning (see, e.g., Thielemann & Arnett 1985; Jones et al. 2013). This is a common approximation for core-collapse models with similarly low masses as those we study (see, e.g., Schneider et al. 2021), but is a source of systematic error. As a guide to the range in which this may be important for our results, we note that Woosley (2019) adopted a full nuclear network for helium stars with initial masses below $4.5 M_\odot$ for this reason, which roughly corresponds to our three (two) lowest-mass stripped (single) stars. We consider that this would not significantly affect the main direct paired comparisons we present, nor our main conclusions.

We chose to perform a single switch of nuclear network, rather than gradually increasing the number of isotopes taken into account for distinct evolutionary steps. This allowed us to minimize numerical artifacts that can be introduced by these switches (Renzo 2015; Renzo et al. 2017). We have visually inspected our models, to confirm that switching networks did not introduce obvious discontinuities in the evolution or artificial features in the structures. We present examples of this with Kippenhahn diagrams in Appendix B.6 (see also Appendix B.1). We employed values from Angulo et al. (1999) for the $^{12}\mathrm{C}(\alpha,\gamma)^{16}\mathrm{O}$ rate.

Mixing – For convective mixing we used the mixing length theory approximation (Böhm-Vitense 1958) with a mixing length parameter $\alpha_{\mathrm{MLT}} = 1.5$. We adopt the Ledoux criterion for evaluating stability against convective mixing and assume efficient semi-convection, with a semi-convection parameter $\alpha_{\mathrm{sc}} = 1.0$ (Langer 1991a). Due to numerical issues in the outer layers of the most massive stellar models, we treated convection using the `MLT++` scheme of MESA (Paxton et al. 2013) before core oxygen depletion. This method artificially increases the energy flux in radiation dominated convectively inefficient layers (cf. Jiang et al. 2015, 2018). We took into account convective overshooting above the core and shells by using a step overshooting parameter of 0.335 pressure scale heights, appropriate for stars in our mass range (see Brott et al. 2011). We did not assume any undershooting.

Winds – For the stellar winds, we used the "Dutch" scheme of MESA (de Jager et al. 1988; Nugis & Lamers 2000; Vink et al. 2001). For the wind mass loss of binary-stripped stars, we employed the extrapolated empirical prescription of Nugis & Lamers (2000) (for more details, see Laplace et al. 2020). The timing and amount of wind mass loss has a significant impact on the pre-collapse core structure of massive stars (Renzo et al. 2017; Gilkis et al. 2019), but we expect the binary interactions to produce a larger effect (because of the shorter timescale and higher mass loss rates). We investigate the effect of varying the wind mass loss rate in Appendix B.4.

Resolution – Numerical spatial resolution, that is, the choice of the number and minimum

step between mass shells, can affect the pre-supernova structure of stellar models (Farmer et al. 2016). Testing showed that converged values of stellar parameters (e.g., the helium core mass) could be obtained by choosing at least 1000 mass cells in each model (with an average of 5000 throughout the evolution) and ensuring that about one thousandth of the total mass be contained in each cell (`max_dq` = 10^{-3}). Our models typically contain 40,000 time steps until core oxygen depletion, and 200,000 more until core collapse. Further details can be found in our MESA inlists available online[1].

The analysis was performed with the following open-source codes: `mesaPlot` (Farmer 2020), `matplotlib` (Hunter 2007), `numpy` (van der Walt et al. 2011), `ipython/jupyter`, (Perez & Granger 2007) and `TULIPS` (Laplace 2021, subm.).

3.3 Comparison of an example single and binary evolutionary model

In this section, we review generic differences in evolution between single star models and binary models of the same initial mass. To this end, we compare the evolution of two representative models that start their evolution with the same initial mass of 11 $M_\odot$. In Fig. 3.1, we present the evolution of these models. In the bottom panels, we display evolutionary tracks on the Hertzsprung-Russell (HR) diagram and on the central density – central temperature ($\log \rho_c$- $\log T_c$) plane. We also show the evolution of the compactness parameter ξ_M, commonly used to characterize the core structure of stars (see also Section 3.5.4), defined as follows (O'Connor & Ott 2011)

$$\xi_M = \frac{M/\,\mathrm{M}_\odot}{R(M)/1000\ \mathrm{km}}\,. \tag{3.1}$$

Here, we evaluate the compactness parameter at $M = 2.5\,\mathrm{M}_\odot$, which approximately corresponds to the boundary between black hole and neutron star masses (Ugliano et al. 2012). We further show composition structure diagrams at specific times of the evolution. Since these diagrams[2] differ from standard representations of the stellar composition found in the literature, we briefly describe them here. Each color in the composition diagrams represents a different isotope. The center and edge of the shaded circles in each of the composition diagrams correspond to the center and surface of each star, respectively, and rings about the center represent intermediate mass coordinates. Specifically, the radius of each ring about the center is proportional to the square root of the Lagrangian mass coordinate. The fraction of each ring which is shaded in a particular color indicates the mass fraction of the corresponding isotope at that mass coordinate. This combination means that the total area of any color in the plot is proportional to the total mass of the corresponding isotope in the stellar model. At each mass coordinate the isotopes are ordered counter-clockwise, by increasing atomic

[1] https://doi.org/10.5281/zenodo.4506804

[2] The composition diagrams are constructed using the python package `TULIPS` that is being prepared for release as open source software, (Laplace 2021, subm.).

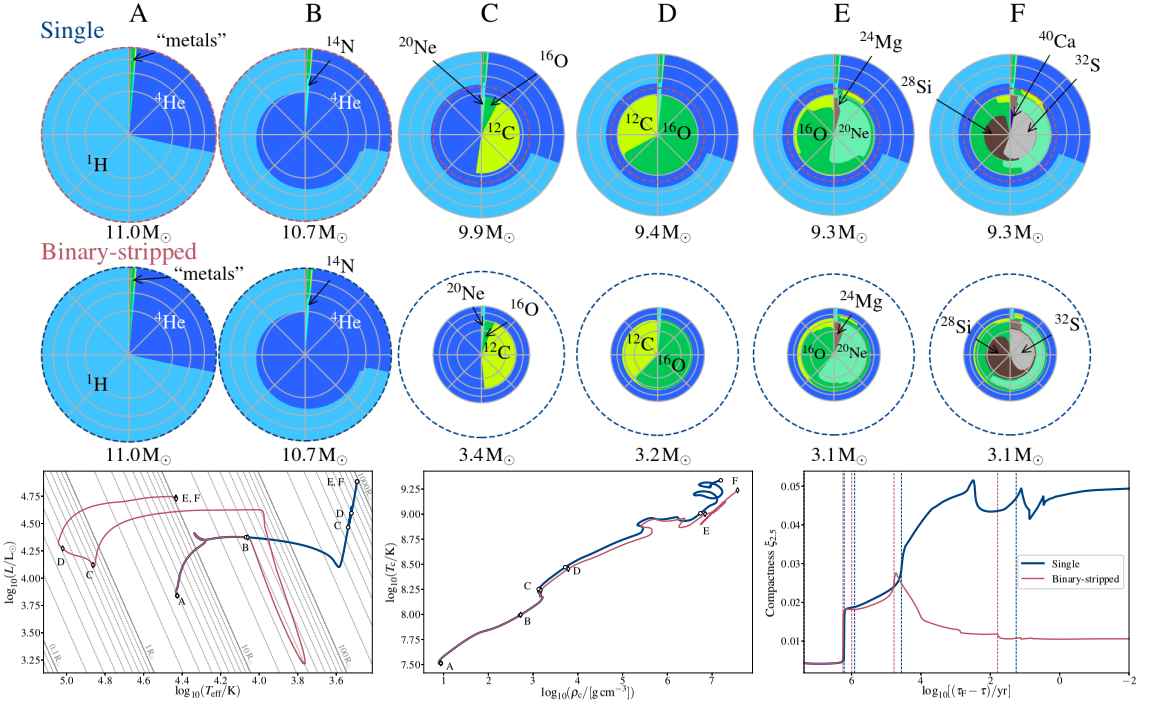

Fig. 3.1: Evolution of example single (blue) and binary-stripped star (red) models with the same initial mass of 11 $M_\odot$ until core oxygen depletion. Key moments of the evolution, discussed in Section 3.3, are marked with letters A to F. **Upper panels** - Chemical structure of the single star (*top*) and the donor star in a binary system (binary-stripped star, *bottom*) with the same initial mass of 11 $M_\odot$ at key moments of the evolution. The radial direction is proportional to the square root of the total mass of the model (see text). The total mass is given below each model. Colors indicate the local mass fraction of each isotope. The surface area spanned by each element is proportional to its total mass. The diagrams are divided into concentric rings. Each ring is a pie chart of the most abundant isotopes in the models. From outside, moving inward, gray circles mark regions containing 100, 75, 50, and 25 percent of the total mass, respectively. Lines are placed at equal intervals of 1/8 of the total fraction of isotopes. To aid the comparison, dashed blue or red circles indicate the total mass of the alternate model (single or binary-stripped) at the same stage. The neon isotope labeled in panel C would be ^{22}Ne in reality, and is only ^{20}Ne as an artifact of the `approx21` network. Likewise, for these relatively low-mass models, the isotope distribution at the end of core oxygen burning (panel F) is significantly affected by the simplifications of `approx21`. **Bottom panels** - Evolution of the single (*blue*) and binary-stripped (*red*) models in the Hertzsprung-Russell diagram (*left*) and the central density - central temperature (*center*) plane. Circles and diamonds mark important evolutionary steps for the single and binary-stripped star model, respectively. We also show the evolution of the compactness parameter (*right*) as a function of the time until core oxygen depletion. Vertical dashed lines mark important evolutionary steps.

number (and, for isotopes with identical atomic number, by increasing mass number). Nuclear fusion typically causes the mass fraction of the dominant, low atomic number, species to decrease. Hence in regions of nuclear fusion, evolutionary composition changes typically cause color patterns to move clockwise on the composition diagram[3]. To aid the comparison between different diagrams, we show dashed red/blue circles that indicate the total mass of the corresponding binary/single star model.

In the sections that follow we describe the example single and binary models at key phases of the evolution, referring to the phases labeled A-F in Fig. 3.1.

3.3.1 Early evolution until mass transfer in binary models (A – B)

The first part of the evolution, starting from the zero-age main-sequence (labeled point A in Fig. 3.1) is identical for the single star model and the primary star in the binary model. Tides and rotational effects due to the binary evolution have a negligible impact at this stage. The stars begin their evolution with a solar metallicity composition, that is, abundances of 0.7174, 0.2684, and 0.0142 for hydrogen, helium, and heavier elements, respectively (Asplund et al. 2009), as shown in the composition diagrams.

After the end of core hydrogen burning, the stars burn hydrogen in a shell and expand, as can be observed on the HR diagram in Fig. 3.1, in which the diagonal lines show loci at constant radii. At point B, the binary star fills its Roche lobe and starts to transfer matter to its companion, leading to a divergence of the evolutionary tracks on the HR diagram. At this point, the stars still have an identical chemical structure (see point B in the composition diagrams of Fig. 3.1), with a pristine composition in the outer layers and a core which is composed mainly of helium, with small mass fractions (less than 0.01) of nitrogen, which has been produced by the CNO cycle. The spiral structure visible in the center of the composition diagram (point B in Fig. 3.1) reflects the chemical gradient developed above the helium core. This is the result of the recession in mass coordinate of the convective core during core hydrogen burning. This can also be seen in the evolutionary tracks on the $\log \rho_c$- $\log T_c$ plane in Fig. 3.1, where the tracks of the single and binary star are indistinguishable between point A and B. The same is true for the compactness parameter.

3.3.2 Development of key differences until the end of core helium burning (B – D)

The donor star in the binary transfers matter to its companion and loses nearly all its outer hydrogen envelope (B – C), becoming a "binary-stripped" star and leading to a dramatic change in chemical structure and surface properties (for a detailed description see, e.g., Götberg et al. 2017; Laplace et al. 2020). This change is apparent on the composition diagrams at point C of Fig. 3.1 (see also the dashed colored circles giving the total mass of the alternate model). Meanwhile, the single star continues to expand and cool while burning hydrogen in a shell.

[3] A movie showing the changes in composition can be found at https://doi.org/10.5281/zenodo.4506804.

At point C, both models have fused roughly half of the helium inside their cores. This is the moment when the central temperature and density conditions of the stars start to diverge (see the $\log \rho_c$- $\log T_c$ diagram and compactness parameter evolution in Fig. 3.1). At the same evolutionary stage (C), the binary-stripped star has a slightly denser and cooler core than the single star, because from this point on, the binary-stripped star behaves, to a first approximation, like the core of a star with a lower initial mass (cf. Kippenhahn & Weigert 1967).

At the end of core-helium burning (D, defined as the moment when the central helium mass fraction drops below 10^{-4}), the helium core mass of the single star model is larger than that of the binary-stripped star (see the dashed circle on the composition diagram at point D in Fig. 3.1). This can be explained by two effects: (1) the helium core mass of single stars increases due to the creation of helium by the hydrogen burning shell (e.g., Woosley 2019); (2) the binary-stripped star loses mass due to winds, leading to a decrease of the helium core mass (see also Appendix B.2). At core helium depletion, the core composition differ significantly between the models (see the composition diagrams at point D in Fig. 3.1). While the cores of both the single and the binary-stripped star model are composed of the same products of core helium burning (namely carbon, oxygen, and neon), the relative ratios of these elements are different. The mass fraction of carbon is larger in the binary-stripped star with an abundance of 0.38 compared to 0.33 for the single star. In contrast, the mass fraction of oxygen is smaller for the binary-stripped star model, 0.60 compared to 0.65 for the single star. This is caused by differences in the mass and density of their cores and by the distinct behavior of their convective cores during core helium burning (cf. Langer 1989b; Woosley et al. 1993a; Brown et al. 2001). Higher core masses and lower densities, together with a growth of the convective helium-burning core, favor a more efficient destruction of carbon through alpha captures in single-star models and leads to the observed differences in central carbon and oxygen mass fractions (Woosley et al. 1993a; Brown et al. 2001, see Section 3.5.1 for more details).

The binary-stripped star model develops an extended carbon/oxygen gradient at the edge of the core (visible on the composition diagram as the lime colored outer "arm" at the bottom of the dark green region at point D in Fig. 3.1). This is due to the convective core shrinking during core helium burning as a result of wind mass loss (Langer 1989b; Woosley et al. 1993a, for more details, see Section 3.5.1 and Appendix B.4). At core helium depletion, the compactness parameter reaches a value of 0.03 for both the single and binary-stripped star models.

3.3.3 Evolution after core helium depletion (D – F)

After the end of core helium burning, both stars expand again while burning helium in a shell (labeled D – E in Fig. 3.1) and reach their final location on the HR diagram[4]. The stars enter the final burning stages of heavier elements, starting with core carbon burning, and the evolution accelerates due to neutrino losses (e.g., Fraley 1968). During this phase, a large

[4] Assuming no dynamical transient happens shortly before core-collapse (e.g., Shiode et al. 2012; Khazov et al. 2016; Fuller 2017; Fuller & Ro 2018)

difference in the evolution of the compactness parameter can be observed in Fig. 3.1. The compactness value of the binary-stripped star model decreases, while it increases for the single star model. This reflects the change in radius evaluated at the same mass of $2.5\,M_{\odot}$.

The previously built-up chemical composition differences remain until the end of core carbon burning (labeled E in Fig. 3.1, which marks the moment when the central mass fraction of carbon drops below 10^{-4}). The binary-stripped star model is less abundant in oxygen and more abundant in neon and magnesium than the single star. This can be attributed to the different composition at the beginning of core carbon burning and to the different burning conditions during core carbon burning as shown in $\log \rho_c$- $\log T_c$ diagram in Fig 3.1. The compactness parameter of the single star shows two prominent maxima, after each of which the compactness parameter decreases significantly. These maxima are coincident with instances of off-center carbon ignition (as shown in Appendix B.6). Such off-center burning has previously been found to be important for compactness evolution (cf. Fig. 7 of Renzo et al. 2017, see also Sukhbold & Woosley 2014).

The composition profiles become increasingly different during this phase of the evolution (E – F, where F we define as the moment when the central oxygen mass fraction drops below 10^{-4}). During this stage, the stars develop a central core mainly composed of silicon, sulfur, and calcium. In the single star model, the mass fraction of silicon is lower than in the binary-stripped model. In contrast, the mass fraction of sulfur and calcium is larger in the single star model compared to the binary-stripped star model.

When massive stars reach oxygen depletion (labeled F in Fig. 3.1), they have less than a few days left to live (e.g., Woosley et al. 2002). This is the moment when oxygen shell-burning followed by core and then shell silicon burning, occur. Immediately after, the iron-rich core begins to collapse. At this point we stop our models, since the high density and extremely neutron-rich material requires a nuclear equation of state and detailed treatments of the neutrino physics. Kippenhahn diagrams that show the entire evolution of the stellar structure for these two example models can be found in Fig. B.12 of the Appendix.

3.4 Differences between single and binary-stripped models at core collapse

In the previous section we compared single and binary-stripped star models with the same initial mass. In this section, we compare the properties of models with similar core masses. This is because the explosion properties are mainly determined by the mass of their carbon/oxygen cores (e.g., Woosley et al. 2002; Farmer et al. 2019). We define the reference core mass as the mass of the helium core at the end of central helium burning. The boundary of the helium core is set as the mass at which the mass fraction of hydrogen decreases below 0.01 and the mass fraction of helium is larger than 0.1. We discuss the robustness of this definition in Appendix B.2.

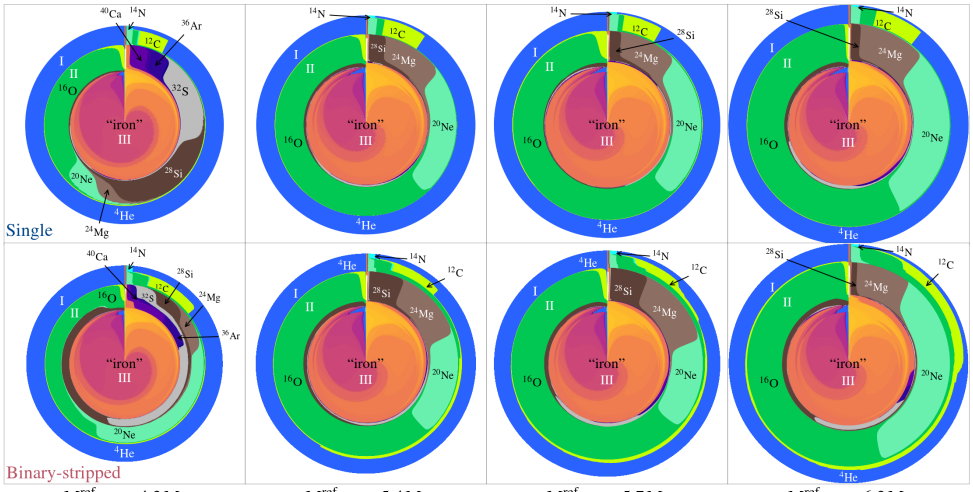

Fig. 3.2: Final composition profiles of selected single (top row) and binary-stripped (bottom row) star models at the onset of core collapse. We show four example models with similar reference core masses, indicated below each column. The diagrams are constructed in a similar fashion as Fig. 3.1, with each color representing an isotope and the surface area spanned by this color being proportional to the mass of this isotope in the star. The radius of each diagram is proportional to the final helium core mass. The hydrogen-rich envelope of single stellar models is not shown. Three prominent regions are marked with roman numerals: I) a helium-rich layer, II) an oxygen-rich layer, and III) an inner iron-rich zone. The lowest-mass example models (left-most column) both show enhanced mass fractions of heavy elements in the oxygen-rich region (II) due to shell merger events. Binary-stripped star models contain an extended carbon/oxygen gradient at the edge of the oxygen-rich region (II) that is absent in single star models.

3.4.1 Composition at core collapse

In Fig. 3.2 we show the interior composition at core collapse of selected single-star models (top row) and binary-stripped star models (bottom row). We select four pairs of models with similar reference core masses of $M^{ref}_{He\,core} \simeq 4.3, 5.4, 5.7, 6.3\,M_\odot$ (see also Table 3.1). We focus on the composition inside the helium core. The radius of each diagram is proportional to the total helium core mass. The hydrogen-rich outer layers in the single star models are not shown for clarity. These diagrams naturally bring into focus three distinct regions that contain a significant fraction of the total mass of the star, given below.

I: Helium-rich layer: This region is mainly composed of ^{4}He. At the outer edge, the ashes of the CNO cycle can be observed with mass fractions of 0.99 for ^{4}He, and up to 0.01 for ^{14}N. Moving inwards, ^{4}He still makes up the largest mass fraction of the region, up to 0.75. The rest of the mass is contained in the products of helium burning, namely ^{12}C, ^{16}O, and ^{20}Ne, in order of decreasing mass fraction. At the inner edge of this region, binary-stripped stars exhibit a composition gradient that is not present in single stars due to the shrinking of the convective core during helium burning (see Section 3.5.1).

II: Oxygen-rich layer: This region is mainly composed of ^{16}O, but also ^{20}Ne, ^{24}Mg, and ^{28}Si with typical mass fractions of about 0.6, 0.2, 0.06, and 0.02, respectively. The exact distribution differs between single and binary-stripped star models with similar reference core masses. In the models with reference core masses of 4.3 $M_\odot$ (left-most column in Fig. 3.2), isotopes such as ^{36}Ar and ^{40}Ca have been mixed outwards into this region (due to shell mergers, see Section 3.4.2).

III: Iron-rich region: This is the center-most region, mainly composed of iron-group isotopes (with atomic mass numbers from 52 to 62). The composition diagrams show a clear, smooth, spiral pattern in the center (Fig. 3.2). This is because isotopes with higher mass numbers (for example ^{58}Fe) are more abundant in the inner-most layers, while light iron-group isotopes (for example ^{54}Fe) are more abundant at the outer edge of the core. Note also the presence of ^{4}He (in blue) produced by late photodisintegration. At the edge of this region, a small fraction of ^{28}Si and products of incomplete ^{28}Si burning such as ^{32}S, ^{36}Ar, and ^{40}Ca is present. It can be identified as a narrow ring around the iron-rich region in the composition diagrams. This ring is more extended in mass for binary-stripped star models than for single stars, indicating binary-stripped stars have higher mass fractions of ^{28}Si and its burning products at the edge of the iron-rich core than their single star counterparts.

Not all the material shown at the moment captured in Fig. 3.2 will be ejected during the supernova. Almost all of region III becomes enclosed in the compact object that forms in the center. The layers above the iron-rich core are mixed and reprocessed by the supernova shock, creating new isotopes through supernova nucleosynthesis, in particular almost all iron-group elements ejected.

In Table 3.1, we give detailed values of core masses and masses of the most important isotopes present at the onset of core collapse. Composition diagrams for the full set of models at the moment of core collapse are shown in Appendix B.3.

3.4.2 Shell mergers

About half of our models experience "shell merger" events, where a convective burning shell merges with the layers above. In our models, we find that the silicon-burning shell merges with the oxygen-rich layers above in the final day before core collapse. This has been found in some three-dimensional core-collapse calculations (e.g., Couch & Ott 2013; Collins et al. 2018; Yoshida et al. 2020; Andrassy et al. 2020; Yadav et al. 2020; Fields & Couch 2020; McNeill & Müller 2020, for a discussion of the uncertainties, see Section 3.6.5). The result is that a high temperature layer containing silicon and its burning products is mixed into a lower-temperature region mainly composed of un-burned oxygen, neon, and magnesium isotopes. This produces alpha particles which, in turn, lead to enhanced alpha-capture reactions that result in high abundances of ^{28}Si, ^{32}S, ^{36}Ar, and ^{40}Ca in the oxygen-rich layer (region II of Fig. 3.2), at the expense of ^{16}O, ^{20}Ne, and ^{24}Mg.

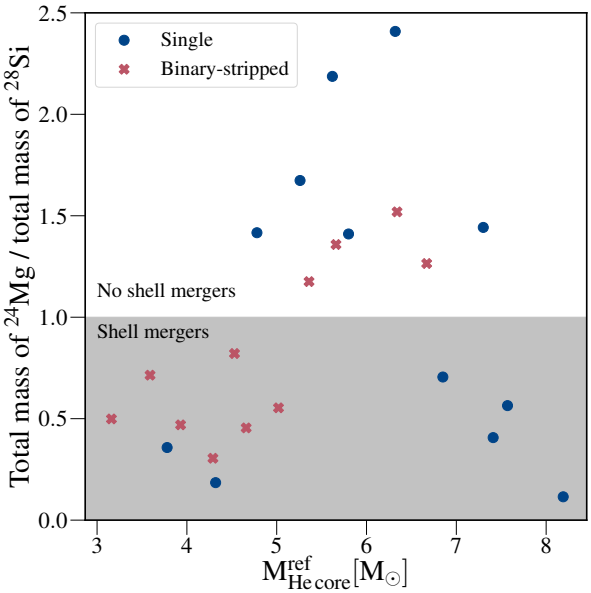

Fig. 3.3: Ratio of the total mass of ^{28}Si and ^{24}Mg at the onset of core collapse as a function of the reference core mass for single (blue) and binary-stripped (red) progenitors. Models with a ratio below one experience shell mergers (gray region). In our models, the occurrence of shell mergers is related to the helium core mass after helium burning.

In Fig. 3.3, we show the ratio of the total mass of ^{24}Mg and ^{28}Si at the onset of core collapse as a function of the reference core mass. Models for which this ratio is lower than one (more ^{28}Si than ^{24}Mg) have experienced shell mergers (see also Appendix B.5). We find that shell mergers occur mainly for the lowest and highest mass models in our grid, although the robustness of this trend is not clear. Most models with reference core masses lower than about 5 $M_\odot$ or higher than 6.8 $M_\odot$ experience shell mergers.

In Fig. 3.4, we show the distribution of ^{40}Ca in the interior of all models at the moment of core collapse as a function of initial mass. We show the profiles of single and binary-stripped star models in the top and bottom panels, respectively. Models with shell mergers have a higher ^{40}Ca abundance outside the silicon core. The presence of ^{40}Ca in the oxygen-rich region can have important observational consequences, which might allow for observational tests of the physical nature of shell mergers (see the discussion in Section 3.6.2).

3.4.3 Final total masses of isotopes for single and binary-stripped stars

Differences in composition at the onset of core collapse are important indicators for differences in chemical yields. In Fig. 3.5, we show the total mass of selected isotopes at the end of the evolution integrated throughout the star as a function of the reference core mass. After the explosion, some of the isotopes will be reprocessed by the supernova shock or become part of the compact object that will form in the center, but the exterior layers (where, $\rho \lesssim 10^6\,\mathrm{g\,cm^{-3}}$)

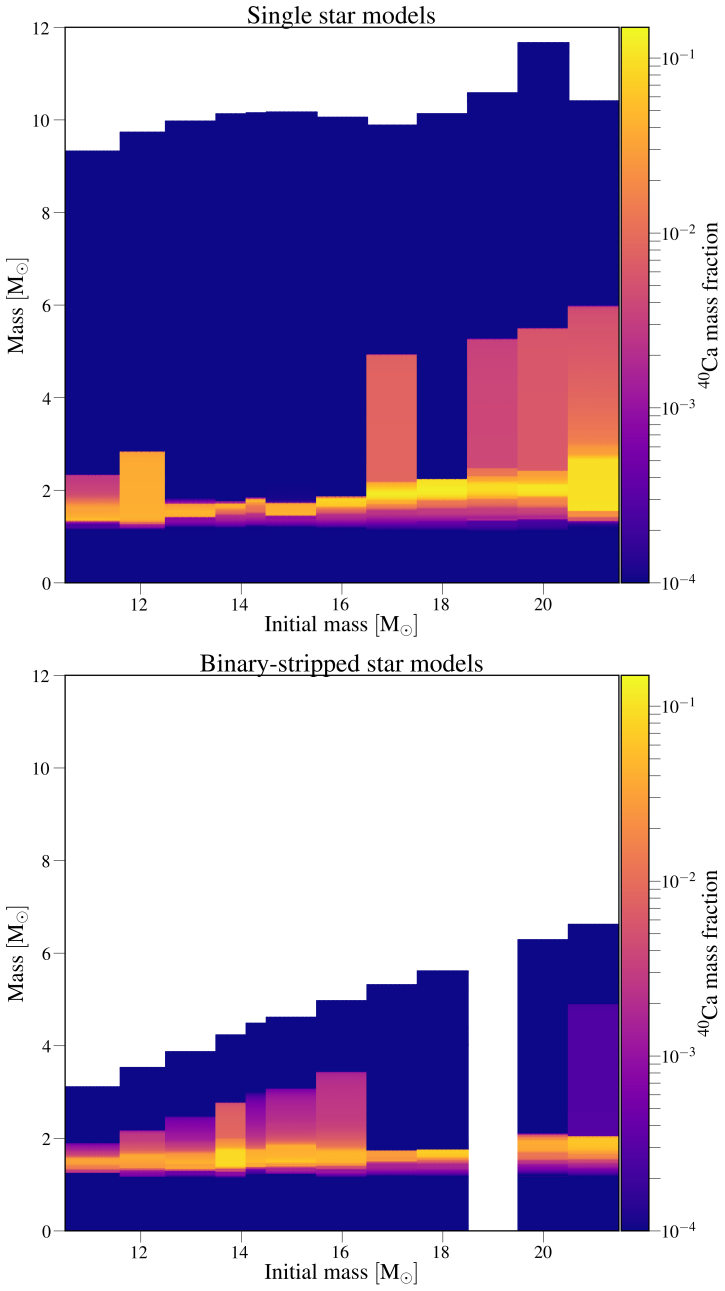

Fig. 3.4: Distribution of ^{40}Ca in the interior of all stellar models as a function of their mass (top: single stellar models, bottom: binary-stripped stars). All models, represented as bars, are shown as a function of their initial mass. The length of each bar gives the mass of this model at the onset of core collapse. The binary-stripped star model with an initial mass of 19 $M_\odot$ is not shown because it did not reach core collapse due to numerical issues.

Table 3.1: Core masses and total masses of the most abundant isotopes at the onset of core-collapse for stars stripped in binaries and single stars with the same initial masses. These models are for solar metallicity (Z = 0.014).

$M_{\rm init}$ [$M_\odot$]	$M_{\rm CC}$ [$M_\odot$]	$M_{\rm He\,core}$ [$M_\odot$]	$M_{\rm CO\,core}$ [$M_\odot$]	$M_{\rm Si\,core}$ [$M_\odot$]	$M_{\rm Fe\,core}$ [$M_\odot$]	$M_{^1\rm H}$ [$M_\odot$]	$M_{^4\rm He}$ [$M_\odot$]	$M_{^{12}\rm C}$ [$M_\odot$]	$M_{^{14}\rm N}$ [$M_\odot$]	$M_{^{16}\rm O}$ [$M_\odot$]	$M_{^{20}\rm Ne}$ [$M_\odot$]	$M_{^{24}\rm Mg}$ [$M_\odot$]	$M_{^{28}\rm Si}$ [$M_\odot$]	$M_{^{32}\rm S}$ [$M_\odot$]	$M_{^{36}\rm Ar}$ [$M_\odot$]	$M_{^{40}\rm Ca}$ [$M_\odot$]	$M_{\rm Fe}$ [$M_\odot$]
Binary stripped stars																	
11.0	3.11	3.11	1.88	1.43	1.32	0.00018	1.13	0.062	0.0060	0.20	0.05	0.05	0.11	0.05	0.008	0.0074	0.54
12.1	3.52	3.52	2.09	1.49	1.33	0.00046	1.21	0.095	0.0045	0.27	0.11	0.07	0.10	0.06	0.013	0.0129	0.62
13.0	3.87	3.87	2.46	1.42	1.32	0.00034	1.25	0.104	0.0064	0.49	0.18	0.1	0.20	0.103	0.019	0.0137	0.46
14.0	4.23	4.23	2.57	1.38	1.27	0.00020	1.28	0.128	0.0064	0.49	0.33	0.08	0.26	0.201	0.044	0.0479	0.46
14.6	4.48	4.48	2.99	1.47	1.37	0.00020	1.29	0.14	0.0044	0.73	0.33	0.16	0.19	0.103	0.021	0.0191	0.55
15.0	4.61	4.61	2.44	1.47	1.36	0.00026	1.28	0.167	0.0033	0.72	0.47	0.09	0.2	0.137	0.029	0.0247	0.55
16.0	4.97	4.97	3.42	1.47	1.33	0.00027	1.28	0.175	0.0052	1.04	0.27	0.19	0.35	0.154	0.026	0.0222	0.55
17.0	5.31	5.31	3.73	1.71	1.47	0.00063	1.29	0.193	0.0063	1.34	0.36	0.27	0.23	0.051	0.009	0.0069	0.67
18.0	5.61	5.61	2.49	1.65	1.46	0.00058	1.25	0.226	0.0051	1.56	0.35	0.32	0.24	0.059	0.014	0.0134	0.70
20.0	6.28	6.28	4.60	1.80	1.52	0.00064	1.16	0.345	0.0032	1.68	0.82	0.26	0.17	0.08	0.016	0.0134	0.82
21.0	6.62	6.62	4.07	1.82	1.54	0.00085	1.07	0.430	0.0007	1.98	0.68	0.34	0.27	0.125	0.027	0.023	0.72
Single stars																	
11.0	9.32	3.78	2.31	1.44	1.32	3.79	2.95	0.113	0.0211	0.42	0.11	0.09	0.25	0.127	0.021	0.0173	0.49
12.1	9.73	4.33	2.81	1.31	1.26	3.68	3.01	0.121	0.0185	0.57	0.12	0.07	0.37	0.273	0.06	0.0596	0.44
13.0	9.97	4.79	3.19	1.53	1.41	3.52	3.04	0.123	0.0167	1.01	0.29	0.20	0.14	0.047	0.011	0.0114	0.58
14.0	10.12	5.28	3.60	1.67	1.47	3.27	3.03	0.137	0.0145	1.23	0.42	0.23	0.14	0.037	0.008	0.0066	0.71
14.6	10.15	5.63	3.90	1.70	1.51	3.03	2.98	0.169	0.0147	1.36	0.50	0.24	0.11	0.035	0.008	0.0071	0.8
15.0	10.16	5.82	4.07	1.69	1.44	2.9	2.96	0.158	0.014	1.61	0.37	0.29	0.20	0.046	0.011	0.0113	0.62
16.0	10.05	6.34	4.47	1.71	1.5	2.44	2.84	0.147	0.0124	1.68	0.74	0.31	0.13	0.061	0.016	0.0162	0.75
17.0	9.88	6.87	4.97	1.85	1.58	1.94	2.72	0.188	0.0106	1.82	0.6	0.22	0.31	0.234	0.081	0.0607	0.77
18.0	10.13	7.32	5.42	1.89	1.62	1.78	2.71	0.178	0.0102	2.10	0.78	0.33	0.23	0.154	0.042	0.0492	0.81
19.0	10.58	7.42	5.49	1.97	1.65	1.84	3.04	0.209	0.0143	2.04	0.72	0.14	0.35	0.262	0.086	0.048	0.83
20.0	11.66	7.59	5.67	1.96	1.63	2.50	3.26	0.204	0.0148	2.06	0.67	0.23	0.41	0.308	0.089	0.0617	0.84
21.0	10.40	8.21	6.20	1.54	1.40	1.00	3.00	0.228	0.0146	2.31	0.72	0.07	0.65	0.547	0.142	0.1503	0.58

Notes. We define the core boundaries as the mass coordinate where the mass fraction of the depleted element (for example ^{1}H in the case of the helium core) decreases below 0.01 and the mass fraction of the most abundant element (for example ^{4}He) increases above 0.1. In the case of the CO core, we calculate the maximum between the values of the ^{12}C and ^{12}O core boundary values. For the mass of iron ($M_{\rm Fe}$) we have added the mass of ^{52}Fe, ^{53}Fe, ^{54}Fe, ^{55}Fe, ^{56}Fe, ^{57}Fe, and ^{58}Fe. Of these isotopes, ^{54}Fe, ^{56}Fe, and ^{58}Fe dominate and contribute with similar amounts.

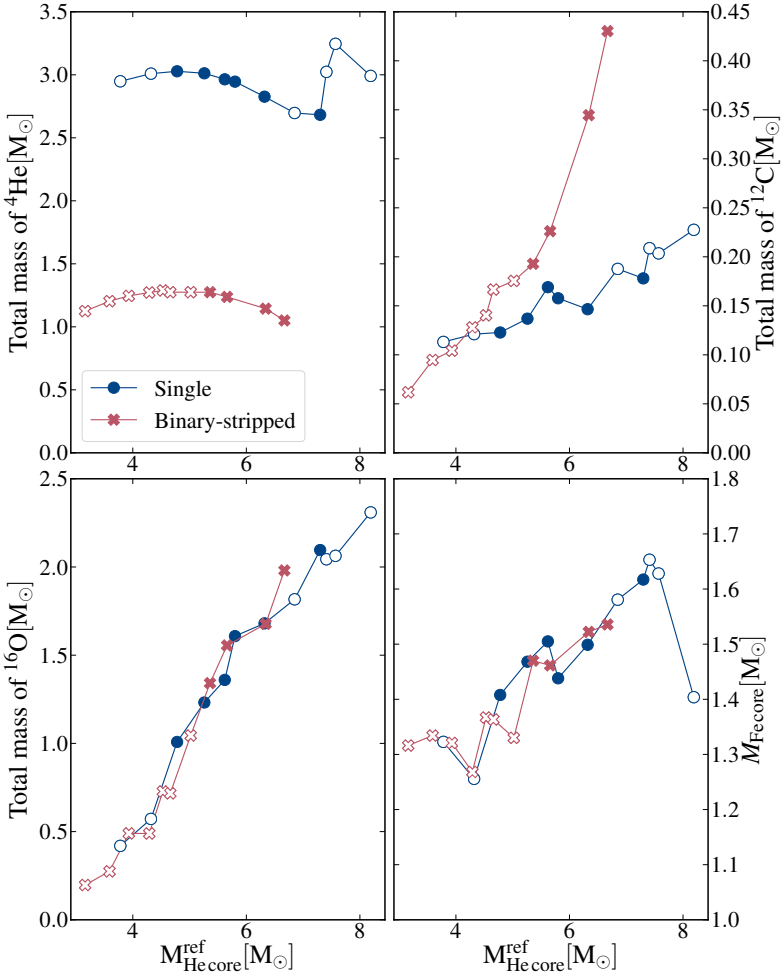

Fig. 3.5: Composition and core properties of single (blue circles) and binary-stripped (red crosses) star models at the moment of core collapse as a function of the reference core mass. Open symbols indicate models that experienced a shell merger event. From top to bottom and left to right: total masses of ^{4}He, ^{12}C, and ^{16}O outside the iron core. The final panel shows the iron core mass.

will leave the star relatively unaffected by the explosion.

Final total mass of helium outside the iron-rich core: The amount of ^{4}He outside the iron-rich core is systematically lower in binary stripped stars compared to single stars (on average, 3 M$_\odot$ for single stars and compared to 1 M$_\odot$ for binary-stripped star models). This is the combined effect of the quenched H-burning shell which does not produce as many ashes in the binary-stripped models, and the stellar winds which tap directly into the helium-rich material for the binary-stripped stars with core mass larger than 7 M$_\odot$.

Final total mass of carbon outside the iron core: Binary-stripped star models in our grid

tend to have higher masses of ^{12}C at the end of their life than the single star models (see top right panel of Fig. 3.5). Below reference core masses of 4.5 $M_\odot$, binary-stripped stars and single stars contain similar masses of ^{12}C above the iron core. For higher masses, the total amount of ^{12}C in binary-stripped star models is significantly higher than their single star counterparts, and the difference increases for more massive models, where the binary models have more than twice as much ^{12}C. We discuss the origin of this difference, the retreat of the convective helium-burning core due to wind-mass loss in binary-stripped stars, in Section 3.5.2.

Final total mass of oxygen outside the iron core: The final total mass of ^{16}O is similar for the single and binary-stripped star models (see bottom left panel of Fig. 3.5). This is because, even though the reactions involved in the creation and destruction of ^{16}O are fractionally different in single and binary-stripped stars, they compensate each other in a similar way. We discuss this further in Section 3.5.2. The total mass of ^{16}O increases linearly with the reference core mass and does not depend on the occurrence of shell mergers.

Final iron core mass: Overall, the iron core mass is similar for all models, with masses from 1.25 to 1.65 $M_\odot$. Here, "iron" includes all species for which the mass number is higher than 46, and the core boundary is computed with respect to ^{28}Si. The iron core mass increases slightly with an increasing reference core mass, except for the most massive single star model. Binary-stripped and single stellar models have similar iron core masses that range from 1.3 and 1.63 $M_\odot$.

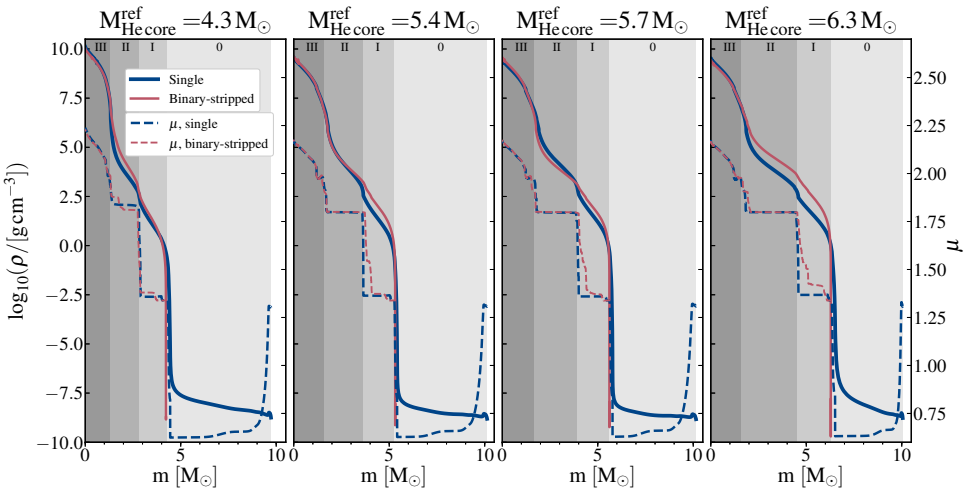

Fig. 3.6: Density profiles at the moment of core collapse for single (blue) and binary-stripped star models (red) with similar reference core masses. The mean molecular weight profiles are indicated with dashed lines. From left to right, shaded regions give the approximate locations of the iron-rich, oxygen-rich, helium-rich, and hydrogen-rich regions, labeled with Roman numerals as in Fig. 3.2. The left-most models, with a reference core mass of 4.3 $M_\odot$, both experience shell mergers during their evolution. The density of the binary-stripped star models in the helium-rich region (I) is systematically higher than that of the single star models with a similar reference core mass.

3.4.4 Density profiles

We find systematic differences in the final density and mean molecular weight profiles of single and binary-stripped star models with similar reference core masses. These differences are of particular importance because even small differences in the density profile have been shown to have a large impact on the explodability of stars (e.g., Vartanyan et al. 2019b). In Fig 3.6, we show the density and mean molecular weight profiles at the onset of core collapse as a function of the mass coordinate for the same example models as in Fig. 3.2.

Overall, the density profiles span similar values for single and binary-stripped star models with the same reference core mass, with central densities of about 10^{10} g cm^{-3}, dropping by almost 20 orders of magnitude throughout the star. However, binary-stripped stars have steeper density profiles at the inner edge of the helium-rich region (at the boundary of regions 0 and I) compared to single star models due to the absence of a hydrogen-rich layer in the binary-stripped stars. In addition, we find that binary-stripped star models have a systematically higher density in the helium-rich region (I) compared to the single star models. At the same mass coordinates, we also find large differences in the mean molecular weight profiles: binary-stripped star models display a shallow drop of the mean molecular weight, whereas single star models contain sharp drops in the mean molecular weight profile. The difference in the mean molecular weight profiles can be attributed to the presence of a carbon/oxygen gradient at the edge of the oxygen-rich region (see Section 3.5.1).

In the oxygen-dominated layers (II), no such trends can be found. Instead, we find that single and binary-stripped star models have large differences in density. At the inner edge of this region, the mean molecular weight reaches a small peak that is linked to the presence of a small silicon-rich layer at this location (see also Fig. 3.2). In the inner-most iron-rich region (III), the density profiles show similar trends. At the surface of the single-star models, the mean molecular weight increases due to recombination of elements.

3.4.5 Properties of the helium core

We present final properties of the helium core in Fig. 3.7. For the same reference core masses, the radius of the helium core is systematically larger for the binary-stripped star models (1.3 to 11.6 $R_\odot$) compared to the single star models (0.6 to 1.2 $R_\odot$). This trend in radius remains for different definitions of the helium core mass (see Appendix B.2). For both the single and binary-stripped star models, the helium core radii decrease with increasing reference core mass. For binary-stripped stars, this trend in radius at solar metallicity is well known (Yoon et al. 2010, 2017).

The final mass of the helium core increases linearly with the reference core mass, i.e. the mass of the helium core at the end of core helium burning, for both the single and binary-stripped star models. A small offset can be observed between the highest-mass binary-stripped star models and the single star models. These are due to the effect of wind mass loss for the binary-stripped stars and to the growth of the helium core after core helium depletion for

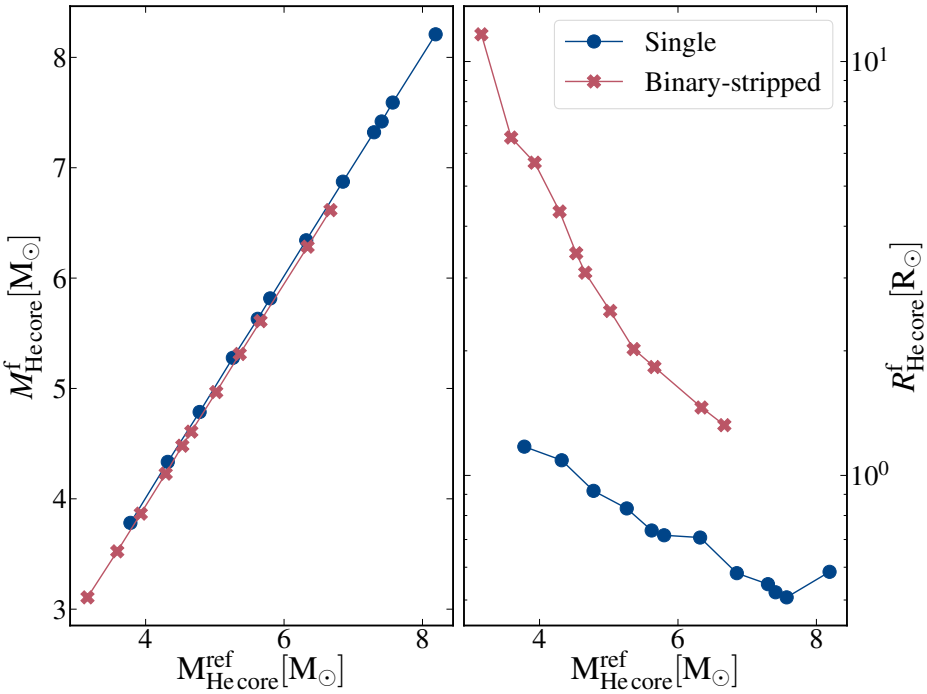

Fig. 3.7: Final helium core mass and radius of single star models (blue circles) and models of stars stripped in binaries (red crosses) at the onset of core collapse as a function of the reference core mass.

the single stars (see also Section 3.3.2 and the evolution of the helium core mass shown in appendix B.2.1).

3.5 Origins of differences between single and binary-stripped star progenitors

In the previous sections, we showed that binary-stripped star models develop systematically smaller helium core masses than single stars with the same initial mass. Since interior properties of stars strongly depend on the core mass, internal differences between these models are expected. What can appear surprising, however, is that the final core properties of single and binary-stripped stars are also different when comparing models with *similar helium core masses*. The origin of these differences is mainly linked to the rate and timing of mass loss, which cannot easily be modeled starting from a naked helium core. We explore these origins mainly with two models, an initially 16 $M_\odot$ single star and a star with an initial mass of 20 $M_\odot$ that is stripped in a binary system before core helium depletion. Both develop a reference core mass of 6.3 $M_\odot$ at the end of core helium burning, and as such, are well suited for a

comparison.

3.5.1 The chemical gradient around the helium-depleted core

Helium burning proceeds differently in the cores of binary-stripped stars and those of single stars, even in cores of similar mass (cf. Woosley et al. 1995). Helium is mainly destroyed through two channels: (1) the triple-alpha process (2) alpha captures onto carbon that create oxygen. The reaction rates of both reactions have a different dependence on the density ρ and on the abundance of ^{4}He nuclei, $X_{\rm He}$. For the triple alpha process, the reaction rate $r_{3\alpha}$ scales with the density cubed:

$$r_{3\alpha} \propto X_{\rm He}^3 \rho^3, \tag{3.2}$$

while the rate of alpha captures onto carbon, $r_{C\alpha}$, is proportional to the density squared:

$$r_{C\alpha} \propto X_{\rm C} X_{\rm He} \rho^2, \tag{3.3}$$

where $X_{\rm C}$ is the abundance of ^{12}C (e.g., Burbidge et al. 1957). As we show in Fig. 3.8, convective helium-burning cores *grow* in mass during core helium burning for single stars due to hydrogen shell burning (see Section 3.3.2), while they *decrease* in mass for binary-stripped stars due to wind mass loss (Langer 1989b, 1991b; Woosley et al. 1993a). For single stars, the growth of the convective helium-burning core brings an additional supply of helium that favors the destruction of carbon through alpha captures (see Eq. 3.3). As a result, the mass fraction of oxygen is higher in the cores of single stars compared to the cores of binary-stripped stars, at the expense of carbon, even for the same reference core mass. The exact fraction of carbon and oxygen is subject to the still uncertain rate of the alpha-capture reaction onto carbon (Weaver & Woosley 1993; Brown et al. 1996; Farmer et al. 2020).

This is illustrated in Fig. 3.9, where we show a subset of composition diagrams at the moment of core helium depletion (when the central mass fraction of helium decreases below 10^{-4}) for single and binary-stripped star models in our grid. We highlight the differences in the central mass fractions of carbon and oxygen, which are indicated on each composition diagram. Models with the same initial mass are shown in each column. We indicate two sets of single and binary-stripped models, $S_{1,2}$ and $B_{1,2}$, respectively, that reach similar reference core masses at the end of core helium burning (marked with the same background color). For both sets, the central carbon mass fractions are smaller in the single star models (0.31 and 0.28, for S_1 and S_2, respectively) compared to the binary-stripped star models (0.35 and 0.31, for B_1 and B_2, respectively) for the same reference core mass. The opposite occurs for the oxygen mass fractions (0.67 and 0.7 for the single star models compared to 0.63 and 0.68 for the binary-stripped star models with a similar reference core mass). This confirms the finding of systematic differences in the chemical structure of single and binary-stripped stars from independent groups (see also Section 3.6.3).

The composition diagrams in Fig. 3.9 emphasize the trend in central carbon and oxygen mass fractions with increasing initial mass. For both the single (top row) and binary-stripped

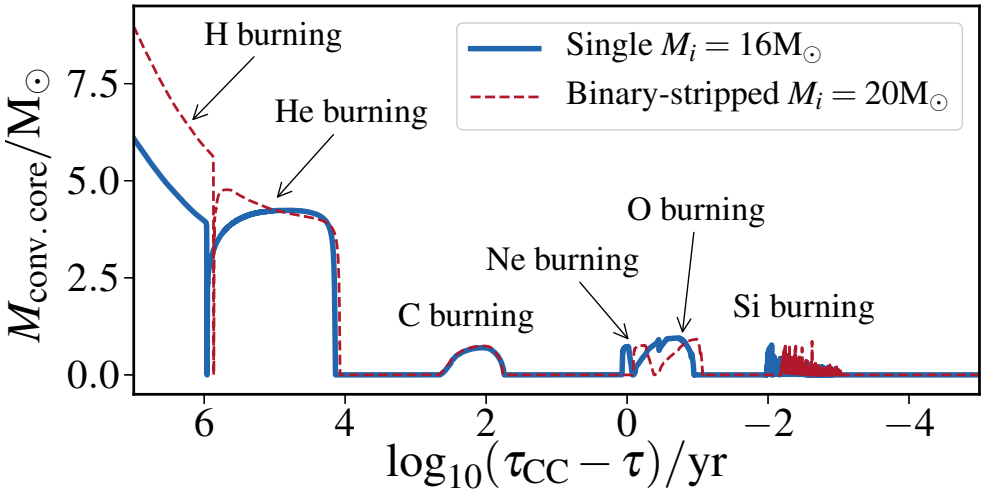

Fig. 3.8: Evolution of the convective core mass of a single and binary-stripped star model with the same reference core mass of 6.3 $\mathrm{M}_\odot$. During core helium burning, the convective core grows in the single star model, while it decreases in the binary-stripped star model due to the effect of wind mass loss.

star models (bottom row), the central carbon mass fraction decreases with increasing initial mass (from 0.31 to 0.24 for the single star models, and from 0.37 to 0.30 in the models of stars stripped in binaries, for the same initial masses of 12 to 21 $\mathrm{M}_\odot$) at the expense of the central oxygen fraction (from 0.67 to 0.74 for the single star models, and from 0.61 to 0.68 in the binary-stripped star models).

The mass dependence of the central mass fractions can be naturally understood as a consequence of the two main nuclear reactions involved in the burning of helium having rates with different density dependencies (see Eq. 3.2 and 3.3). Stars with higher reference core masses have lower core densities and higher temperatures, and this favors alpha-captures onto carbon. Thus, carbon is destroyed more efficiently in the cores of more massive stars during core helium burning (cf. Woosley et al. 1995; Brown et al. 2001).

Fig. 3.9 also shows the presence of a composition gradient of carbon and oxygen around the helium-depleted core. The composition gradient is left behind by the convective helium-burning core, which recedes in the binary-stripped star models due to the effect of wind mass loss. This is the red region just outside the helium-depleted core (indicated with a yellow dashed circle in the composition diagrams of Fig. 3.9). The carbon/oxygen gradient around the helium-depleted core is not visible in the cores of single stars because the helium-burning core grows in mass instead of receding, leading to a steep composition gradient at the edge. The composition gradient of binary-stripped stars becomes more pronounced and more extended in mass as the total mass of the model increases. This can be seen by the growth of the red and purple rings (highlighting ^{12}C and ^{16}O, respectively) just outside the helium-depleted core in Fig. 3.9. Higher mass binary-stripped star models experience stronger wind mass loss, which

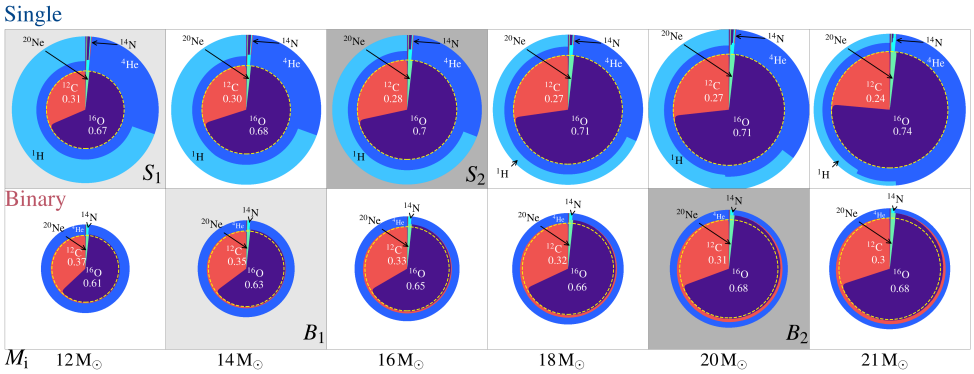

Fig. 3.9: Composition structure at core helium depletion for a subset of the single (top) and binary-stripped star (bottom) grids. Below each set, we indicate the initial masses of these models. Single (S_1 and S_2) and binary-stripped star (B_1 and B_2) models with similar reference core masses are highlighted with the same gray background color. Dashed yellow circles indicate the edge of the helium-depleted core. Outside the helium-depleted core, binary-stripped star models contain a layer that consists of a gradient of ^{12}C, ^{16}O, and ^{20}Ne, whose extent increases with an increasing helium core mass. This layer is not present in single star models.

leads to a faster and more pronounced retreat of the convective helium-burning core and to the observed effect on the carbon/oxygen gradient (see also Appendix B.4). The chemical gradient at the edge of the helium core brings a different chemical environment at the location helium-burning shell in binary-stripped stars, ultimately leading to different total masses of carbon compared to single stars (see also Section 3.5.2).

The differences in chemical structure also have consequences for the interior density structure. In Fig. 3.10, we compare the density structure and mean molecular weight at core helium depletion of two models with the same reference core mass. To highlight the differences, we show the interpolated ratio of the density in binary-stripped and single star models in the bottom panels. Approximate locations of the oxygen-rich, helium-rich, and hydrogen-rich regions are indicated with colors as in Fig. 3.6. The density of the innermost, oxygen-rich core (II, up to $m = 4.5\,\mathrm{M}_\odot$) is the same for the single and binary-stripped star model. At the boundary between the oxygen-rich and helium-rich layers (shaded regions II and I in Fig. 3.10, respectively), the density drops in both models, though this decrease is slower for the binary-stripped star model. At the same mass coordinate, we observe a sharp drop in mean molecular weight for the single star model, while the binary-stripped star model shows a more shallow profile. This difference is due to the extended carbon-oxygen gradient at the edge of the helium-depleted core in the binary-stripped star model. Because the gradient contains some ^{22}Ne, the value of the mean molecular weight is different from the value of 1.33 expected for a layer entirely composed of ^{4}He, ^{12}C, ^{16}O, or ^{20}Ne.

At the outer edge of the CO-enhanced region ($m \approx 5\,\mathrm{M}_\odot$ in Fig. 3.10), both models reach

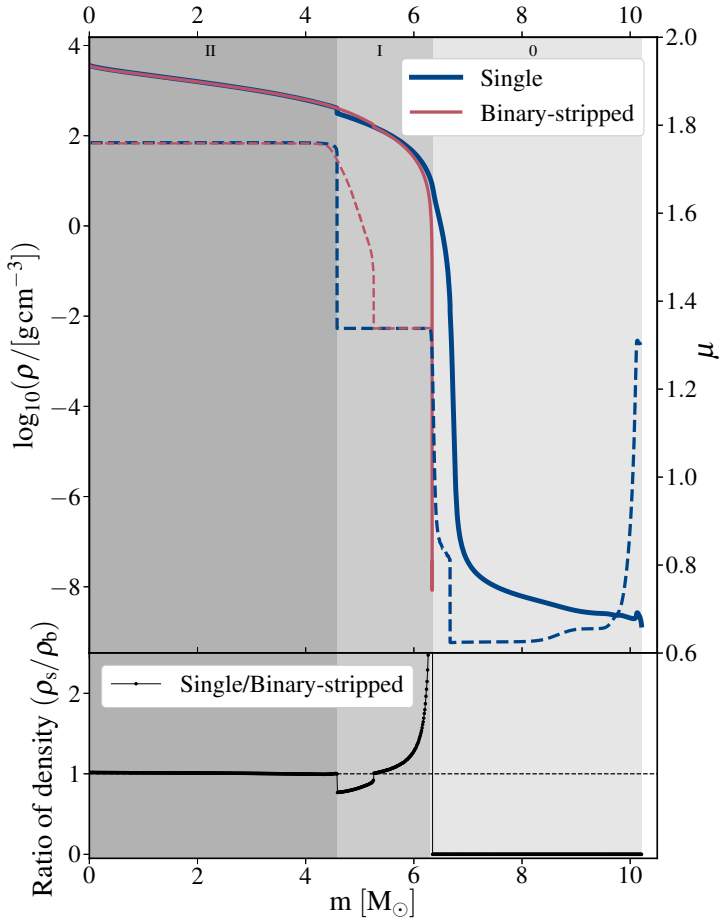

Fig. 3.10: (top) Density and mean molecular weight profile of a single and a binary-stripped star model with the same reference core mass of 6.3 $M_\odot$ at the moment of core helium depletion (D). Gray background colors indicate approximate location of the oxygen-rich (II), helium-rich (I), and hydrogen-rich (0) regions. (bottom) Ratio of the density of the single and binary-stripped star models as a function of mass.

the same values for the density and mean molecular weight, 1.34. However, at the outer edge of the helium-rich layer, differences are visible. The single star model has a higher density than the binary-stripped star model, as can be observed in the lower panel. This is because the single star contains a hydrogen-burning shell at the outer edge of the helium-rich region and a hydrogen-rich envelope. In contrast, the binary-stripped star model has lost its hydrogen envelope at this point, and the outer edge of the helium-rich layer (shaded region I in Fig. 3.10) corresponds to the surface of the star.

3.5.2 Origin of distinct final total isotopic masses: the importance of the composition gradient

In Section 3.4.3, we showed that binary-stripped star models end their lives with higher total masses of ^{12}C compared to single star models (see Fig. 3.5), while the total masses of ^{16}O remain similar. Here we discuss how these differences in composition arise. In Fig. 3.11, we present the evolution of the total mass of ^{12}C, ^{16}O, and ^{20}Ne as a function of time until core oxygen depletion for the example binary-stripped and single star models with a reference core mass of 6.3 $M_\odot$ (with initial masses of 20 $M_\odot$ and 16 $M_\odot$, respectively). During the helium-shell burning phase (first half of D-E), the total mass of carbon decreases slightly in the binary-stripped star, while it increases in the single star model. In contrast, the total mass of oxygen increases in the binary-stripped star model, while it remains unchanged in the single star model. The shaded bands highlight the mass of each isotope outside the helium-depleted core (label D in Fig. 3.11). Meanwhile, the total masses of carbon and oxygen inside the helium-depleted core remain constant. The binary-stripped star model retains a more massive layer of ^{12}C (0.2 $M_\odot$) and ^{16}O (0.25 $M_\odot$) outside the helium depleted core than the single star model (about 0.07 $M_\odot$ and 0.02 $M_\odot$ for ^{12}C and ^{16}O, respectively) throughout the evolution. This is because of differences in the relative rates of helium-burning channels: alpha captures onto carbon dominate in the binary-stripped model. In contrast, the single star model burns helium primarily through the triple-alpha process. This is because of the differences in composition at the location of the helium-burning shell in the single stars compared to the binary-stripped stars.

At the end of core oxygen burning (label F in Fig. 3.11), the interior ^{12}C mass of both models (triangles) is similar. However, the total ^{12}C mass, shown with circles, is higher for the binary-stripped star model due to the mass of ^{12}C outside the helium-depleted core. The interior ^{16}O mass is lower for the binary-stripped star model than for the single star model since helium burning through the triple-alpha process is favored over alpha-captures onto ^{12}C (see Section 3.5.1). Despite the differences, the total mass of ^{16}O is similar in the single and binary-stripped star models. Although ^{16}O is created during helium shell burning and more actively during neon burning in the binary-stripped star model compared to the single star model, oxygen is also destroyed more rapidly during carbon core and shell burning. These effects compensate each other and create a similar final total mass of ^{16}O for the single and binary-stripped star model.

3.5.3 Differences in shell burning

In Section 3.4.4 we found a systematic difference between the density profiles of single and binary-stripped stars with same reference core mass. Specifically, the He-rich layer of binary-stripped stars is systematically denser than that of single star. This impacts the subsequent shell burning phases and thus the pre-collapse structure.

In Fig. 3.12, we show the evolution of density profiles at notable moments of the evolution

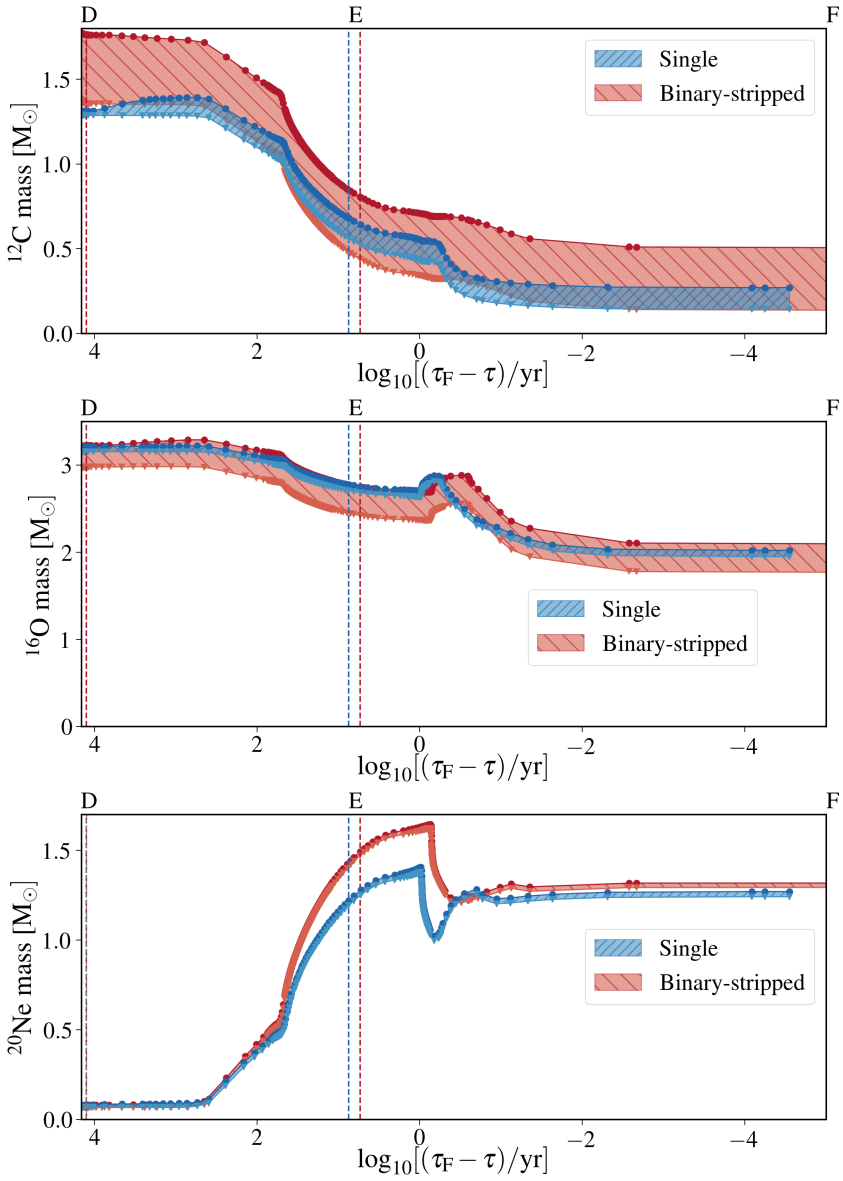

Fig. 3.11: Evolution of the total mass of ^{12}C (*top*), ^{16}O (*middle*), ^{20}Ne (*bottom*) for a single (blue) and a binary-stripped star model (red) with the same reference core mass of 6.3 $M_\odot$. The evolution is shown from the moment of core helium depletion as a function of the time until core oxygen depletion. The curve marked by inverted triangles (i.e. the lower boundary of the colored bands in each plot) mark the total mass of each isotope inside the helium-depleted core. The upper boundary marked by circles shows the total mass of this isotope in the star. The red and blue shaded regions thus highlights the mass of this isotope in the shell above the core.

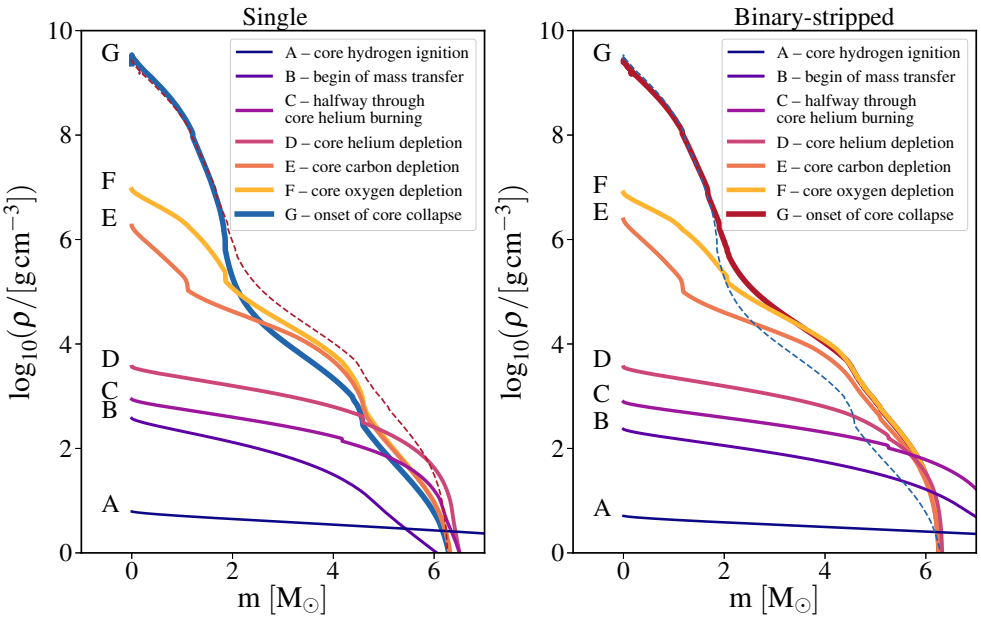

Fig. 3.12: Density profile evolution of a single (left) and stripped (right) star model with the same reference core mass of 6.3 $M_\odot$ from ZAMS to core-collapse. Dashed lines show the corresponding profiles at the onset of core-collapse.

(marked with the same labels as in Fig. 3.1) for our example pair composed of a single and a binary-stripped star model that both reach a similar reference core mass of 6.3 $M_\odot$ at the end of core helium burning. We show the profiles from the onset of core hydrogen burning (A) to core collapse (G). We focus on the inner 7 $M_\odot$ of the stellar structures. The evolution of the density profile is similar for both models until core helium depletion (label D). As the star evolves, the density of the inner core (up to 5 $M_\odot$) increases monotonically. At core helium depletion (point D), the density profile of the binary-stripped star shows a sharp drop at 6.3 $M_\odot$, corresponding to the surface of the star.

The change in density between the single and binary-stripped star in the helium-rich layer ($5\,M_\odot \lesssim m \lesssim 6\,M_\odot$) happens between core helium depletion and the end of core carbon burning (D-E). While the density of this layer increases for the binary-stripped star model, it decreases for the single star model. This phase of the evolution is marked by the ignition of the helium shell and the start of core carbon burning.

We show the nuclear burning profiles for the specific points of the evolution in Fig. 3.13. We represent the single and binary-stripped stellar model pair as half circles (left: single star models, right: binary-stripped star models), where the size of the circle is directly proportional to the mass coordinate. The nuclear energy generation rate throughout the stellar structures is shown with colors.

At the moment of core helium depletion (panel D in Fig. 3.13), we find various differences in the burning structure of the example single and binary-stripped star model. The single

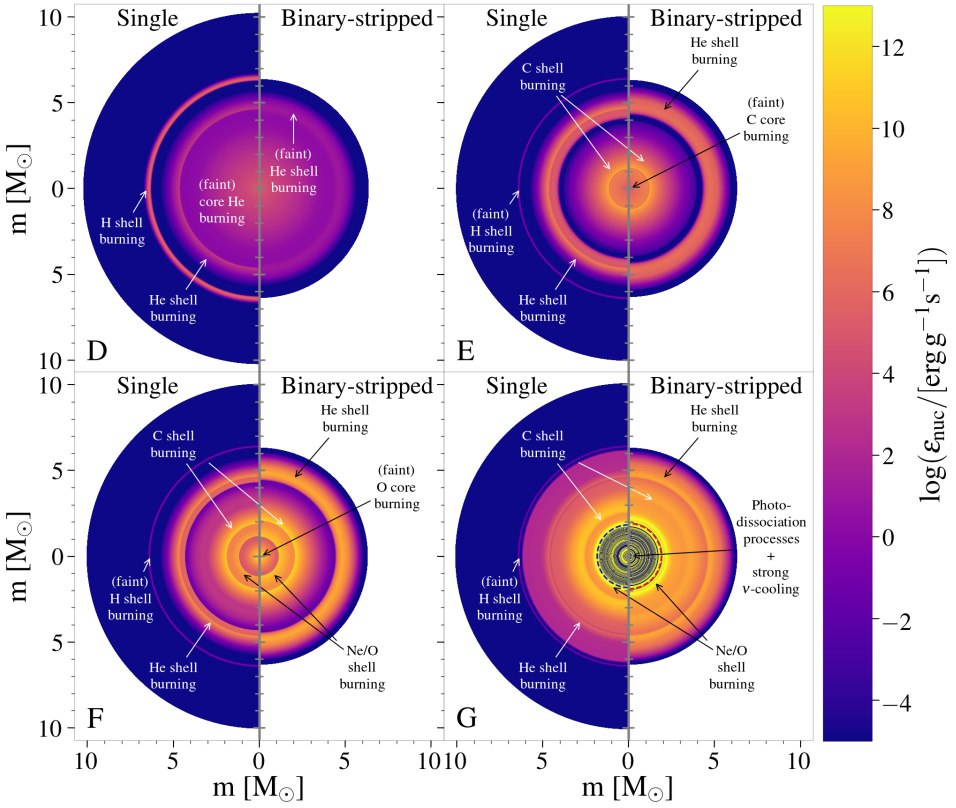

Fig. 3.13: Comparison of the nuclear burning structures of a single (left half-circle) and binary-stripped (right half-circle) star model with the same reference core mass of 6.3 $M_\odot$. Each stellar model is represented as a multitude of 2D - half circles, where the radius of each circle is directly proportional to the mass coordinate. The nuclear energy generation rate is indicated with colors. All models are compared for the same evolutionary steps (D: core helium depletion, E: core carbon depletion, F: core oxygen depletion, G: onset of core collapse). In panel G (onset of core collapse), we give the location of the mass boundary above the compact object that forms in the center (defined as the mass coordinate where the specific entropy drops below a value of 4 erg g^{-1} K^{-1}, Ertl et al. 2016) with a dashed blue (single) and red (binary-stripped) line, respectively. The binary-stripped star model forms a more massive compact object in its core than the single star model (1.90 $M_\odot$ compared to 1.83 $M_\odot$).

star model contains a hydrogen-burning shell which is absent in the binary-stripped star. In addition, it has a helium-burning shell (m = 4.5 $M_\odot$ in Fig. 3.13). In contrast, at the same mass coordinate, the binary-stripped star model has a specific energy generation rate that is two orders of magnitude smaller.

Between core helium depletion and core carbon depletion (points D and E in Fig. 3.13), a large change occurs in the burning structures. In the single star, the specific energy generation rate in the hydrogen-burning shell decreases significantly, while it increases in the helium-burning shell. This decline of the output from the hydrogen-burning shell is linked to the change in density in the helium-rich region.

We also note large differences between the helium shell burning of single and binary-stripped star model from this point on until the end of the evolution (points E to G in Fig. 3.13). In the binary-stripped star model, the helium shell-burning region is more extended ($4.2\,M_\odot < m < 5.5\ M_\odot$). The single star model has a higher maximum energy generation rate (up to $\epsilon_{\rm nuc} = 10^8 {\rm erg\,g^{-1}s^{-1}}$, compared to $10^7 {\rm erg\,g^{-1}s^{-1}}$ for the binary-stripped star model). However, for the binary-stripped star model, a high specific energy generation rate is found in the entire helium-burning region, while for the single star model, it drops quickly outside of the region with the maximum value. These differences can be understood by the differences in composition at the location of the helium burning shell at the end of core helium burning. Because of the extended chemical gradient at the edge of the helium-depleted core, the binary-stripped star model contains a significantly higher mass fraction of carbon next to the helium-burning shell, while the single star model contains very little carbon near the burning shell at the beginning of helium shell burning. This means, just as in the case of central helium burning (see Section 3.5.1), that there are differences in the relative contributions of nuclear reactions involved in helium shell burning. For helium shell burning, the situation is reversed from core helium burning: more alpha captures onto carbon occur in the binary-stripped star model than in the single star model (see also the change in total carbon mass and total oxygen mass between point D and E in Fig 3.11).

After the end of core carbon burning (panel F in Fig. 3.13), additional changes arise in the density and nuclear burning structure. The stars ignite carbon in a shell around the core. However, the location of this shell is significantly different between the single and binary-stripped star models. In the single star model, the carbon shell ignites at $m \approx 1.7\,M_\odot$, while in the binary-stripped star, it ignites further out, at $m \approx 2.1\,M_\odot$. This can be explained by the differences in carbon mass fractions at the end of core helium burning (Chieffi & Limongi 2020). The binary-stripped star has a higher core carbon abundance and the carbon shell ignites further out from the center than in the single star model with the same reference core mass. However, the extent (in mass) of convective core oxygen burning is similar (up to $m \approx 1.2\,M_\odot$). We also give the location of the mass boundary expected for the compact object created during the explosion. We set this boundary at the mass coordinate where the specific entropy drops below a value of $4\,{\rm erg\,g^{-1}\,K^{-1}}$ (Ertl et al. 2016). For the same reference helium core mass, the binary-stripped star model creates a compact object that is more massive than for the single star model ($1.90\,M_\odot$ compared to $1.83\,M_\odot$).

3.5.4 Compactness evolution

The compactness parameter is often used to characterize the core structure of stars. It has been shown to correlate with the explodability with one-dimensional parametric SN explosion models (O'Connor & Ott 2011; Ugliano et al. 2012), although studies of three-dimensional explosion of stars have questioned this (e.g., Ott et al. 2018; Kuroda et al. 2018). Nevertheless, it can be used to predict the type of compact object resulting from a supernova explosion (typically, neutron stars for low values of the compactness and black holes for higher values).

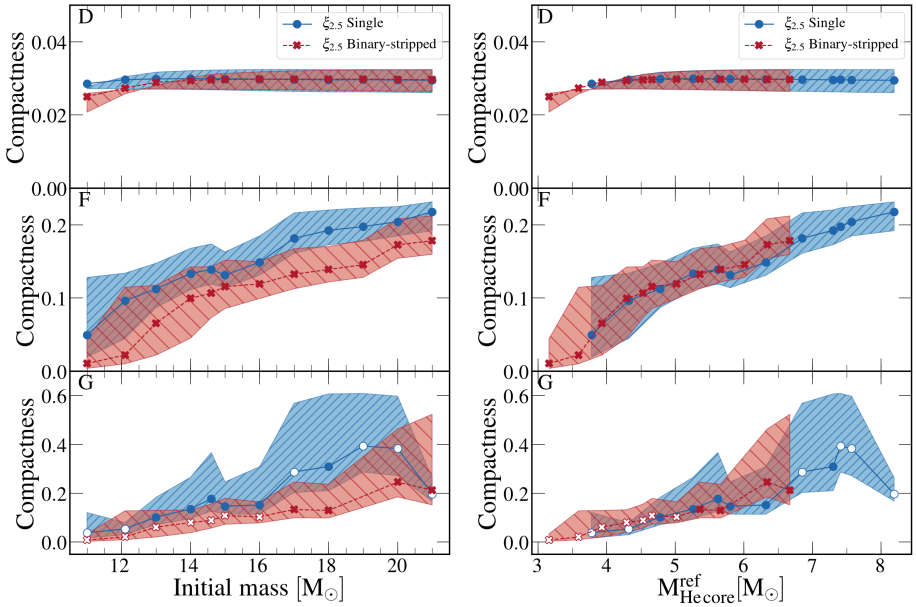

Fig. 3.14: Evolution of the compactness parameter for the full grid of single (blue) and binary binary-stripped (red) models as a function of initial mass (*left*) and reference core mass (*right*). From top to bottom, we show the compactness at the moment of core helium depletion (D, *top*), core oxygen depletion (F, *middle*), and the onset of core collapse (G, *bottom*). For the models at the onset of core collapse, open symbols indicate model that have experienced shell mergers. For every phase of the evolution, we indicate the range of changes in the compactness parameter with blue and red shaded regions. The upper bound of this region corresponds to the compactness evaluated at $m = 2\,M_\odot$ and the lower bound to the compactness evaluated at $m = 3\,M_\odot$. Trends in the compactness parameter as a function of mass are consistent between different definitions of the compactness for the range considered. The reference core mass is defined as the mass of the helium core at the moment of core helium depletion.

Other measures of explodability have been proposed from 1D parametric simulations (for a recent example, see Ertl et al. 2020) or multi-dimensional simulations.

We show the evolution of the compactness parameter for the full grid of models in Fig. 3.14 at three moments of the evolution: D core helium depletion, F core oxygen depletion, and G the onset of core collapse. In addition, we give general properties of the models at the moment of core collapse in Table 3.2. We also evaluate the compactness at mass coordinates 2 and 3 $M_\odot$, shown as a blue (red) band in Fig. 3.14 for the single star (binary-stripped) models. We find that trends in compactness are robust against variations of the mass coordinate at which the compactness parameter is evaluated for all moments of the evolution presented here (Ugliano et al. 2012). In the left panels, we show the compactness as function of initial mass, and in the right panels, as a function of the reference core mass.

At core helium depletion, the compactness parameter is similar for models of all initial masses, with a value of about 0.03. Only the three lowest mass model show differences between single and binary-stripped models. At that epoch, binary-stripped star models with initial masses smaller than 13.5 $M_\odot$ have a slightly smaller compactness than their single

star counterparts. This is because the mass coordinate at which the compactness is evaluated lies outside of the oxygen core in these models, which means the compactness parameter captures the relative expansion of the helium-rich envelope compared to the single stars (see also Table 3.1).

By the time of core oxygen depletion (panels marked F in Fig. 3.14), the value of the compactness parameter changes significantly between all models (Renzo et al. 2017). Higher mass models have higher compactness. Binary-stripped star models have systematically lower values of the compactness (0.01 to 0.18) than single star models of the same initial mass (0.05 to 0.21). However, when comparing models with the same reference core mass (defined as the helium core mass at core helium depletion) the compactness is similar between single and binary-stripped star models, except for the two most massive binary-stripped star models. The difference for the highest mass models could be due to the transition to radiative core carbon burning around this mass range for binary-stripped stars that changes the compactness of the core (Brown et al. 1996, 1999, 2001; Sukhbold & Woosley 2014; Woosley 2019; Schneider et al. 2021).

At the onset of core collapse (panel G in Fig. 3.14), the differences between the compactness of single and binary-stripped star models of the same initial mass increases even further. The compactness of binary-stripped star models remains systematically smaller than that of single star models. For the same reference core mass, we find similar values between single and binary-stripped star models. Changes in the compactness are qualitatively similar to those from similar recent studies (e.g., Woosley 2019; Chieffi & Limongi 2020; Patton & Sukhbold 2020; Schneider et al. 2021). We do not find clear differences in compactness for models that experience shell mergers before core collapse (marked with open symbols in the lower panels of Fig. 3.14). This is because the Si/O shell mergers observed in this study typically occur at mass coordinates of $m \simeq 1.3\,\mathrm{M}_\odot$, below the mass range we chose to evaluate the compactness and the merged convective shells do not extend beyond the mass cuts chosen for the compactness.

When comparing the electron fraction Y_e in Table 3.2, we also find different values for single and binary-stripped star models. Different values of the electron fraction imply that the late nuclear burning conditions in the cores of single and binary-stripped stars are different.

3.6 Discussion

3.6.1 Implications for explodability

For the same initial mass, binary-stripped star models have a smaller reference core mass, a smaller compactness, and a different distribution of isotopes compared to single stars. Both the smaller mass and compactness suggest that binary-stripped stars will explode more easily than if they had not interacted with a companion (though explodability might be better described with more sophisticated means, e.g., Ertl et al. 2016, 2020). Multi-dimensional calculations indicate that the explosion depends on details of the stellar structure, especially the density

Table 3.2: Core properties of single and binary-stripped star models at the onset of core collapse.

$M_{\rm init}$ $[M_\odot]$	$M_{\rm CC}$ $[M_\odot]$	$M^{\rm ref}_{\rm He\,core}$ $[M_\odot]$	$\xi_{2.5}$	Y_e $(m < 1\,M_\odot)$	Shell merger
Binary stripped stars					
11.0	3.11	3.16	0.01	0.446	True
12.1	3.52	3.59	0.02	0.446	True
13.0	3.87	3.93	0.06	0.446	True
14.0	4.23	4.29	0.08	0.446	True
14.6	4.48	4.53	0.09	0.447	True
15.0	4.61	4.66	0.11	0.447	True
16.0	4.97	5.02	0.10	0.448	True
17.0	5.31	5.36	0.13	0.452	False
18.0	5.61	5.66	0.13	0.452	False
20.0	6.28	6.34	0.25	0.453	False
21.0	6.62	6.67	0.21	0.453	False
Single stars					
11.0	9.32	3.78	0.04	0.446	True
12.1	9.73	4.32	0.05	0.444	True
13.0	9.97	4.78	0.10	0.448	False
14.0	10.12	5.26	0.14	0.452	False
14.6	10.15	5.62	0.18	0.453	False
15.0	10.16	5.80	0.15	0.449	False
16.0	10.05	6.32	0.15	0.452	False
17.0	9.88	6.85	0.29	0.454	True
18.0	10.13	7.30	0.31	0.455	False
19.0	10.58	7.41	0.39	0.455	True
20.0	11.66	7.57	0.38	0.455	True
21.0	10.40	8.19	0.20	0.448	True

profile (e.g., Vartanyan et al. 2018). Müller et al. (2019) did not find significant differences between the explosions of low-mass single and binary-stripped stars (based on naked helium core models from Tauris et al. 2015) of the same core mass. However, even for the same reference core mass, we find systematic differences in the density structure of single and binary-stripped stars we computed. In the helium-rich region binary-stripped stars have higher densities than single stars, and at the edge of the helium-rich region the density drops more sharply in the binary-stripped star models. In addition, we find distinct electron fractions in the cores of single and binary-stripped stars, which imply differences in the late nuclear burning conditions. These differences in structure can affect the accretion rates during core collapse and the explosion dynamics. This could have a significant impact for population synthesis models of compact objects. We explore detailed explosion models and implications for the supernova explodability of single and binary-stripped stars in a companion paper (Vartanyan et al. 2021).

3.6.2 Implications for nucleosynthesis and nebular lines

Our models reveal that the composition structures of stellar cores at the moment of core collapse is complex. We identified three main regions, the helium-rich, oxygen-rich, and iron-rich layers.

The distribution of isotopes in the cores of binary-stripped stars is different from the homogeneous distribution often assumed for the evolution of naked carbon-oxygen cores, (e.g., Patton & Sukhbold 2020). For instance, stars stripped in binaries contain an extended gradient of carbon, oxygen, and neon above the helium-depleted core that is not present in single stellar structures. This extended composition gradient leads to changes in the final density, mean molecular weight, and composition profiles. This difference is first induced by changes during the central helium burning phase and is further accentuated in the subsequent nuclear burning stages.

These differences imply that the supernova nucleosynthesis expected from single and binary-stripped stars might be systematically different. In particular, we expect ^{12}C and ^{16}O yields to remain different after the supernova explosion. This is because during supernova nucleosynthesis, part of the remaining carbon will be synthesized into oxygen. Large consequences can be expected by this difference in yields because it would affect nebular oxygen lines, that are currently widely used to infer the progenitor masses of core-collapse supernova explosions. In addition, a systematic difference in the nucleosynthesis from binary-stripped and single stars would have implications for the interpretation of galaxy chemical evolution models. We explore the differences in nucleosynthesis for ^{12}C in Farmer et al. in prep.

3.6.3 Comparison with models in the literature

Our models show a consistent trend of systematically higher central carbon mass fraction for binary-stripped star models compared to single star models, as do other models in the literature. We show the central carbon mass fraction as a function of the mass of the carbon/oxygen core evaluated at the moment of core helium depletion in Fig. 3.15 and compare our models to single star models from Sukhbold et al. (2018) and pure helium star models from Woosley (2019) (as shown in Fig. 6 of Patton & Sukhbold 2020). These models were computed with the KEPLER stellar evolution code with similar physical assumptions to each other. We also compare our models to single star and case B mass transfer binary models from Schneider et al. (2021), computed with MESA. The physical assumptions are similar.

There is a good agreement between our models and the values reported in Schneider et al. (2021) for both the single and binary-stripped star models. Especially for the binary-stripped star models, we barely find any differences in central mass fraction, except at the lowest mass end. This agreement originates from the similar physical assumptions regarding the choice of wind mass loss, overshooting, and of the $^{12}\mathrm{C}(\alpha,\gamma)^{16}\mathrm{O}$ rate. We expect that the small differences at the lowest mass end are linked to the treatment of mass transfer. Schneider et al. (2021) parameterize mass loss on a thermal timescale until an arbitrary surface

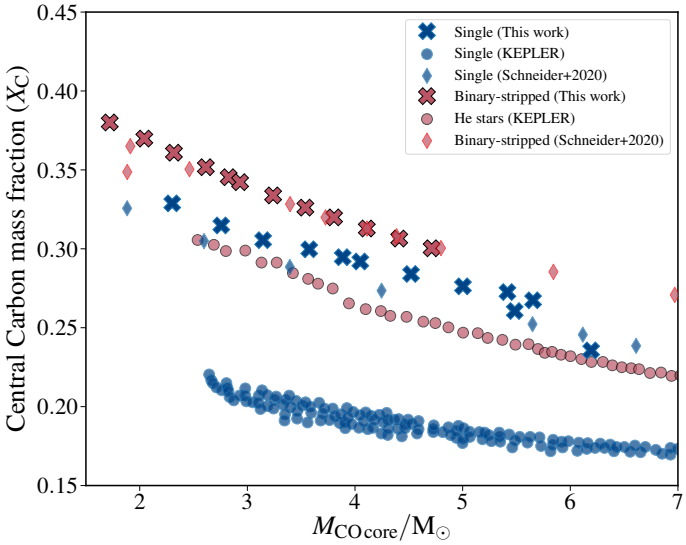

Fig. 3.15: Comparison of our models to models from the literature on the central carbon mass fraction to CO-core mass plane. These values are evaluated at the end of core helium depletion. All models show higher central carbon mass fractions for binary-stripped star models compared to single star models.

composition is reached, while in our models the binary mass-transfer phase is computed self-consistently. Our single star models have systematically higher core carbon abundances than the models from Schneider et al. (2021), despite similar assumptions regarding core overshooting. These differences can be attributed to different choices for the wind mass-loss rate. Much larger differences are found between our work and models computed with the KEPLER code. These models have core carbon abundances that are a factor 1.7 lower than in our models. These differences probably stem from different physical assumptions, such as the choice for overshooting, but also from the value used for the uncertain carbon alpha-capture reaction rate. The models shown in (Patton & Sukhbold 2020) have a $^{12}C(\alpha,\gamma)^{16}O$ rate that is a factor 1.2 higher than what we assume.

To obtain pre-supernova structures of binary-stripped stars at the onset of core collapse, we have modeled donor stars in binary systems. These stars are often modeled as "naked" helium stars, with or without mass loss (e.g., Woosley 2019). It is expected that binary-stripped stars at low metallicity retain a substantial hydrogen-rich layer after mass transfer, sufficient to change their future evolution, and so for those cases helium stars are not a good approximation (Götberg et al. 2017; Yoon et al. 2017; Laplace et al. 2020). However, we are not aware of systematic work which has studied which results from the helium-star approximation significantly differ, in modeling supernova progenitors, from otherwise identical calculations using binary-stripped stars. We encourage a careful investigation to determine which parts of the parameter space, and for which questions, these stars can be adequately approximated with helium-star models.

3.6.4 Wind mass loss

Wind mass-loss rates remain a major uncertainty in stellar astrophysics, and are particularly poorly constrained for stripped stars in the mass range of our models (Yoon et al. 2010; Yoon 2015; Götberg et al. 2017). Very few such stars have been observed so far, and the best observational constraint on the relevant mass-loss rates to date comes from a single system, the quasi-WR star in the system HD 45166 (e.g., Groh et al. 2008). Radiative transfer models have just begun to make mass-loss predictions for stripped stars in this mass range, and a large parameter space remains to be explored (Vink 2017; Sander & Vink 2020).

Wind mass loss plays a crucial role in the evolution, future interactions, and on the supernova properties of binary-stripped stars (Yoon et al. 2010; Yoon 2015; Gilkis et al. 2019). The extended gradient of the carbon and oxygen composition above the helium-depleted core of binary-stripped stars is a consequence of the receding outer edge of the convective core during central helium burning due to wind mass-loss (Langer 1989b, 1991b; Woosley et al. 1995).

We find a non-negligible effect of wind mass loss on the core structure of binary-stripped stars at solar metallicity. Appendix B.4 presents tests adopting a large range of possible wind mass loss rates and their effect on the core structure of binary-stripped stars, spanning from low mass loss rates predicted from the Monte Carlo radiative transfer models of Vink 2017 to the wind mass loss rates inferred from observations of WC and WO stars (Tramper et al. 2016). We confirm that our main conclusions would still be apparent for lower wind mass loss rates than we assume, especially at the higher mass end, though they would be less pronounced.

The wind mass loss rate employed in our models is close to, but slightly smaller, than the wind mass loss inferred from HD 45166. Tramper et al. (2016) found that the wind mass loss rate of WC/WO stars is higher than the mass loss rate from Nugis & Lamers (2000) assumed for our default model. If binary-stripped stars have similar stellar winds to those inferred by Tramper et al. (2016), the differences between single- and binary-stripped stars in the core composition and density structure could be even larger in reality than those we describe.

The vast majority of rapid population synthesis models rely on stellar structures for binary-stripped stars that were computed without mass loss (Hurley et al. 2000, 2002; Pols et al. 1998) and are based on calculations from single stars or naked helium stars only. In addition, these models are typically stopped at the end of core carbon burning. This means the core structures used in those rapid stellar population calculations are similar to those of single stars, and the core mass distribution is different from more detailed stellar models. This directly affects the number and properties of compact objects predicted from such calculations.

3.6.5 Convection modeling and shell mergers

Our calculations model convection with the mixing-length theory (MLT) approximation (Böhm-Vitense 1958, using the form from Cox & Giuli 1968), with composition mixing treated as a diffusion process. These are common assumptions, even though they are imperfect

approximations (Renzini 1987), because MLT has not yet been replaced by a widely-accepted practical alternative (see, e.g., Arnett et al. 2015). This simplification in the modeling necessarily introduces uncertainties in some aspects of our results, especially during late phases in which mixing and burning occur on similar timescales (e.g., Bazán & Arnett 1998). In particular, this leads to caution regarding the models in which material from the oxygen-rich layer is mixed down into the convective silicon-burning shell. The details of the predictions for such shell mergers may well change with a more sophisticated theory of convection (see also the discussion in Collins et al. 2018, who found merging oxygen and neon shells in many of their single-star models). Nonetheless, mixing downwards into convective burning shells has also been seen in multi-dimensional hydrodynamic models of late burning stages (e.g., Bazan & Arnett 1994; Bazán & Arnett 1998; Andrassy et al. 2020; Yadav et al. 2020; McNeill & Müller 2020).

These shell mergers, if they occur in real stars as they do in our models, produce distinctly different distributions of alpha-chain elements in the oxygen-rich layer at the time of the explosion. A consequence of these shell mergers is a potentially-observable abundance signature that allows for the occurrence of such shell mergers to be tested observationally. Potential implications of late-stage shell mergers for stellar nucleosynthesis have been studied by, e.g., Rauscher et al. (2002) and Ritter et al. (2018). Dessart & John Hillier (2020) have also noted that such shell mergers in supernova progenitors would affect the interpretation of Ca/O abundance ratios from core-collapse supernovae. In our grid the oxygen-silicon shell mergers preferentially occur for reference core masses below 5 $M_\odot$ and above 6.8 $M_\odot$, which could produce an identifiable systematic pattern in observed stripped-envelope supernovae.

3.7 Conclusions

We have studied the pre-supernova structures of single star models from 11 to 21 $M_\odot$ and stars of the same initial mass that are donor stars in binary systems (binary-stripped stars). In the binary models, the stars transfer the majority of their hydrogen-rich envelopes to a companion right after the end of core hydrogen burning (early case B mass transfer). We computed models at solar metallicity and, to obtain accurate information for the composition profile at the onset of core collapse, used a large, fully-coupled nuclear network of 128 isotopes after core oxygen burning. We focused on the systematic differences in the core density and composition structure at the moment of core-collapse. Overall, we confirm that binary-stripped stars in this mass range end their lives with systematically less massive helium cores than single stars with the same initial mass.

Our main findings regarding the core composition structure are:

- Our composition diagrams confirm that the composition profiles are described by three main regions: (I) a helium-rich region; (II) an oxygen-rich region that contains high abundances of oxygen, neon, and magnesium; (III) an iron-rich region, that contains various isotopes of iron-group elements (see Fig. 3.2 and B.7). These structures do

not contain a clearly distinct carbon-rich layer, in contrast to simplified depictions of pre-supernova structures.

- Binary-stripped and single star models have distinct chemical profiles at the onset of core collapse (see Fig. 3.2), even for helium cores of similar mass. In agreement with previous studies, we find that stars stripped in binaries develop an extended gradient of carbon and oxygen at the edge of the helium-depleted core that does not exist in single stars. We show that this layer remains until core collapse, and is more extended in mass for higher initial stellar masses due to the mass-dependence of winds (see Fig. 3.9).

- We find that this extended chemical gradient is responsible for a systematically larger total mass of carbon in binary-stripped star models than comparable single star models at the onset of core collapse (see Fig. 3.11 and Fig. 3.5). In contrast, the total mass of oxygen remains similar (see Fig. 3.11 and 3.13).

- The difference in total carbon mass will probably affect the chemical yield predictions, pending possible alterations as the supernova shock propagates through the interior, which we have not modeled here (but will be presented in Farmer et al. in prep.).

- Shortly before core collapse, about half of our models experience a merging of the convective silicon-burning shell with the oxygen-rich layer that results in an enrichment of heavier alpha elements (mainly ^{28}Si, ^{32}S, ^{36}Ar, ^{40}Ca) in the outer oxygen-rich regions. Although their physical accuracy in 1D models is unclear, similar effects are observed in multi-dimensional simulations. If shell mergers do occur in nature, these peculiar abundances could be observationally testable.

In addition, we investigate systematic differences in the core density structure and come to the following conclusions:

- For the same reference helium core mass, stars stripped in binaries reach systematically larger helium core radii at the onset of core collapse than single stars (see Fig. 3.7).

- Systematic differences can be observed in the core density structure of single and binary-stripped stars at the onset of core collapse (see Fig. 3.6). In the helium-rich region binary-stripped stars have higher final densities than single stars, and at the edge of the helium-rich region the density drops more sharply in the binary-stripped star models. The core density structures begin to diverge during core helium burning (see Fig. 3.12 and 3.13).

- We find that for the same initial mass, the compactness of binary-stripped stars is systematically lower than that of single stars. For the same reference core mass, the compactness is similar.

The differences in composition structures may lead to a systematically different creation of isotopes from the supernovae of single stars and binary-stripped stars. We expect the distinct

density and shell-burning structures to have a significant impact on the dynamics following core-collapse, on the propagation of the supernova shock through the stellar structure, and on the nature of the compact remnant. Multi-dimensional supernova simulations, based on stellar models similar to those presented here, are needed to quantify these effects and to compare them with supernova observations.

We are grateful to the referee for a thorough and careful review and for helpful suggestions, which have led to a significant improvement of the manuscript. We thank A. Burrows, L. van Son, T. Moriya, and M. Modjaz for useful discussions. The research was funded by the European Union's Horizon 2020 research and innovation program from the European Research Council (ERC, grant agreement No. 715063), and by the Netherlands Organisation for Scientific Research (NWO) as part of the Vidi research program BinWaves with project number 639.042.728. YG acknowledges the funding from the Alvin E. Nashman fellowship for Theoretical Astrophysics. RF is supported by the Netherlands Organisation for Scientific Research (NWO) through a top module 2 grant with project number 614.001.501 (PI de Mink). DV acknowledges funding from the U.S. Department of Energy Office of Science and the Office of Advanced Scientific Computing Research via the Scientific Discovery through Advanced Computing (SciDAC4) program and Grant DE-SC0018297 (subaward 00009650).

Chapter 4

Binary-stripped stars as core-collapse supernovae progenitors

D. Vartanyan, E. Laplace, M. Renzo, Y. Götberg, A. Burrows, and S. E. de Mink

The content of this chapter was published in The Astrophysical Journal Letters, 2021, 916, L5

Abstract

Most massive stars experience binary interactions in their lifetimes that can alter both the surface and core structure of the stripped star with significant effects on their ultimate fate as core-collapse supernovae. However, core-collapse supernovae simulations to date have focused almost exclusively on the evolution of single stars. We present a systematic simulation study of single and binary-stripped stars with the same initial mass as candidates for core-collapse supernovae ($11 - 21\ M_\odot$). Generally, we find that binary-stripped stars core tend to have a smaller compactness parameter, with a more prominent, deeper silicon/oxygen interface, and explode preferentially to the corresponding single stars of the same initial mass. Such a dichotomy of behavior between these two modes of evolution would have important implications for supernovae statistics, including the final neutron star masses, explosion energies, and nucleosynthetic yields. Binary-stripped remnants are also well poised to populate the possible mass gap between the heaviest neutron stars and the lightest black holes. Our work presents an improvement along two fronts, as we self-consistently account for the pre-collapse stellar evolution and the subsequent explosion outcome. Even so, our results emphasize the need for more detailed stellar evolutionary models to capture the sensitive nature of explosion outcome.

4.1 Introduction

Studies on the core-collapse supernovae (CCSNe) explosion mechanism have focused almost exclusively on single-star progenitors (e.g. Burrows 2013; Janka et al. 2016; Roberts et al. 2016; Radice et al. 2017; Summa et al. 2018; Ott et al. 2018; Vartanyan et al. 2018, 2019b; Burrows et al. 2018, 2019a,b; Burrows & Vartanyan 2021; O'Connor & Couch 2018; Nagakura et al. 2019b,a; Glas et al. 2019; Kuroda et al. 2020). However, the vast majority of stars massive enough to reach core-collapse are members of multiple systems (e.g., Mason et al. 2009; Almeida et al. 2017). Sana et al. (2012) conclude that the majority of massive stars should interact with a close companion during their lifetime. Binary evolution is commonly required to explain the high intrinsic rate of hydrogen poor (type IIb, Ib, Ic) CCSNe (Podsiadlowski et al. 1992; Eldridge et al. 2008; Yoon et al. 2010; Li et al. 2011; Claeys et al. 2011; Zapartas et al. 2017; Shivvers et al. 2019; Sravan et al. 2019) and their ejecta mass distributions peaked at low values of about 2 $M_{\odot}$ (e.g., Lyman et al. 2016; Taddia et al. 2018). It is also required to explain the properties of several SN progenitors observed through direct imaging, including the triple-ring structure of SN1987a (e.g., Eldridge et al. 2013, 2017; Utrobin et al. 2021). Moreover, direct imaging provides evidence for surviving companions after CCSNe (e.g., Maund et al. 2004; Fox et al. 2014; Ryder et al. 2018). Binary population synthesis studies have recently shown binary interaction should also affect $\sim 50\%$ of hydrogen-rich (type II) SNe (e.g., Eldridge et al. 2018; Zapartas et al. 2019, 2021a).

Thus, we expect that a large fraction of CCSN progenitors experiences binary interactions, which might change the core structure (Langer 1989b; Woosley et al. 1993a; Laplace et al. 2021) and thus "explodability" of stars of a given initial mass. This is buttressed by a growing anthology of observed stripped SNe (Shivvers et al. 2019) with interesting implications for the formation of double compact objects (De et al. 2018; Taddia et al. 2018; Prentice et al. 2019) and rapidly evolving transients (Pursiainen et al. 2018).

CCSNe explosion simulations of progenitors computed accounting self-consistently for binary interactions are as-yet rare, as are detailed stellar evolution models of binary stars computed to core-collapse. The preponderance of studies to date simplify the binary mass exchange (Schneider et al. 2021) or focus on the structure of naked cores (He cores, Woosley 2019; Ertl et al. 2020; and CO cores, Patton & Sukhbold 2020, but see Tauris et al. 2015), and prompt explosion through parametrized or prescriptive means (Woosley 2019; Zapartas et al. 2021a; Ertl et al. 2020; Schneider et al. 2021). We emphasize that, as pointed out in Laplace et al. 2021, the final core properties of single and binary-stripped stars differ even when comparing models with similar helium core masses due to the rate and timing of mass loss, which are not easily captured in naked He cores. Furthermore, self-consistent mass loss in binaries may leave some remnant hydrogen, which will further alter the composition and structure of the stripped star in comparison with a naked He core.

The work of Müller et al. (2018, 2019) considered the impact of binary evolution modeling on the explodability of the donor star with 3D explosion simulations, although with several approximations to the neutrino radiation transport and binary evolution modeling. They

focused on the explosion of ultra-stripped stars from Tauris et al. (2015), motivated by the relevance of this channel for gravitational-wave progenitors. The binary evolution models from Tauris et al. (2015) start from initial conditions with a compact object (NS) orbited by a naked He star, i.e. starting the evolution from after the first mass transfer or common envelope phase in a binary. The binary evolution leads to a second mass transfer phase (case BB RLOF, Roche-lobe overflow) which further reduces the mass of the star, making it ultra-stripped. They found that these ultra-stripped stars blow up with weak explosion energies ($E \simeq 10^{50}$ erg) and with prompt explosions resulting in small SN natal kicks.

Our study, using the progenitors developed in Laplace et al. (2021), is complementary to the work of Müller et al. (2018, 2019) and Tauris et al. (2015), since we focus instead on the first RLOF phase and what impact it can have on the explodability of stripped (but not ultra-stripped) CCSN progenitors. The most common kind of binary interaction is mass transfer with a post main sequence donor (so-called case B RLOF, de Mink et al. 2008; Klencki et al. 2020), which is predicted to leave only a very thin layer of H-rich material on the donor star at the end of the mass transfer phase at solar metallicity (Yoon et al. 2017; Götberg et al. 2017; Gilkis et al. 2019). At solar metallicity, such a layer is likely removed by stellar winds in the post-mass transfer, pre-collapse evolution, leaving an exposed He core which will likely be the progenitor of a Ib SN explosion, or, if the helium-rich layers are removed, of a Ic. Therefore, albeit with numerous caveats affecting any stellar evolution simulations, we provide the first self-consistent binary models and supernovae simulations used to explore the impact of the most common binary evolution channel, case B mass transfer, on the explodability of the donor stars core with the added advantage of using a more-detailed radiation transport scheme to simulate the resulting supernovae.

Here, we report on one of the first comprehensive, self-consistent simulation study comparing CCSNe outcomes for a suite of 11 single-star and binary-stripped progenitors with the same initial mass (Laplace et al. 2021). We note that Ertl et al. 2020 also performed a similar comparison, including comparisons to the single-star models of Sukhbold et al. 2016, but with the qualifications mentioned above (namely, He cores, instead of binary-stripped stars, that are subsequently exploded through a parametrized model). Schneider et al. 2021 perform a binary-stripped to single-star comparison as well, but also simplify the binary mass loss and parametrize the subsequent explosion modeling. Our work allows for the systematic study of the viability of stripped stars as CCSNe progenitors and explores the role of massive star evolutionary history on CCSNe outcome (see, e.g., Podsiadlowski et al. 1992; Yoon et al. 2010; Dessart et al. 2011; Tauris et al. 2015; Patton & Sukhbold 2020; Ertl et al. 2020; Woosley et al. 2020, 2021; Zapartas et al. 2021a; Chieffi & Limongi 2020; Schneider et al. 2021). We find preferential explosion of binary-stripped progenitors over single-star progenitors of the same ZAMS mass. After describing the salient points of our pre-explosion and explosion modeling in Sec. 4.2, we first compare a representative pair of models with the same initial mass in Sec. 4.3. We find that overall donor stars in binaries are easier to explode, and among pairs of the same initial mass, lower compactness parameter corresponds to easier explodability, but highlight key exceptions to this general trend and present explosion diagnostics with

observational ramifications. We present our conclusions in Sec. 4.4.

4.2 Methods

4.2.1 MESA

The stellar evolution models are presented and described in detail in Laplace et al. (2021). The models were computed with the open-source 1D stellar evolution code MESA (version 10398, Paxton et al. 2011, 2013, 2015, 2018, 2019) at solar metallicity ($Z = 0.0142$, Asplund et al. 2009). Until core oxygen depletion (central oxygen mass fraction lower than 10^{-4}), we used a nuclear network comprising 21 isotopes that produces sufficiently accurate reaction rates in the cores of massive stars from core hydrogen burning until the end of core oxygen burning (`approx21`, Timmes 1999; Timmes et al. 2000; Paxton et al. 2011). Because of the sensitivity of the further evolution to nuclear burning and especially electron captures, we used a 128-isotope network after oxygen depletion (Farmer et al. 2016) and stop our models when the iron-core infall velocity reached 1000 km s^{-1}. Mass loss from the binary-stripped stars was included in the pre-supernova evolution. For stars with effective temperatures of $T_{eff} > 10^4$ K we used mass loss rates from Vink et al. (2001) when the surface hydrogen mass fraction $X_H > 0.4$ and the rates from Nugis & Lamers (2000) for the cases with $X_H < 0.4$. For effective temperatures $<10^4$ K, we employ the de Jager et al. (1988) empirical wind mass loss prescription for stars across the Hertzsprung-Russell diagram. For the binary-stripped stars, the pre-supernova mass is very close to the helium core mass (evaluated at the end of core helium burning), but slightly smaller due to wind mass loss in late phases of the evolution.

Our grid consists of two sets of 11 models with the same initial masses M_1 ranging from 11 to 21 $M_\odot$. The first set follows the evolution of single stars. For the second set, we considered the most common binary interaction, that is, a stable mass transfer phase after the end of the donor's main sequence (case B mass transfer, e.g., Kippenhahn & Weigert 1967). We examined binaries with initial periods of 25–35 d and a point-mass secondary of mass $M_2 = 0.8M_1$, and assumed fully conservative mass transfer. All stellar models and MESA inlists are publicly available upon publication (see Laplace et al. 2021).

4.2.2 FORNAX

To simulate the collapse, core-bounce, and initial shock propagation in the first seconds, we use Fornax (Skinner et al. 2019). Fornax is a multi-dimensional, multi-group radiation hydrodynamics code originally constructed to study core-collapse supernovae. The models referenced herein were evolved in 2D axisymmetry on a spherical grid extending to 20,000 km and resolved with 678 radial cells and 256 angular cells. The angular grid resolution varies smoothly from 0.64° along the equator to 0.94° along the poles. Following Marek et al. (2006) we used a monopole approximation for relativistic gravity and employed the SFHo equation of state (Steiner et al. 2013), which is consistent with all currently known constraints (Tews

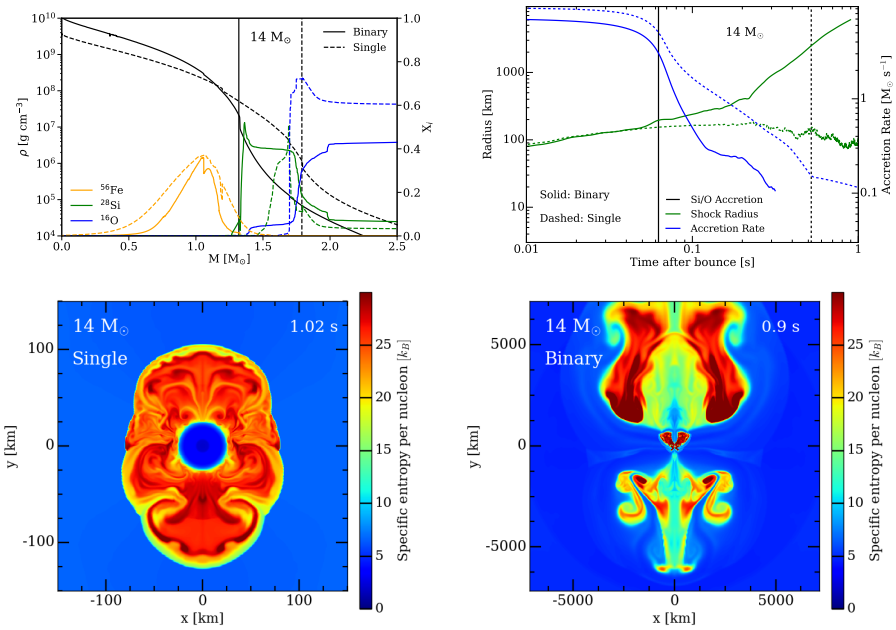

Fig. 4.1: **Top Left**: Initial density profiles (black) and the mass fraction of Fe-56 (red), Si-28 (green), and O-16 (blue) distributions in the interior 2.5 $M_\odot$ for the binary-stripped (solid) and single (dashed) 14 $M_\odot$ model. The vertical solid and dashed lines indicate the compositional interface, respectively. **Top Right**: Mean shock radii (km, green) and the accretion rate at 200 km, just exterior to the shock, ($M_\odot$ s^{-1}, right y-axis) for the 14-$M_\odot$ progenitor, a typical binary/single pair as a function of time after bounce (s). The vertical lines illustrate when the Si/O interface is accreted onto the expanding shock. For both cases, the accretion of the Si/O interface corresponds to the onset of turbulence in the expanding shock front, illustrated by variations in the mean shock radii. The concurrent accretion rate plummets as a result of the drop in density and pressure outside the interface. The shock begins to expand rapidly for the binary-stripped model, resulting in an explosion. However, the Si/O interface for the single star is further out and less pronounced, and proving insufficient to revive the already stalled shock. Nevertheless, even the single-star model shows a bump in the shock radii shortly after accretion of the Si/O interface. **Bottom**: We show the two-dimensional entropy profiles of the 14 $M_\odot$ model for the non-exploding single star on the left and the exploding binary-stripped star on the right. Note the vastly different scales plotted.

et al. 2017) on the nuclear equation of state. Our intention in this study is to identify trends in a large set of models, and hence simulating in 2D axisymmetry is favorable. Although 3D simulations still are required, earlier works show similarities in explosion outcome and diagnostics between 2D and 3D simulations (e.g, Vartanyan et al. 2018; Burrows et al. 2019b; Burrows & Vartanyan 2021), and such a broad suite of 2D simulations as presented here sets the groundwork for more selective 3D simulations in the future.

We solve for radiation transfer using the M1 moment closure scheme for the second and third moments of the radiation fields (Vaytet et al. 2011) and follow three species of neutrinos: electron-type (ν_e), anti-electron-type ($\bar{\nu}_e$), and "ν_μ"-type (ν_μ, $\bar{\nu}_\mu$, ν_τ, and $\bar{\nu}_\tau$ neutrino species collectively). We use 12 energy groups spaced logarithmically between 1 and 300 MeV for

the electron neutrinos and to 100 MeV for the anti-electron- and "ν_μ"-neutrinos. The M1 solver avoids simplification to the neutrino transport, such as the fast-multigroup transport scheme with the ray-by-ray approximation, which introduces numerical artifacts into explosion outcome.

4.3 Results

We present a study of 11 pairs of progenitors, for a total of 22 models, corresponding to progenitors, spanning 11 – 21 $M_\odot$ ZAMS mass and following single and binary-stripped post-main sequence evolution. We find that all but four of the 22 models explode, where we identify explosion as the shock reaching runaway expansion and failed explosion as the shock stalling. Models explode between within 100 – 800 ms post-bounce. The 13- and 14 $M_\odot$ single-star models fail to explode, as do the 17 $M_\odot$ and 21 $M_\odot$ binary-stripped progenitors.

We compare here a typical single star with a binary-stripped star with the same ZAMS mass and identify the explosion trends. We then highlight the exceptions below. We plot in Fig. 4.1 the evolution of the 14 $M_\odot$ progenitor pair as a case study of the differences between binary-stripped and single star evolution. The shock radii and density profiles of all progenitors studied are summarized in the Appendix in Fig. C.1 and Fig. C.2, respectively. In the top left panel of Fig. 4.1, we illustrate the chemical composition of the interior 2.5 $M_\odot$ for the binary-stripped/single star pair of the same initial mass. We identify a composition interface – which often corresponds to the location of the silicon/oxygen (Si/O) transition – illustrated by a sharp drop in the density, as one metric of explodability (see also Vartanyan et al. 2018).[1] The Si/O interface is more pronounced for the binary-stripped progenitor, where the density drops by a factor of ∼2.5 over an annulus of ∼0.005 $M_\odot$, than the single star progenitor, which shows a density drop of only ∼1.6 at the interface. Additionally, the interface is located deeper in, at ∼1.3 $M_\odot$ for the binary-stripped, than for the single star, at ∼1.8 $M_\odot$.

We illustrate the shock radii and highlight the time of Si/O interface accretion and corresponding accretion rate in the top right panel of Fig. 4.1. The binary-stripped star has a sharper Si/O interface located deeper within the stellar progenitor than the single-star model (by ∼0.5 $M_\odot$ for this progenitor mass), and hence the interface is accreted earlier by the expanding shockwave. For the binary-stripped model, the shock intersects the Si/O interface within the first 100 ms. The accretion rate plummets, the ram pressure exterior to the shock drops, and the shock is revived. For the single-star analog, the Si/O interface is less sharp and located further out. It is accreted at ∼500 ms post-bounce, 400 ms after the the binary-stripped model. The drop in accretion rate, and hence ram pressure, is noticeably smaller. The single-star 14 $M_\odot$ progenitor does show a small bump in the shock radii at the time of Si/O accretion

[1] Categorically, this transition has been associate with a silicon/oxygen boundary (see also Timmes et al. 1996; Fryer 1999; Ott et al. 2018). However, we found that the density drop corresponding to a compositional interface, especially if fragmented, could also correspond to iron/silicon or oxygen/neon/magnesium boundaries. We refer to the Si/O interface, and more broadly, the silicon-group and oxygen-group compositional boundary, interchangeably. See Appendix and Fig. C.2 for more detail.

and short-timescale variations as turbulence develops, but the accretion of the Si/O interface is insufficient to revive the stalled shock. Note that in both models, the shock radii are very similar until ~70 ms post-bounce. Stellar collapse and shock revival proceeds quasi-spherically until this point, when turbulence develops around the shock front (Couch & Ott 2013). The evolution paths diverge in part due to the different compositional interfaces. We find that the binary-stripped models studied here typically have a sharper interface located deeper in the stellar interior and a smaller compactness parameter than their single-star counterparts, and, as a result, are more explodable (see Table 4.1, see also Woosley 2019; Ertl et al. 2020; Schneider et al. 2021).

In the bottom panels of Fig 4.1, we plot entropy profiles for the chosen 14 $M_\odot$ pair. The single-star shock stalls interior to 100 km roughly one second after bounce, whereas it has reached almost 10,000 km for the exploding binary-stripped star. We see typical entropies as high as 30 k_B per nucleon, with the explosion occupying a volume-filling fraction of ~20% at late times. Note the large dipolar asymmetry seen in the exploding model in bottom right panel. Although we did see similar 'wasp's waist' morphologies of explosion in various 3D simulations (Vartanyan et al. 2019b; Burrows et al. 2019b), 3D simulations seem to be less asymmetric than 2D equivalents.

4.3.1 Compactness

We find that the compactness parameter provides a viable relative metric of explodability for a given binary/single-star pair of the same ZAMS mass. The compactness parameter characterizes the core structure and is defined as (O'Connor & Ott 2011):

$$\xi_M = \frac{M/M_\odot}{R(M)/1000\,\mathrm{km}} \tag{4.1}$$

where the subscript M denotes the mass where the compactness parameter is evaluated. For our purposes, we evaluate at the compactness parameter $\xi_{1.75}$ at M = 1.75 $M_\odot$, encompassing the Si/O interface for many of our models, though the trends between single-star and binary-stripped star $\xi_{1.75}$ remain largely unaffected for M = 2-3 $M_\odot$ (see also Laplace et al. 2021). However, for the models studied, shock revival is determined prior to accretion of the material exterior to two solar masses, so $\xi_{1.75}$ of the interior profile is more salient to our discussion. Generally, binary-stripped models tend to have a lower $\xi_{1.75}$ than their corresponding single-star progenitors, which correlates with an earlier explosion in our models for a given initial mass (see Woosley (2019); Ertl et al. (2020); Schneider et al. (2021), we note the exceptions below). Additionally, the early accretion of a sharp Si/O density interface promotes explodability (Vartanyan et al. 2018) and corresponds to a smaller $\xi_{1.75}$ (due to the prompt and sharp density drop). The difference in the compactness parameter between binary-stripped and single-stars has been explored in detail (Woosley 2019; Ertl et al. 2020; Chieffi & Limongi 2020). The higher carbon mass fraction in binary-stripped stars shifts the transition from convective to radiative central carbon burning to higher masses Sukhbold & Woosley (2014), above a

final He core mass of ~7.2 $M_\odot$ (Woosley 2019). None of our final He core masses exceed this (Table 4.1, Laplace et al. 2021), but we do see an increase in compactness for the two most massive binary-stripped stars (Table 4.1), above ~6.3 $M_\odot$. Furthermore, we measure the compactness at 1.75 $M_\odot$, which lies interior to the CO core for all models. Thus, we do not find a straightforward association with the CO core mass and carbon mass fraction with compactness for the majority of our binary-stripped models. Rather, we simply associate the smaller compactness parameter with greater mass loss in the binary-stripped stars and with the presence of a deeper Si/O interface, which results in a deeper density drop.

For all progenitor pairs except the 17 $M_\odot$, 18 $M_\odot$ models, progenitors with a smaller $\xi_{1.75}$ more explodable, even where the Si/O interface may be less pronounced. Note that earlier studies have found no correlation between compactness and explodability across progenitor mass (e.g, Vartanyan et al. 2018; Radice et al. 2017; Burrows et al. 2019a,b; Summa et al. 2016, but see Ott et al. 2018), or a scattered correlation with higher compactness but disfavoring very high compactness (Sukhbold & Woosley 2014; Sukhbold et al. 2018; Nakamura et al. 2015; Ott et al. 2018). The compactness parameter does correlate with certain properties of the explosion, with a higher compactness parameter yielding higher neutrino energies and luminosities and a higher accretion rate, as well as a higher binding energy of the stellar envelope, and perhaps can serve to distinguish remnant neutron stars from black holes. However, the interplay between accretion, luminosity and explosion outcome is nuanced (see our discussion of the critical condition below) and hence a monotonic relation between compactness and explosion outcome is not expected (O'Connor & Ott 2013). Our conclusion is not at odds with this – we emphasize that the correlation of the relative compactness with explodability here only holds for models with the same ZAMS mass, but different (single vs binary-stripped) post-main sequence evolution. We find no "absolute compactness parameter" that delineates explosion from non-explosion, and a model with a smaller compactness parameter may fail to explode while a different ZAMS mass model with a higher compactness parameter may. The results are summarized in Table 4.1, where we show the compactness, explosion outcome, the final proto-neutron star mass, and the final helium core mass for all 11 pairs of models presented here.

4.3.2 Exceptions

Contrary to the general trend of donor stars in binaries being more easily exploded than single stars of the same initial mass, we find that the 12.1- and 21 $M_\odot$, as well as the 17 $M_\odot$ and 18 $M_\odot$ single star progenitors are more explodable. The former pair can be explained by merger of the Si/O shells, resulting in a steeper Si/O interface, a smaller $\xi_{1.75}$, and hence a progenitor more conducive to explosion. The 12.1 and 21 $M_\odot$ single-star progenitors do indeed have a smaller compactness parameter, and more explodable, than the corresponding binary-stripped models. We find that the shell mergers happen stochastically and are not a hallmark difference of the single vs binary evolution (see Laplace et al. 2021).

For the 17 and 18 $M_\odot$ progenitors, we find a contrasting behavior. The single-star progeni-

tors have a higher compactness parameter than their stripped counterparts, with Si/O interfaces further out. Surprisingly, these models with a higher $\xi_{1.75}$ are more explodable than their stripped counterparts. We explore why the explosion trend is reversed for these models with a discussion of the critical condition for explosion below.

4.3.3 Luminosity-Accretion Tracks and Criticality

We explore the proximity to a critical condition for explosion. The critical curve (Burrows & Goshy 1993; Summa et al. 2016) quantifies the competing but coupled effects of accretion and neutrino luminosity in driving explosion. Accretion provides a ram pressure exterior to the shock which the shock must overcome to produce an explosion, while simultaneously providing an accretion-powered luminosity that contributes to neutrino heating of the stalled shock. In Fig. 4.2, we illustrate luminosity−accretion rate tracks for the enigmatic 17 and 18 $M_\odot$ models. The two single-star progenitors have a higher luminosity for a given accretion rate than the binary-stripped counterparts. The single-star progenitors for these two models have a shallower density profile that provides a higher accretion rate and a higher accretion luminosity conducive to explosion. Their subsequent explosion can be explained by their proximity to this critical condition for explosion. In addition, we find that, prior to explosion, the binary-stripped 18 $M_\odot$ progenitor has a slightly higher neutrino luminosity than the 17 $M_\odot$ binary-stripped model, and only the former explodes despite having quite similar progenitor profiles with the latter. This highlights how sensitive explosion outcome can be to small differences in this mass range.

However, the critical condition does not sufficiently explain explodability for other models. For instance, the 21 $M_\odot$ stripped progenitor has a higher luminosity for a given accretion rate than its single-star counterpart, but fails to explode. Thus, compactness and criticality provide valuable and complementary insight, and neither alone necessarily provides a definitive determinant of explosion outcome. Quantifying the exact transition from non-explosion to explosion has been a subject of previous work (Summa et al. 2016, 2018), but often requires fine-tuning the studied parameters and lies outside our present focus. We draw attention only to the point that compactness and the critical condition focus on two distinct factors of explosion outcome: the density profile, including the presence of a strong Si/O interface (see Fig. C.2), and the accretion/accretion-luminosity tracks, respectively. Additionally, more detailed prescriptions for predicting explosion exist (Pejcha & Thompson 2012; Raives et al. 2018, Murphy & Dolence 2017, Müller et al. 2016, Ertl et al. 2016). These parametrizations are in the context of one-dimensional spherically-symmetric explosions, dependent on the simulation results for tuning, and beyond our scope in the context of multi-dimensional simulations.

Progenitors with a sufficiently small compactness parameter or in our models, analogously field a prominent Si/O or equivalent compositional interface, explode regardless of their proximity to criticality. Those that are not need to satisfy the critical condition. Our results illustrate the following trend for explosion outcome by progenitor: amongst lower mass

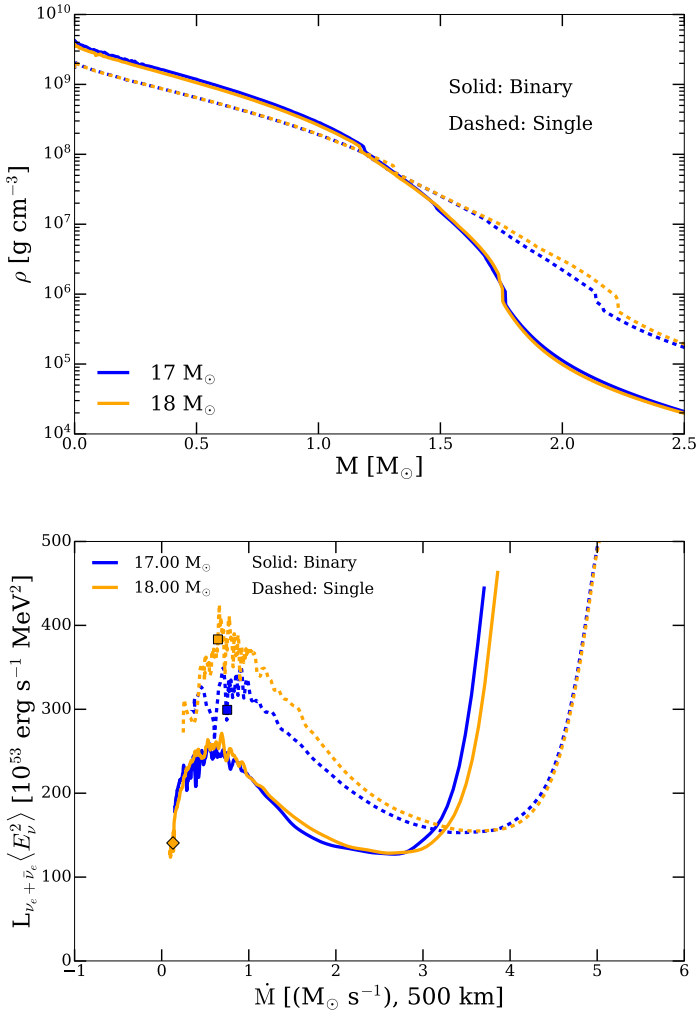

Fig. 4.2: **Left**: We illustrate the density profiles of the 17 $M_\odot$ and 18 $M_\odot$ progenitors for the both the binary-stripped (solid) and single stars (dashed), which behave as an exception to the general trend with lower compactness parameter preferentially promoting explosion for a given initial mass. Note that the the single-stars, with a higher $\xi_{1.75}$, are more explodable, and also how similar the binary-stripped density profiles are for these two models. **Right**: We show the luminosity-accretion tracks for the 17 $M_\odot$ (orange) and 18 $M_\odot$ progenitors (red). We illustrate the neutrino luminosity weighted by the RMS neutrino energy (at 500 km and in 10^{53} erg s^{-1}, summing over electron neutrinos and anti-neutrinos) as a function of accretion rate (at 500 km, in $M_\odot$ s^{-1}). The solid lines indicate the binary-stripped progenitors and the dashed the single-star progenitors. The stars evolve leftward along the illustrated tracks. The colored squares show when the single-star models explode, and the colored diamond when the stripped 18 $M_\odot$ model explodes. The stripped 17 $M_\odot$ progenitor does not explode. We see that the single-stars have a higher RMS-energy weighted neutrino luminosity for a given accretion rate than their stripped counterparts. The stripped 18 $M_\odot$ progenitor has a slightly higher neutrino luminosity than the stripped 17 $M_\odot$ prior to explosion, and the former explodes but not the latter, despite having nearly identical profiles. Near the onset of explosion, the dynamics become turbulent, as evidenced by the variations in the plotted quantities.

progenitors (10−15 $M_\odot$), with steeper density profiles, the model with a smaller $\xi_{1.75}$ is more explodable. Higher mass progenitors (17 $M_\odot$, 18 $M_\odot$ single-star progenitors, and both single-star and stripped profiles for the 20-M⊙ progenitors) have shallower density profiles and Si/O interfaces located further out. Here, sustained accretion powers a sufficient neutrino luminosity for the star to explode, with the star with a smaller $\xi_{1.75}$ again being more explodable. For intermediate mass stars (e.g., the 17 $M_\odot$, 18 $M_\odot$ binaries), the Si/O interface lies between ∼1.7−1.9 $M_\odot$ and is too far to be accreted for prompt shock revival, while the density profile is not shallow enough to maintain high persistent accretion to promote later shock revival. These models do not satisfy either criterion for explodability: a prominent interface or the critical condition.

It is difficult to find a-priori indicators of explosion outcome from progenitor dependence alone, but we attempt to provide a broad categorization across progenitor mass here. No single parametrization is sufficient to capture or predict the complex nature of explosion, but jointly studying the compactness and the proximity to the critical condition span the range of possible outcomes. We emphasize that the phase space of interest for explosion outcome is really the density profile, $\rho(M) - M$, and not simply the ZAMS or He core mass of the star. A simple parametrization or explosion criterion eludes our, and the broader supernova community's, efforts.

4.3.4 Explosion Diagnostics

Explodability, and explosion timing, provides a diagnostic of the explosion properties, including remnant masses, nucleosynthetic yields, and energetics. For instance, early work (Burrows & Vartanyan 2021) suggests that perhaps stars that explode later may do so more energetically. In this study, this is further buttressed by the fact that the less-explodable single-stars also have a heavier mantle to sustain higher accretion energies.

Here, we find a distribution of baryonic proto-neutron star (PNS) masses spanning 1.3 to 2.2 $M_\odot$ (see Table 4.1) at the end of our simulations, higher than the values found in Ertl et al. (2020) for similar helium core masses. Just after core bounce, the PNS masses are close to the Chandrasekhar mass of 1.3 $M_\odot$, and the divergence of behavior afterwards is a function of the accretion density profile. The heavier progenitors accrete almost as much as one solar mass within the first second of core bounce. In many of our models, the PNS masses are still growing. Categorically, the binary-stripped stars, with a smaller compactness parameter, yield PNS masses a few tenths of a solar mass smaller than their single-star pairs of the same initial mass. The exceptions, as expected, are the 12.1 and 21 $M_\odot$ progenitors, for which the single star progenitors have a smaller compactness parameter and yield a smaller PNS mass. Surprisingly, both the 17 $M_\odot$ and 18-$M_\odot$ binary-stripped progenitors produce less massive PNS, despite being less explodable than their single-star counterparts, suggesting that progenitor density profile and compactness may be additionally critical to determining PNS mass than simply the explosion time alone.

The 18- and 20 $M_\odot$ stripped-star progenitors both yield PNS masses over 2 $M_\odot$, and both

successfully explode as well, providing simulation insight into the upper mass limits of neutron stars. After explosion within the first second, multiple solar masses of material remain in the stellar envelope to be ultimately accreted and, in smaller part, blown out as a wind. The possible existence of a mass gap (Bailyn et al. 1998; Özel et al. 2010; Farr et al. 2011) between the most massive neutron stars (e.g., Cromartie et al. 2020) and the least massive black holes (e.g., The LIGO Scientific Collaboration et al. 2020), lying between ~2.5 to 5 $M_\odot$ could be populated by fallback accretion onto the PNS remnants of stripped stars in binaries (Fryer et al. 2012; Woosley et al. 2020; Schneider et al. 2021; Ertl et al. 2020). Late time simulations of CCSNe that encompass mass fallback are lacking, as is our understanding of the details of fallback accretion. However, we can approximate fallback by assuming the morphology of the shock (e.g., bottom right panel of Fig. 4.1) is sustained and we can estimate a volume-filling fraction of the expanding shock. At 5000 km, this is ~20%, suggesting that more than half of the envelope will accrete at later times. Indeed, we only require sustained accretion of less than half the helium core mass of binary-stripped stars (see Table 4.1), or around 1-2 solar masses, to populate this mass gap. We emphasize again that this is just a cursory estimate, and detailed, long-term 3D simulations are necessary.

The successfully exploding models present a typical diagnostic explosion energy of ~0.2 Bethe (1 Bethe $\equiv 10^{51}$ erg) within the first second. The more massive single 17 $M_\odot$,18 $M_\odot$ progenitors have energies of upwards 0.4 Bethe, and both the single and binary-stripped 20 $M_\odot$ progenitors have diagnostic energies of more than 0.5 Bethe. However, correcting for the gravitational binding energy of the material exterior to our grid, we find that all of our models are still gravitationally-bound, albeit tenuously. This is to be expected for a short simulation, spanning less than one second post-bounce. Furthermore, many of the models show significant early energy growth rates (consistent with Burrows et al. 2019b; Burrows & Vartanyan 2021), suggesting that longer simulations are necessary to see the final explosion energies for many of these models, as well as the remnant PNS masses, nucleosynthetic yields, and possible remnant kick velocities.

Additionally, although some single-star models (such as the 18 $M_\odot$, 20 $M_\odot$ models) have higher diagnostic explosion energies, all binary-stripped models have more weakly bound and less massive envelopes. Thus, correcting for the gravitational overburden of the envelope, all of our exploding binary-stripped models have higher net explosion energies than the corresponding single stars, at least within the first second of simulation. However, our preliminary results seem to suggest that single stars have faster energy growth rates than their binary-stripped pairs, which we attribute to a larger accreting mass. This is at odds with Schneider et al. (2021), who find a higher accreting mass and higher energies in their binary-stripped models using a parametric supernova code. Resolution of this necessitates longer simulations in self-consistent 3D. In addition, we find that single stars tend to have higher gravitational-ave energies, potentially due to more massive envelopes ultimately yielding greater turbulent energy impinging on the PNS (Radice et al. 2019; Vartanyan et al. 2019a; Vartanyan & Burrows 2020).

Though the helium core mass correlates with the core compactness, compactness itself

does not provide a global metric for explosion outcome. Rather, we find that core compactness serves as a relative metric for explodability for progenitors of the same ZAMS mass but different evolutionary channels. Insofar as the helium core mass correlates with the compactness, which we find is a useful relative metric for explodability of binary-stripped and single star pairs, we find a weak and scattered correlation with more massive helium cores exploding later and with higher PNS masses. However, the helium core extends too far in mass to significantly affect the early nature of shock revival, whereas the interior density profile is critical to a successful explosion.

4.4 Conclusions

In this study, we presented a comparison of binary-stripped stars with single-star counterparts of the same initial mass. Compared to current literature, our work provides an improvement along two avenues – we follow a self-consistent evolution of both the pre-collapse progenitors, including binary interactions as our initial condition and the subsequent explosion outcome. We illustrated that binary-stripped progenitors typically have a smaller compactness parameter and tend to be more explodable (see also Woosley 2019; Ertl et al. 2020; Schneider et al. 2021) than single stars with the same initial mass. The latter remains to be confirmed – our detailed simulations post-bounce and stellar evolution pre-bounce are hostage to uncertainties in the understanding of stellar theory, including the development of convection (Renzini 1987; Renzo et al. 2020), nuclear burning reactions (Farmer et al. 2016), winds (Renzo et al. 2017), overshooting (Davis et al. 2019), and the detailed of role of neutrino microphysics. However, these initial results are promising to resolve possible discrepancy between the stellar mass function and the rate of supernovae, as well as populate the possible neutron-star black hole mass gap. The higher explodability of binary-stripped stars may also help explain the large fraction of stripped-envelope supernovae. We expect the nucleosynthesis of single and binary-stripped stars to be different (R. Farmer et al. in prep.) due to the systematic differences in composition at the onset of core collapse (Laplace et al. 2021). If binary-stripped stars are more explodable, then these differences in nucleosynthesis are even more important.

Stars of similar initial masses can have very different density profiles (e.g., Sukhbold & Woosley 2014; Sukhbold et al. 2018) and hence different explosion outcomes. Here, we have seen stars of different masses, e.g. the 17 $M_\odot$, 18 $M_\odot$ models, with very similar density profiles but qualitatively different explosion outcomes (explosion vs. no explosion). We find only a weak, scattered dependence on explosion outcome with the helium core mass.

Earlier work on binary progenitors of CCSNe have either evolved only until the formation of a carbon-oxygen core, or evolved an isolated carbon-oxygen core until collapse (Patton & Sukhbold 2020). Additionally, these studies have either artificially inducing explosion through parametrized heating (Woosley 2019; Schneider et al. 2021; Ertl et al. 2020), or have used prescriptive formulae to predict explosion outcome, introducing uncertainty in both the progenitor profile and its final fate. Here we present a self-consistent study of explosion

outcome of stripped-models with their single-star counterparts. We find that the progenitor density profile is critical to explosion outcome. The sensitivity of the explosion to details necessitates a through study of the physical uncertainties in the progenitor models – the initial conditions for core-collapse simulations – before we can confidently claim resolution of the core-collapse problem. Recent results would indicate we have reached a tipping point where uncertainties in the stellar evolution models dwarf uncertainties in the neutrino-heated explosion of core-collapse supernovae.

We acknowledge Tony Piro, Stephen Justham, Robert Farmer, and Daniel Kasen for valuable discussion. DV and AB acknowledge support from the U.S. Department of Energy Office of Science and the Office of Advanced Scientific Computing Research via the Scientific Discovery through Advanced Computing (SciDAC4) program and Grant DE-SC0018297 (subaward 00009650) and support from the U.S. NSF under Grants AST-1714267 and PHY-1804048 (the latter via the Max-Planck/Princeton Center (MPPC) for Plasma Physics). EL and SdM acknowledge the European Union's Horizon 2020 research and innovation program from the European Research Council (ERC, grant agreement No. 715063) and the Netherlands Organisation for Scientific Research (NWO) as part of the Vidi research program BinWaves with project number 639.042.728. YG acknowledges the funding from the Alvin E. Nashman fellowship for Theoretical Astrophysics. The authors employed computational resources provided by the TIGRESS high performance computer center at Princeton University, which is jointly supported by the Princeton Institute for Computational Science and Engineering (PICSciE) and the Princeton University Office of Information Technology.

Table 4.1: Explosion Properties

Model	Explosion?		Compactness Parameter		PreSN Mass ($M_\odot$)		PNS Mass ($M_\odot$)*		He Mass ($M_\odot$)		CO Mass ($M_\odot$)	
($M_\odot$)	Binary	Single	Binary	Single	Binary	Single	Binary	Single	Binary	Single	Binary	Single
11.0	✓✓	✓	0.140	0.215	3.11	9.32	1.47	1.48	3.16	3.78	1.88	2.31
12.1	✓	✓✓	0.246	0.110	3.52	9.73	1.52	1.33	3.93	4.78	2.09	2.81
13.0	✓✓	✗	0.213	0.364	3.87	9.97	1.50	1.83	4.29	5.26	2.46	3.19
14.0	✓✓	✗	0.200	0.597	4.23	10.1	1.45	1.86	4.53	5.62	2.57	3.60
14.6	✓✓	✓	0.280	0.656	4.48	10.1	1.56	1.86	4.66	5.80	2.99	3.90
15.0	✓✓	✓	0.285	0.478	4.61	10.2	1.53	1.75	5.03	6.32	2.44	4.07
16.0	✓✓	✓	0.274	0.647	4.97	10.1	1.52	1.89	5.36	6.85	3.42	4.47
17.0	✗	✓✓	0.552	0.740	5.31	9.88	1.85	1.99	5.66	7.30	3.73	4.97
18.0	✓	✓✓	0.569	0.756	5.61	10.10	1.79	2.01	6.01	7.41	2.49	5.42
20.0	✓✓	✓	0.678	0.723	6.28	11.7	1.92	2.16	6.34	7.57	4.60	5.67
21.0	✗	✓✓	0.730	0.363	6.62	10.4	2.16	1.61	6.67	8.19	4.07	6.20

Table of our 2D simulation results: models with a checkmark explode, and models with an ✗ do not explode. Models with two checkmarks explode first compared to their single/binary counterpart, if the latter explodes at all. We also show the compactness parameter (at 1.75 $M_\odot$), the final PNS mass for the binary-stripped and single star pair, and the preSN mass as well as the He and CO core masses (all in $M_\odot$) at the onset of core-collapse. *Note that these PNS masses are lower limits – many of the models continue to accrete (and explode) at the end of our simulations.

Chapter 5

The cosmic carbon footprint of massive stars stripped in binary systems

R. Farmer, E. Laplace, S. E. de Mink, and S. Justham

Submitted to The Astrophysical Journal

Abstract

The cosmic origin of carbon, a fundamental building block of life, is still uncertain. Yield predictions for massive stars are almost exclusively based on single star models, even though a large fraction interact with a binary companion. Using the `MESA` stellar evolution code, we predict the carbon ejected in the winds and supernovae of single and binary-stripped stars at solar metallicity. We find that binary-stripped stars are twice as efficient at producing carbon (1.5–2.6 times, depending on choices on the slope of the initial mass function and black hole formation). We confirm that this is because the convective helium core recedes in stars that have lost their hydrogen envelope, as noted previously. The shrinking of the core disconnects the outermost carbon-rich layers created during the early phase of helium burning from the more central burning regions. The same effect prevents carbon destruction, even when the supernova shock wave passes. The yields are sensitive to the treatment of mixing at convective boundaries, specifically during carbon-shell burning (variations up to 40%) and improving upon this should be a central priority for more reliable yield predictions. The yields are robust (variations less than 0.5%) across our range of explosion assumptions. Black hole formation assumptions are also important, implying that the stellar graveyard now explored by gravitational-wave detections may yield clues to better understand the cosmic carbon production. Our findings also highlight the importance of accounting for binary-stripped stars in chemical yield predictions and motivates further studies of other products of binary interactions.

5.1 Introduction

Understanding the Cosmic production of the elements that form the building blocks of life is still one of the main quests for modern astronomy. Massive stars are known to play a critical role in the synthesis of heavy elements over cosmic time, but many questions remain open (e.g. Burbidge et al. 1957; Cameron 1959; Woosley & Weaver 1995; Nomoto et al. 2006). Our current understanding of the nucleosynthesis products of massive stars is still almost exclusively based on single star progenitor models (Maeder 1992; Woosley et al. 1993a; Kobayashi et al. 2006; Curtis et al. 2019). However, observational studies of young massive stars have indicated that massive stars are nearly always born in multiple systems (Abt 1983; Mason et al. 2009), with at least one companion star nearby enough for binary interaction (Sana et al. 2012; Moe & Di Stefano 2017). Such interactions can dramatically change the final fate of massive stars (Podsiadlowski et al. 1992; Wellstein & Langer 1999; Langer 2012). How such interactions may change the chemical yields of massive stars is still not fully clear, see however Woosley (2019).

The source of carbon in the Universe is still uncertain (Bensby & Feltzing 2006; Romano et al. 2017). Observations, and theoretical modelling, suggest contributions from the winds of asymptotic giant branch (AGB) stars (Nissen et al. 2014), massive star winds and their core collapse supernovae (Franchini et al. 2020), and type Ia supernovae (Leung & Nomoto 2020). The source of carbon matters not just for the amount of carbon expected in the Universe, but also for understanding when and where it is formed (Carigi et al. 2005; Cescutti et al. 2009). Which can then be used to understand the star formation history of a galaxy (Carilli & Walter 2013; Romano et al. 2020).

Massive stars are able to eject carbon a few million years after formation (Woosley et al. 1993b), while AGB winds and type Ia supernovae require much longer timespans before releasing their carbon (Henry et al. 2000; Akerman et al. 2004). The relative contribution from each source may vary over time as the metallicity, and thus wind mass loss, increases (Dray et al. 2003; Lau et al. 2020).

Carbon plays a crucial role in the interstellar medium (ISM) through its complex chemistry and its ability to form a wide range of carbon-rich molecules (Herbst & van Dishoeck 2009) and carbonaceous dust (Li & Draine 2001; Weingartner & Draine 2001). Atomic carbon plays key roles in heating and cooling interstellar gas (Wolfire et al. 1995) as well as in tracing the properties of the ISM (Wolfire et al. 2003). The presence of CO is an important observational tracer of molecular gas (Frerking et al. 1982; Solomon et al. 1987). Dust formation from supernovae is also governed by the presence of carbon (Bevan et al. 2017; Sarangi et al. 2018; Lau et al. 2020; Brooker et al. 2021). Thus understanding the formation of carbon and its distribution is key to understanding the ISM (Burton & Gordon 1978; Gullberg et al. 2018).

Here we study the effect of binary evolution on the carbon yields ejected by massive stars (Langer 1991b). Previous work by Laplace et al. (2020, 2021) explored the evolution of binary-stripped stars up to core collapse, and showed how the mass loss during a binaries evolution alters the final structure of a star. These structural differences in binary-stripped

stars, as compared to single stars, is expected to lead to differences in the final supernova and the yields (Woosley 2019; Schneider et al. 2021).

We take this work further by exploring the nucleosynthetic yield of carbon (^{12}C) before and after core collapse and over a larger range of initial masses. We consider here the fate of binaries that are stripped by their companion in case B mass transfer, i.e they lose mass during their evolution after core hydrogen depletion but before core helium ignition. An analysis of all nucleosynthetic yields is deferred to later work.

Our paper is structured as follows, in Section 5.2 we describe our method for following the evolution of single and binary stars, as well as their supernova explosions. In Section 5.3 we compute the carbon yields for single and binary stars. We discuss the uncertainties in our pre-supernova evolution and supernova explosions in Section 5.4. In Section 5.5 discusses the initial mass function (IMF) weighted yields. Finally, we discuss our results in Section 5.6 and conclude in Section 5.7.

5.2 Method

5.2.1 Pre-supernova evolution

We use the MESA stellar evolution code (version 12115, Paxton et al. 2011, 2013, 2015, 2018, 2019) to evolve massive single and binary stars from the zero-age main sequence to core collapse. Our single stars and the primary (initially most massive star) in the binary have initial masses between $M_{init} = 11 - 45\,M_{\odot}$. For binary stars we set the initial period to be between 38–300 days. This period range ensures that all binary stars undergo case B mass transfer (Paczyński 1967). We set the secondary star's mass such that the mass ratio $M_2/M_1 = 0.8$. All models are computed with a initial solar metallicity of Z=0.0142 and are non-rotating. Single stars and binary stars are evolved with initial Y=0.2684 ($Y = 2Z + 0.24$ Pols et al. 1995; Tout et al. 1996). Inlists with all input parameters and models are made available online at https://zenodo.org/10.5281/zenodo.4545837.

To evolve the systems we build upon the method in Laplace et al. (2020, 2021). We follow in detail the structure of the primary star and the period evolution of the system during Roche lobe overflow. We take the secondary star in the binary to be a point mass and do not follow its evolution. Mass transfer is assumed to occur conservatively such that no mass is lost from the system. With the initial periods chosen we do not expect further Roche lobe overflow (RLOF) to occur during the systems lifetime (Laplace et al. 2020). After core helium burning ceases we evolve only the initial primary star of the binary.

Wind driven mass loss follows the prescriptions of Vink et al. (2001) for stars with $T_{eff} > 10^4$K and surface hydrogen mass fraction $X_H > 0.4$, Nugis & Lamers (2000) for $T_{eff} > 10^4$K and surface $X_H < 0.4$, and de Jager et al. (1988) at all other times, with wind-scaling factors of 1.0. In binary systems we define all of the mass lost when the radius of the primary is greater than its Roche lobe radius to be RLOF, even though mass loss via winds will still occur. This is a reasonable assumption as the mass loss via winds during Roche lobe

overflow is small due to the short timescale over which RLOF occurs.

Convective overshoot is calibrated to that of Brott et al. (2011), with a step overshoot value of $f = 0.385$ and $f_0 = 0.05$. In MESA overshoot starts inside a convection zone at a distance of f_0 (in pressure scale heights), and extends from this point a distance of f (in pressure scale heights). Therefore, overshoot will extend a distance $f - f_0$ from the edge of the convective boundary. We also apply the same amount of overshooting above the metal burning zones during the late stage evolution of the models. We add a small amount of overshoot ($f = 0.05$, $f_0 = 0.01$) below metal burning shells to improve numerical stability. We use MLT++ for all models to improve the numerical stability of the low density envelopes (Paxton et al. 2013). We include semiconvection with a mixing efficiency of $\alpha_{\rm semi} = 1.0$ and we do not include thermohaline mixing. Additional physics choices are specified in Appendix D.1.

We evolve our stars with MESA's `approx21.net` which contains 21 isotopes, following the alpha-chain up to iron. Farmer et al. (2016) has shown the need to use larger nuclear networks when evolving stars to core-collapse, to compute the core structure accurately. However, we show in Appendix D.2.1 that models computed with `approx21.net` predict similar ^{12}C yields to models using such a larger network (`mesa_128.net`).

We define the helium core mass of the star as the first point in time (and space) when the helium mass fraction, $X_{\rm He} > 0.1$ and the hydrogen mass fraction (at the same mass coordinate) is $X_{\rm H} < 0.01$. Core oxygen depletion is defined when the oxygen mass fraction at the center of the star drops below $X_{\rm O} < 10^{-4}$. Finally, we define core collapse to occur when the inner regions of the star infalls at 300km s^{-1}.

5.2.2 Core-collapse supernovae

To model the supernova explosion, its shock, and the resulting nucleosynthesis we place a "thermal bomb" at the center of our model (Aufderheide et al. 1991; Sawada & Maeda 2019). First we excise a portion of the star's core, the material that will form a compact object, by placing the inner boundary of our model at the point where the entropy per baryon $S = 4$ (Brown & Woosley 2013). We then inject energy into the base of the material outside this boundary over a mass range of 0.01 $M_\odot$, over 0.0045 seconds. We inject sufficient energy to bring the total energy of the star (the sum of the kinetic plus thermal energy minus the gravitational binding energy) to 10^{51}erg/s. These values specify our default model assumptions.

This injection of energy then generates a hydrodynamic shock which travels from the inner boundary of the star to the surface. As it passes through the star it shock heats material and begins nuclear burning. This nucleosynthesis is computed with MESA's `mesa_128.net` which contains 128 isotopes up to ^{64}Zn. In Section 5.4.2 we discuss how our choice of explosion parameters affects the resulting nucleosynthesis. Also in Section 5.4.2 we discuss our choice of temporal and spatial resolution during the explosion. The star is then evolved until the shock reaches a location 0.1 $M_\odot$ below the surface, by which time the shock has cooled to the point of no further nucleosynthesis occurring, except for beta decays. We do not add by hand

any ^{56}Ni to the stars.

During the shock propagation through the star we track the energy change due to photo-disintegrations and nuclear burning. At shock breakout our models will have a different final energy as compared to the amount of energy we injected during the explosion. The total energy is 1.05–1.20×10^{51} erg/s at shock breakout while the kinetic energy at shock breakout is between 0.5–1.3×10^{51} erg/s.

We define the yield of an isotope as (Karakas & Lugaro 2016):

$$\text{Yield} = \sum_{\text{T}} \Delta \text{M}_{\text{T}} \times \left(\text{X}_{\text{j}} - \text{X}_{\text{j,int}} \right) \tag{5.1}$$

Where $\Delta \text{M}_{\text{T}}$ is the mass lost over the time interval T, X_{j} is the surface mass fraction of isotope j, and $\text{X}_{\text{j,int}}$ is the initial mass fraction of isotope j. With this definition negative yields will occur in cases of net destruction of an isotope. In this case, the mass fraction in the ejected material will be lower than in the initial composition of the ejected material. We use the solar composition of Grevesse & Sauval (1998) which sets $\text{X}_{\text{C}_{12},\text{int}} = 0.00244$.

5.3 Total carbon

Figure 5.1(a) shows the total ^{12}C yields from our single and binary stars, from all sources of mass loss. Figure 5.1(b) shows the ^{12}C yield from winds, while Figure 5.1(c) shows the ^{12}C yield from core-collapse ejecta. In appendix D.3 we include Table D.1 that breaks down the total carbon yield by its source.

The ^{12}C yield from the mass loss during RLOF is negative and small $\approx -0.01\,\text{M}_{\odot}$ and approximately independent of the initial mass of the primary star. This is due to the envelope being unprocessed and its carbon content reflects this initial abundance. The deeper layers of the envelope have been processed by CN and CNO-cycling and show depleted carbon abundances (Maeder 1983). The most massive stars show a slight decrease in ^{12}C ejected during RLOF as a larger fraction of the envelope is processed by CN(O)-cycling.

Figure 5.1(b) shows the ^{12}C yields due to wind mass loss. The mass loss due to winds (for all stars) can be broken into two groups, for stars with $\text{M}_{\text{init}} \lessapprox 35\,\text{M}_{\odot}$ their winds are not ^{12}C enriched as compared to their initial composition, and thus not visible in Figure 5.1(b). Stars with $\text{M}_{\text{init}} \gtrapprox 35\,\text{M}_{\odot}$ have ^{12}C enriched winds. This is due to both the single and binary stars becoming fully stripped, removing both the hydrogen and helium layers of the star. In this initial mass range carbon rich material has been mixed out of the core and is then ejected. This occurs at $\text{M}_{\text{init}} = 37\,\text{M}_{\odot}$ for single stars and $\text{M}_{\text{init}} = 35\,\text{M}_{\odot}$ for the binaries. The transition occurs at a lower initial mass for the binaries due to RLOF removing some of the envelope. Lower mass objects which are not fully stripped do not eject more ^{12}C in their stellar winds than they started with.

Figure 5.1(c) shows the ^{12}C yields for core-collapse ejecta, assuming that all stars eject their envelopes. The ^{12}C yield is relatively flat as a function of initial mass for stars with

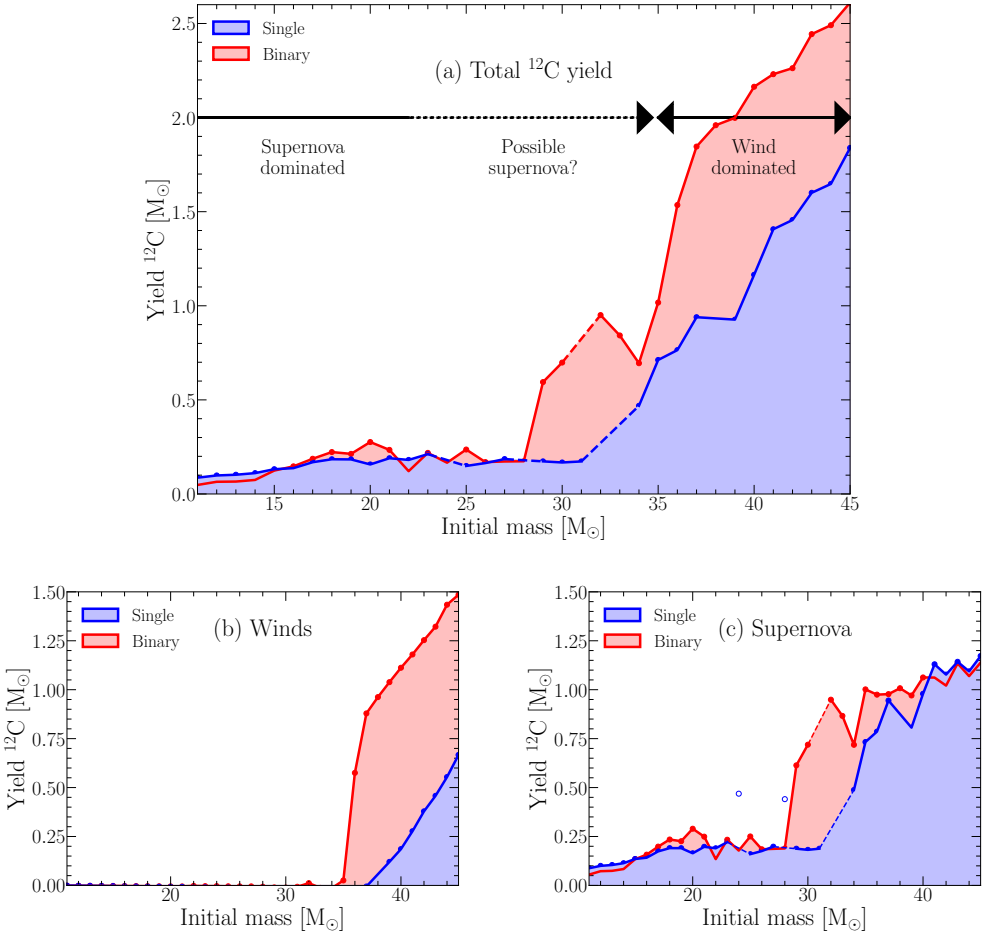

Fig. 5.1: Top panel: The total ^{12}C yield from all ejection sources, Left Panel: The ^{12}C yield ejected during wind mass loss, Right Panel: The ^{12}C yield ejected during core collapse. The core-collapse yields assume all stars eject their envelope. In all panels red regions denote binary models while blue regions denote single star models. Open circles mark models which show anomalous carbon-burning behavior, see section 5.3.3. Dashed lines in panels (a) and (c) denote extrapolations over the anomalous carbon-burning behavior and models which do not reach core collapse. The black arrows show the approximate location where each type of mass loss dominates the ^{12}C yield, taking into account reasonable assumptions for which stars eject their envelopes (Sukhbold et al. 2016; Zapartas et al. 2021b).

$M_{init} \lessapprox 27\,M_\odot$, at $\approx 0.2\,M_\odot$. Above this initial mass the yield rapidly increases up to $\approx 1.25\,M_\odot$. This transition between low and high carbon yields occurs between $27 \lessapprox M_{init}/M_\odot \lessapprox 35$. The increased ^{12}C yields are due to the wind mass loss removing the hydrogen envelope but not all of the helium envelope from the stars. Thus there is enough mass loss to alter the core structure of the star, leaving behind a carbon layer but not enough wind mass loss to then expose that layer (see Section 5.3.2).

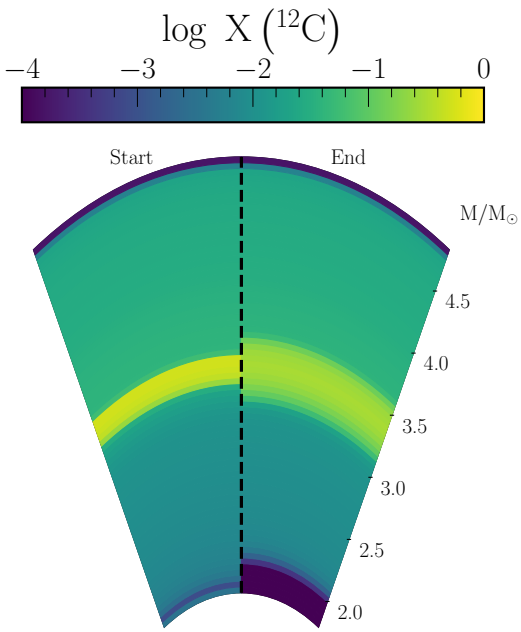

Fig. 5.2: The composition profile of a 15 $M_\odot$ binary-stripped star at the start and end of the shock propagation phase of core collapse. The colors denote the mass fraction of ^{12}C. The animated version shows the shock propagation and resulting nucleosynthesis with time.

5.3.1 Shock nucleosynthesis

Figure 5.2 shows the distribution of ^{12}C inside a binary-stripped star with $M_{init} = 15\,M_\odot$ at the start and end of the shock propagation phase during core collapse. The online animation shows the propagation of the shock and the explosive nucleosynthesis this generates.

At the start of the core-collapse phase, we can see that the ^{12}C is concentrated in the helium shell, with only small amount of material near the core. As the shock propagates it photo-disintegrates some of the ^{12}C near the inner boundary, and cools from a peak temperature of $\approx 10^{10}$K, to $\approx 3\times10^{8}$K when it reaches the carbon-rich helium shell, and to $\approx 10^{7}$K near shock breakout. By the time the shock reaches the carbon-rich layers it has cooled sufficiently that it can no longer burn those layers. The difference in pre- and post- supernova nucleosynthesis is $\approx$ 1% for ^{12}C. The main effect on the ^{12}C yield is to smear the ^{12}C distribution over a slightly larger range of mass coordinates. Thus for future studies it is not necessary to model the supernova explosion itself to predict ^{12}C yields. This was already found for single-star progenitors (e.g Thielemann et al. 1996; Young & Fryer 2007), and we now confirm it for self-consistent binary-stripped structures.

5.3.2 Differences in core structure

To understand the differences between single stars and stripped binaries in Figure 5.1 it is instructive to examine the evolution of two stars (a single and a binary-stripped) of the same initial mass. Figure 5.3 shows the time evolution of a single and a binary-stripped star with $M_{init} = 19,\ 37$, and $45\,M_\odot$. Considering the $M_{init} = 19\,M_\odot$ case, both stars start on the main sequence and lose only a very small amount of mass before they evolve into Hertzsprung gap stars. At this point the donor star in the binary exceeds its Roche lobe radius and begins losing mass, via RLOF. In Figure 5.3b this occurs at $\log_{10}\ (\tau_{cc} - \tau)\,/\mathrm{yr} \approx 5.9$. Most of the binary star's envelope is lost at this point, bringing its mass down to $\approx 8.0\,M_\odot$, but the RLOF does not completely remove the hydrogen envelope (Götberg et al. 2017; Yoon et al. 2017).

However, the mass that was lost was only comprised of the stellar envelope (light blue region), which has a composition similar to the star's birth composition. Thus the mass loss from the binary during RLOF does not enrich the Universe in ^{12}C. In fact, the material is slightly carbon poor, due to some of the material having been CNO processed before the outer edge of the convective hydrogen-burning core receded (dark blue region).

As the binary loses mass from its outer layers the core structure of the binary is altered. The binary-stripped star forms a smaller helium core, and the edge of the convective core recedes during core helium burning (Langer 1989b; Woosley et al. 1993a), while in the $M_{init} = 19\,M_\odot$ single star the mass in the convective helium-burning core stays constant. This receding convective core leaves behind ^{12}C that was produced by the 3α process but had not yet been converted into oxygen in $^{12}\mathrm{C}\,(\alpha,\gamma)^{16}\mathrm{O}$ (Langer 1991b). This left-over ^{12}C is outside of what will become the CO core of the star (denoted by the red lines).

Any ^{12}C that is produced, and stays, inside the helium core will either be burnt into oxygen at the end of core helium burning, destroyed during $^{12}\mathrm{C} + {}^{12}\mathrm{C}$ burning, or will be accreted onto the compact object during core-collapse. Thus only the ^{12}C that is mixed out of the core has a chance to survive until core-collapse. Some of this outwardly mixed ^{12}C will not, however, survive until core collapse as it will be converted into oxygen during helium shell burning, or be mixed back into the core during carbon burning via the carbon convection zone intersecting the helium shell (see Section 5.3.3).

Figure 5.3(c,d) shows a single and binary-stripped star with $M_{init} = 35\,M_\odot$. Here the wind mass loss is sufficient to remove the remaining helium layers above the core. This exposes ^{12}C rich material, which is then ejected in a wind, similar to the process in the binary-stripped star with $M_{init} = 19\,M_\odot$. Thus the single star has a net positive ^{12}C yield for its winds. The mass loss due to winds is also now strong enough in the single-star case to force the helium core to recede.

Figure 5.3(e,f) shows stars with $M_{init} = 45\,M_\odot$. At this initial mass the winds of the single star are sufficient both to cause the helium core to recede and to expose the ^{12}C rich layers to be ejected in a wind. Though this occurs at a slightly later time than in the binary star case (as the binary-stripped star lost some mass in RLOF), thus there is less time for the star to eject this carbon rich material leading to a lower total carbon wind yield for the single star.

5.3.3 Carbon shell burning

In Figure 5.1 there is significant noise in the ^{12}C yields from core-collapse ejecta, especially at the higher masses. There are also several models marked with open symbols in the right panel of Figure 5.1. These are M_{init} = 24, 28, and 33 $M_\odot$ for the single stars and M_{init} = 31 $M_\odot$ for the binary-stripped stars. These variations occur due to changes in the behavior of carbon burning shells during the star's carbon and oxygen burning phases.

During the carbon shell burning phase, carbon initially ignites either at the center of the star or off-center and burns outwards (Arnett & Truran 1969; Sukhbold & Adams 2020). Figure 5.4 show the ignition of carbon in a 23 $M_\odot$ single star. This star ignites ^{12}C at the center at $\log_{10}\ (\tau_{cc} - \tau)\,/\mathrm{yr} \approx 1.2$, radiatively, this burning then moves outwards before it begins driving an off-center convection zone. This initial burning phase stops, before an additional ^{12}C burning zone ignites off-center, at $\log_{10}\ (\tau_{cc} - \tau)\,/\mathrm{yr} \approx 0.0$ at the same time as the core ignites ^{20}Ne. It is this burning zone that causes the variability in the ^{12}C yields.

As this convection zone extends outwards, it mixes ^{12}C from the outer layers of the core inwards where the ^{12}C is then burnt. Thus the maximal extent of this zone and the amount of time that it has to mix ^{12}C downwards sets the final ^{12}C yields. Figure 5.4 shows that in this model a small pocket of ^{12}C survives between the outer edge of the carbon convection zone and the lower edge of the helium burning shell (Laplace et al. 2021). This pocket is a mix of ^{12}C and ^{4}He (left over when the helium core receded at the end of core helium burning). At core collapse, we find that for most models this pocket will contribute $\approx 50\%$ of the final ^{12}C yield, with the remaining ^{12}C yield coming from ^{12}C produced in the helium shell.

We expect that differences in the treatment of mixing boundaries during carbon-shell burning are also important for understanding the differences between the results obtained with different codes, see Appendix D.2.2.

5.4 Physics variations

5.4.1 Sensitivity to physics choices

The sensitivity to the size and timing of the carbon-burning shells may suggest that our models are under resolved, or that our choice of convective overshoot above the carbon shell is significantly expanding the size of the convection zone. To test this we ran two grids of additional models. Firstly we ran models for with a 23 $M_\odot$ single star model varying our resolution controls. Next we randomly varied our choice of overshoot controls (f and f_0) above the carbon shell for the same 23 $M_\odot$ single star model (with our default resolution controls). We varied f and f_0 between 0.0 and 0.05, with $f_0 < f$. For both sets of models we keep our default model assumptions until the end of core helium burning, where we then change our model assumptions and evolve the models until core oxygen depletion.

We randomly picked values for each of the following spatial resolution controls, `mesh_delta_coeff` (0.5–1.0), `mesh_delta_coeff_for_highT` (0.5–1.0), and `max_dq` (10^{-4}–

10^{-3}). For our temporal controls we varied `dX_nuc_drop_limit` ($10^{-4.5}$–$10^{-3.0}$) and `varcontrol_target` ($10^{-4.5}$–$10^{-3.0}$). With our choices we increase the spatial resolution by up to a factor of 5 and increase (decrease) the temporal resolution by a factor of 3 (10). This leads to the highest resolution models having $\approx 100,000$ time steps (for just carbon and oxygen burning) and $\approx 15,000$ mesh points. Overall, we are primarily sensitive to the choice of `dX_nuc_drop_limit`, which limits the timestep based on the rate of change of the most abundant isotopes, primarily variations in the ^{12}C and ^{16}O abundances at the center of the star.

Figure 5.5 shows the relative change in the total mass of ^{12}C in our model measured at the end of the core oxygen depletion for both variations in the resolution and the amount of convective overshoot above the carbon burning shell. The black plus symbols in Figure 5.5 show a comparison with a model ran with `mesa_128.net` from the ZAMS, which has only a $\approx 2\%$ difference in the total mass of ^{12}C (measured at core oxygen depletion).

Figure 5.5a shows the relative change in the total mass of ^{12}C compared to the relative change in the average time step taken. As the time resolution increases the total mass of ^{12}C at the end of core oxygen burning decreases, relative to our default choices. However, even with at our highest resolutions, there is still a large spread possible in the final mass of ^{12}C ($\approx 40\%$). We do not plot the spatial resolution variations as they show no correlation with the carbon yields.

Figure 5.5b shows the relative change in the ^{12}C yields as a function of the amount of overshoot beyond the top of the carbon burning shells convective boundary (with all other overshoot regions keeping their same values). There is a slight trend for both the final total mass of ^{12}C to decrease, and the spread in ^{12}C values to decrease, as the amount of overshoot increases. However, it is possible to achieve the same final total mass of ^{12}C as our default model with the full range of overshoot values considered here. While this shows we may not be sensitive to the overall amount of overshoot (above the carbon burning shells), there is considerable scatter in the final total mass of ^{12}C with the the same choice of the amount of overshoot. Thus `MESA` users should consider carefully their physical choices for the amount of overshoot ($f - f_0$) and the individual numerical choices (f and f_0) needed to achieve this value.

More work is needed to understand convection during this burning phase (Cristini et al. 2017), as well as the role of convective overshoot that can enhance this effect by extending the region over which the carbon convection zone can mix. We may be seeing a similar effect as shown in Paxton et al. (2018) and Paxton et al. (2019) with the improper placement of the convective boundary. We tested with both the predictive mixing (Paxton et al. 2018) and convective pre-mixing schemes (Paxton et al. 2019). Both schemes still show scatter in how large the carbon convective shell grows, and for how long it is able to mix ^{12}C into the core. We note however that both predictive mixing and convective pre-mixing assume that the mixing timescale is shorter than the computational timestep, which breaks down during carbon burning.

5.4.2 Sensitivity to the explosion properties

To explore the sensitivity of our results to the assumptions made we perform two sets of tests on a $M_{init} = 16\,M_\odot$ binary-stripped star. We do not extensively test the pre-supernova physics variations as they have previously been explored in Farmer et al. (2016); Renzo et al. (2017); Laplace et al. (2021). Figure 5.6 shows the effect of varying the physics assumptions made during the core-collapse supernovae and the effects of varying the numerical assumptions made during the core-collapse supernova. Each row of Figure 5.6 tests two physics/numerical assumptions at a time. The vertical spread in the distribution of points at a fixed x-coordinate shows how sensitive the ^{12}C yield is to the *other* parameter shown in the same row. Thus a tight correlation indicates that the *other* parameter in the same row only minimally affects the predicted ^{12}C yield. A horizontal line implies that the ^{12}C yield is insensitive to *that* parameter. Negative $(M_{c_{12}} - M_{c_{12},def})/M_{c_{12},def}$ values indicate that more ^{12}C was destroyed than in our default model, while positive values indicate that less ^{12}C was destroyed.

In Figure 5.6a and 5.6b we randomly sampled $\approx$ 200 times both the injected energy (between $0.5 - 5 \times 10^{51}$erg/s) and the mass cut (between $1.4 - 2.0\,M_\odot$). Figure 5.6a shows the effect of varying the injected energy on the total mass of ^{12}C ejected during the supernovae. We can see a strong correlation between injected energy and ^{12}C ejected, increasing the energy decreases the ^{12}C mass ejected. However, the change is $< 1\%$ in the total mass of ^{12}C and in the context of Figure 5.1 the change would only be of the order of the size of the symbols.

Figure 5.6b shows the effect as we vary the mass cut. We find no correlation with the mass of ejected ^{12}C for this range of mass cuts. These trends can be explained as follows: most of the ^{12}C resides in the helium shell and only a small amount has been mixed down (or produced during late stage burning) to near where the compact object will form. Thus changing the mass cut has little effect, as the total mass of ^{12}C ejected is much greater than the change possible by moving the inner boundary.

The injected energy has a correlated (but small) effect on the ^{12}C yield due to the shock processing the small amount of ^{12}C that exists near the inner boundary (see Figure 5.2). However by the time the shock reaches the bulk of the ^{12}C in the helium shell the shock has cooled below 10^8K, thus it can no longer burn the ^{12}C present.

In Figure 5.6c and 5.6d we randomly sampled $\approx$ 200 times both the time over which we inject energy during the explosion ($10^{-3} < T_{inj}/s < 10^0$) and the mass over which we inject energy ($10^{-2} < \Delta M_{inj}/M_\odot < 5 \times 10^{-1}$). When either the T_{inj} is small ($T_{inj} < 0.1$s) or ΔM_{inj} is small ($M_{inj} < 0.1\,M_\odot$) their effects on the ^{12}C yield is small. Only once M_{inj} exceeds $0.1\,M_\odot$ does it begin to dominate the ^{12}C yield. However, once $T_{inj} > 0.3$s it begins to dominate the ^{12}C yield instead. When either T_{inj} or ΔM_{inj} increases the generated shock is weaker as either its power is lower (as it spreads over more time) or its deposited energy per unit mass is lower (as its spread over more mass) . This weakening of the shock lowers the amount of ^{12}C destroyed in the initial burning phases of the explosion (Sawada & Maeda 2019). The variations here are comparable to the uncertainty in the injected energy (though with an opposite sign).

Table 5.1: Ratio of the IMF weighted yields between an equal number of massive binary-stripped stars and single stars for different assumptions about the ejection of the envelope during core collapse and the IMF power-law α, see also Equation \ref{eq:ratio}. In case of BH formation we assume that the carbon-rich layers fall back onto the BH.

BH formation assumption	Ratio of ^{12}C yields (binary-stripped/single)		
	$\alpha = -1.9$	$\alpha = -2.3$	$\alpha = -2.7$
All stars explode successfully	1.51	1.44	1.3
BHs form from stars with initial masses $M_{init} > 22\,M_\odot$	1.79	1.55	1.35
BHs form from stars final core masses $M_{He,final} > 7\,M_\odot$	2.59	2.22	1.91

For Figure 5.6e and 5.6f we randomly sampled $\approx$ 100 times both the temporal controls and the mesh controls, simultaneously, to probe the sensitivity of our predictions to the numerical resolution of our models. We varied a series of mesh controls (`split_merge_amr_nz_baseline` (500–8000), `split_merge_amr_MaxLong` (1.1–2.5), and `split_merge_amr_MaxShort` (1.1–2.5)), during the explosion, as seen in Figure 5.6e. These controls force `MESA` to distribute its mesh according to the radius of each zone (See section 4 of Paxton et al. (2018)). We varied `dt_div_min_dr_div_cs_limit`, which sets the timestep based on the sound-crossing timescale for spatial zones near the shock front, between 0.1 – 10. While `MESA` is an implicit code and thus not limited by the sound-crossing timescale, it provides a physical and convenient timescale over which to probe the numerical sensitivity of our models.

As can be seen in Figure 5.6e, increasing the mesh resolution by a factor of 5 shows changes smaller than those which result from the variations we tested in the injected energy or choice of mass cut. Increasing (or decreasing) the temporal resolution also shows changes in ejected ^{12}C mass of $\lessapprox 0.05\%$ (Figure 5.6f). Thus our numerical uncertainties during the supernova are much smaller than our uncertainties due to either the stellar models or the physical explosion parameters.

These results suggest our ^{12}C estimates are therefore not sensitive to the uncertain parameters assumed for the explosion, however other isotopes which are formed deeper into the star are more affected by both the injected energy and the mass cut (Young & Fryer 2007; Suwa et al. 2019; Sawada & Maeda 2019). While our results show that the total amount of ^{12}C ejected is insensitive to the physical explosion parameters considered here, the amount of ^{12}C that is observable (via the production of carbon-rich dust at late times) is sensitive to the explosion physics (Brooker et al. 2021).

5.5 IMF weighted yields

The limit between stars which form neutron stars (and are assumed to eject their envelopes) and those that form black holes (which may or may not eject their envelopes) is uncertain (O'Connor & Ott 2011; Brown & Woosley 2013). Whether a star ejects its envelope or not will strongly affect the final yields from that star. To probe this uncertainty in whether a star ejects its envelope during core collapse we test several different ejection assumptions. Table 5.1 show

the IMF weighted ratio of the total ^{12}C yields for binary-stripped massive stars and single massive stars at solar metallicity. We define the ratio as:

$$\text{Ratio} = \frac{\int_{11}^{45} (Y_{b,ccsn} f_b + Y_{b,winds} + Y_{b,rlof}) M_{init,b}^{\alpha} \, dM}{\int_{11}^{45} (Y_{s,ccsn} f_s + Y_{s,winds}) M_{init,s}^{\alpha} \, dM} \tag{5.2}$$

Where we assumed a Salpeter-like IMF with different values of α (Schneider et al. 2018), $M_{init,b}$ and $M_{init,s}$ are the initial mass of the primary star in the binary and the mass of the single star in solar masses, Y_b and Y_s are the yields of ^{12}C in solar masses for the respective stars and for each type of mass loss, and f_b and f_s are filter functions that are either 0 or 1 depending on whether we assume that the star ejects its envelope. The integration limits are taken over the entire range of initial masses considered in this work.

Firstly assuming that all stars eject their envelopes at core-collapse then we find binary-stripped stars contribute $\approx 40\%$ more ^{12}C compared to the same initial mass of single massive stars, assuming a standard Salpeter IMF $\alpha = -2.3$. This is due to extra mass loss in binary systems, leading both to a higher ^{12}C yield in the winds and in the final supernovae for $M_{init} \approx 30 - 40\,M_\odot$ binary-striped stars as compared to single stars.

As we do not expect all stars to eject their envelopes at core-collapse we can also filter out systems which we do not expect to eject their envelope. Sukhbold & Woosley (2014) found that single stars with $M_{init} \lessapprox 22\,M_\odot$ had a low compactness (O'Connor & Ott 2011), suggesting they would be likely to successfully eject their envelope, this would set the maximum helium core mass as $M_{He} \lessapprox 7\,M_\odot$.

Assuming all stars eject their envelopes with $M_{init} < 22\,M_\odot$, then stripped primary stars in massive binaries contribute even more to the ^{12}C in the Universe than single massive stars.

Finally taking the helium core mass at $M_{He,final} < 7\,M_\odot$, measured at core collapse, binary-stripped massive stars eject approximately twice as much carbon than single massive stars (for $\alpha = -2.3$). This is due to the extra mass loss binaries undergo, lowering the final helium core masses. Thus for a given helium core mass at core-collapse binary-stripped systems have a higher initial mass (Kippenhahn & Weigert 1967; Habets 1986a), expanding the range in initial masses over which we assume a successful explosion occurs (Vartanyan et al. 2021). For our systems, a cut of $M_{He,final} < 7\,M_\odot$ is equivalent to a cut of $M_{init} < 19\,M_\odot$ for single stars and $M_{init} < 22\,M_\odot$ for binaries.

As the IMF α increases, thus favoring the production of more massive stars, the contribution that binary-stripped makes to the ^{12}C yields increases. This is due the greater weight now given to the ^{12}C yields from wind mass loss (as only the most massive stars in our grid contribute to wind mass loss yields), which is where the difference between the binary-stripped and single star yields is greatest (See Figure 5.1).

For all envelope assumptions the contribution from the wind mass loss is greater for stripped binaries then for the single stars. This is due to both the binary-stripped stars having ^{12}C positive yields at lower initial masses, and due to the higher ^{12}C yield at the equivalent initial masses due to the extra mass loss from RLOF altering the core structure (Section

5.3.2). Table D.2 in Appendix D.3 shows how the ^{12}C yields from only core-collapse vary as a function of the envelope ejection assumptions.

The actual contribution to carbon enrichment in the Universe also depends on an additional scaling factor weighting the fraction of stars that are single against those that are binary-stripped (Sana et al. 2012), as well as the fraction of binary systems which do not self-strip. Note also that we are comparing equivalent total initial masses for ensembles of massive single stars and the one star in each binary that we model as stripped, not the full initial stellar mass of the binaries. We have also not included the ^{12}C yields from the secondary stars in the binaries. If the secondary gains significant mass by accretion, we anticipate that this would further increase the relative efficiency of massive binary systems in producing ^{12}C.

We can combine the result shown in Figure 5.1(b), indicating that the ^{12}C yields from winds of massive stars are not positive until $M_{init} \approx 35\,M_{\odot}$, with the expectation that only massive stars with $M_{init} \lessapprox 22\,M_{\odot}$ eject their envelopes at core collapse. This combination suggests that stars with initial masses $22 \lessapprox M_{init}/M_{\odot} \lessapprox 35$ do not contribute to the net production of ^{12}C in the Universe. The contribution of massive stars with $M_{init} < 22\,M_{\odot}$ can be well described by only their ^{12}C supernovae yield, while stars with $M_{init} > 35\,M_{\odot}$ are well described by only their wind yields.

5.6 Discussion

This work has only modelled solar-metallicity stars, has neglected the potential importance of rotational mixing, and our binary-stripped models all underwent early case B mass transfer. We have also tested only one set of physics assumptions for stellar evolution, even though there are many uncertainties in the evolution of massive stars. Here we discuss potential limitations from those approximations.

Wind mass loss prescriptions for massive stars are uncertain (Renzo et al. 2017). Sander & Vink (2020) found that we would expect weaker Wolf-Rayet winds, at solar metallicity, for stars in the $M = 10 - 15\,M_{\odot}$ range than for our choice of Nugis & Lamers (2000). Lowering the wind mass-loss rate in this mass range would likely lead to lower supernova ^{12}C yields from binaries (Langer & Henkel 1995; Eldridge & Tout 2004). As the stripped star would lose less mass during core helium burning, the helium core would recede less, leaving behind less ^{12}C in the helium shell. This would decrease the significance of binary-stripped stars on the total ^{12}C yields. Single stars would be unaffected as they do not self-strip until much higher masses, where the models of Sander & Vink (2020) agree with those of Nugis & Lamers (2000) (until the initial masses go above those considered here, where Sander & Vink (2020) would predict higher mass loss rates). See also Dray et al. (2003) for discussion of the effects of the choice of wind mass-loss prescription on carbon yields from Wolf-Rayet stars.

Correlated with the wind mass loss is the modeled metallicity. Lower metallicity models would show a similar effect as having a lower assumed wind mass loss rate by changing the fraction of stars that become stripped (Eldridge & Vink 2006). Also at low metallicities, RLOF

in binaries may not fully strip the star due to changes in the envelope physics (Götberg et al. 2017; Yoon et al. 2017; Laplace et al. 2020). Without the envelope becoming fully stripped we would not see the helium core recede which would lower both the wind and core-collapse ^{12}C yields.

Our binary star models were each given an initial period such that they would undergo early case B mass transfer, before the onset of core helium burning. However, binaries may also interact earlier during the main sequence (case A), or after core helium burning has started (case C). Mass lost during case A will primarily lead to the star having a smaller core mass (Wellstein & Langer 1999; Yoon et al. 2010). If the mass loss ceases before the star undergoes core helium burning, and the star retains its hydrogen envelope, then the helium core will not recede. As the core did not recede it will not leave behind a pocket of ^{12}C above it. Thus the winds from the binary-stripped star will not be enhanced in ^{12}C yields relative to single stars. Countering this, smaller cores would lead to more successful explosions, ejecting the envelope, which acts to increase the total ^{12}C yields. More work is needed to understand which effect dominates. Mass lost during case C will occur after core helium burning has started. By this time the core mass of the star is set, thus we would be unlikely to see an enrichment of the helium shell with ^{12}C from the helium core.

Rotation plays a key role in the evolution of stars (Meynet & Maeder 2000) and the observed chemical composition of massive stars (Hunter et al. 2007, 2008, 2009). The extra chemical mixing rotation generates inside the star can lead to larger core masses (Ekström et al. 2012; Murphy et al. 2021), as well as mixing elements to the surface of the star (Meynet et al. 2006; Maeder et al. 2014; Groh et al. 2019). Prantzos et al. (2018) found enhancements in ^{12}C of a approximately a factor of three, between initial rotation rates of 0 – 300km s^{-1} for a 20 M$_\odot$ star. Hirschi et al. (2004, 2005) found that the ^{12}C yields increase by a factor 1.5 – 2.5 for stars M$_{\rm init}$ < 30 M$_\odot$, and with initial rotation rates of 0 – 300km s^{-1} due to the more massive core that the rotating models produce.

Fields et al. (2018) explore the sensitivity of a 15 M$_\odot$ solar metallicity star to variations when all reaction rates in the model were varied within their measured uncertainties. They found that at core helium depletion the central carbon fraction can vary ±80% compared to the model which adopts median reaction rates, driven by variations in ^{12}C$(\alpha,\gamma)^{16}$O and the triple-α rates. Sukhbold & Adams (2020) showed how the type of carbon burning, radiative or convective, is altered by changing the ^{12}C$(\alpha,\gamma)^{16}$O rate, in 14 – 26 M$_\odot$ stars. The location of carbon ignition plays a key role in determining how compact the core will become and thus how likely it is to successfully explode (Brown et al. 1999, 2001), and thus whether it will eject its envelope (Weaver & Woosley 1993; Timmes et al. 1996). Sukhbold & Adams (2020) found that variations in the $\approx 1\sigma$ uncertainty in the ^{12}C$(\alpha,\gamma)^{16}$O can move the location between convective and non-convection carbon ignition by ±2 M$_\odot$ in initial mass. That change in initial masses is similar to the change in initial masses seen in Section 5.5 when assuming stars with a fixed final helium core mass eject their envelopes.

5.7 Conclusion

Motivated by the high binary fraction inferred for young massive stars and the importance in improving chemical yield predictions, we have started a systematic investigation of the impact of binarity on the chemical yields of massive stars. In this paper, intended as the first in a series, we focus on ^{12}C yields. We present a systematic comparison of the differences between massive stars stripped by a binary companion and single stars with the same initial mass at solar metallicity.

To achieve this, we modeled the evolution of from the onset of hydrogen burning until core collapse. We then followed the nucleosynthesis through the resulting supernova shock and compute the ejected ^{12}C yield for different mass loss processes.

Our results can be summarized as follows:

1. We find that massive stars stripped in binaries during hydrogen-shell burning are nearly twice as efficient at contributing to the cosmic ^{12}C production as a similar number of massive single stars (a factor 1.4–2.6 depending on the assumptions for black hole formation and the slope of the initial mass function, see Equation 5.2 and Table 5.1).

2. We confirm that the difference in yields between binary-stripped and single massive stars can be explained by considering the outer-most ^{12}C-rich layers produced in the early phases of central helium burning. In single stars these layers tend to get mixed into the growing convective core, leading to destruction of ^{12}C by alpha captures and later carbon burning. In binary-stripped stars (and in single stars stripped by stellar winds) the convective helium-burning core cannot grow and may even retreat. The outer-most ^{12}C-rich layers disconnect and form a pocket where the temperature never becomes high enough for ^{12}C destruction (Figure 5.3), not even when a supernova shock wave passes through and ejects these layers (Figure 5.2) (cf. Langer 1991b; Woosley 2019; Laplace et al. 2021).

3. Stellar winds also eject ^{12}C once the carbon-rich layers are exposed to the surface. This only happens for the most massive stars in our grid (initial masses $> 36\,M_\odot$ and $> 38\,M_\odot$ for our solar-metallicity binary-stripped and single stars respectively). Comparing stars of the same initial mass, we find that the wind yields for binary-stripped stars are higher because the carbon-rich layers are more massive and appear earlier at the surface (see Figure 5.1 and 5.1b).

4. Mass loss from binary systems during conservative mass transfer does not contribute to ^{12}C yields, in our models. These layers are either pristine or contain CNO-processed material which is ^{12}C poor (c.f., de Mink et al. 2009).

5. Our yield predictions are remarkably robust with respect to choices in the treatment of the explosion, such as the explosion energy, how the energy is inserted, and the mass

that promptly forms a compact object. These lead to variations smaller than ≈ 0.5% (See Figure 5.6).

6. We show that the ^{12}C yield predictions of both single and binary-stripped stars are sensitive to the treatment of overshooting, specifically during carbon-shell burning. We find variations up to ≈ 40% in the final carbon yields for individual models (see Figure 5.5), depending on the size and lifetime of the shells. We identify this as a primary source of uncertainty and cause for noise in our predictions of the supernova yields.

7. We note that the variations between the predictions of ^{12}C yields for massive stars presented in other recent studies (Pignatari et al. 2016; Limongi & Chieffi 2018; Griffith et al. 2021) is large and of a similar order as the differences we find between binary-stripped and single stars.

We conclude that the yields of massive binary-stripped stars are systematically different from those of massive single stars. The effects of binarity should therefore not be ignored if we want to obtain more reliable yield predictions for carbon and better understand the relative contribution of massive stars with respect to the other proposed sources of carbon, namely Asymptotic Giant Branch stars and type Ia supernova.

However, the main priority would be to better understand how to treat boundary mixing, especially during the carbon shell burning phase, as this seems to be the primary uncertainty in both single and binary star models. Further aspects, which deserve further investigation, include the effects of metallicity and how these interplay with uncertainties in the stellar wind mass loss, and the still unknown conditions for which stars lead to successful supernova explosions. Advancing in these areas would require efforts on both the theory and observation side.

Finally, we emphasize that the binary-stripped stars studied here represent only one of the many possible final fates for a star born in the close vicinity of a companion. Binary interaction can affect massive stars in many other ways. This study is thus only a first step towards answering the bigger question of how binarity impacts the chemical yields of stars.

We acknowledge helpful discussions with B. Paxton, F. Timmes, L. van Son, and T. Wagg. The authors acknowledge funding by the European Union's Horizon 2020 research and innovation program from the European Research Council (ERC) (Grant agreement No. 715063), and by the Netherlands Organization for Scientific Research (NWO) as part of the Vidi research program BinWaves with project number 639.042.728 and a top module 2 grant with project number 614.001.501. This work was also supported by the Cost Action Program ChETEC CA16117. This work was carried out on the Dutch national e-infrastructure with the support of SURF Cooperative. This research has made use of NASA's Astrophysics Data System.

Software used for this work: `mesaPlot` (Farmer 2020), `mesaSDK` (Townsend 2019), `ipython/jupyter` (Perez & Granger 2007; Kluyver et al. 2016), `matplotlib` (Hunter 2007), `NumPy` (van der Walt et al. 2011), `MESA`(Paxton et al. 2011, 2013, 2015, 2018, 2019), and `pyMesa` (Farmer & Bauer 2018).

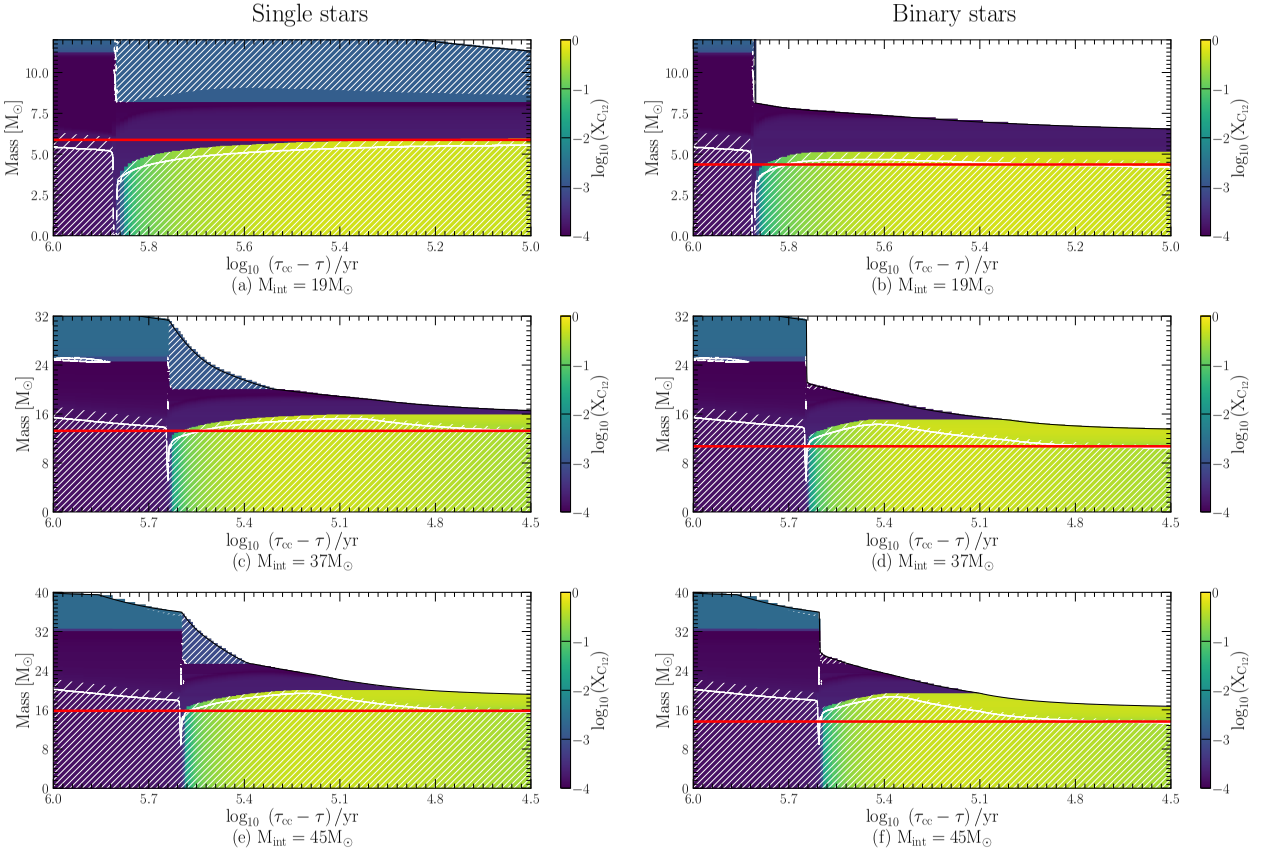

Fig. 5.3: Kippenhahn diagrams for the inner regions of single and binary-stripped stars with M_{init} = 19, 37, and 45 $M_\odot$, during core hydrogen and core helium burning. The left column shows single star models, while the right column shows binary-stripped models. The x-axis shows the time until core-collapse. Colors show the mass fraction of ^{12}C at each mass co-ordinate. Hatching shows mixing regions due to convection and overshoot. The red horizontal line shows the mass coordinate for what will become the CO core at the end of core helium burning.

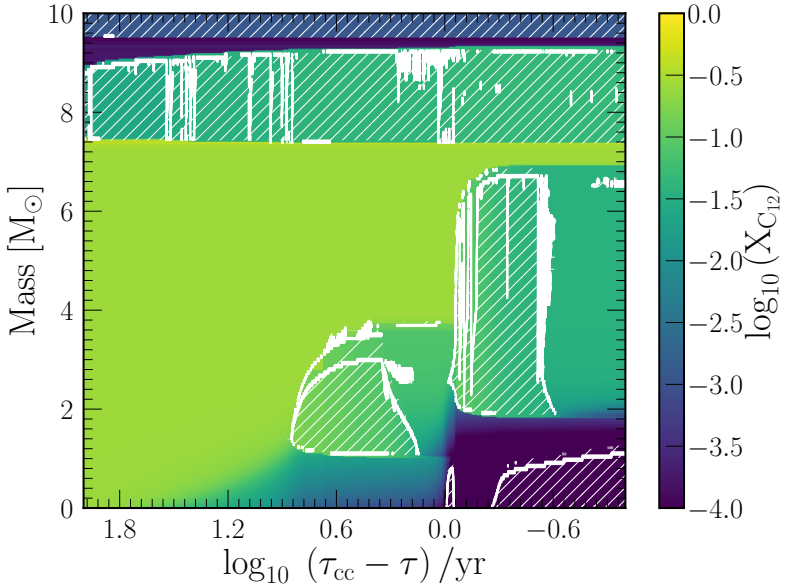

Fig. 5.4: Kippenhahn diagram for a 23 $M_\odot$ single star during carbon and oxygen burning. Colors show the mass fraction of ^{12}C at each mass co-ordinate. Hatching shows mixing regions due to convection and overshoot.

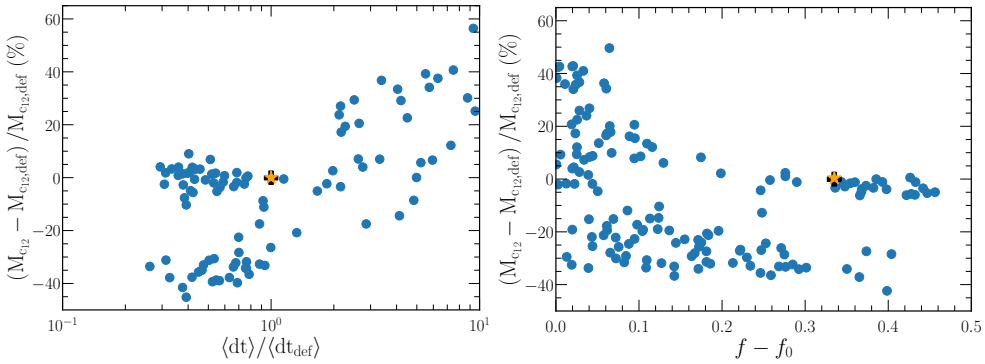

(a) Temporal resolution (b) Overshoot

Fig. 5.5: The relative change in the final total mass of ^{12}C in the star measured at the point of core oxygen depletion, as a function of the temporal resolution and strength of convective overshoot for a 23 $M_\odot$ single star. In panel (a) we vary a range of `MESA`'s temporal and spatial resolution controls. In panel (b) we vary both of the overshoot parameters f and f_0. The x-axis in panel (a) is the average timestep relative to our default model, where the resolution increases towards the left. The x-axis in panel (b) is the physical extent of convective overshoot beyond the convective boundary above carbon burning shells. In both panels the orange star denotes our default model assumptions, and the black plus symbol denotes a model which was evolved with `mesa_128.net` from the ZAMS (with otherwise default assumptions).

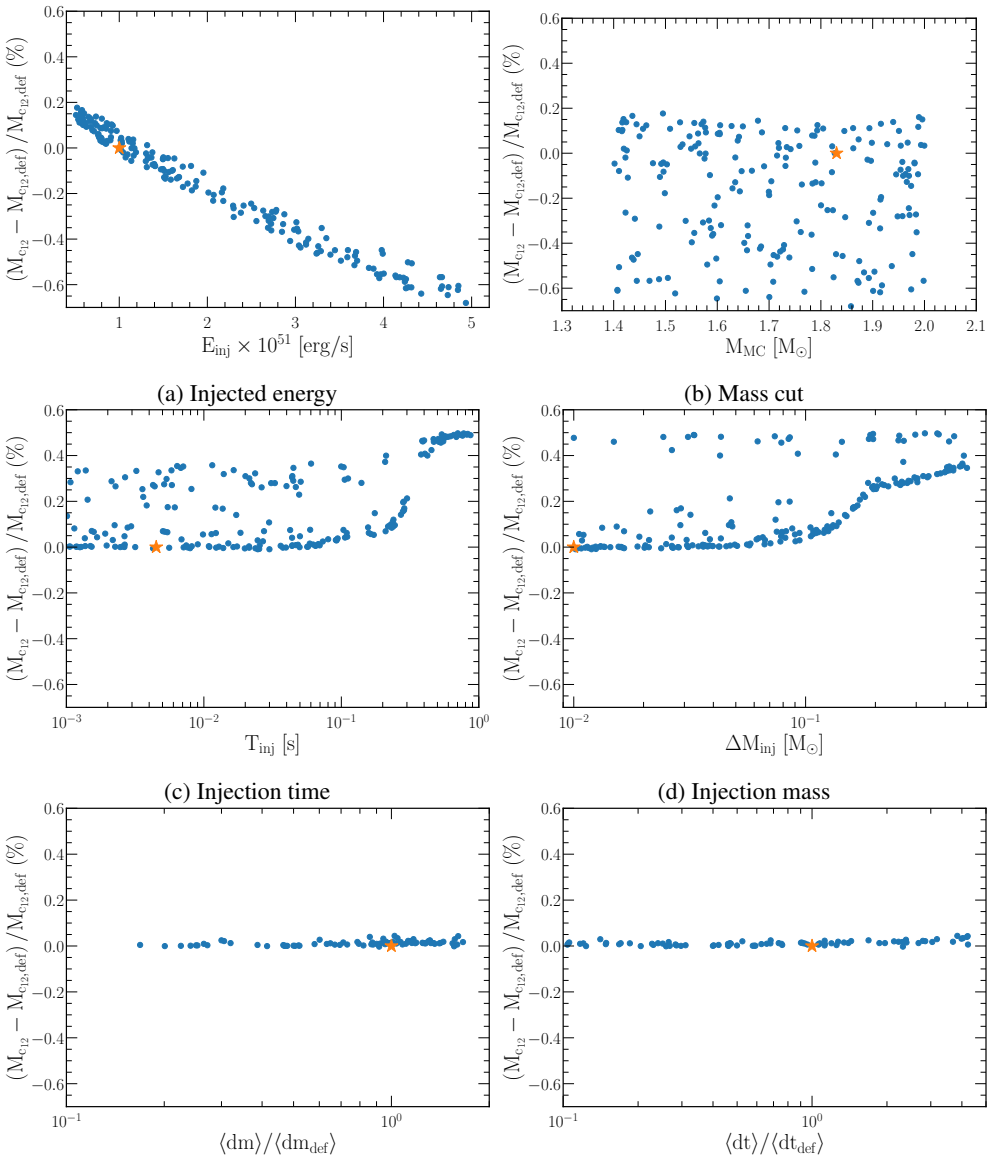

Fig. 5.6: The relative difference in the amount of ^{12}C ejected by supernovae of our binary-stripped star model with M_{init} = 16 $M_\odot$, compared to our default (def) model. Panel (a) shows the variation with respect to the injected energy, Panel (b) shows the variation with respect to the mass cut, Panel (c) shows variations with respect to the time the energy is injected over, Panel (d) shows variations with respect to the range of masses that the energy is injected over, Panel (e) shows the variation with respect to changes in the spatial resolution, and Panel (f) shows the variation with respect to changes in the temporal resolution. $\langle dm \rangle$ is the time-weighted average cell mass in $M_\odot$, $\langle dt \rangle$ is the average timestep in seconds. The spatial and temporal resolution increases to the left. For each row, we simultaneously Monte Carlo sampled both the parameters shown while keeping the other explosion parameters set to our default assumptions. The orange star denotes our default assumptions.

Chapter 6

TULIPS: a Tool for Understanding the Lives, Interiors, and Physics of Stars

E. Laplace

The content of this chapter has been submitted to Astronomy & Computing

Abstract

Understanding the lives and interior structures of stellar objects is a fundamental objective of astrophysics. Research in this domain often relies on the visualization of astrophysical data, for instance the results of theoretical simulations. However, the diagrams commonly employed to this effect are usually static, complex, and can sometimes be non-intuitive or even counter-intuitive to newcomers in the field. To address some of these issues, this paper introduce `TULIPS`, a python package that generates novel diagrams and animations of the structure and evolution of stellar objects. `TULIPS` visualizes the output of one-dimensional physical simulations and is currently optimized for the MESA stellar evolution code. Utilizing the inherent spherical symmetry of such simulations, `TULIPS` represents the physical properties of stellar objects as the attributes of circles. This enables an intuitive representation of the evolution, energy generation and loss processes, composition, and interior properties of stellar objects, while retaining quantitative information. Users can interact with the output videos and diagrams. The capabilities of `TULIPS` are showcased by example applications that include a Sun-like star, a massive star, a low-metallicity star, and an accreting white dwarf. Diagrams generated with `TULIPS` are compared to the Hertzsprung-Russell diagram and to the Kippenhahn diagram, and their advantages and challenges are discussed. `TULIPS` is open source and free. Aside from being a research tool, it can be used for preparing teaching and public outreach material.

6.1 Introduction

Visualizing observational data and theoretical simulations of the stellar systems that populate the Universe - stars, planets, galaxies, or interstellar clouds - is an essential part of astronomical research (Hassan & Fluke 2011). Graphs, maps, charts, diagrams, and sketches are used for the purposes of understanding and explaining concepts, analyzing data, and conveying findings both to peers and to the wider public.

Astronomy has a long history of employing such visualization, (see, e.g., Funkhouser 1936), from abstract to cinematic (Aleo et al. 2020).

The field of stellar astrophysics seeks to understand the lifecycle of stars, from their formation to their death. Properties of stars are derived from the analysis of observational data using, e.g., models of their atmospheres or dynamical motion. Such properties in turn serve as constraints for models that describe the dynamical and temporal evolution of single and multiple systems, such as binary star systems, or star clusters. These analyses and simulations rely heavily on data visualization. Some visualizations in particular have brought fundamental insights into this field and are now widespread and standard. The Hertzsprung-Russell diagram (HRD, Maury & Pickering 1897; Hertzsprung 1909; Russell 1914) revealed that stars follow specific patterns of color and magnitude. Extensive theoretical work and analyses from complementary observational data unveiled the connection between these patterns and the evolutionary stage and mass of stars. Ever since, the HRD has been ubiquitous in stellar astrophysics as a tool to describe and understand the life cycle of stars. Other examples include visualizations of the evolution of the interior energy generation and mixing structure of stars, known as Kippenhahn diagrams (Hofmeister et al. 1964, see also Hayashi et al. 1962), or visualizations of evolutionary sequences of interacting binary stars (van den Heuvel & Heise 1972).

However, although widespread and standard, many of these visualizations are abstract, static, non-intuitive or even counter-intuitive for those who are new to the field, or suffer from a high density of information.

It is well established in the field of data visualization that the complexity of information displayed directly affects how easily this information can be retained (Lusk & Kersnick 1979; Evergreen & Metzner 2013) and its general appeal (Harrison et al. 2015). Evidence suggests that visualizations that are perceived as more appealing convey the information they display more easily (Kurosu & Kashimura 1995; Tractinsky 1997), attract a more diverse audience (Korkmaz 2009; Harrison et al. 2015), and capture the audience's attention for longer (Cawthon & Moere 2007). There is supporting evidence that visualizations using real-world objects can convey information more effectively to a diverse audience (Lewis & Sheppard 2006). Dynamic visualizations can make information more understandable and evocative (Valkanova et al. 2013) and interactive elements are generally better at capturing and retaining the audience's interest than static ones (Newell et al. 2016).

This paper introduces the Tool for Understanding the Lives, Interiors and Physics of Stars (`TULIPS`). It is a python software package that visualizes the evolution and structure of stellar

objects based on one-dimensional stellar evolution calculations. This software addresses some of the important issues of current visualizations employed in stellar astrophysics by introducing a novel approach to visualizing the evolution of stars. TULIPS represents stellar objects as circles, closer to their real-world shape. It visualizes physical properties by employing colors and shadings. In addition, TULIPS enables an interactive visualization of the temporal evolution of these properties by means of animations that can be saved in standard video formats.

Latest state-of-the-art calculations for stellar astrophysics are now wide-spread thanks to the rise of open-source and community-maintained codes, such as MESA (Paxton et al. 2011, 2013, 2015, 2018, 2019). TULIPS visualizes the results of such one-dimensional calculations and is currently optimized for MESA.

The development of this tool began as an effort to better communicate the evolution of stars to students of stellar evolution classes and has evolved into a research tool employed both for analyzing the results of stellar evolution calculations and for communicating these findings in a more intuitive way (Laplace et al. 2021).

TULIPS is open source[1] and free for anyone to use as a research, outreach, or education tool (under a GNU general public license, v.3). It is intended to make the structure and evolution of stellar objects more accessible and understandable to a broader community, and as a way to better display and convey the beauty of the physics that governs the lives and interiors of stars. In the spirit of open science, users are encouraged to contribute by sharing the animations and plots they produce with TULIPS with others, and by testing, reporting of bugs, and extending of the capabilities. Contributions are encouraged by submitting a pull request on the bitbucket repository.

This article is structured as follows. First, the TULIPS software and the underlying concept behind it are described in Section 6.2. Section 6.3 and Section 6.4 present an overview of the different types of TULIPS diagrams and their animations, respectively. Section 6.5 compares TULIPS to classic diagrams and 6.6 contains a discussion and conclusion.

6.2 TULIPS

6.2.1 Basic concept: spherical symmetry

Assuming that stars are spherically symmetric is at the heart of the classical theory of stellar astrophysics (e.g., Eddington 1926). This is a good approximation for isolated stellar objects that are mainly subject to self-gravity. Effects of rotation, strong magnetic fields, and binary interactions can lead to deviations from the spherical shape, but for the majority of stellar physics problems, this assumption holds. Furthermore, while these deviations primarily affect the outer layers, spherical symmetry is still a fair approximation for the deeper interior layers

[1] The code can be found at https://bitbucket.org/elaplace/tulips/ and is also listed in the Python Package Index https://pypi.org/project/astro-tulips/.

of stars where nuclear burning, which drives the life cycle of stars, takes place. A powerful consequence of assuming spherical symmetry is that the mathematical description of the structure and evolution of stellar objects is greatly simplified. The entire problem can be captured by a small set of non-linear partial differential equations. The vast majority of stellar evolution calculations consist in solving these one-dimensional equations with various numerical methods and physical assumptions [2].

The basic concept behind `TULIPS` is to make use of the intrinsic spherical symmetry to represent any physical (one-dimensional) property of a star as the radius, surface area or color of a (two-dimensional) circle. Physical properties of stars are generally expressed as a function of their position r (known as Eulerian coordinate), where r varies from 0 at the center of the star to the total radius R at the surface. They can also be expressed as a function of the mass m of a small shell inside the star (known as Lagrangian coordinate), where m varies from 0 at the center to the total mass M at the surface. `TULIPS` can visualize the physical properties of stars in either form by representing stellar models as circles whose radius represents one or the other coordinate.

6.2.2 The `TULIPS` software

The first version of the `TULIPS` python software is written with functional design. To create diagrams or animations, users call specific functions. `TULIPS` contains a set of core functions that create visualizations of stellar properties. By default, these functions create a visualization at a fixed point in time (see Section 6.3). By changing the time argument, the same functions can be used to create animations from a start point to an end point (see Section 6.4). `TULIPS` relies on `matplotlib` functionalities to create plots and animations that can be saved in standard image or video formats. The visual aspect of `TULIPS` diagrams and animations can be customized easily. Basic and advanced use of the `TULIPS` is described in detailed in the documentation and tutorials[3]. TULIPS builds upon several existing open-source python packages, including `mesaPlot` (Farmer 2020), `matplotlib` (Hunter 2007), `numpy` (van der Walt et al. 2011), `ColorPy`[4], `astropy` (Astropy Collaboration et al. 2013, 2018), `CMasher` (van der Velden 2020), and `ipython/jupyter` (Perez & Granger 2007).

6.2.3 Input physical simulations

`TULIPS` itself does not solve the stellar structure equations. Instead, it uses the solutions generated by existing simulations as input to generate diagrams and animations. Although `TULIPS` can be adapted for use with any one-dimensional simulation, in principle, it has been optimized for use with the open-source Modules for Experiments in Stellar Astrophysics

[2] Multi-dimensional calculations of stellar evolution also exist (recent examples include e.g., Arnett et al. 2009; Fields & Couch 2020; Yadav et al. 2020). However, due to the extreme spatial and time scales involved, only short portions of stellar lives can be computed.

[3] The documentation and tutorials can be found at https://astro-tulips.readthedocs.io/en/latest/

[4] ©Mark Kness, http://markkness.net/colorpy/ColorPy.html

(MESA, version 15140; Paxton et al. 2011, 2013, 2015, 2018, 2019). The example stellar evolution models shown in this work are based on default stellar models from the MESA test suite and on models from Laplace et al. (2021). MESA inlists and data products will be made available upon publication[5].

For reading output files from `MESA` simulations, `TULIPS` uses the open-source python package `mesaPlot` (Farmer 2020). With this package, the entire information contained in output files from a `MESA` computation can be stored in a single python object that allows easy access to all physical quantities contained in the output files. All core `TULIPS` functions that create visualizations require this object as an argument. Depending on the information they visualize, `TULIPS` functions necessitate different types of MESA output files. Two types of output files exist: MESA *history* files include the evolution of one-dimensional physical properties as a function of time, while MESA *profile* files are snapshots of the interior properties of stellar objects as a function of their mass coordinate at one particular moment in time. The names of functions that require the latter output type contain the suffix `_profile`.

6.3 TULIPS diagrams: overview

Fig. 6.1 showcases the four basic diagrams that `TULIPS` produces for the default MESA stellar model of a Sun-like star (`1M_pre_ms_to_wd` model in the MESA test suite). The diagrams are all generated at the end of core helium burning (when the central mass fraction of helium becomes lower than 10^{-4}). By calling the corresponding function, the following TULIPS diagrams are shown in the Figure, from left to right and top to bottom:

a. `perceived_color`: a diagram that shows a physical property of the entire star, for example its total radius and the (approximate) color of a star as perceived by the human eye.

b. `energy_and_mixing`: a diagram that shows the energy generation and losses, and the mixing processes in stellar objects.

c. `chemical_profile`: a diagram that represent the interior composition profile of a star.

d. `property_profile`: a diagram that represent an internal physical property, for example the density as a function of the mass coordinate.

In addition, `TULIPS` allows comparisons with typical diagnostic diagrams used in stellar astrophysics, such as the HRD, by including these as insets in the corner of a `TULIPS` diagram.

6.3.1 Diagram a: a star's radius and its color as perceived by the human eye

It can be challenging to apprehend the observable properties of a stellar object at a particular evolutionary stage or at a particular location on the HR diagram. `TULIPS`' `perceived_color`

[5]The data is available at https://doi.org/10.5281/zenodo.5032250

(a) `perceived_color` diagram

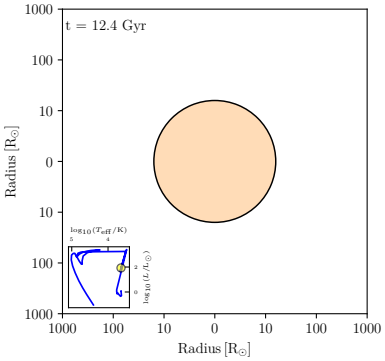

(b) `energy_and_mixing` diagram

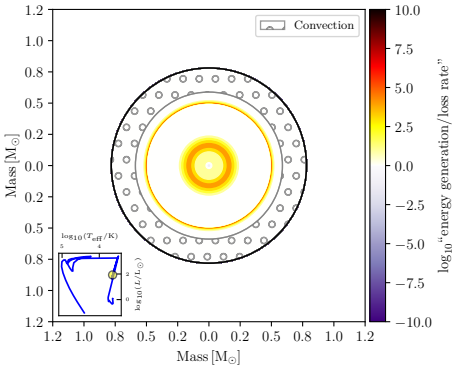

(c) `property_profile` diagram

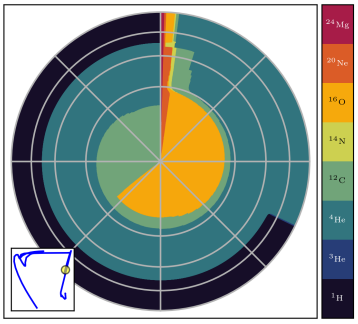

(d) `property_profile` diagram

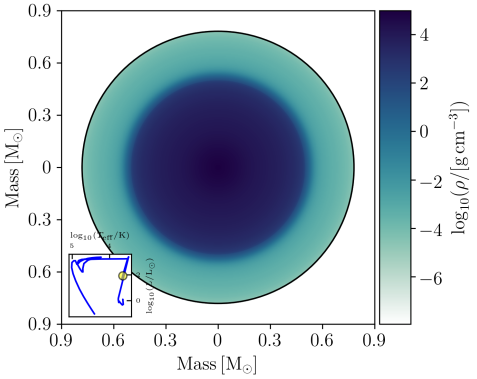

Fig. 6.1: Overview of the four basic TULIPS diagrams for a Sun-like star at the end of core helium burning. Inset diagrams at the bottom left of each panel show the location of the star on the HRD. **a.** The star has a radius of about 12 $R_\odot$ and appears orange, as expected for a red clump star. **b.** The star contains a hydrogen-burning shell and a helium-burning core. In the very center, energy losses can be observed. **c.** From the center outwards, the star is composed of carbon and oxygen, followed by a layer that predominantly contains helium, and then by an extended envelope mainly composed of hydrogen and helium. Here, the radial direction is proportional to the square root of the mass of the star. Overlayed circles give the location of particular mass fractions of the star. From the center, moving outward, these are 0.25, 0.5, 0.75, and 1 times total mass of the star **d.** The density throughout the stellar interior. The star contains a dense stellar core surrounded by a lower-density region, and has a low-density envelope.

diagrams help address this by representing basic properties of a stellar object as the radius and color of a circle, where the color corresponds to the (approximate) color of a star as perceived by the human eye[6]. In the example shown in the panel a of Fig. 6.1, the diagram visualizes how a Sun-like star that has just completed central helium burning, with an effective temperature of 4395 K may be perceived by the human eye: the star is represented as an orange circle with a radius of 12 $R_\odot$, which correspond to a red clump star. The location of the star on the HRD at

[6]In reality, at close distance stars are so luminous that most colors would be saturated and appear as white to the human eye.

this evolutionary stage is shown in an inset located in the bottom left corner of the diagram.

With these diagrams, TULIPS can represent not only the radius, but any one-dimensional physical property of a star (for example its mass or density) as the radius of a circle. To compute the (approximate) human-perceived color of the stellar object, TULIPS makes use of the `ColorPy` python package. With this tool, the intensity spectrum of a star is approximated as the blackbody spectrum expected for a given effective temperature. This spectrum is converted to the approximate range of colors a human eye can perceive by using the 1931 color matching functions of the Commission Internationale de l'Éclairage (Smith & Guild 1931). This process results in a color for each effective temperature. Animations of this diagram visualize how the stellar property shown (e.g., the radius) varies as a function of time and can help better appreciate the scales involved (see Section 6.4.1).

6.3.2 Diagram b: energy generation/losses and mixing in the stellar interior

The `energy_and_mixing` diagram helps to visualize the interior properties of stars at a certain evolutionary stage, at a particular location on the HR diagram, or when a certain condition is met (for example, when the central temperature of the star reaches a certain value). Energy generation and losses are indicated with colors (as computed by `mesaPlot`, see also Farmer et al. 2015). Optionally, various types of mixing that occur in the stellar interior can be indicated with hatched regions. The example shown in the panel b of Fig. 6.1 presents the interior burning and mixing processes of a Sun-like star at the end of core helium burning. The radius of the outermost circle gives the total mass of the star, which is just under a solar mass at this moment due to previous mass loss during the giant phase. Two sets of yellow and orange rings indicate shell burning: helium shell burning near the center and a weaker hydrogen-burning shell further out. The purple circle in the very center represents energy losses in the innermost region due to neutrino emission. Grey rings containing small gray circles indicate that convection is occurring in the outermost layers of the star. For simplicity, the energy/loss rate ϵ is not written out in the colorbar label. In fact, this quantity is computed as follows: $\epsilon = \mathrm{sign}(\epsilon_{\mathrm{nuc}} - \epsilon_\nu)\log_{10}(\max(1.0, |\epsilon_{\mathrm{nuc}} - \epsilon_\nu|)/[\mathrm{erg\ g^{-1}s^{-1}}])$, where ϵ_{nuc} is the nuclear burning rate and ϵ_ν the neutrino energy loss rate. These diagrams contain similar information as Kippenhahn diagrams for a particular moment in time. Animations of `energy_and_mixing` diagrams contain similar information as Kippenhahn diagrams (see also Section 6.5.3).

6.3.3 Diagram c: the star's interior composition

For many problems in stellar physics, it is important to know the interior composition of a stellar object at a particular moment in time. With TULIPS, this information can be displayed as the property of a circle that contains nested pie charts, as first introduced in Laplace et al. (2021). Each of these pie charts represent the mass fractions of isotopes at a particular coordinate in the stellar interior. Each isotope correspond to a particular color, as shown

in the legend. By default, the radial direction is proportional to the square root of the mass coordinate. As a result, the surface area spanned by a certain color is proportional to the total mass of the isotope it represents in the star. Fig. 6.1 contains an example composition diagram for a Sun-like star at the end of central helium burning in the panel c. From outside, moving inward, it is composed by a hydrogen-rich envelope that contains mass fractions of 0.7, 0.25, and 0.01 of hydrogen, helium, and heavier elements, respectively, as expected for a Solar-like composition (Asplund et al. 2009). Below the envelope, at 75% of the total mass of the star, the model contains a helium-rich layer with low fractions of carbon, oxygen, and neon. The mass of the innermost core is divided in 0.33 carbon and 0.66 oxygen, and low fractions of neon and magnesium. Overlayed grey circles and lines help read quantitative information from these composition diagrams. For example, they clarify that the boundary of the innermost core coincides with about a quarter of the total mass of the star.

To create these diagrams, `TULIPS` automatically identifies all isotopes present in the stellar interior[7] and assigns them a color based on a custom colormap. For efficiency, the stellar interior is then divided (down-sampled) into a number of concentric rings (by default, 300). The code then interpolates the changes in composition at the location of these rings. For each ring, `TULIPS` constructs a pie chart based on the mass fractions of isotopes within the mass or radius extent of the ring. By default, all pie charts start at a 12 o'clock position. The isotopes are shown counter-clockwise in order of increasing mass number. For a typical stellar object composed primarily of hydrogen, helium, and "metals" this means the pie chart begins with ^{1}H, followed by ^{4}He, and ends with an iron-group element, such as ^{56}Fe. As a consequence, when animated as a function of time, the growing mass fraction of isotopes in the stellar interior (for example helium during core hydrogen burning) produce a clockwise motion in the composition diagrams (see the example animation described in Section 6.4.1 in the supplementary material).

6.3.4 Diagram d: a physical property throughout the stellar interior

`TULIPS`' `property_profile` function visualizes how a certain physical property, such as the density, changes from the center to the surface of a stellar object. These type of diagrams are commonly referred to as the profile of such a property. An example of a `TULIPS` diagram representing the density profile of a Sun-like star at the end of core helium burning is shown in the panel d of Fig. 6.1. The star is divided into multiple rings where each ring corresponds a zone within the stellar model (here, 1000 zones). The radii of all rings are chosen such that their location is proportional to the enclosed mass of the star. The color of each ring corresponds to the density ρ of the star, as specified by the color scale. In this example, the outer layers have a very low density of $\log_{10}(\rho/[\mathrm{g\,cm^{-3}}]) = -5$, while the core has a higher density of the order of $\log_{10}(\rho/[\mathrm{g\,cm^{-3}}]) = 3$ and is surrounded by a lower density ring of about $\log_{10}(\rho/[\mathrm{g\,cm^{-3}}]) = -2$.

[7] A list of isotopes of interest can also be specified by the user.

6.3.5 Combining multiple TULIPS diagrams

Because the information displayed in diagrams a, b, and d is independent from the angle chosen, these diagrams can be combined in the same figure. This is demonstrated in Fig. 6.2, where information from three different types of TULIPS diagrams for the same Sun-like stellar model at core helium depletion as shown in Fig.6.1 is combined. All diagrams display stellar properties as a function of the mass coordinate. This figure reveals that the outer, hydrogen-burning shell of the star is located just above the edge of the helium-rich core. It also demonstrates that electrons are degenerate in the very center of the star (degeneracy parameter η larger than zero), below the helium-burning region. The figure shows that the electron degeneracy varies greatly between the outer envelope and the inner helium-rich core of the star. For each diagram, we specify a different starting and end angle. This feature of TULIPS can also be used to compare of different MESA models at similar evolutionary stages (for an example, see Fig. 13 in Laplace et al. 2021).

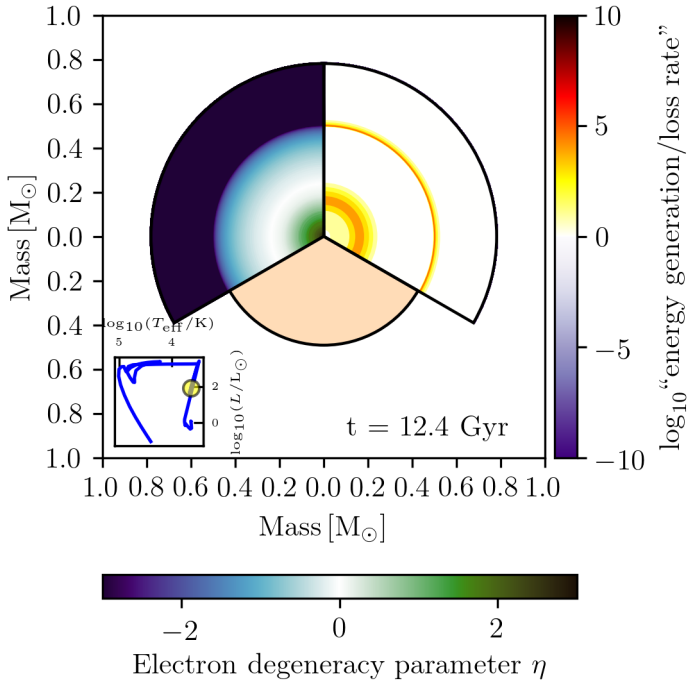

Fig. 6.2: Example combination of TULIPS diagrams in one plot. All diagrams represent properties of the same model of a Sun-like star at the end of core helium burning. From left to right, the dimensionless electron degeneracy parameter η (electrons are degenerate when $\eta > 0$, Paxton et al. 2011), the mass of the helium core with the perceived color of the star, and the energy generation processes in the stellar interior, are shown.

6.4 TULIPS animations

Animations are the centerpiece of TULIPS' capabilities. Every diagram produced with TULIPS can be animated. This enables an interactive exploration of the properties of stellar objects as a function of time and can help the users gain more insight into the meaning of particular features in classic diagrams, such as the HRD or Kippenhahn diagrams.

TULIPS animations are created with the `matplotlib` Animation module (Hunter 2007). TULIPS offers multiple options to adapt the time step and frame rate of the resulting animation (see documentation). By default, the time step follows the MESA `model_number` of a simulation, a number that keeps track of models generated in a MESA calculation. In addition, options that follow the evolutionary time are also available. Because of the vastly different time scales involved in the various evolutionary stages of a star (for a typical single massive star, millions of years during the main sequence compared to days for the last burning stages, Woosley et al. 2002), it is often useful to re-scale the evolutionary time such that most evolutionary phases will span a similar duration in the animation. This scaling can be applied in TULIPS animations by using the `log_to_end` time scaling option. An option that follows the age of the star linearly is also available. For TULIPS functions that rely on MESA profile output, it is essential to have a larger number of profiles generated at regular intervals to accurately capture the time evolution (for more details, see the TULIPS documentation).

6.4.1 Understanding features on the HRD tracks of stellar objects

TULIPS animations can help gain a better understanding of particular evolutionary stages in the lives of stellar objects and to develop an intuition for tracks on the HRD. In Fig. 6.3, a series of snapshots from an example animation is shown. The animation features the radius and perceived color evolution of an 11 $M_\odot$ single star at solar metallicity (see Section 6.3.1). Inset diagrams in the lower left corners help compare the evolution of this massive star on the HRD. In step 1, the star starts its evolution on the main sequence and experiences a slow radial expansion until hydrogen is exhausted in the core in step 2. In step 3, the star experiences a sudden increase in size of two orders of magnitude after having left the main sequence, and changes in perceived color, becoming a red supergiant. In step 4, the star slowly climbs the red supergiant branch and expands slightly. Between step 4 and step 5, the stellar radius decreases again as core helium burning begins. This radius evolution can easily be missed on the HRD because the evolutionary track on the HRD overlaps with the previous evolution. After this moment, the star expands again slowly before reaching its final location on the HRD, shown in step 6.

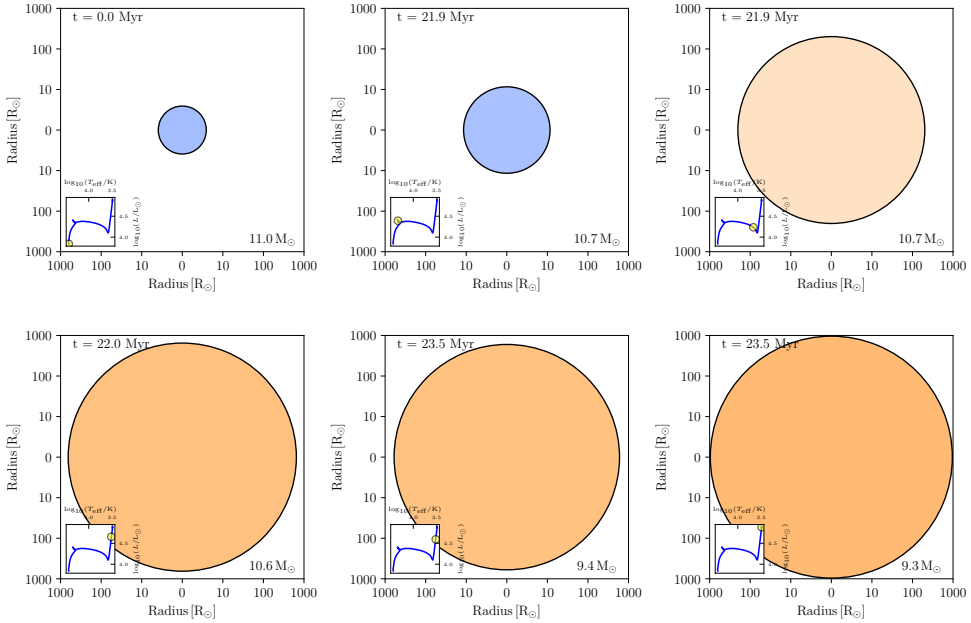

Fig. 6.3: Snapshots of a TULIPS animation that shows the evolution of a single 11 $M_\odot$ star at solar metallicity from the onset of core hydrogen burning to the end of core oxygen burning. The diagrams represent the perceived color and radius evolution of the star. Inset diagrams indicate the evolution on the HRD.

6.4.2 Animations to develop physical intuition: accretion onto a white-dwarf leading to stable hydrogen burning

TULIPS can help understand the consequences of physical processes, such as accretion, on stellar structures. Fig. 6.4 shows how the stellar structure of a 1 $M_\odot$ CO white dwarf reacts to accretion of hydrogen-rich material at a rate of $2 \times 10^{-7} M_\odot\,\mathrm{yr}^{-1}$ (`wd_stable_h_burn` model in the MESA test suite). The figure contains snapshots of a property profile animation that visualizes both the evolution of the radius of the white dwarf and of hydrogen burning in its interior (the animation can be found in the supplementary material). The radial direction is proportional to the radius of the white dwarf and the color indicates the values of the specific energy generation rate due to hydrogen burning from the proton-proton chain reaction, which is the dominant burning process. Step 1 shows the initial model of the white dwarf. The dark purple color indicates that no hydrogen burning is taking place initially. In step 2, hydrogen-shell burning is triggered in the white dwarf due to the accretion of hydrogen-rich material. In step 3, the white dwarf experiences a nova: the hydrogen burning intensifies and the released heat causes the radius to increase. By step 4, the radius has increased by more than an order of magnitude, and the outer radius is so large that it exceeds the edges of the plotted region. At this moment, the specific energy generation rate of hydrogen-burning

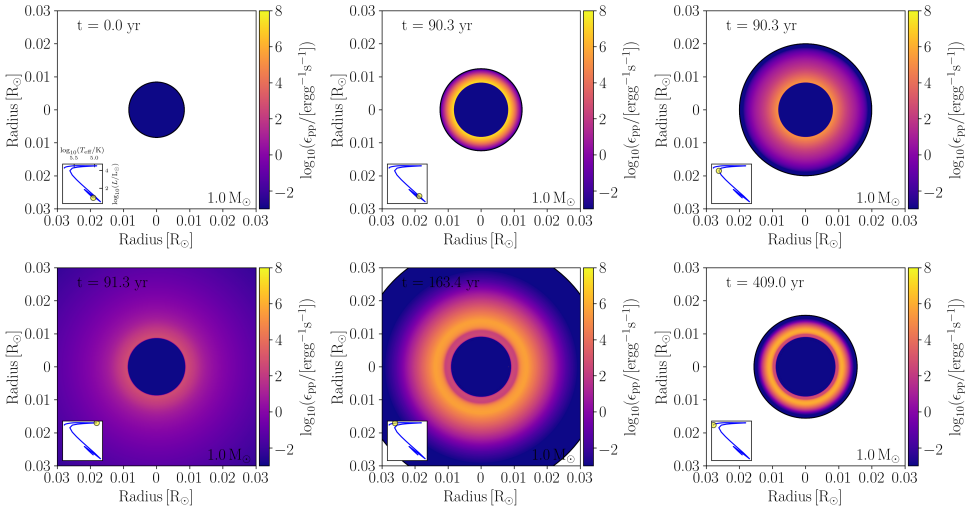

Fig. 6.4: Snapshots of a TULIPS animation that shows the evolution of a 1 $M_\odot$ white dwarf that is accreting hydrogen-rich material stably at $2\times10^{-7} M_\odot\,\mathrm{yr}^{-1}$. The diagrams show the radius evolution of the white dwarf. Colors indicate the energy generated by hydrogen burning through the proton-proton chain. From steps 2-4 the white dwarf experiences a violent nova event which leads to an increase in radius of an order of magnitude, exceeding the plot limits.

decreases drastically. In step 5, the radius of the white dwarf decreases after the nova and the hydrogen-burning luminosity increases again. From step 5 to the last step, the white dwarf experiences stable hydrogen shell-burning. The radius of the white dwarf, while larger than in the beginning of the simulation, remains constant.

6.4.3 Animations to understand the chemical evolution of stellar objects: low metallicity

A major goal of stellar astrophysics is to understand the chemical evolution of the Universe. Stars are the main drivers of this chemical evolution, as they create new elements in their interior while they evolve and eject them into their surroundings through winds and outflows (Burbidge et al. 1957; Woosley et al. 2002; Heger et al. 2003; Hopkins et al. 2014). With TULIPS, the interior evolution of stars can be visualized in a simple manner. This is illustrated in Fig. 6.5, which shows snapshots of a `chemical_profile` animation of the evolution of an 11 $M_\odot$ star at low metallicity (Z=0.001) until the end of core helium burning (the animation can be found in the supplementary material). The first snapshot shows the onset of hydrogen burning in the star. The outermost layers contain initial hydrogen mass fraction of 0.76 and a helium mass fraction of 0.24. The mass fractions of heavier elements are so small that they are barely visible in the diagram since they are located behind the vertical line. In the region that contains about half the total mass of the star (indicated by the second gray circle from the center), the mass fraction of helium is slightly larger than a quarter, indicating that hydrogen

burning has just begun. The second snapshot shows the effect of core hydrogen burning on the composition of the star. After more than 8 Myr, more than half of the hydrogen has been fused into helium nuclei in the stellar core. The mass fraction of hydrogen is decreasing in favor of the helium mass fraction, creating a clockwise motion in the animation. The mass extent of the convective hydrogen-burning core is decreasing due to changes in the opacity, which leads to a smaller extent of the helium-rich region at the bottom of the diagram (6 o'clock) compared to the right-hand side (4 o'clock). In the next snapshot (step 3 in Fig. 6.5), the composition profile at the end of the main sequence is shown. Almost the entire core region is now composed of helium. The spiral form of the helium-rich region in the center of the diagram is a consequence of the shrinking of the hydrogen-burning core during the main sequence. Step 4 in Fig. 6.5 shows the next evolutionary phase, hydrogen-shell burning, which only has a very modest effect on the stellar composition profile: the helium mass fraction outside the helium-rich core increases slightly. In the next snapshot (step 5 in Fig. 6.5), carbon and oxygen mass appear in the center, marking the start of core helium burning. In the animation, a clockwise motion can be observed in the center once again. Carbon is created first and in larger amounts than oxygen through triple-alpha captures. When the mass fraction of helium is only about 10%, the mass fraction of oxygen starts to overtake that of carbon. At the same time, the dark blue region becomes larger, reflecting the mass increase of the helium core up to about a quarter of the total stellar mass. In the last snapshot, the star has reached the end of core helium burning and its core mass is comprised of about 11/16 oxygen and 5/16 carbon. The outer edge of the helium core displays a smooth gradient in composition due to the effect of convective mixing in the envelope.

6.5 Comparison between TULIPS and classic diagrams

TULIPS diagrams provide an alternative to classic representation of the physical properties of stars. Here, we compare diagrams created with TULIPS with classic representations of the same properties.

6.5.1 Composition of a star

In Fig. 6.6, classic composition diagrams are compared to corresponding TULIPS diagrams, based on both the radius and the mass coordinate. The difference between the two visualizations is immediately apparent. The classic representation requires more space to be readable and contains a large number of cluttered lines. It facilitates the reading of quantitative information, in particular for individual isotopes. However, reading this information is difficult in the cluttered region in the innermost solar mass that contain a large number of lines representing various isotopes. For the untrained eye, finding distinct layers in the stellar interior requires effort.

The TULIPS representations in Fig. 6.6 enable a simple overview of the distribution of isotopes in the stellar interior. Four distinct layers can immediately be identified in the form

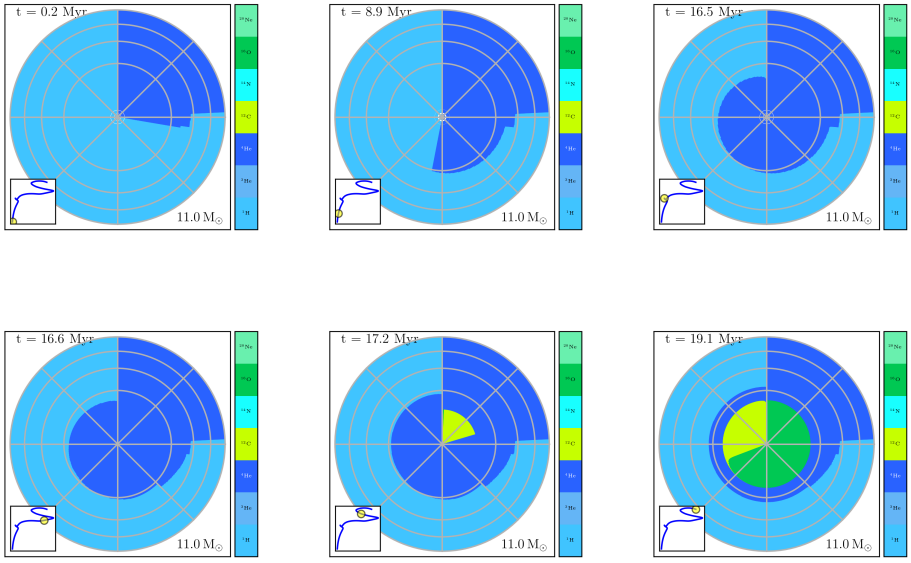

Fig. 6.5: Snapshots of a TULIPS animation that shows the evolution of an 11 $M_\odot$ star at low metallicity (Z=0.001) until the end of core helium burning. The diagrams show how the composition of the star changes over time. Gray circles indicate the location of mass coordinates at 0.25, 0.5, 0.75, and 1 times the total mass of the star, respectively.

of distinct rings and circles containing from outside, moving inward, a hydrogen-rich layer, a helium-rich layer, an oxygen/neon layer, and an inner iron-rich core. The mass fraction of every isotope can be read off easily for each ring. For example, in the outermost layers, the mass of the star is divided as 0.75 hydrogen, and approximately 0.25 of helium, which corresponds to a solar-like composition (Asplund et al. 2009) and approximately to most zero-age main-sequence stars in the Universe. In contrast to the classic representation, all isotopes are shown and can be identified, even in the innermost layers. However, reading the exact mass fraction of an element at a particular mass or radius coordinate is more challenging in these diagrams. The rings help give general information about the mass or radius, but it is not possible to find the mass coordinate of a particular composition boundary.

6.5.2 Comparing the interior structure of stars

In Fig. 6.7 we compare a typical representation of two interior properties of a 16 $M_\odot$ single stars with TULIPS diagrams of the same properties. Both diagrams present the specific nuclear energy generation rate as a function of the mass coordinate. In the standard representation, the quantity is visualized by a line. This figures enables a fast reading of quantitative information, but connecting the variations in the property shown to the overall stellar structure (e.g., realizing

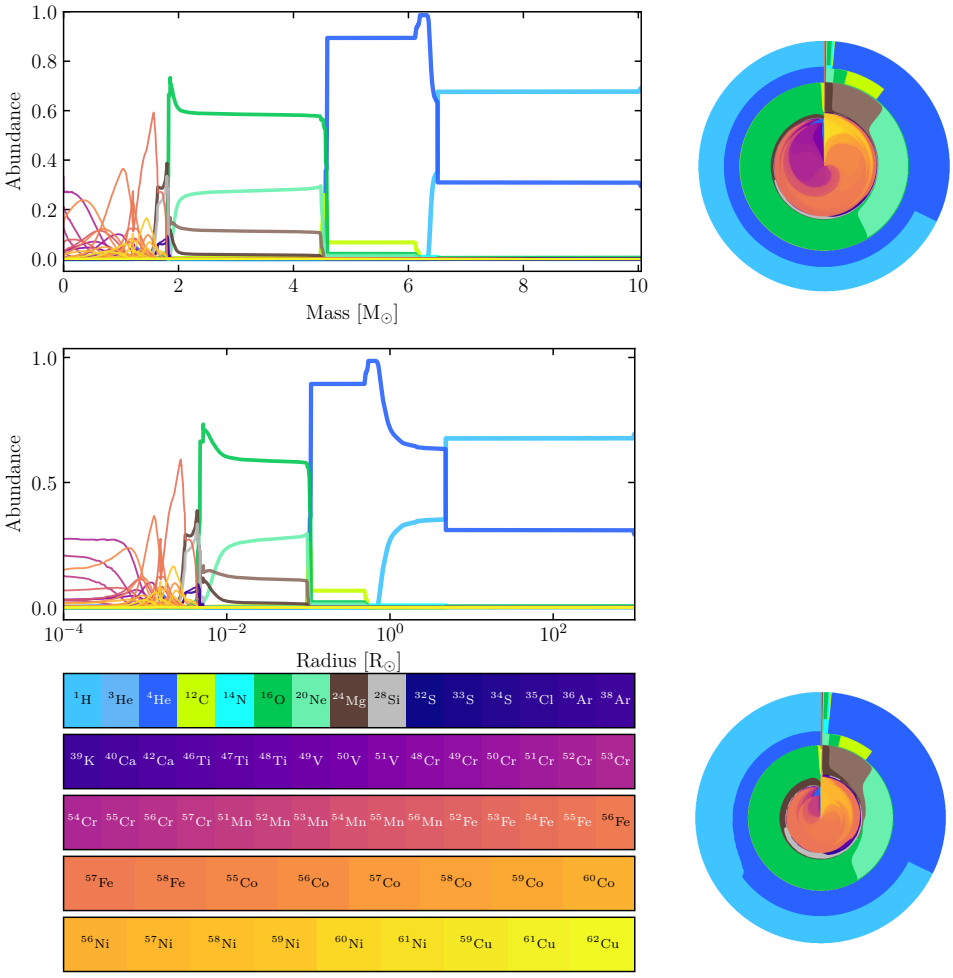

Fig. 6.6: Comparison between classical stellar interior composition diagrams (left) and diagrams produced with TULIPS (right), containing the same information. All diagrams show the composition of a single star model at solar metallicity with an initial mass of 16 $M_\odot$ at the onset of core collapse. For clarity, out of the 128 isotopes, only those with maximum mass fractions greater than 10^{-4} are shown. The upper panels give the stellar composition as a function of the mass coordinate, and the lower panel as a function of the radial coordinate (on a logarithmic scale) for both the TULIPS and classical diagrams.

that the peak in nuclear energy generation rate corresponds to a shell-burning structure in the star) can be challenging for the untrained eye.

Instead of lines, TULIPS represents physical properties as a color gradient on a circle. This diagram emphasizes the mass coordinates for which the properties shown reach their highest values. For example, in the case of the nuclear energy generation rate, three regions can easily be identified. With these diagrams, it is immediately apparent that the energy generation is

located in shells inside the star. Reading quantitative information on the mass coordinate is facilitated by the central and outside axes. However, with this representation, it is generally more challenging to make out quantitative information about the property itself.

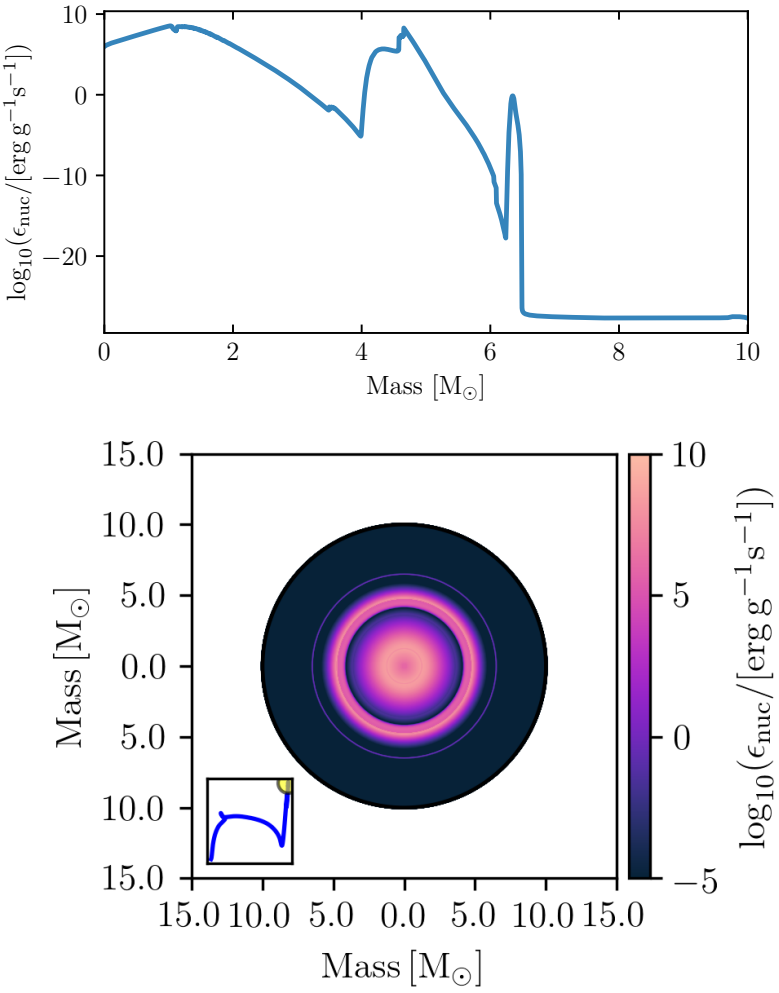

Fig. 6.7: Comparison between a typical diagram showing the nuclear energy generation rate profile of an 11 $M_\odot$ star at the end of core carbon burning (top) and a diagram produced with `TULIPS` (bottom) that contains the same information.

6.5.3 Interior energy generation and losses, and mixing processes: comparison with the Kippenhahn diagram

TULIPS animations can be used to better interpret the evolution of the energy generation and losses, as well as mixing processes in the interior of stellar objects. This evolution is traditionally shown with Kippenhahn diagrams (Hofmeister et al. 1964) that represent the interior stellar structure as vertical profiles as a function of time, where the vertical direction is proportional to the mass coordinate. In Fig. 6.8, we compare the Kippenhahn diagram of our example model of an 11 $M_\odot$ star (see also Section 6.4.1) to TULIPS animations that show the interior burning and mixing processes particular moments in time that are marked by vertical lines on the Kippenhahn diagram.

The Kippenhahn diagram is information-dense and allows an overview of the burning and mixing processes throughout the evolution. Distinct core burning stages can be easily distinguished by the advent of a convective region in the center of the diagram, where energy is being generated. Short phases are difficult to distinguish on this diagram, as are details of the burning and mixing structure at one given moment in time. The snapshots of the corresponding TULIPS animation represent the star as a circle that is divided into rings. Colors and hatching indicate the burning and mixing regions, respectively. In the first snapshot, the star contains a convective hydrogen-burning core. The animation visualizes how the convective regions change in mass extent over time and shows that shell burning regions occupy a small fraction of the total mass of the star. The change in mass extent of convective regions can be easily recognized by following the evolution of regions that are shaded with small circles. After core carbon depletion (snapshot 5), energy losses due to neutrino emission clearly dominate in the core. The TULIPS representation also highlight the complex variations in energy generation and losses towards the end of the evolution of such a massive star. However, it does not enable a quick overview of all burning process that occur in the star over its lifetime.

6.6 Discussion, conclusion, and outlook

TULIPS is a novel visualization tool for stellar astrophysics. It enables intuitive visualizations of the physical properties of stellar objects based on state-of-the-art one-dimensional stellar evolution simulations. It is currently optimized for stellar models computed with the MESA code. Making use of the intrinsic assumption of spherical symmetry in one-dimensional simulations, TULIPS represents the physical properties of stellar objects as the properties of circles. The basic functionalities of TULIPS include creating diagrams that visualize (a) the size and apparent color of stellar objects, (b) the interior burning and mixing processes, (c) the composition of stellar objects, and (d) the interior physical properties. The heart of TULIPS' capabilities consists in creating interactive animations that show the time evolution of these diagrams and the physical properties they represent.

This paper demonstrates how TULIPS can be used as an analysis tool for understanding the evolution of stellar objects. It shows that TULIPS can help to visualize physical processes, such

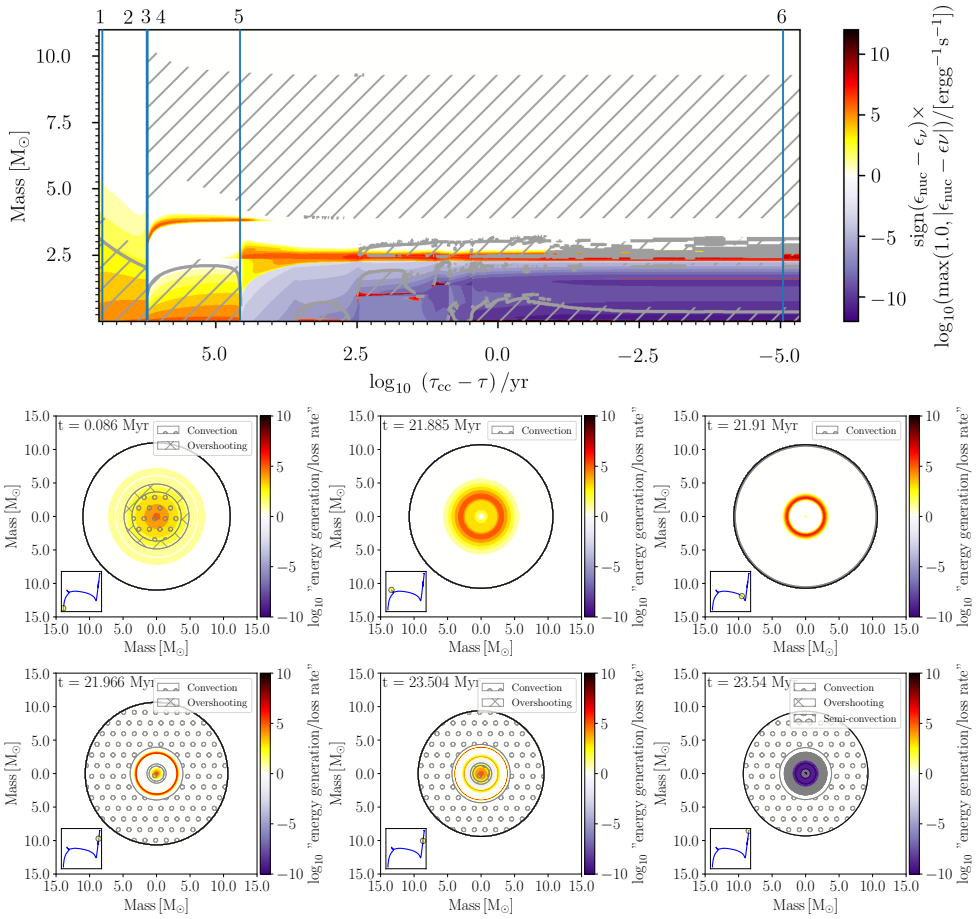

Fig. 6.8: Comparison of a Kippenhahn diagram (top) to snapshots of a TULIPS animation that shows the energy generation and losses, together with mixing regions in the stellar interior (bottom). These plots showcase the evolution of the same single 11 $M_\odot$ star model at solar metallicity. In the TULIPS snapshots, the stellar model is represented by a circle whose radius represents the total mass of the model. Inset diagrams indicate the evolution on the HRD. In both the Kippenhahn diagram and the TULIPS diagrams, convective regions are indicated by hatching and colors indicate the logarithmic difference between the specific nuclear energy generation rate ϵ_{nuc} and the specific energy rate due to neutrino emission ϵ_ν. Blue vertical lines on the Kippenhahn diagram mark the moments at which the TULIPS snapshots were generated.

as accretion and mixing processes. Compared to classic representations, TULIPS diagrams typically require less space, easily represent qualitative information, and help appreciate the scales of stellar objects. These diagrams are better in line with design principles for data visualization (Evergreen & Metzner 2013), closer to the actual shape of these objects, and as such, probably more intuitive (Lewis & Sheppard 2006). However, quantitative information is harder to apprehend with TULIPS diagrams. The amount of information that can be conveyed is limited and they do not allow an overview of the global time evolution of physical quantities.

Research in data visualization indicates that while dynamic visualizations are better at drawing and holding attention, making it more evocative, deeper understanding can be gained with static ones (Valkanova et al. 2013; Newell et al. 2016).

In summary, TULIPS does not replace the classic representations of physical properties, but allows complementary insight and a change of perspective. This in turn has the potential to trigger and hold the attention of the readers (Treisman 1988; Hillstrom & Yantis 1994). Because they can convey the same information in a simpler manner and attention has been given to increasing their appeal according to design principles, these diagrams hold the potential to improve communication and understanding of stellar astrophysics (Lusk & Kersnick 1979; Cawthon & Moere 2007; Evergreen & Metzner 2013).

Aside from a tool for research, TULIPS can be applied as a means to teach others the evolution and structure of stellar objects and also as a means to produce material for public outreach.

In the future, TULIPS could be further extended, for example by including the evolution of binary stars, by enabling more interactions with the diagrams, and by adapting it for use with other one-dimensional physical simulations.

The author is grateful to S. Justham for important insights and suggestions that led to improvements of the project, and for devising the unforgettable acronym. This work has benefited from valuable input and guidance by S. E. de Mink. The author thanks R. Farmer for making the `mesaPlot` package open source, and for help with debugging and testing of the code. L. Kaper and A. de Koter provided helpful feedback on the manuscript. The author thanks the entire BinCosmos/BinWaves group for helpful suggestions and testing. This project was funded by the European Union's Horizon 2020 research and innovation program from the European Research Council (ERC, grant agreement No.715063) and the Netherlands Organisation for Scientific Research (NWO) as part of the Vidi research program BinWaves with project number 639.042.728. The author gratefully acknowledges the ET Outreach award of the Royal Holland Society of Sciences and Humanities and its sponsors E. van Dishoek and T. de Zeeuw that made it possible to fund the excellent work of I. de Langen on the TULIPS documentation and tutorials. The author is grateful to A. Faber for designing a logo that captures the essence of TULIPS. Finally, the author thanks B. Sutlieff, L. A. C. van Son, and H. J. G. L. M. Lamers for their unwavering enthusiasm and support, and for helpful discussions about TULIPS, without which this project would not have come into bloom.

Chapter 7

Outlook: next steps in the research on binary-stripped stars and their explosions

In this thesis, we have discussed the late evolution, deaths, and afterlives of binary-stripped stars based on theoretical simulations performed with the MESA stellar evolution code. We have shown that stars that experience stripping by a companion can retain some of their hydrogen-rich envelopes, especially at low metallicity. Those that do, can expand to giant sizes at late stages of their evolution and are likely to interact again with a companion (Chapter 2). Further, we found that binary stripping not only affects the outer layers, but also the deep interiors of our massive star models (Chapter 3), and that this has interesting consequences for their explodability (Chapter 4) and nucleosynthesis (Chapter 5). In Chapter 6, we presented `TULIPS`, a visualization tool that was developed and applied to the research presented in this thesis. This tool enables novel visualizations of the structure and evolution of stars.

Actual understanding of the properties of binary-stripped stars close to, or at the moment of, their death can only be gained by confronting theoretical predictions, such as the ones presented in this thesis, with observations. In this final chapter, we explore future research directions that will help to understand the observational consequences of binary stripping on the explosions of massive stars. In Section 7.1 we show an example of how supernova (SN) light-curve models could be used to study stripped-envelope supernovae (SESNe) and their progenitors in the near future and present preliminary results. In Section 7.2 we conclude this thesis with an outlook on general developments that have the potential to lead to significant progress in this field.

7.1 Preliminary results on the effect of binary stripping on supernova light-curves

Supernova light-curves carry important information about the properties of the supernova explosion. Features of the light-curve can give valuable insights about the progenitor properties, such as its pre-explosion mass and radius (see Section 1.2.3 and also, e.g., Arnett 1979, 1987; Piro & Nakar 2013).

With the rise of automated transient facilities, increasingly large samples of SESNe light-curves and spectra exist (e.g., Drout et al. 2011; Modjaz et al. 2014; Bianco et al. 2014; Taddia et al. 2015, 2018; Stritzinger et al. 2018; Shivvers et al. 2019; Prentice et al. 2019). The near-future prospective of the availability of large homogeneous data-sets of SN light curves

is exciting and provides new opportunities to study the deaths of massive stars in a statistical manner. In particular, future surveys with rapid time cadence will be able to probe the deaths of the stripped-envelope stars that are the central topic of this thesis.

Several statistical studies on the light-curves of SESNe have already been performed (see, e.g., Drout et al. 2011; Lyman et al. 2016; Taddia et al. 2018) and provided valuable constraints on the distribution of explosion properties among SESNe. In particular, these studies have found that the ejecta mass is typically very low, with values peaked at about $2\,M_\odot$, which is significantly lower than the values of $\sim 6\,M_\odot$ expected from massive single wind-stripped progenitors. In addition, these studies have reported that the inferred mass of ^{56}Ni synthesized during the explosion is approximately $0.1\,M_\odot$; about a factor 3 larger than for type II explosions.

Most studies make use of analytical formulae to derive properties of observed SN light curves (see however Taddia et al. 2018 for an exception). The scarcity of studies that make use of detailed progenitor models is probably due to, at least in part, the limited availability of large numbers of simulated light curves that explore the proposed progenitor channels. These include stripping by a binary companion and stripping massive single stars by stellar winds. There is mounting evidence for the binary channel (Eldridge et al. 2008; Smith et al. 2011; Lyman et al. 2016; Taddia et al. 2018; Prentice et al. 2019; Graur et al. 2017b, see also Section 1.2.5). Predictions for SESN light-curves based on detailed binary-stripped star models are as-yet rare (but see Eldridge et al. 2018). Most investigations rely on single-star models, in particular pure helium star models (e.g., Nomoto & Hashimoto 1988; Kleiser & Kasen 2014; Kleiser et al. 2018; Taddia et al. 2018; Ertl et al. 2020; Dessart et al. 2020).

In this section, we present light-curves of SESNe computed using our detailed binary models presented in Chapter 2 as progenitors. We then show a comparison with an observed light curve and briefly discuss the similarities and differences. We then discuss the feasibility of applying this method to large samples of observed light curves to derive statistical constraints on the explosion properties of SESNe, in particular their explosion energies, and the mass of synthesized ^{56}Ni they produce.

7.1.1 Method

For creating light-curve models, we employ the open-source, one-dimensional hydrodynamic SuperNova Explosion Code (`SNEC`, Morozova et al. 2015, 2016). This code simulates the effect of a SN explosion on the stellar interior and the resulting SN light-curve by injecting thermal energy around the compact object that forms in the core of a specified stellar structure model. It relies on user-specified values for the total mass of synthesized ^{56}Ni, M_{Ni}, for the input energy E, for the assumed final mass of the remnant M_{NS}, and for the ^{56}Ni mass distribution. `SNEC` calculates how the shock wave that results from the energy injection propagates from the deeper layers to the surface. This code assumes local thermodynamic equilibrium (LTE), i.e., that matter and radiation are strongly coupled, such that the SN can be described by a single temperature for each location. Among other things, `SNEC` provides estimates for the bolometric

light-curve, the ejecta velocity, and the absolute magnitude in typical wavelength ranges employed for SN observations. This code relies on severe approximations and simplification (among others, spherical symmetry, LTE, and using pre-computed bolometric corrections for magnitudes), but it is an appropriate tool to simulate the overall evolution of the light curve and is sufficiently accurate for our purposes at early times. Moreover, the approximations make this code computationally efficient. The computation of one light curve costs about 0.2 CPU hours, which makes it a very suitable tool to create extensive grids of simulated light curves. This makes it ideal for our purposes.

We employ `SNEC` to model SN light curves resulting from the explosion of our binary-stripped star models at solar ($Z = 0.0142$) and low metallicity ($Z = 0.001$) with initial masses M_i varying from $9\,\mathrm{M}_\odot$ to $15\,\mathrm{M}_\odot$. We assume explosion parameters that are thought typical for SESNe explosions: $E = 10^{51}$ erg = 1 B, $\mathrm{M_{Ni}} = 0.1\,\mathrm{M}_\odot$, and $\mathrm{M_{NS}} = 1.4\,\mathrm{M}_\odot$ (e.g., Lyman et al. 2016). For all models presented here, we assume that ^{56}Ni is mixed through the ejecta up to a fixed boundary mass of $3\,\mathrm{M}_\odot$.

In addition, we explore the impact of varying the explosion energy and nickel mass. For this we use our $13\,\mathrm{M}_\odot$ solar metallicity model. We systematically vary E (from 0.55 to 5.1 B, in steps of 0.35 B) and $\mathrm{M_{Ni}}$ (from 0.03 to $0.5\,\mathrm{M}_\odot$, in steps of $0.035\,\mathrm{M}_\odot$).

7.1.2 Light-curves of solar and low metallicity models

In Fig. 7.1 we present our computed bolometric light-curves at solar and low metallicity. All light-curves have a similar shape, with an initial peak that corresponds to shock cooling emission, followed by a rapid drop of the luminosity. They then display a second peak from the radioactive decay of ^{56}Ni (see also Section 1.2.3), followed by an exponential decrease. Because the explosion energy is fixed, a larger initial mass results in a lower peak luminosity and in longer light-curve time scale. The models at solar metallicity reach lower luminosities for their initial peak (less than $2 \times 10^{42}\mathrm{ergs}^{-1}$) than the models at lower metallicity, which reach peak values of up to $2 \times 10^{44}\mathrm{ergs}^{-1}$. This is because the radii of the lower metallicity models are significantly larger (e.g., Piro & Nakar 2013).

Since the low-metallicity models retain a hydrogen layer, spectral classification would likely categorize them as type IIb SNe. In contrast, because the solar metallicity models are hydrogen-poor, they would likely be classified as type Ib SNe. Hachinger et al. (2012) estimate at least $0.06\,\mathrm{M}_\odot$ of hydrogen are required for a type IIb SN classification (see also Dessart et al. 2012).

7.1.3 Testing model fits to observations

We investigate the possibility of using predicted light-curves such as these to infer the explosion parameters (explosion energy, ^{56}Ni mass, and ejecta masses) of observed SESNe. To this end, we employ our second grid of models with the same progenitor ($M_\mathrm{i} = 13\,\mathrm{M}_\odot$) and systematic variations of the explosion energy and of the ^{56}Ni mass. At the moment of explosion, the

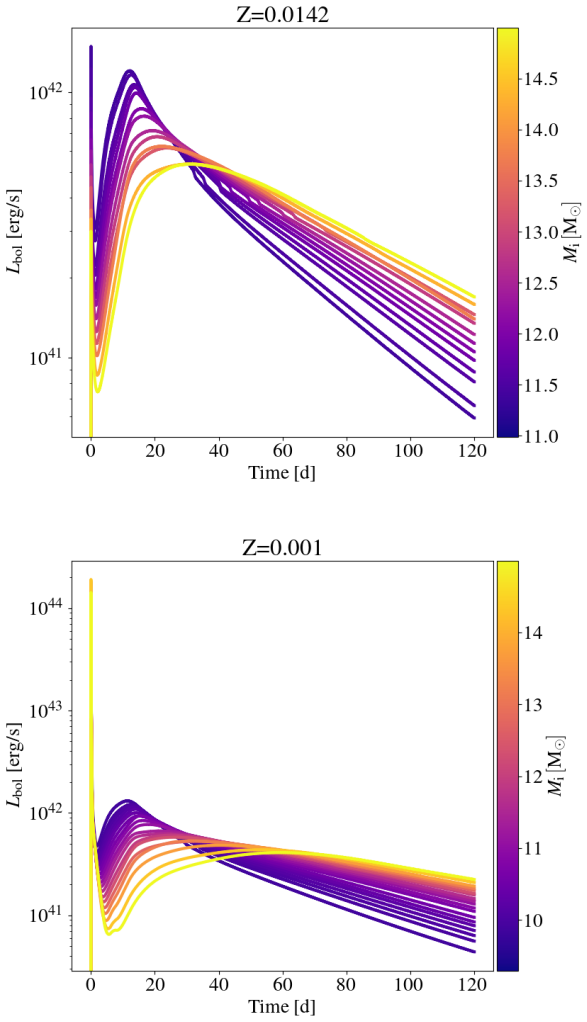

Fig. 7.1: Bolometric light curves of binary-stripped star models at solar (top) and low (bottom) metallicity simulated with the SuperNova Explosion Code (SNEC). Colors indicate the initial mass of the progenitor models. We assume an explosion energy of $E = 10^{51}$ erg and a total mass of synthesized ^{56}Ni of $M_{Ni} = 0.1\,M_\odot$.

progenitor has a mass of 3.88 $M_\odot$, which corresponds to an ejecta mass of 2.48 $M_\odot$ because we assume the compact object has a mass of M_{NS}=1.4 $M_\odot$.

For the observation sample, we use available bolometric SESNe light curves that were inferred by Taddia et al. (2018) from the Carnegie SESN sample[1]. These light curves were corrected for host extinction and reddening by the authors. They also inferred an explosion

[1] https://csp.obs.carnegiescience.edu/

time (corresponding to day 0 in the light curve) and adopted the distance to the host galaxy for the distance to the SN. We show an approximate uncertainty range of ±10 percent for the bolometric luminosity (guided by Lyman et al. 2016), dominated by systematic uncertainties in the conversion from the observed data to the bolometric values.

We perform fits by using χ^2 minimization. Here we define χ^2 as the weighted sum of the difference between the observed ($L_{\rm obs}$) and modeled ($L_{\rm data}$) data points i: $\sum_i (L_{\rm obs} - L_{\rm data})^2 / N\sigma^2_{\rm obs}$, where N is the number of data points and $\sigma_{\rm obs}$ the uncertainty. An example fit result for SN2004gq, a type Ib SN from the sample, is shown in Fig. 7.2. In the upper panel of Fig. 7.2, we show how χ^2 varies as a function of the explosion parameters. Low values of the fitting parameter (shown with colors) are indicative of a good fit. For this particular SN, best fit values are concentrated in a region with ^{56}Ni masses of 0.1 $M_\odot$ and explosion energies around 1.6 B. These values are in good agreement with the values inferred from Arnett model fits in Taddia et al. (2018) for this SN: $E = 2.0 \pm 1.3$B, and $M_{\rm Ni} = 0.08 \pm 0.02\,M_\odot$.

In the upper panel we show how the light curve compares with the model and we find good agreement. We find residuals, defined as $(L_{\rm obs} - L_{\rm model})\,/L_{\rm model}$ of less than 0.2.

We see systematically negative residuals between 30-60 days past explosion time. This occurs around the moment the photosphere has reached the center, which means the assumption of LTE breaks down and the model does not accurately describe the light curve any longer (Morozova et al. 2015).

7.1.4 Discussion and feasibility of inferring explosion properties of a large sample of stripped envelope SNe

We have presented light curves obtained by simulating the explosion of binary-stripped star models at solar and low metallicity. The lower metallicity models have a larger radius than the solar metallicity models (see also Tables A.2 and A.3), which results in a higher shock cooling peak in their light curves. Models with higher initial masses have longer light-curve time scales. In general, the light curves we obtain are in good agreement with values found in the literature (for an example, see Fig. 1 in Lyman et al. 2016). The code we have used is fast but has limitations. In the future it would be important to test these models against more sophisticated light curve models, such as for example STELLA (Blinnikov & Bartunov 2011; Kozyreva et al. 2020), SuperNu (Wollaeger & van Rossum 2014) or SEDONA (Kasen et al. 2006).

We conducted preliminary tests on the possibility to use such models for inferring explosion parameters and found promising first results, that agree with earlier work. This indicates that it would be feasible to analyze the full sample of observed SNe against an extended version of our grid where we allow for variations in the initial progenitor mass and further explosion parameters. For this we can use Bayesian inference, as has recently been applied to similar studies (e.g., Guillochon et al. 2018; Gomez et al. 2019; Martinez et al. 2020). In the future, such a technique could be applied in combination with large grids of theoretical models to better constrain the explosion and progenitor properties of SESNe, and their uncertainties, from

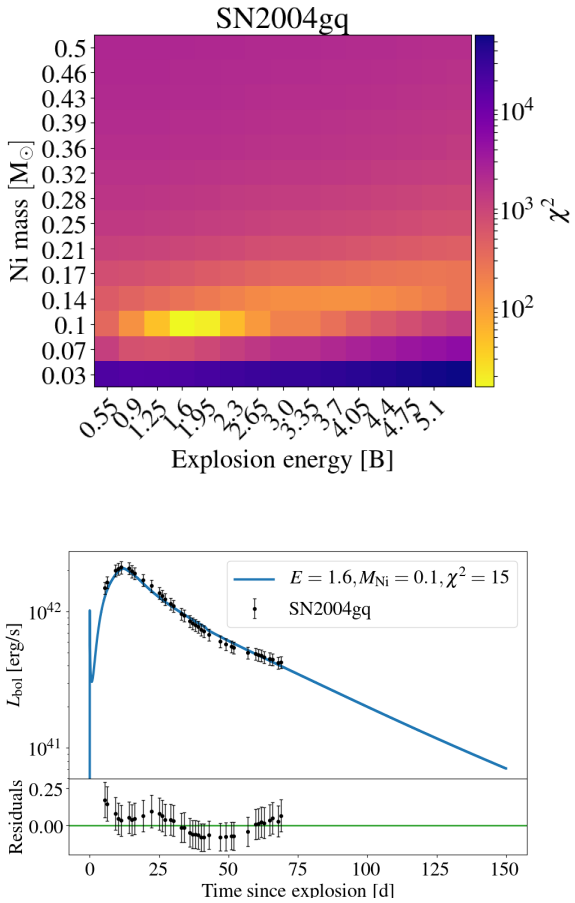

Fig. 7.2: Upper panel: we show χ^2, indicated with colors, as a function of assumed ^{56}Ni mass and explosion energy, assuming a progenitor mass of 13 $M_\odot$. Low values correspond to a better fit. Lower panel: Resulting best-fit bolometric light-curve (in blue) for SN2004bq. The black dots represent the bolometric luminosity derived by Taddia et al. (2018) for the type Ib SN2004bq, for which we assume a systematic uncertainty of 10%. The lower panels indicate the residuals (see text for the definition).

the large untargeted samples that will become available in the near future. More specifically it could be used to explore the full posterior for the distribution of all SN in the sample and to investigate trends such as relations between the explosion energy (or nickel mass) and progenitor mass.

7.2 Outlook

How can we make progress in the field of binary-stripped stars beyond the theoretical explorations we have shown in this thesis? Below, we discuss avenues for which upcoming observations have the potential to provide constraints on important aspects of binary-stripped stars:

Life and late evolution of binary-stripped stars

During the majority of their lives, the binary-stripped stars we discuss in this thesis are notoriously difficult to detect. This is because during this phase they are very small, with radii of $\approx 1\,R_\odot$, and their peak emission lies in the extreme ultraviolet. In the optical range, they are so faint that bright companion stars may easily outshine them (Götberg et al. 2017). The short wavelength range in which the emission of binary-stripped star dominates, is unfortunately probed by only few active missions (Götberg et al. 2018). However, as shown in Chapter 2 (see also Habets 1986b; Yoon et al. 2010, 2017), this does not necessarily apply to the later evolutionary phases, during which these stars can reach giant sizes. At this point, they could be observed as helium giants (for which Upsilon Sagitarii is a promising candidate, Schoenberner & Drilling 1983; Kipper & Klochkova 2012) and could potentially be identified through the additional observational characteristics we point out in Section 2.6.3. We note that they may be difficult to distinguish from regular hydrogen-rich giants, both in color and spectral morphology.

In these late phases, binary stripped stars could be the main contributors to their binary system's emission and be identified by observing binary systems in the right temperature range whose luminosity exceeds that expected from their Keplerian masses and that show chemical surface abundances with signs of CNO processing. Such systems may, for example, be detected in massive star surveys, such as the targeted binary surveys TMBM (Almeida et al. 2017) and BBC (Villaseñor et al. 2021) of the Tarantula program (Evans et al. 2011), or the GOSSS survey (Maíz Apellániz et al. 2016).

In addition, the number of stars found in the pre-explosion images of SESNe will increase (Cano 2013), providing further constraints (Kim et al. 2015). Indirect constraints will come from better understanding the initial conditions of binary systems. For example, the Gaia mission is expected to provide better constraints on the multiplicity fraction of stars in the near future (Eyer et al. 2012; Collaboration et al. 2016). In addition, the fast developing field of asteroseismology has the potential to provide constraints on the uncertain core sizes of massive stars (e.g., Aerts et al. 2003), potentially providing an observational initial mass/stripped star mass relation.

Death of binary-stripped stars

As we have shown in Section 7.1, observations of the explosions of stripped-envelope stars have the potential to provide constraints on the properties of binary-stripped stars. We are

reaching the golden age of optical transient surveys. Nearly the entire sky is now being monitored by several wide-field surveys. Untargeted, systematic surveys hold the potential for a statistical, less biased understanding of transient populations, and among them stripped-envelope supernovae (e.g., Modjaz et al. 2019). The true value of these surveys will come from fast spectral follow-up and from accumulating enough data at the right cadence to obtain meaningful information about individual events. In particular for SESNe, which are generally fainter and shorter-lived than other SNe, it will be crucial to observe them with the right cadence.

The new technique of extremely rapid spectral follow-up, that allows "flash spectroscopy" is a particularly exciting new development in the field (e.g., Khazov et al. 2016). It can provide tight constraints on progenitor radii and on their circumstellar environment and has already revealed a puzzling diversity (e.g., Bruch 2019). Constraining the stellar radius of the exploding progenitor of SESNe will help to understand to what extend stripped stars expand, and with large data sets, also at what metallicity. This may allow first observational tests our predictions discussed in Chapter 2.

Early light curves, next to spectra, will also help reveal whether asymmetries play a large role (e.g., Nakar & Sari 2010; Matzner et al. 2013; Afsariardchi & Matzner 2018). This could be particularly interesting for binary-stripped stars that retain a hydrogen envelope, of which a large fraction may fill their Roche lobe at the moment of explosion and will thus differ from a spherical shape, as we discuss in Chapter 2.

Furthermore, UV survey telescopes have been proposed that may be launched in the near future, such as ULTRASAT (Asif et al. 2021) or LUVOIR (Roberge et al. 2021). These have the potential to observe the shock breakout emission of several transients, and in particular for SESNe, whose shock breakout emission lies in the far ultraviolet/soft X-ray range (e.g., Nakar & Sari 2010; Schawinski et al. 2008; Piro & Nakar 2013).

In addition, increasing numbers of late time spectra of SESNe and new upcoming observations of supernova remnants will give us a better idea of the elements synthesized during the explosion (Matheson et al. 2000; Jerkstrand et al. 2015), which we expect to be different for binary-stripped stars compared to single stars (see Chapter 3). In particular, we show in Chapter 5 that the binary-stripped stars we modeled are twice as efficient at producing carbon as single stars.

Another interesting recent development is the detection of possible surviving companions of stars exploding as SESNe (e.g., Fox et al. 2014; Van Dyk et al. 2016; Zapartas et al. 2017). With more follow-up searches, their numbers will increase and give crucial information on preferred formation channels for binary-stripped progenitors of SESNe. Further, characterizing host galaxy environments will give crucial independent insight on the nature and environment of the SN progenitors (Graur et al. 2017a; Modjaz et al. 2020). For SN that occur closer to Earth, it may be possible to characterize the surrounding population directly, gaining further insight about the environment (e.g., Williams et al. 2014; Díaz-Rodríguez et al. 2021).

Afterlife of binary-stripped stars

With the rapid expansion of the new field of gravitational-wave (GW) observations, the population of stellar remnants is being revealed from a completely new angle (LIGO Scientific Collaboration and Virgo Collaboration et al. 2019). This population is already providing interesting constraints on the formation channels of GW sources, and on the landscape of explodability. For instance, The LIGO Scientific Collaboration et al. (2020) recently reported the detection of a GW source consisting of a $\sim 23\,M_\odot$ black hole and a $\sim 2.3\,M_\odot$ compact object. This is exciting in the context of the "lower mass gap" that may exist between the most massive neutron stars and the least massive black holes ($2-5\,M_\odot$, Bailyn et al. 1998; Özel et al. 2010; Farr et al. 2011) and whose presence is debated. In fact, as we discuss in Chapter 4, we expect that binary-stripped stars may populate this region through fallback accretion onto the proto-neutron star that forms in their center, in agreement with previous studies (Fryer et al. 2012; Woosley et al. 2020; Ertl et al. 2020; Schneider et al. 2021). We estimated that the binary-stars we modeled could accrete more than half of their helium-rich envelopes, which would be more than enough to create compact remnants in this mass range (see also Table 4.1).

With improved and more numerous models of binary-stripped stars and their explosions, the mass and type of compact remnants resulting from stripped stars can be further explored. However, ultimately, a well-sampled mass distribution for black holes and neutron stars is going to provide the best constraints. With the rapidly rising number of GW detections our knowledge of the compact object mass function will improve. This will be especially true in the era of third-generation detectors, such as the Cosmic Explorer (Reitze et al. 2019) and the Einstein telescope (Maggiore et al. 2020), which will dramatically increase the statistics and start to probe this population as a function of redshift (Kalogera et al. 2019).

In addition, we will soon see a completely new population of GW sources thanks to LISA (Amaro-Seoane et al. 2017; Colpi et al. 2019). Binary-stripped stars with compact object companions (typically a white dwarf or a neutron star) can have such tight orbits that the GWs they produce will likely be observable with LISA. They will form part of the verification sources for this mission that will produce valuable constraints on the dynamics and properties of compact binary systems (Kupfer et al. 2018; Götberg et al. 2020b). These systems may be X-ray bright and might also be detected with ongoing and future X-ray missions, such as Swift (Roming et al. 2005), eROSITA (Predehl et al. 2021), ATHENA+ (Nandra et al. 2013), and Chandra (Weisskopf et al. 2000, 2002). In addition, such missions will also help find new X-ray binaries with stripped star donors.

To conclude, this is an exciting time to work in the field of stellar physics and there are very promising times ahead for better understanding the properties of stars stripped in binary systems. We stress that the aspects explored in this thesis are but a tiny part of the many beautiful and diverse ways stars live and end their lives, and much remains to be explored, especially when it comes to multiple systems.

The expansion of stripped-envelope stars: Consequences for supernovae and gravitational-wave progenitors

A

A.1 Parameters of the models

We provide relevant parameters of our models at solar and low metallicity in Table A.2 and A.3, respectively. Definitions for the symbols used in both tables are given in Table A.1.

Table A.1: Parameter definitions for tables A.2 and A.3

Parameter	Unit	Definition
$M_{\rm i}$	($M_\odot$)	Initial total ZAMS mass
$M_{\rm a}$	($M_\odot$)	Total mass after the end of mass-transfer, when the nuclear helium-burning luminosity exceeds 85% of the nuclear luminosity
$M_{\rm b}$	($M_\odot$)	Total mass at core helium depletion, when the mass fraction of helium reaches values smaller than 10^{-4}
$M_{\rm f}$	($M_\odot$)	Total mass at the end of the simulation when the mass fraction of carbon drops below 10^{-4}
$M^{\rm f}_{\rm CO}$	($M_\odot$)	Mass of the carbon/oxygen core at the end of the simulation
$M^{\rm a}_{\rm H}$	($10^{-2}M_\odot$)	Total hydrogen mass after the end of mass-transfer
$M^{\rm f}_{\rm H}$	($10^{-2}M_\odot$)	Total hydrogen mass at the end of the simulation
$R_{\rm min}$	($R_\odot$)	Minimum radius
$R_{\rm b}$	($R_\odot$)	Radius at core helium depletion
$R_{\rm p}$	($R_\odot$)	For low-metallicity models, radius at the peak of the first radius expansion
$\Delta t_{\rm p}$	(kyr)	For low-metallicity models, difference between the final stellar age and the time of the peak of the first radius expansion
$R_{\rm C\,ign.}$	($R_\odot$)	Radius at core carbon ignition, when the luminosity of carbon exceeds 98% of the nuclear luminosity
$R_{\rm max}$	($R_\odot$)	Maximum radius
$R_{\rm f}$	($R_\odot$)	Radius at the end of the simulation
$T^{\rm f}_{\rm eff}$	(K)	Effective temperature at the end of the simulation
$L_{\rm f}$	($L_\odot$)	Luminosity at the end of the simulation
$g_{\rm f}$	($\mathrm{cm\,s^{-2}}$)	Surface gravity at the end of the simulation
$S_{\rm f}$		Approximate final stellar type derived based on the effective temperature (see section 2.4.1)

A.2 Effects of winds on the expansion of stripped stars at low metallicity

In Sections 2.3.2 and 2.4.2, we discuss the expansion of stripped stars. At low metallicity, the models retain a hydrogen-rich layer. The mass of that layer is linked to the maximum radius each star can achieve. However, the mass of the hydrogen-rich envelope retained by a stripped star is not only determined by the binary interaction, but can also be affected by wind mass loss. The wind mass-loss rates for stripped stars are not well known (Yoon 2015; Götberg et al. 2017, 2018; Gilkis et al. 2019). In most stellar evolution models for stripped stars, winds are typically assumed to follow the empirically-derived prescription for Wolf-Rayet stars from Nugis & Lamers (2000). At low metallicity, the effect of winds is expected to be limited due to the metallicity dependence of line-driven winds (Vink & de Koter 2005; Mokiem et al. 2007). This expectation affects predictions for the mass of the leftover hydrogen-rich layer at low metallicity and, consequently, the maximum radii of stripped-star models. We discuss the uncertainties introduced by this assumption below, showing comparisons for both our example model from Section 2.3 and the most massive model from our grid.

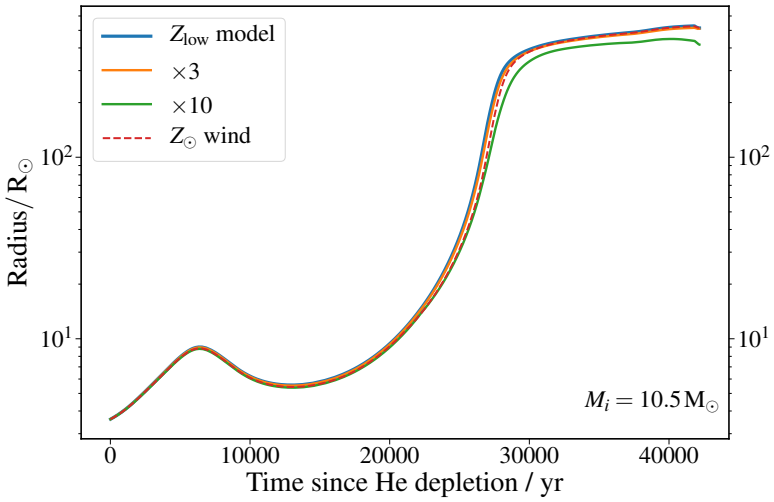

Fig. A.1: Radius evolution of low-metallicity stripped-star models with an initial mass of 10.5 $M_\odot$ as a function of time after core helium depletion. The blue curve represents a model computed with our default wind scheme, while the orange and green curves are for models with mass-loss rates 3 and 10 times higher than the default, respectively. The dashed red curve represents a low-metallicity model computed with the solar metallicity mass-loss scheme.

Figures A.1 and A.2 demonstrate the effects of increasing our assumed wind-loss rates on our exemplary model, with an initial mass of 10.5 $M_\odot$. Figure A.1 shows the evolution

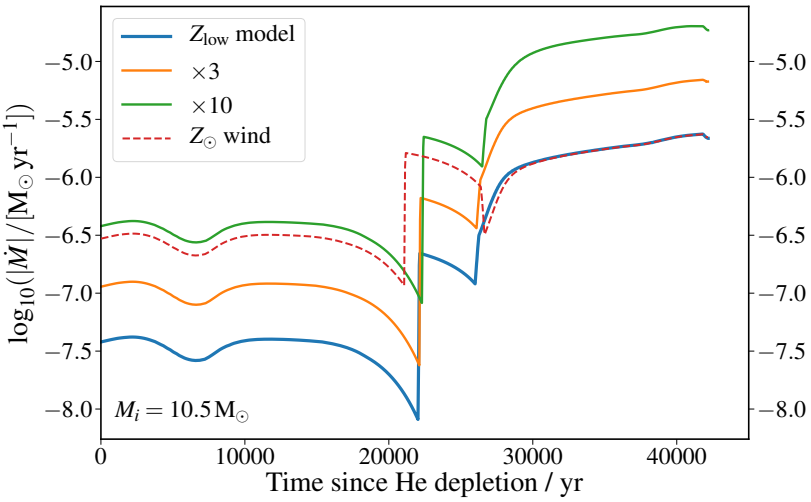

Fig. A.2: Evolution of the wind-mass loss rate for the low-metallicity 10.5 $\mathrm{M}_\odot$ stripped-star model as a function of time after core helium depletion. The line styles are associated with the same models as in Fig. A.1.

of the stellar radius after core helium burning as a function of time. We compare our default model to two models for which the mass-loss rate is increased by constant factors of three and ten. We also present a model with the mass-loss scheme behaving as if the star was at solar metallicity. For the first 20,000 years of the radius evolution, no significant impact of the wind mass-loss rate can be observed. Differences appear towards the end of the evolution. The model with a factor of ten higher mass-loss rate ends its evolution with a smaller radius, of 417 $\mathrm{R}_\odot$, compared to the 515 $\mathrm{R}_\odot$ of the model with our default wind mass-loss scheme. The model with the solar-metallicity wind mass-loss scheme ends its life with a radius of 516 $\mathrm{R}_\odot$, a value that is very similar to that of the default model.

Figure A.2 shows the evolution of the wind mass-loss rates of the models in Fig. A.1. For all models, the dominant mass loss is late in the evolution, when the stars have become giants. The model with a solar-metallicity wind mass-loss rate closely follows the ten-times-higher mass-loss rate for the first 20,000 yr. This is due to the metallicity dependence of the Vink et al. (2001) mass-loss rate, which is $(Z)^{0.85}$, thus, approximately ten times higher for solar metallicity. The sharp changes in the mass-loss rates can be attributed to the bistability jumps of the winds. Because the temperature at which these take place is metallicity-dependent (Vink et al. 2001), they occur earlier for the solar-metallicity model. Towards the end of the evolution, the model assuming solar-metallicity winds follows the same mass-loss rate as our default model because we assume these cool-star winds to be metallicity-independent. However, even if our model predictions had been close to the green curve our conclusions would have remained qualitatively unchanged.

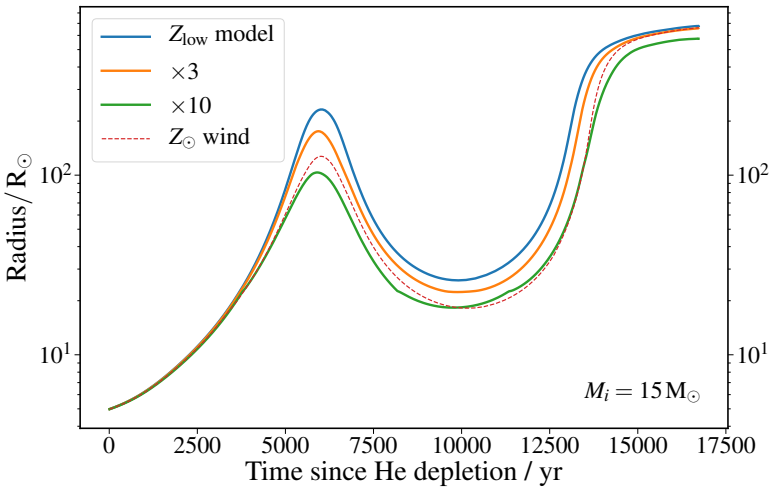

Fig. A.3: Same as Fig. A.1 for the low-metallicity model with an initial mass of 15 $M_\odot$.

Since the effect of wind-mass loss is mass-dependent, we also investigate the impact of increased wind mass-loss rates on the highest-mass model in our grid, which has an initial mass of 15 $M_\odot$. We present the results of this test in Fig. A.3. The impact of changing these assumptions on the radius evolution is more pronounced throughout the evolution than for the 10.5 $M_\odot$ model, but the differences in final radii are still not enough to affect our qualitative conclusions. The largest relative differences can be observed at the peak of the first radius expansion phase, with radii of 232, 175, 104 $R_\odot$ for the default wind assumptions, three-times higher, and ten-times higher mass-loss rates, respectively. However, the predicted radius at the end of the evolution is less affected. The model with a ten-times higher wind mass-loss rate has a final radius only 15% lower than the default model (and only 3% lower than the default model for the three-times higher wind mass-loss rate variation). Again, we also show the radius evolution of a model assuming solar-metallicity winds. The majority of the evolution again follows the same trend as the model with a ten-times-higher wind mass-loss rate. At the peak of the first radius expansion, the solar-metallicity wind model has a radius of 127 $R_\odot$. However, the final radius is only 2% smaller than that of the default mass-loss model.

From these tests, we conclude that the effect of reasonable uncertainties in wind mass loss on the maximum radius these stars are predicted to reach is very small.

A.3 Effects of the orbital period on the expansion of stripped stars at low metallicity

In Appendix A.2, we demonstrate that plausible ranges of stellar winds have only a very small impact on the expansion of stars stripped in binaries at low metallicity. The binary interaction is mainly responsible for determining the mass of the remaining hydrogen layer at low metallicity. Yoon et al. (2017) explored how the choice of orbital separation has a large impact on the final effective temperature and radius of stripped stars at low metallicity, for stars that retain a hydrogen layer with a mass that exceeds 0.15 $M_\odot$. In this section, we discuss how our choice of the orbital separation at low metallicity affects our results. We first show results for models with one initial stellar mass, which are stripped in a binary computed at multiple orbital separations. We then compare the maximum radii obtained for the grid of models presented in the main text with two grids at alternative orbital separations.

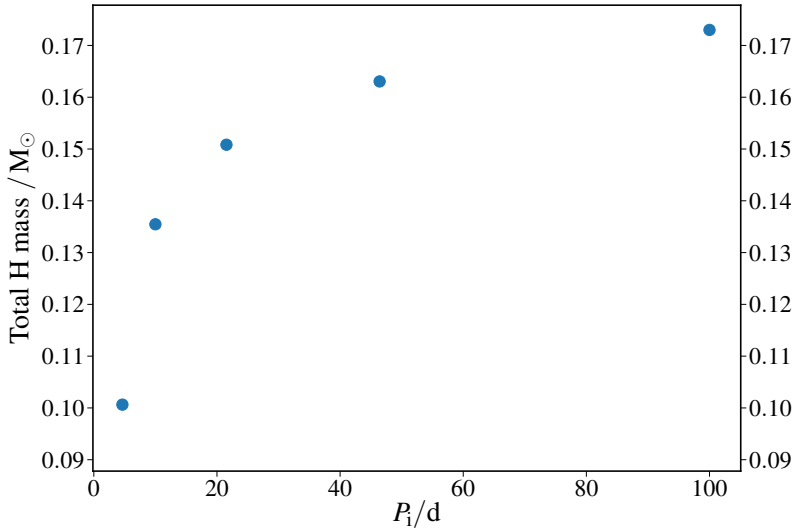

Fig. A.4: Total hydrogen mass at the moment of core helium depletion for low-metallicity models with an initial mass of 11.3 $M_\odot$, shown as a function of initial orbital period, P_i.

Figs. A.4 and A.5 show the impact of the initial orbital separation on the remaining hydrogen mass and radius evolution for stellar models with the same initial mass of 11.3 $M_\odot$. These results are based on a set of calculations with logarithmically-spaced orbital periods ranging from 1 d to 100 d. We did not find converged solutions for the model with an initial orbital period of 1 d. We plot the full evolution of all models on the Hertzsprung-Russell diagram in Fig. A.6. The model with the shortest orbital period interacts with its companion

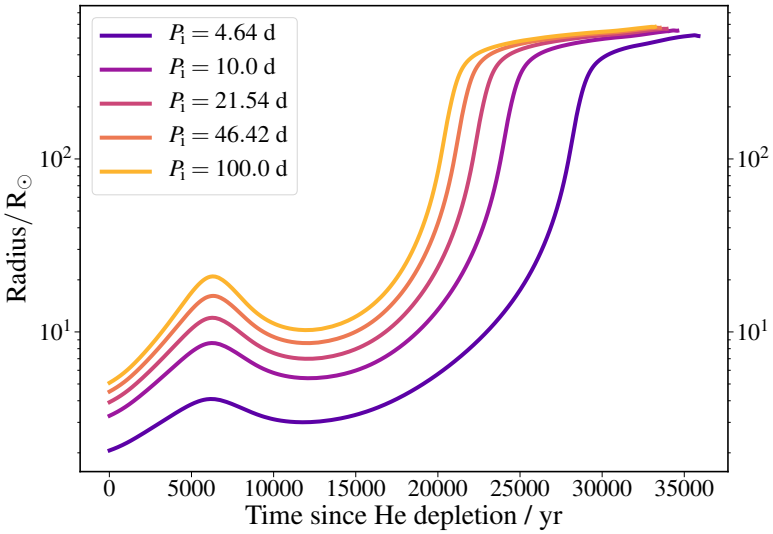

Fig. A.5: Radius evolution of low-metallicity stripped star models with an initial mass of 11.3 $M_\odot$ as a function of time after core helium depletion. Colors indicate the initial orbital period as specified in the legend.

as early as in the course of the main-sequence (case A mass transfer), which is why it has a distinct evolutionary track. We focus on the case B mass-transfer models and thus do not discuss this model below. In Fig. A.4, we display the total hydrogen mass at core helium depletion as a function of the initial orbital period. As expected, the mass of the hydrogen-rich layer increases for longer orbital periods, but it is still within a factor of two.

Fig. A.5 demonstrates the consequent effect of the remaining hydrogen-rich layer on the radius evolution of these low-metallicity stripped stars after core helium depletion (cf. Fig. 2.4). The models display a parallel radius evolution, where models with longer orbital periods have larger radii overall. However, all models reach similar final radii (between 514 and 580 $R_\odot$).

Because the radius evolution also depends on the total stellar mass, we compare the maximum radii of our default model grid at low metallicity with two model grids computed with initial orbital periods of 5 d and 35 d, respectively. Results from these grids are displayed in Figs. A.7 and A.8 (for comparison with Figs. A.4 and A.5, we note that the post-stripping masses from the models shown in those figures ranges from 4 to 4.35 $M_\odot$.) Figure A.8 presents the total hydrogen mass at the moment of core helium depletion as a function of mass. All models display a linear trend of increasing hydrogen mass as a function of mass, except for the highest mass models, which have slightly lower hydrogen mass that can be attributed to the increased effect of stellar winds. As discussed in appendix A.2, the impact of stellar winds on the evolution is very small at this low metallicity. However, since the hydrogen layer has

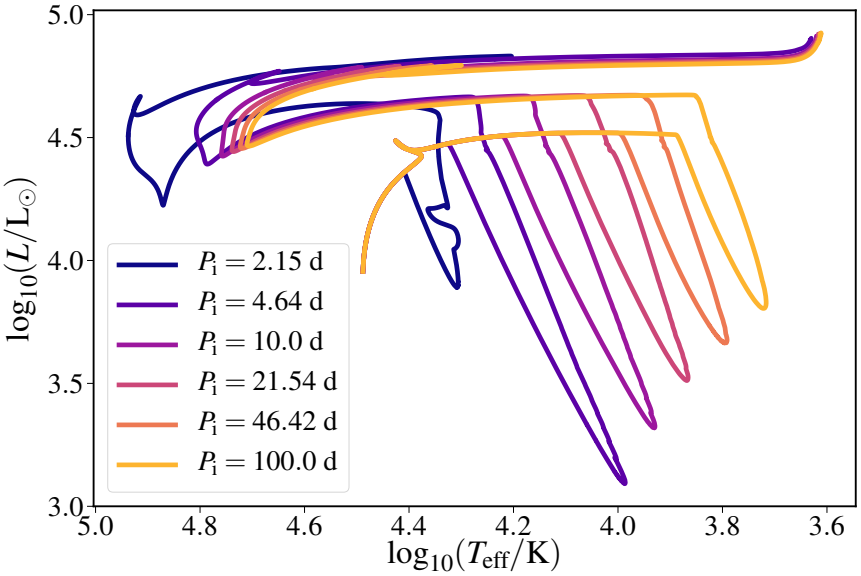

Fig. A.6: Full evolution of models with an initial mass of 11.3 $\mathrm{M}_\odot$ with varying initial orbital periods on the Hertzsprung-Russell diagram. Colors indicate the initial orbital period as specified in the legend. All models with an initial orbital period longer than three days interact with their companions after leaving the main-sequence (case B mass-transfer).

such a low mass (below 0.3 $\mathrm{M}_\odot$), even a small effect can have large consequences. The total hydrogen masses for the models with initial orbital periods of 25 and 35 d are very similar, and the models with a shorter orbital periods have only slightly smaller total hydrogen masses. The total hydrogen masses are notably smaller for the models with an orbital period of 5d. We demonstrate the impact of the orbital period on the maximum radius in Fig. A.7, where we find very similar trends as in the total hydrogen mass. Overall, models with the same initial mass and for these different orbital periods reach very similar final radii.

From a population perspective, assuming the initial orbital periods are distributed uniformly in log space, only a minority of the stars in this mass range stripped by stable mass transfer in the Hertzsprung Gap would have initial orbital periods that lead to final radii which are marginally (within 100 $\mathrm{R}_\odot$) different from the predictions of the grid shown in the main text. This effect does not impact our main finding, which is that the radii of such stripped stars are severely underestimated in population synthesis models, especially at low metallicity. We conclude that for case B mass-transfer, our choice of the orbital period has only a small effect on the maximum radius of stripped stars and is representative for the population. For stripped stars created by other channels (e.g., case A mass-transfer or common envelope evolution), the maximum radius at low metallicity could be significantly different because the mass of the

remaining hydrogen-rich layer could be much smaller.

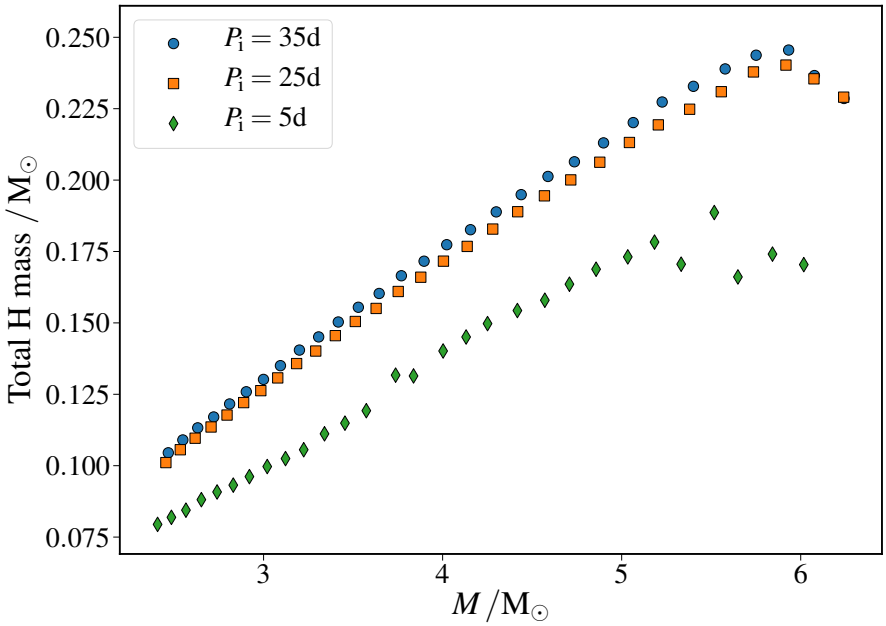

Fig. A.7: Total hydrogen mass at the moment of core helium depletion as a function of stellar mass. Green diamonds, orange squares, and blue circles indicate grids computed with fixed orbital periods of 5, 25, and 35 d, respectively.

A.4 Analytic fitting functions for the radius of stripped stars

For the sake of convenience, we provide simple analytic fits to the minimum and maximum stellar radii from our stripped-star models. These fits accurately represent our models to within a few percent.

In the following formulae, M is the total mass of the stripped star at the relevant time, that is, at the minimum radius following post-stripping contraction or at the maximum radius towards the end of the nuclear burning. The difference between those masses is small for these relatively low-luminosity models and our adopted winds.

At solar metallicity, the minimum radius, $R_{\rm min}$, for each model stripped star is well-

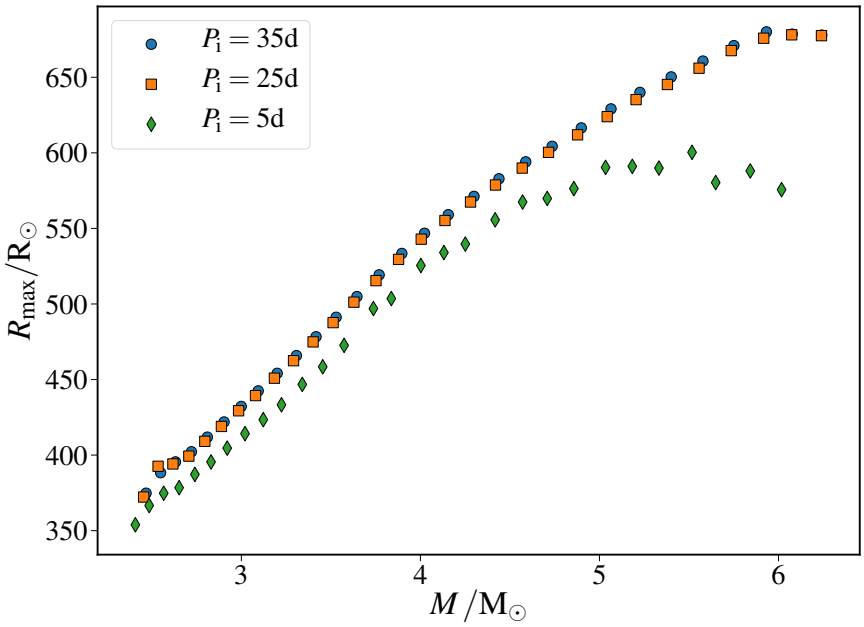

Fig. A.8: Maximum radius as a function of mass for the same models as in Fig. A.8.

described by:

$$\log\left(\frac{R_\mathrm{min}}{\mathrm{R}_\odot}\right) = \max\left\{-0.069\left(\frac{M}{\mathrm{M}_\odot}\right) - 0.23,\right. \\ \left. -0.0142\left(\frac{M}{\mathrm{M}_\odot}\right)^2 + 0.153\left(\frac{M}{\mathrm{M}_\odot}\right) - 0.744\right\}. \tag{A.1}$$

This fit is shown in Fig. A.9, together with the ratio of the model to the fit (in all cases these ratios are for linear quantities, for example, the computed model radius in $\mathrm{R}_\odot$ over fitted radius in $\mathrm{R}_\odot$).

The maximum radii, R_max, of the solar-metallicity stripped-star models above $2.28 M_\odot$ can be expressed by:

$$\log\left(\frac{R_\mathrm{max}}{\mathrm{R}_\odot}\right) = \min\left\{1258\exp\left(-2.64\left(\frac{M}{\mathrm{M}_\odot}\right)\right) + 0.67,\right. \\ \left. -0.63\left(\frac{M}{\mathrm{M}_\odot}\right) + 3.76\right\}. \tag{A.2}$$

This fit is presented in Fig. A.10. The maximum radius of the most massive progenitor was excluded from this fit due to numerical uncertainties in this model; otherwise, this fit has a

maximum deviation from our models of about 2 $R_\odot$. For stripped stars with solar metallicity in our grid of 2.28 $M_\odot$ and below, we find setting $\log(R_{\max}/R_\odot) = 2.8$ is reasonable. The model with a radius of $\log(R/R_\odot) = 2.3$ did not reach core carbon ignition, and so was excluded from the fit.

For our lower-metallicity models, we fit the minimum and the maximum radii for each model with:

$$\log\left(\frac{R_{\min}}{R_\odot}\right) = -9.8\times10^{-8}\left(\frac{M}{M_\odot}\right)^8 + 0.015\left(\frac{M}{M_\odot}\right)^2 + 0.013, \tag{A.3}$$

$$\log\left(\frac{R_{\max}}{R_\odot}\right) = -0.016\left(\frac{M}{M_\odot}\right)^2 + 0.21\left(\frac{M}{M_\odot}\right) + 2.2. \tag{A.4}$$

This fit to $R_{\min}$ is shown in Fig. A.11. The fit to $R_{\max}$ is in Fig. A.12, and matches our low-metallicity models to within approximately 1 $R_\odot$.

For these low-metallicity models, it would be mistaken to take the initial stripped-star mass as a helium-core mass since the helium core grows as a result of the helium produced by hydrogen shell burning. So for these low-metallicity models, we also provide a fit for the initial $M^{\min}_{\rm Hecore}$ and final $M^{\max}_{\rm Hecore}$ helium core masses, as:

$$\left(\frac{M^{\min}_{\rm Hecore}}{M_\odot}\right) = 0.91\left(\frac{M}{M_\odot}\right) - 0.047, \tag{A.5}$$

$$\left(\frac{M^{\max}_{\rm Hecore}}{M_\odot}\right) = 0.89\left(\frac{M}{M_\odot}\right) - 0.037. \tag{A.6}$$

These fits are shown in Fig. A.13 and A.14, respectively.

We intend our fits to be used as a first improvement to current population synthesis calculations, especially focusing on predictions for double neutron-star systems. However, we do not provide a full way to integrate with the Hurley prescriptions. Our detailed calculations show that stars at low metallicity are partially stripped and exhibit intermediate behavior, which does not fit into the powerful but relatively simple scheme provided by Hurley and collaborators. Although one could add an extra parameter to keep track of the mass of the remaining envelope, this would still not be sufficient to, for example, predict the response of such stars to mass loss. More extended grids of detailed models would be needed to encompass multiple variations of the orbital period, the metallicity, and the mass-transfer efficiency, and for an even wider mass range than we present here. The use of such dense grids of stellar models for population studies would be preferable to current population synthesis models given the approximations we point out in Section 2.5.

A.5 Binding energy of the envelope

In Section 2.4.3, we present the envelope binding energies computed from our models. However, the magnitude of the envelope binding energy is sensitive to the location of the boundary

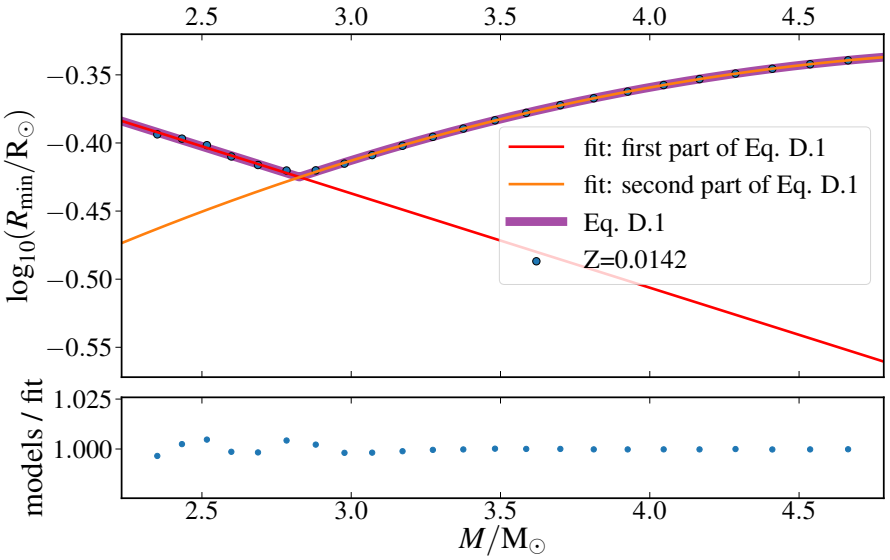

Fig. A.9: Minimum radii of stripped-envelope stars as a function of their total masses at solar metallicity. The best fit obtained (Eq. A.1) is shown in purple and letters indicate the best fit parameters obtained. The lower panel shows the residuals of the fit, which are defined as fractional (i.e., dimensionless).

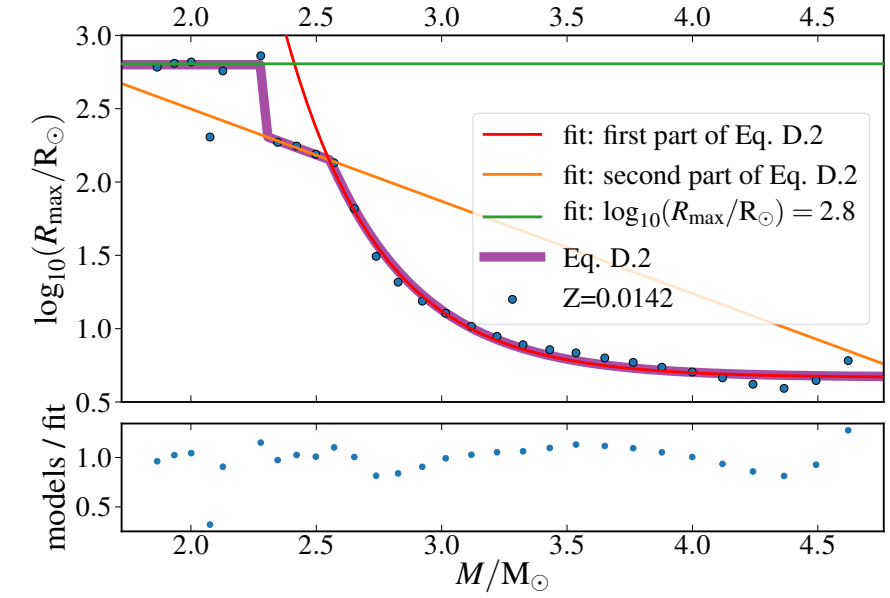

Fig. A.10: Maximum radii of stripped-envelope stars as a function of their total masses at solar metallicity, extended to lower mass models. The fit is shown in purple. The lower panel shows the fractional residuals of the fit.

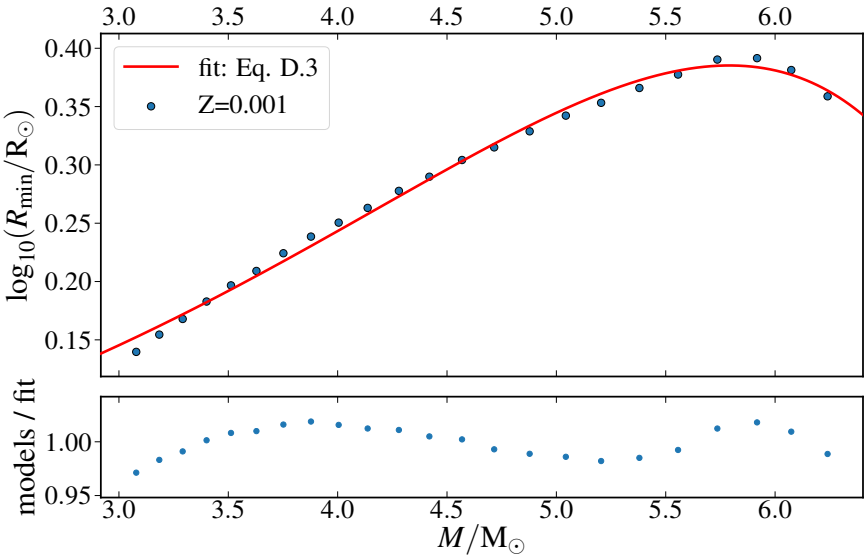

Fig. A.11: Minimum radii of stripped-envelope stars as a function of their total masses at low metallicity. The best fit obtained (eq. A.3) is shown in red. The lower panel shows the residuals of the fit.

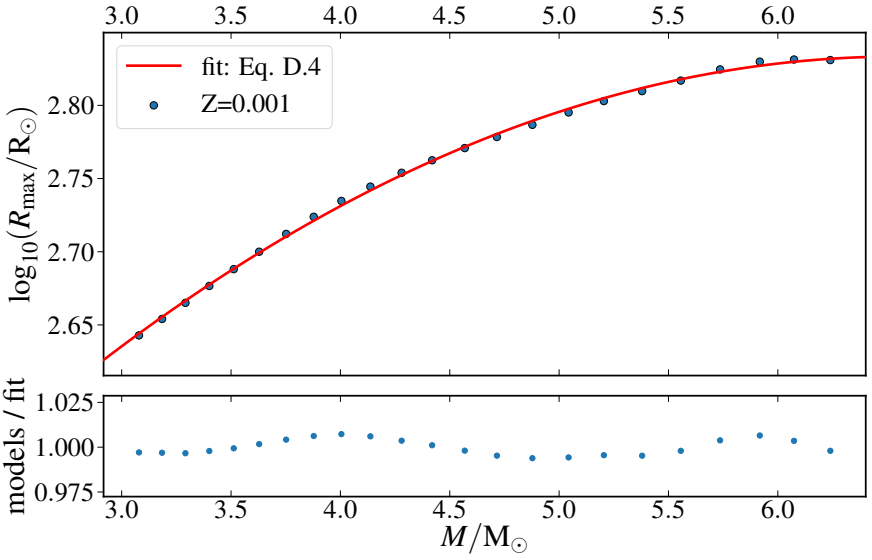

Fig. A.12: Maximum radii of stripped-envelope stars as a function of their total mass at low metallicity. The best fit obtained (eq. A.4) is shown in red. The lower panel shows the residuals of the fit.

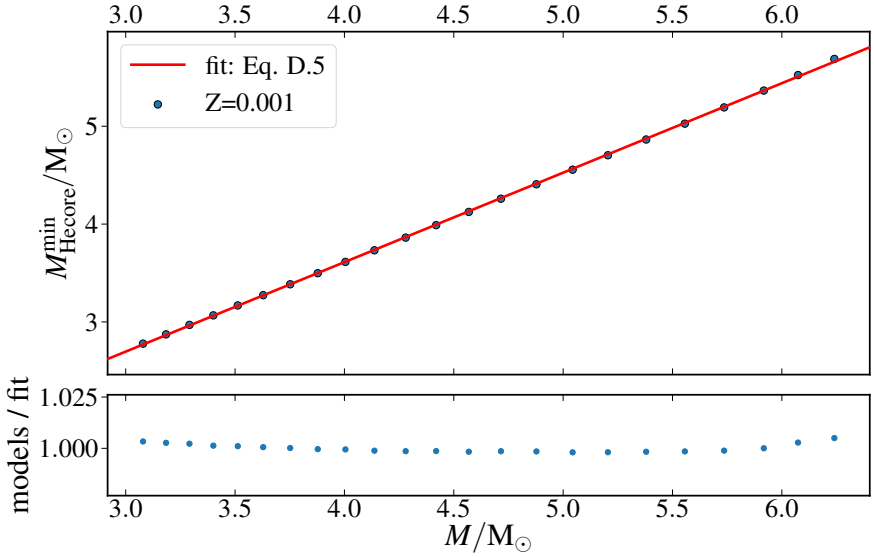

Fig. A.13: Helium core mass at the minimum radius as a function of their total masses at low metallicity. The best fit obtained (eq. A.5) is shown in red. The lower panel shows the residuals of the fit defined as the difference between the fit and the models in solar masses.

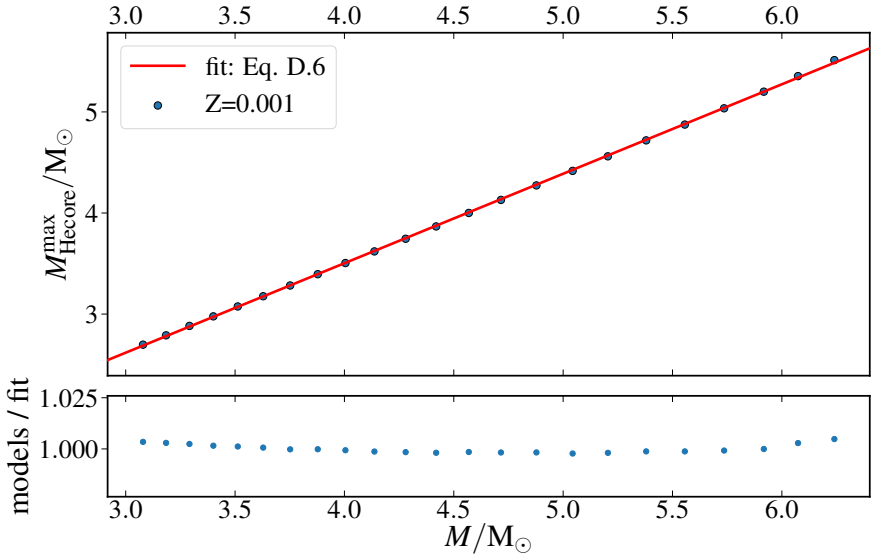

Fig. A.14: Helium core mass at the maximum radius as a function of the total mass at low metallicity. The best fit obtained (eq. A.6) is shown in red. The lower panel shows the residuals of the fit defined as the difference between the fit and the models in solar masses.

between core and envelope and to whether or not internal energy terms are incorporated in the calculation (see, e.g., Ivanova et al. 2013). We discuss this further below.

A.5.1 Binding energy with and without internal energy

When considering common-envelope evolution, the term "binding energy" is inconsistently used in the literature. Sometimes the term is used purely for the gravitational binding energy, without including either the thermal internal energy of the envelope material or the electrostatic potential energy of ionized and dissociated matter. In this context it is common to refer to the thermal energy and recombination energy terms (including molecular dissociation energy) collectively simply as "internal energy," as we do. The difference between binding energies which ignore or include these terms can be substantial, and can qualitatively affect common-envelope outcomes (e.g., Han et al. 1994; Podsiadlowski et al. 2003; Ivanova et al. 2013, and references therein). In Fig. A.15, we compare the effect of including or excluding the internal energy terms for the calculation of the binding energy for our grids at high and low metallicity. Models for which the binding energy was computed with the internal energy terms have a lower magnitude of binding energy – that is, they are less bound – and span a smaller absolute range of binding energies at the beginning of the evolution.

The dimensionless λ parameter is commonly employed to encode how the structure of an envelope affects its binding energy. This was introduced by de Kool (1990) for calculating the outcome of common-envelope evolution with the "alpha prescription." It is defined as

$$\lambda = \frac{GM_1 M_{1,\mathrm{env}}}{E_\mathrm{B} R_1}\,, \tag{A.7}$$

where M_1 is the mass of the primary star transferring mass, $M_{1,\mathrm{env}}$ the mass of its envelope, and R_1 its radius. We show the λ parameter at high and low metallicity for both definitions of the binding energy in Fig. A.16.

A.5.2 Choice of core/envelope mass boundary

Subtle differences in the definition of the core and envelope boundary mass can also significantly affect the value of the binding energy (see, e.g., Han et al. 1994; Tauris & Dewi 2001; Podsiadlowski et al. 2003; Ivanova et al. 2013). We do not investigate the effect of choosing such different definitions for the core-envelope boundaries on our results.

However, for these stripped stars we do investigate the differences between choosing a hydrogen-rich or helium-rich boundary. We compare the binding energy computed using Eq. 2.1 for the hydrogen-rich (H) and the helium-rich (H + He) envelope in Fig. 2.5 as a function of time after core helium depletion at high and low metallicities. For both grids, the binding energy of the H-envelope is an order of magnitude lower than that of the the H + He envelope. This is unsurprising, given that the potential well is deeper and steeper closer to the core of the star. For both regions, the magnitude of the total absolute binding energy increases

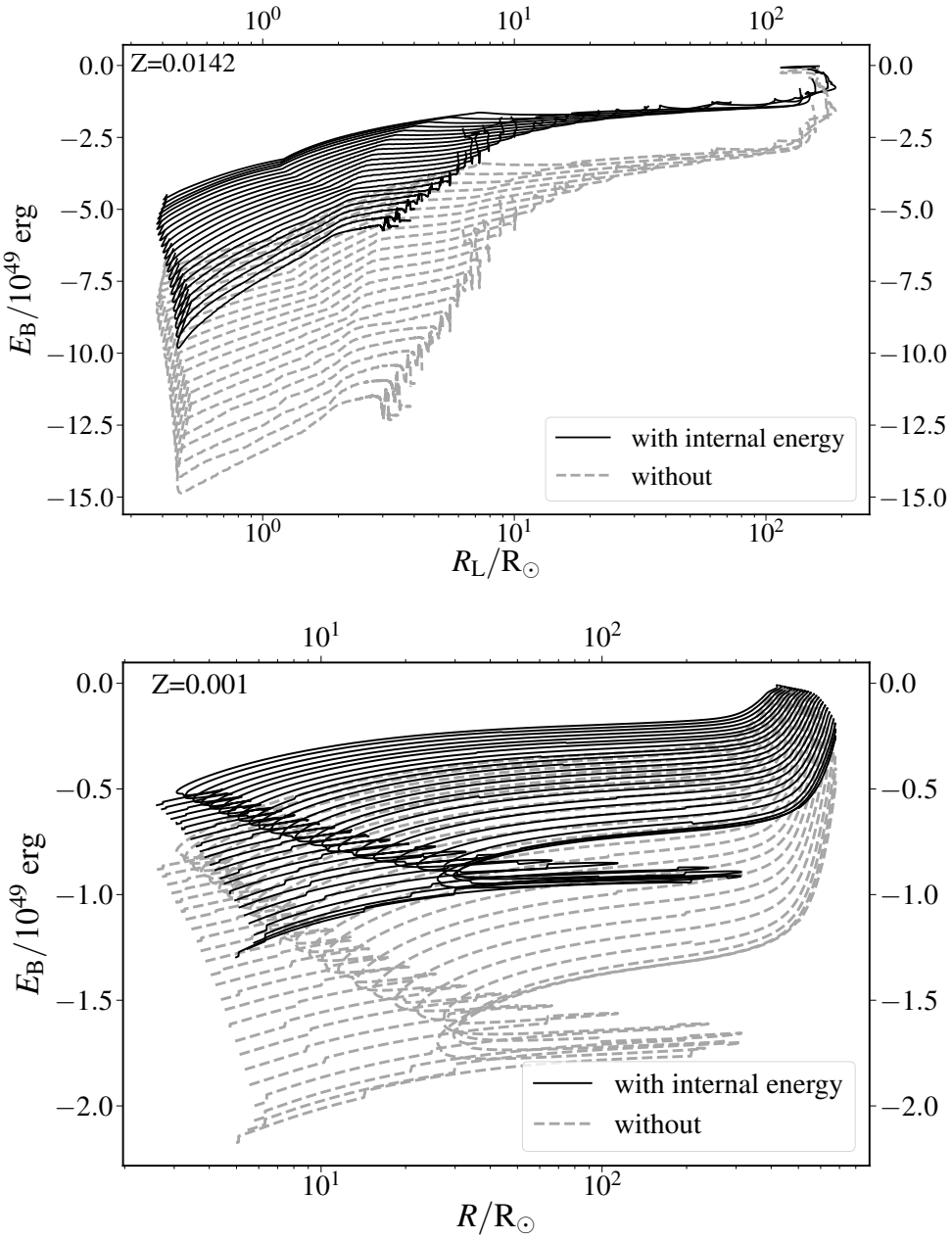

Fig. A.15: Binding energy of the hydrogen-rich envelope as a function of the radius after core helium depletion at solar (top) and lower (bottom) metallicity. Here, we compare the binding energy computed with and without the internal energy terms. On the top axis, we indicate the orbital separation at which a neutron star companion would be expected if the star would fill its Roche lobe.

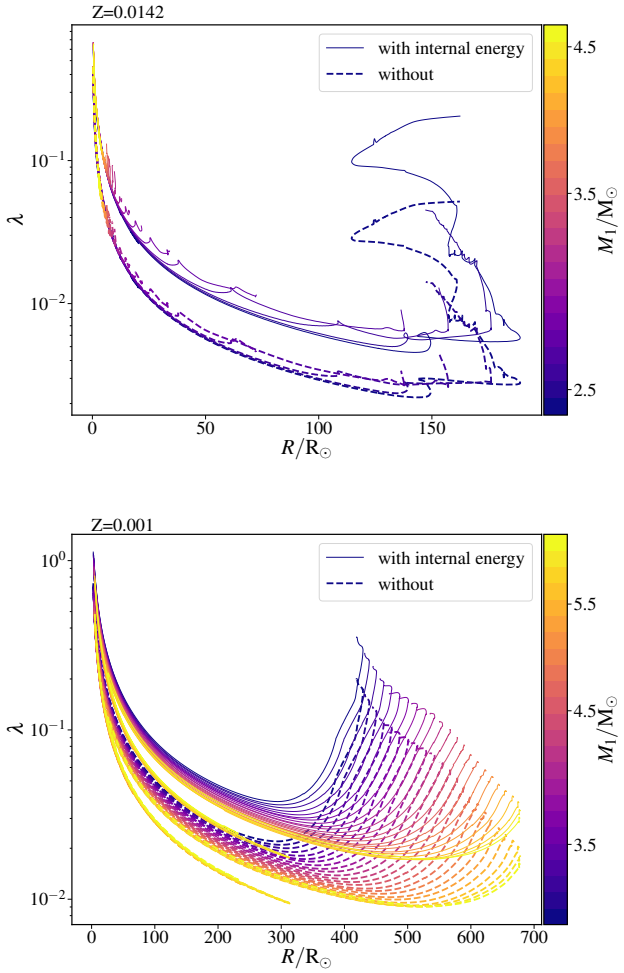

Fig. A.16: Envelope structure parameter λ as a function of the radius after core helium depletion at solar (top) and lower (bottom) metallicity. The dashed line indicates λ parameters computed using only the gravitational energy term for the binding energy.

with increasing initial mass.

At solar metallicity, only the lowest mass models have a hydrogen envelope shortly after core helium depletion before it disappears due to wind mass loss after about 30 kyr.

In contrast, at low metallicity, all models retain a hydrogen envelope. At the moment of the first radius expansion, the binding energy of the H-envelope drops before increasing shortly, and decreasing again, while that of the H + He envelope increases, and later decreases. This is consistent with the double-mirror effect.

Table A.2: Parameters of the solar metallicity (Z=0.0142) models.

$M_{\rm i}$/ ($M_\odot$)	$M_{\rm a}$/ ($M_\odot$)	$M_{\rm b}$/ ($M_\odot$)	$M_{\rm f}$/ ($M_\odot$)	$M^{\rm f}_{\rm CO}$/ ($M_\odot$)	$M^{\rm a}_{\rm H}$/ ($10^{-2}M_\odot$)	$M^{\rm f}_{\rm H}$/ ($10^{-2}M_\odot$)	$R_{\rm min}$/ ($R_\odot$)	$R_{\rm b}$/ ($R_\odot$)	$R_{\rm C\,ign.}$/ ($R_\odot$)	$R_{\rm max}$/ ($R_\odot$)	$R_{\rm f}$/ ($R_\odot$)	$\log_{10}(T^{\rm f}_{\rm eff}/{\rm K})$	$\log_{10}(L_{\rm f}/L_\odot)$	$\log_{10}(\frac{g_{\rm f}}{[{\rm cm\cdot s^{-2}}]})$	$S_{\rm f}$
8.86	2.51	2.39	2.35	1.40	3.06	0.003	0.404	0.416	4.64	186	162	3.77	4.45	0.391	YSG
9.08	2.59	2.47	2.42	1.45	3.13	0.001	0.401	0.414	3.74	176	169	3.77	4.49	0.364	YSG
9.30	2.68	2.55	2.50	1.49	3.26	7.98e-05	0.397	0.410	3.22	155	153	3.79	4.50	0.468	YSG
9.52	2.77	2.63	2.57	1.53	3.37	4.78e-06	0.389	0.403	2.91	135	133	3.83	4.53	0.598	YSG
9.75	2.87	2.71	2.65	1.58	3.46	2.79e-07	0.384	0.399	2.69	65.9	65.9	4.00	4.59	1.22	BSG
9.99	2.97	2.80	2.74	1.63	3.57	8.80e-09	0.380	0.396	2.51	31.1	31.1	4.17	4.62	1.89	BSG
10.2	3.07	2.88	2.83	1.69	3.69	1.42e-10	0.380	0.397	2.37	20.7	20.5	4.27	4.65	2.27	BSG
10.5	3.19	2.98	2.92	1.75	3.84	4.00e-13	0.384	0.402	2.26	15.4	15.4	4.34	4.69	2.53	BSG
10.7	3.30	3.07	3.02	1.82	3.94	1.45e-16	0.390	0.409	2.16	12.7	12.7	4.39	4.72	2.71	BSG
11.0	3.43	3.17	3.12	1.88	4.02	6.61e-20	0.396	0.417	2.07	10.4	10.4	4.44	4.74	2.90	BSG
11.3	3.55	3.28	3.22	1.95	4.14	6.05e-25	0.402	0.425	2.00	8.87	8.87	4.48	4.76	3.05	BSG
11.5	3.68	3.38	3.32	2.02	4.29	1.35e-22	0.408	0.433	1.92	7.77	7.64	4.51	4.76	3.19	WR
11.8	3.81	3.48	3.43	2.10	4.43	1.52e-22	0.414	0.441	1.87	7.19	7.12	4.54	4.81	3.27	WR
12.1	3.95	3.59	3.54	2.19	4.56	2.55e-21	0.419	0.449	1.80	6.83	6.80	4.56	4.84	3.32	WR
12.4	4.10	3.70	3.65	2.27	4.66	1.16e-23	0.424	0.457	1.76	6.31	6.30	4.58	4.86	3.40	WR
12.7	4.24	3.82	3.76	2.36	4.80	1.4e-24	0.429	0.465	1.69	5.89	5.83	4.60	4.88	3.48	WR
13.0	4.39	3.93	3.88	2.45	4.93	1.37e-22	0.434	0.473	1.64	5.46	5.41	4.62	4.90	3.56	WR
13.3	4.55	4.05	4.00	2.55	5.04	1.11e-24	0.439	0.481	1.59	5.07	5.07	4.64	4.93	3.63	WR
13.6	4.71	4.17	4.12	2.65	5.18	1.74e-22	0.443	0.489	1.55	4.62	4.62	4.67	4.95	3.72	WR
14.0	4.88	4.29	4.24	2.75	5.30	1.15e-22	0.448	0.497	1.51	4.18	4.18	4.69	4.97	3.82	WR
14.3	5.05	4.42	4.37	2.85	5.39	5.09e-31	0.451	0.505	1.46	3.97	3.79	4.72	5.00	3.92	WR
14.6	5.23	4.54	4.49	2.97	5.54	9.49e-32	0.455	0.513	1.41	4.43	3.44	4.75	5.02	4.02	WR
15.0	5.41	4.67	4.62	3.09	5.65	3.3e-28	0.458	0.521	1.35	3.26	3.13	4.77	5.04	4.11	WR

Table A.3: Parameters of the low metallicity (Z=0.001) models.

M_i/ ($M_\odot$)	M_a/ ($M_\odot$)	M_b/ ($M_\odot$)	M_f/ ($M_\odot$)	M^f_{CO}/ ($M_\odot$)	M^a_H/ ($10^{-2}M_\odot$)	M^f_H/ ($10^{-2}M_\odot$)	R_{min}/ ($R_\odot$)	R_b/ ($R_\odot$)	R_p/ ($R_\odot$)	Δt_p/ (kyr)	$R_{C\,ign.}$/ ($R_\odot$)	R_{max}/ ($R_\odot$)	R_f/ ($R_\odot$)	$\log_{10}(\frac{T^f_{eff}}{K})$	$\log_{10}(\frac{L_f}{L_\odot})$	$\log_{10}(\frac{g_f}{[cm\cdot s^{-2}]})$	S_f
8.86	3.11	3.10	3.08	1.70	13.6	9.80	1.38	2.72	4.79	68.3	391	439	432	3.61	4.67	-0.345	RSG
9.08	3.22	3.21	3.18	1.76	14.2	10.2	1.43	2.83	5.2	61.9	402	451	445	3.61	4.70	-0.357	RSG
9.30	3.32	3.32	3.29	1.82	14.6	10.5	1.47	2.93	5.58	56.6	413	462	456	3.61	4.72	-0.364	RSG
9.52	3.43	3.43	3.4	1.88	15.1	11.0	1.52	3.06	6.08	51.5	426	475	463	3.61	4.74	-0.361	RSG
9.75	3.55	3.54	3.51	1.95	15.7	11.4	1.57	3.20	6.68	47.1	437	488	471	3.61	4.75	-0.363	RSG
9.99	3.66	3.66	3.63	2.02	16.2	11.7	1.62	3.29	7.23	43.0	450	501	487	3.61	4.78	-0.377	RSG
10.2	3.79	3.78	3.75	2.10	16.8	12.2	1.68	3.46	8.05	39.2	462	515	507	3.61	4.82	-0.397	RSG
10.5	3.91	3.90	3.88	2.18	17.3	12.6	1.73	3.61	8.95	36.1	475	530	515	3.61	4.83	-0.397	RSG
10.7	4.04	4.03	4.00	2.27	17.8	13.0	1.78	3.72	9.83	33.0	488	543	536	3.61	4.87	-0.417	RSG
11.0	4.17	4.16	4.14	2.36	18.5	13.4	1.83	3.87	11.1	30.3	502	555	551	3.61	4.89	-0.427	RSG
11.3	4.32	4.31	4.28	2.47	19.1	13.9	1.90	4.05	12.8	27.7	516	567	567	3.61	4.92	-0.439	RSG
11.5	4.46	4.45	4.42	2.57	19.8	14.4	1.95	4.21	14.8	25.5	529	579	579	3.62	4.94	-0.442	RSG
11.8	4.61	4.60	4.57	2.68	20.4	14.8	2.01	4.40	17.5	23.4	543	590	590	3.62	4.96	-0.444	RSG
12.1	4.76	4.74	4.72	2.79	21.1	15.2	2.07	4.54	20.4	21.7	556	601	601	3.62	4.98	-0.446	RSG
12.4	4.92	4.91	4.88	2.9	21.9	15.7	2.13	4.74	25.5	19.9	570	612	612	3.62	5.00	-0.447	RSG
12.7	5.09	5.07	5.04	3.04	22.6	16.2	2.20	4.95	32.7	18.3	584	624	624	3.62	5.02	-0.449	RSG
13.0	5.25	5.23	5.20	3.16	23.4	16.7	2.26	5.13	43.4	17.0	598	635	635	3.62	5.04	-0.451	RSG
13.3	5.43	5.41	5.38	3.3	24.3	17.0	2.32	5.35	66.1	15.6	610	645	645	3.62	5.06	-0.451	RSG
13.6	5.61	5.59	5.56	3.44	25.0	17.4	2.38	5.56	113	14.4	623	656	656	3.62	5.08	-0.451	RSG
14.0	5.80	5.77	5.74	3.58	25.9	17.9	2.46	5.80	238	13.3	635	668	667	3.62	5.10	-0.452	RSG
14.3	5.98	5.95	5.92	3.73	26.4	18.0	2.46	5.77	312	12.4	644	676	676	3.63	5.12	-0.449	RSG
14.6	6.14	6.11	6.07	3.87	26.4	17.6	2.41	5.47	311	11.5	644	678	678	3.63	5.14	-0.441	RSG
15.0	6.30	6.27	6.24	4.02	26.0	17.1	2.28	4.98	232	10.7	638	678	677	3.63	5.15	-0.428	RSG

Different to the core: the pre-supernova structures of massive single and binary-stripped stars

B

B.1 Impact of the nuclear network

Toward the end of the evolution of massive stars, the core is composed by a multitude of synthesized isotopes, many of which are short-lived and neutron-rich. The properties of the stellar core are sensitive to weak interaction processes that can only be accounted for by tracking the many electron and positron captures, and β-decays from rare and unstable isotopes. This usually requires the quasi-statistical nuclear equilibrium approximation approach (Hix & Thielemann 1996) or to keep track of a large number of isotopes in the nuclear network (e.g., Farmer et al. 2016). In this work, we present simulations where we simultaneously solve for the structure and nuclear burning using with a large nuclear network of 128 isotopes. Farmer et al. (2016) showed that a nuclear network with at least 127 isotopes is required to obtain resolved core structures after the end of core oxygen burning. This is what we adopt in our models. For the prior evolution up to and including central oxygen burning, we employ an α-chain nuclear network containing 21 isotopes, which is considered adequate to capture the energy generation rate during earlier nuclear burning phases. However, the accuracy of an α-chain network decreases with the evolution, especially during core oxygen burning (see, e.g., Renzo 2015).

Here, we test the impact of computing the evolution of stars from birth to core oxygen depletion with a nuclear network that contains 128 isotopes compared to our default setup. We perform this test for two stellar models (1) the single star model with an initial mass of $16\,M_\odot$ (2) a binary-stripped model with an initial mass of $20\,M_\odot$. Both models reach almost exactly the same core mass of 6.3 $M_\odot$ at the end of core helium burning. In Figure B.1, we compare these models on the central density-central temperature space. Until central carbon depletion, the models have almost exactly the same evolution independently from the size of the nuclear networks. However, after this moment, differences start to appear. The models with a larger network reach higher densities. This is true for both the single and the binary-stripped star model. After this moment, differences in the binary-stripped model become more prominent.

The central temperatures and densities between the models do vary with the use of a larger nuclear network in the late evolutionary phases. However, the relative differences between the single and binary-stripped stellar models remain similar.

In Figure B.2, we show the evolution of the electron fraction Y_e for the same models with and without a large nuclear network from the beginning of the simulation. Generally,

the evolution is similar between all models, and final values agree within 2%. The largest difference can be observed after core oxygen depletion, where both the single and binary-stripped models with a large nuclear network from the start display smaller values than the alternate models.

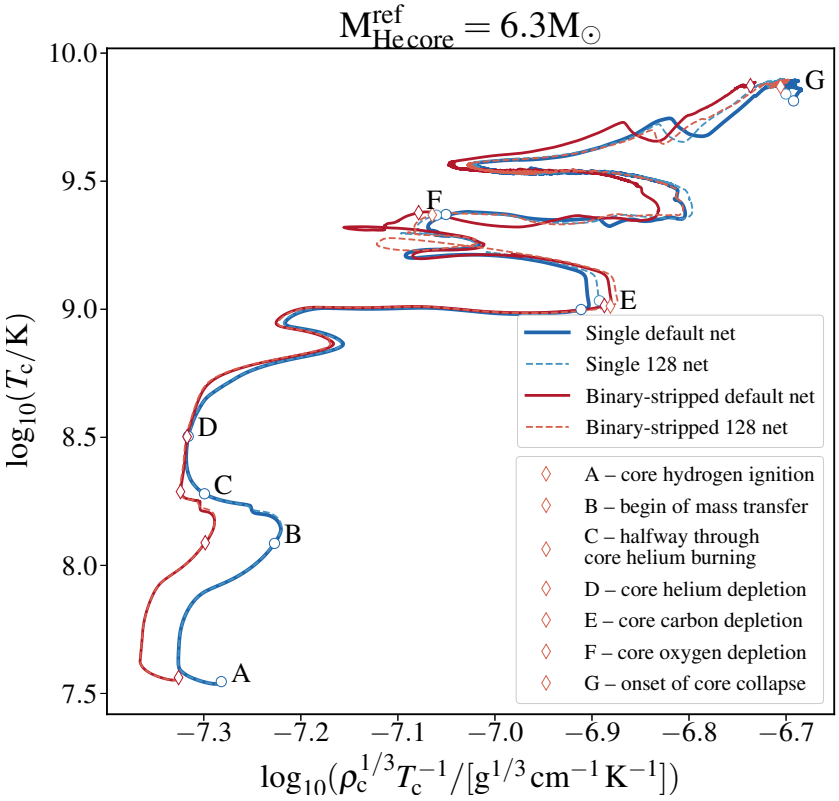

Fig. B.1: Comparison on the central temperature, central density plane between using a large nuclear network with 128 isotopes throughout the evolution and switching from a nuclear network with 21 isotopes to a nuclear network with 128 isotopes after core oxygen depletion. To better show the differences between the models, we have re-scaled the horizontal axis by the dependence expected for homologous contraction of an ideal gas.

We conclude that models with larger nuclear networks throughout the evolution, though expensive, are desirable for the future, but we expect that our conclusions about the relative differences between single and binary-stripped star models are not significantly affected.

B.2 Reference core mass

Giving an exact definition of the boundary between the core and the envelope of a star is not trivial and varies between different studies (Sukhbold & Woosley 2014). That is because,

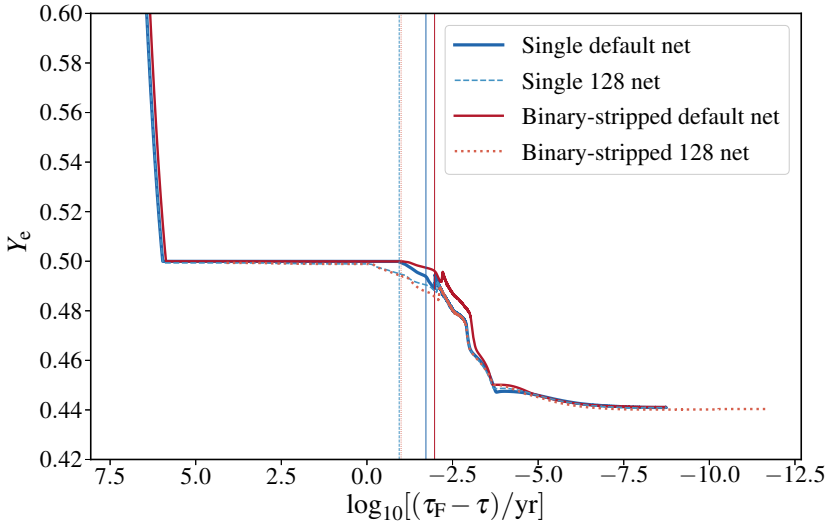

Fig. B.2: Comparison of the electron fraction Y_e evolution between using a large nuclear network with 128 isotopes throughout the evolution and switching from a nuclear network with 21 isotopes to a nuclear network with 128 isotopes after core oxygen depletion. Vertical lines mark the moment of core oxygen depletion for each model, which is when the switch between networks occurs for the models with the default network.

while a drop in density of several orders of magnitude, together with a larger change in composition, can typically be observed between the edge of the inner core and the envelope, there is a gradient in composition and density at this edge that make it difficult to define an exact boundary. In addition, details of semi-convection and core overshoot can have a large effect on the stellar core mass and on the core edge and complicate this definition even further (e.g., Schootemeijer et al. 2019). For this study, we compare the late properties of stellar models as a function of their reference core mass, which we define as the mass of the helium core (i.e., the mass coordinate where the mass fraction of hydrogen decreases below 0.01) at the moment of core helium depletion (when the central mass fraction of helium decreases below 10^{-4}). Here, we investigate the impact of this definition on our conclusions. We discuss the sensitivity to the evolutionary stage for which we define the reference core mass in Section B.2.1 and to the exact choice of the helium core mass boundary in Section B.2.2.

B.2.1 Evolution of the helium core mass

In Fig. B.3, we present the reference core mass as a function of initial mass for both single and binary models. We verify that donor stars in early case B mass-transfer binaries have systematically less massive cores at the end of their lives than single stars with the same initial mass (cf. Podsiadlowski et al. 1992). For both the single and binary-stripped models, the reference core mass increases as a function of initial mass. The highest-mass single star models deviate from the linear trend due to mass loss.

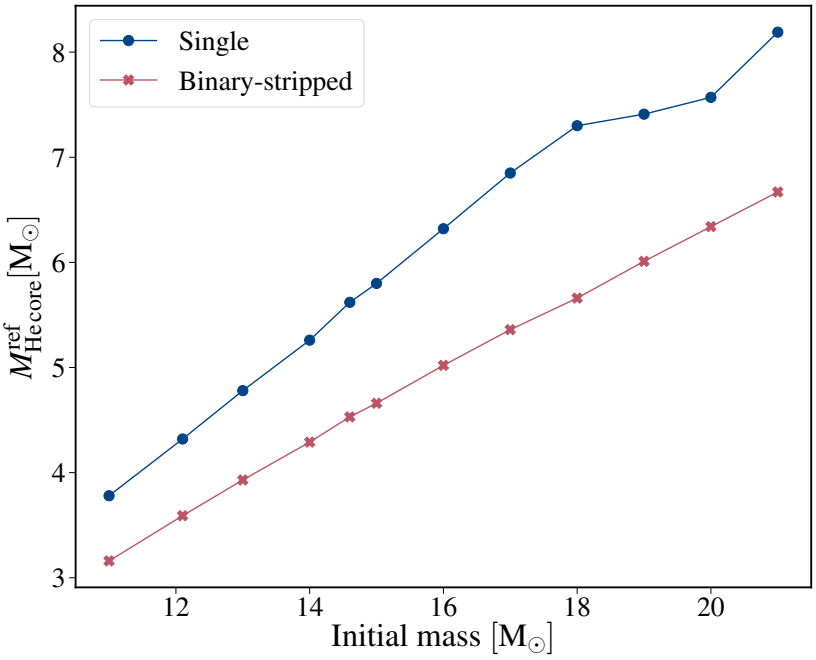

Fig. B.3: Helium core mass at core helium depletion as a function of initial mass for single stars and star that were stripped due to Roche-lobe overflow in a binary system during the hydrogen shell burning phase.

We present the evolution of the helium core mass as a function of time for all of the single (full lines) and binary-stripped (dashed lines) models in Fig. B.4. We indicate the initial mass of the models with colors and mark key evolutionary steps with symbols. All single star models show the same trend of an increasing helium core mass with time. In contrast, the helium core mass of binary-stripped star models first increases, then reaches a plateau, and then decrease towards the end of their life. This is because single stars undergo hydrogen shell burning, which leads to an increase of about 1 $M_\odot$ in helium core mass from the beginning of core helium burning onward (circles in Fig. B.4) until core oxygen depletion (squares in Fig. B.4). In contrast, binary-stripped stars at this metallicity stop hydrogen shell-burning shortly after mass transfer. Eventually most of their hydrogen-rich envelope is removed due to the solar-metallicity wind mass loss rate assumed here (we discuss the impact of the wind mass loss rate in Appendix B.4). For lower-metallicity stars, a hydrogen-rich layer is retained because the stripping process is less effective (Götberg et al. 2017; Yoon et al. 2017; Laplace et al. 2020). Halfway through core helium burning (central helium fraction < 0.5, indicated by star markers in Fig. B.4), the helium core mass of the binary-stripped stars reaches a plateau for all masses considered. For all the binary-stripped models, this happens after the end of mass transfer (triangle markers in Fig. B.4). At this moment, hydrogen shell burning stops, and only a small hydrogen layer remains on the stellar surface. Soon after, the helium

core mass begins to decrease for all models due to the effect of winds that remove the outer layers. This effect is mass dependent (cf. Langer 1989a). For the stellar wind mass loss rate we assume in this study, the decrease in mass due to wind mass loss in binary-stripped stars ranges from 0.1 $M_\odot$ for the lowest-mass model (with an initial mass of 11 $M_\odot$) to 1.2 $M_\odot$ for the highest-mass model (with an initial mass of 21 $M_\odot$).

After core helium depletion, the lifetime of stars is so short that winds have a negligible impact on the helium core mass, as shown by the overlapping markers after this moment (diamonds, squares, and crosses in B.4). The strongest effect we observe is a decrease of the helium core mass by 0.1 $M_\odot$ for the highest-mass binary-stripped star model.

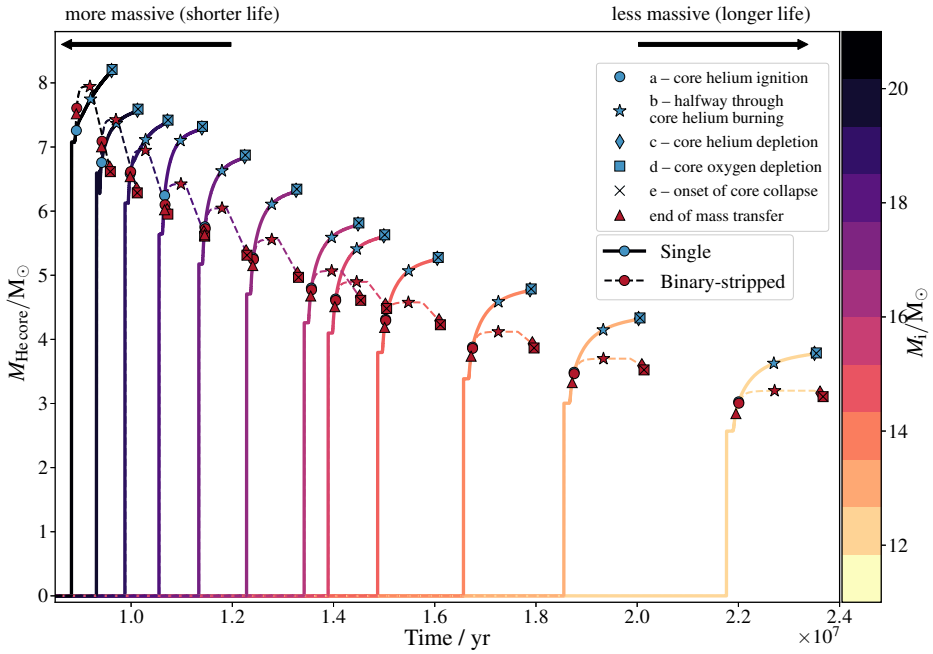

Fig. B.4: Evolution of the helium core mass of every model as a function of time. Full lines correspond to single stars and dashed lines to binary-stripped stars. Symbols indicate key evolutionary stages for the development of the helium core and colors give the initial mass of the stars. Because massive stars live shorter lives, the more massive models are located on the left side and the less massive models on the right side of the plot.

B.2.2 Helium core boundary

Various definitions are possible for the helium core mass, as illustrated in Fig. B.5. We discuss whether the choice of the core definition impacts our conclusions, in particular regarding structural differences between the helium cores of single and binary-stripped stars (see Section 3.4.5).

In Fig. B.5 we show the interior helium and hydrogen abundances of an example single star model with an initial mass of 20 $M_\odot$ at core helium depletion. Our definition of the helium core mass (1) is shown as the mass coordinate where the hydrogen mass fraction $X_H < 0.01$ and the helium mass fraction $X_{He} > 0.1$ and corresponds to the edge of the helium-rich region at 7.5 $M_\odot$. The definition employed in Sukhbold & Woosley (2014) is somewhat further out and corresponds to the mass where $X_H < 0.2$ (2). The definition where $X_{He} > 0.5$ leads to an even higher helium core mass and coincides with the beginning of a helium-enriched layer due to hydrogen-shell burning (corresponding to the peak of the nuclear energy generation rate around 7.6 $M_\odot$). Another possible definition is the mass coordinate where the mass fraction of hydrogen is strictly larger than the mass fraction of helium (4). This boundary is however set outside the hydrogen-burning shell and does therefore not follow the growth of the helium-rich core due to shell burning.

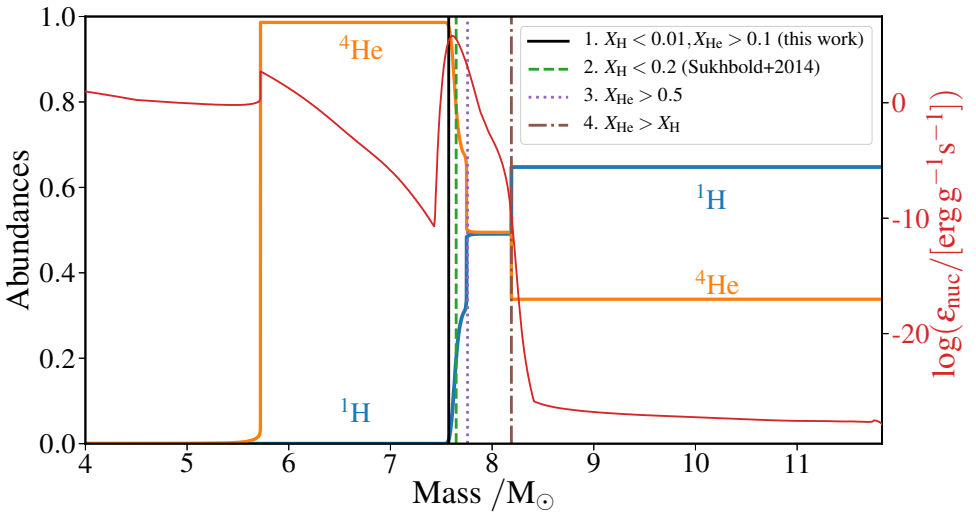

Fig. B.5: Mass fraction of ^{1}H (blue line) and ^{4}He (orange line) as a function of mass coordinate for an example single star model with an initial mass of 20 $M_\odot$ at core helium depletion. Vertical lines mark different choices of the helium core mass definition. In red, we indicate the specific nuclear energy generation rate throughout the model. The first peak in the nuclear energy generation rate around 5.8 $M_\odot$ corresponds to helium shell-burning and the second peak around 7.6 $M_\odot$ to hydrogen shell-burning.

We show how the radius of the helium core changes when we change the definition of the helium core mass boundary in Fig. B.6. The figure presents the radial coordinate of each stellar model (top: single, bottom: binary-stripped) as a function of the initial stellar mass. Every model in our grid is shown as a rectangle whose height corresponds to the surface radius of the model. The width of every rectangle is set as 1 $M_\odot$. We indicate the mass fraction of helium at each radius coordinate by color shading it. For the binary-stripped models at this metallicity, all helium core definitions correspond to the surface of the star and are thus

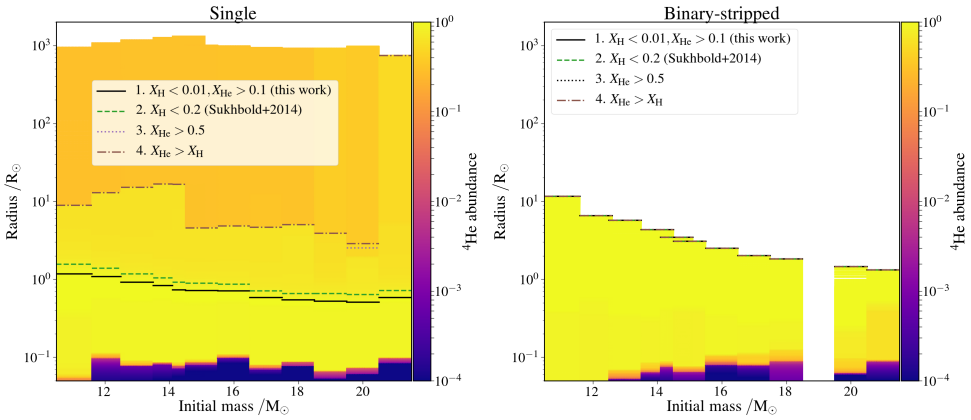

Fig. B.6: Radial coordinate as a function of the initial mass for the single star models (*left*) and the binary-stripped star models (*right*) at the onset of core collapse. Colors indicate the mass fraction of ^{4}He at each radial coordinate. Four different helium core mass definitions are indicated with horizontal lines.

identical. The choice of the helium core boundary is thus only relevant for the single-star models.

For the single star models, the helium core radius changes depending on the core boundary chosen. With definition 3, the boundary of the helium core corresponds to the boundary between the helium-rich region and the hydrogen-rich envelope for all models, except for the highest mass model. This is because for the highest-mass model, some helium has been mixed in the hydrogen-rich envelope. This means the core-mass definition is not consistent across all masses. Furthermore, this boundary lies above the hydrogen-burning shell and can therefore not account for the growth in core mass due to shell burning. The other two definitions give similar trends to each other. The definition 2 from (Sukhbold & Woosley 2014) results in systematically larger helium core radii, of about 0.5 $R_\odot$ larger than for definition 1. However, this difference is negligible compared with the difference to the helium core radii of the binary-stripped models. The helium core mass does not change significantly after core helium depletion, and our findings on the differences in helium core radii are robust against sensible variations of the core mass definition. We conclude that the reference core mass we have chosen is robust for our purpose.

B.3 All final composition diagrams

In Section 3.4, we discuss general trends in final chemical structure and compare single and binary-stripped star models with similar values of the reference core masses. In Fig. B.7, we present composition diagrams at the moment of core collapse for the full set of models. The figure is divided into two sets of two rows that contain single (top) and binary-stripped

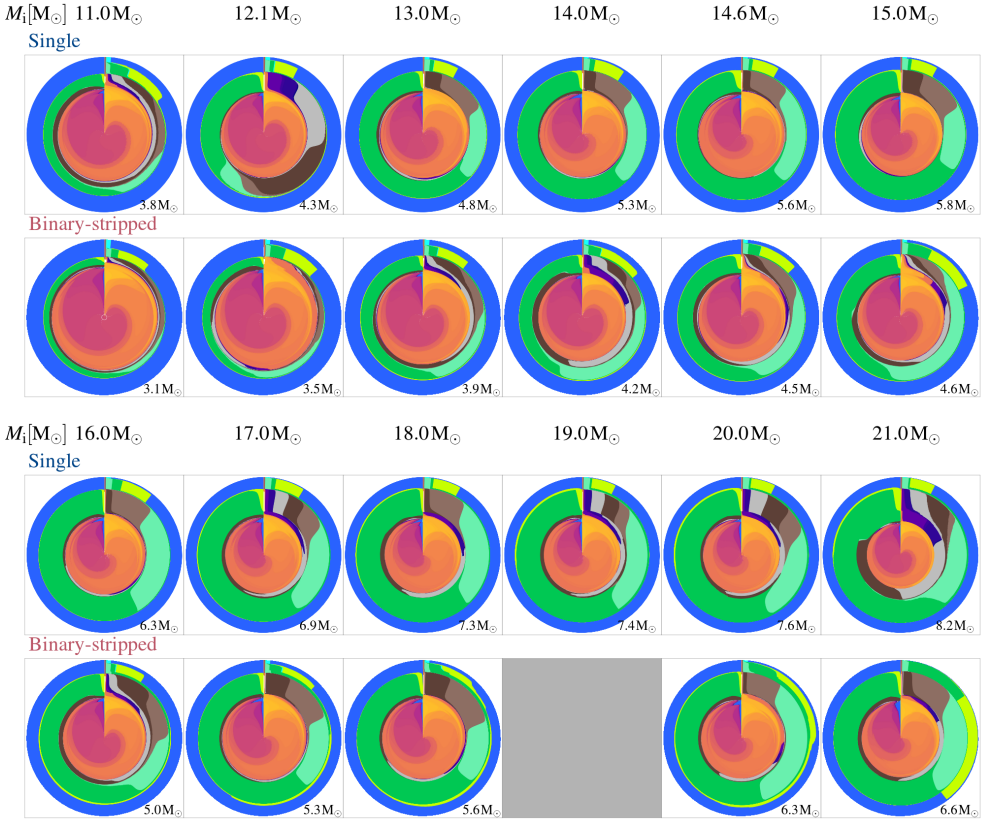

Fig. B.7: Composition diagrams showing the core composition interior to the helium core at the onset of core collapse for the entire grid of models. The two pairs of rows show single and binary-stripped star models with the same initial masses. All models are scaled such that the radius of the diagram is proportional to the square root of the helium core mass (the helium core mass is indicated at the bottom of each diagram). The binary-stripped model with an initial mass of 19 $M_\odot$ is not shown because it did not reach core collapse. Colors represent the same isotopes as in Fig. 3.2
.

(bottom) stellar models with the same initial masses. The binary-stripped model with an initial mass of 19 $M_\odot$ is not shown because it did not reach core collapse due to numerical issues. Below each model we indicate its reference core mass.

B.4 Effect of winds on the cores of binary-stripped stars

How much mass massive stars lose to winds is one of the biggest open question in stellar astrophysics (Smith 2014). The choice of stellar winds assumed for stellar evolution models greatly impacts the evolution of massive stars and in particular their core structure (Renzo et al. 2017). Stellar winds of binary-stripped stars are among of the most unconstrained (Götberg

et al. 2017; Vink 2017) and can have a large impact on their evolution, future interactions, and on their supernova properties (Yoon et al. 2010; Yoon 2015; Gilkis et al. 2019), though efforts are being made to better constrain these with new-generation stellar atmosphere models (e.g., Sander & Vink 2020). Here, we investigate the effect of changing the adopted wind mass loss rate for binary-stripped stars on the core properties. To this end, we simulated two example models with initial masses of 11 and 20 $M_\odot$, at the extremes of the mass range we chose, and varied the wind mass loss rate by a constant factor after the end of mass-transfer.

We varied the wind mass loss rate from a factor 10 smaller to a factor three higher than the default wind mass loss rate. These values are motivated by the range of mass loss rates inferred from binary-stripped stars both through observations and from latest theoretical studies (Yoon et al. 2010; Yoon 2015; Vink 2017). In Table B.1, we give values for the surface properties and wind mass loss rates halfway through core helium burning (when the central mass fraction of helium decreases below 0.5). The values for the lowest wind mass loss rates (wind factors of 0.10 and 0.33) are similar to the solar-metallicity wind mass loss rate computed by Vink (2017) through Monte Carlo radiative transfer models. Our lowest mass model with an initial mass of 11 $M_\odot$ can be compared to observations of the quasi-WR star in the system HD 45166, which has a wind mass loss rate of $\log_{10} \dot{M}/(M_\odot\,\mathrm{yr}^{-1}) = -6.66$ and a luminosity of $\log_{10}(L/L_\odot) = 3.75 \pm 0.08$ (Groh et al. 2008). Though the luminosity of this star, and therefore its mass, is smaller than the luminosity of the model, its wind mass loss rate is similar to the mass loss rates we obtain when increasing the wind mass loss rate by a factor between 1.25 or 2. For the binary-stripped star model with an initial mass of 20 $M_\odot$, the values for the highest wind mass loss rates (wind factors 2 and 3) are similar to the wind mass loss rates derived from observations of WC/WO stars ($\log_{10} \dot{M}/(M_\odot\,\mathrm{yr}^{-1}) = -5$ for $\log_{10}(L/L_\odot) = 5$, Tramper et al. 2016).

Varying the wind mass loss rate factor has a systematic impact on the stellar structure. The total mass of the binary-stripped star, and with it its density profile in the outer layers at core helium depletion, strongly depends on the wind mass loss rate, as shown in Fig. B.8. In the top panel of Fig. B.8, we show the models with an initial mass of 11 $M_\odot$, and in the bottom panel, the models with an initial mass of 20 $M_\odot$. Independently of the initial mass, we find that models with increased wind mass loss rates have more centrally concentrated density profiles, a lower mass core and a lower total mass. In contrast, models with decreased wind mass loss rates have higher total masses and achieve smaller densities at the surface. The models with the smallest wind mass loss rates have density profiles with a similar shape as for the single-star profiles because they retain a hydrogen-rich layer above the helium core. The 20 $M_\odot$ binary-stripped model (bottom panel of Fig. B.8) with the lowest wind mass loss rate achieves a helium core mass that is larger than that of the single star model with the same initial mass.

In Fig. B.9 we show that the central mass fraction of ^{12}C and ^{16}O at the moment of core helium depletion is also systematically affected by a changing wind mass loss rate. The higher the wind mass loss, the lower (higher) the central mass fraction of ^{12}C (^{16}O). For models with low wind mass loss rates, we find a more pronounced effect on the central mass fraction.

Table B.1: The effect of a modified wind mass loss factor after mass transfer on the stellar properties of binary-stripped stars, taken halfway through central helium burning (defined as the moment when $X_{\rm He} = 0.5$).

Wind factor	M_* ($M_\odot$)	$\log_{10}$ ($T_{\rm eff}$/K)	$\log_{10}$ ($L/L_\odot$)	$\log_{10}$ ($\dot{M}/[M_\odot\,{\rm yr}^{-1}]$)
Binary-stripped star model: $M_i = 11\,{\rm M}_\odot$				
0.10	3.50	4.84	4.19	-7.79
0.33	3.46	4.85	4.17	-7.28
0.50	3.43	4.85	4.15	-7.11
0.75	3.39	4.86	4.14	-6.94
1.00	3.36	4.86	4.12	-6.82
1.25	3.32	4.87	4.11	-6.73
2.00	3.22	4.89	4.08	-6.52
3.00	3.08	4.92	4.03	-6.27
Binary-stripped star model: $M_i = 20\,{\rm M}_\odot$				
0.10	8.10	4.92	5.04	-6.68
0.33	7.94	4.95	5.02	-6.17
0.50	7.84	4.97	5.00	-5.98
0.75	7.68	4.99	4.99	-5.80
1.00	7.52	5.02	4.97	-5.62
1.25	7.34	5.04	4.95	-5.46
2.00	6.81	5.03	4.88	-5.34
3.00	6.22	5.02	4.80	-5.27

The wind mass loss rate affects the extent of the carbon-rich gradient above the helium-depleted core, as we show in the composition profiles in Fig. B.10. Models with high wind mass loss rates have a more extended carbon-rich layer. This can be understood as the consequence of a more pronounced retreat in mass of the convective core during central helium burning (see also 3.5.1), that leaves helium burning products behind. Even for lower wind mass loss rates, the carbon-rich layer is still present in the binary-stripped stars and more extended than for single-star models. Models with reduced wind mass loss rates retain a hydrogen-rich layer (as shown by the dashed lines in Fig. B.10).

For the example binary-stripped star model with an initial mass of $20\,{\rm M}_\odot$, the effect of winds is more pronounced than for the $11\,{\rm M}_\odot$ model, due to the indirect mass dependence of winds. In the two models with the highest wind mass loss rates (a factor two and three larger, respectively), the winds are so strong that even the helium-rich layer is removed, and the carbon-rich layer reaches the surface of the star (indicated with a circle in the bottom panel of Fig. B.10). Observationally, such stars would likely be observed as carbon- or oxygen-rich Wolf-Rayet stars (type WC/WO) and a supernova resulting from such stars would most likely be of type Ic.

We conclude that variations of the wind mass loss rate have a systematic effect on the core structure of binary-stripped stars. The extent of the carbon-rich layer above the helium-depleted core strongly depends on the wind mass loss rate. However, the mass extent of the carbon-rich layer and the central fraction of carbon remains larger for binary-stripped star

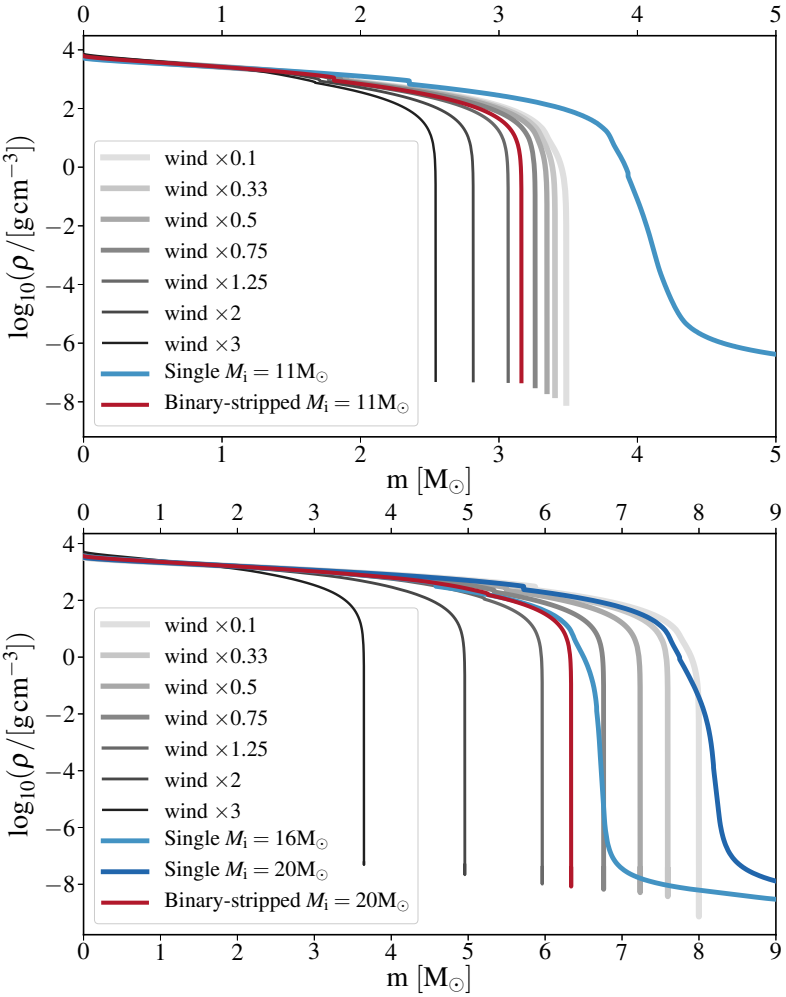

Fig. B.8: Impact of wind variations on the density profiles of binary-stripped stars. We show the profiles at the moment of core helium depletion for a single (blue) and binary-stripped (red) star model with the same initial mass of 11 $M_\odot$ (*top panel*) and 20 $M_\odot$ (*bottom panel*). Grey lines show variations of the density profile for the binary-stripped star when we vary the wind mass-loss rate after Roche-lobe overflow by the factor indicated in the legend.

models than for single-star models with the same initial mass, even for the lowest wind mass loss rates (a factor 10 weaker, and similar to the wind mass loss inferred by Vink 2017).

B.5 Shell mergers

About half of the models in our grid experience the merging of silicon-burning shells with oxygen-rich layers (e.g., Couch & Ott 2013; Yoshida et al. 2019; Andrassy et al. 2020; Fields

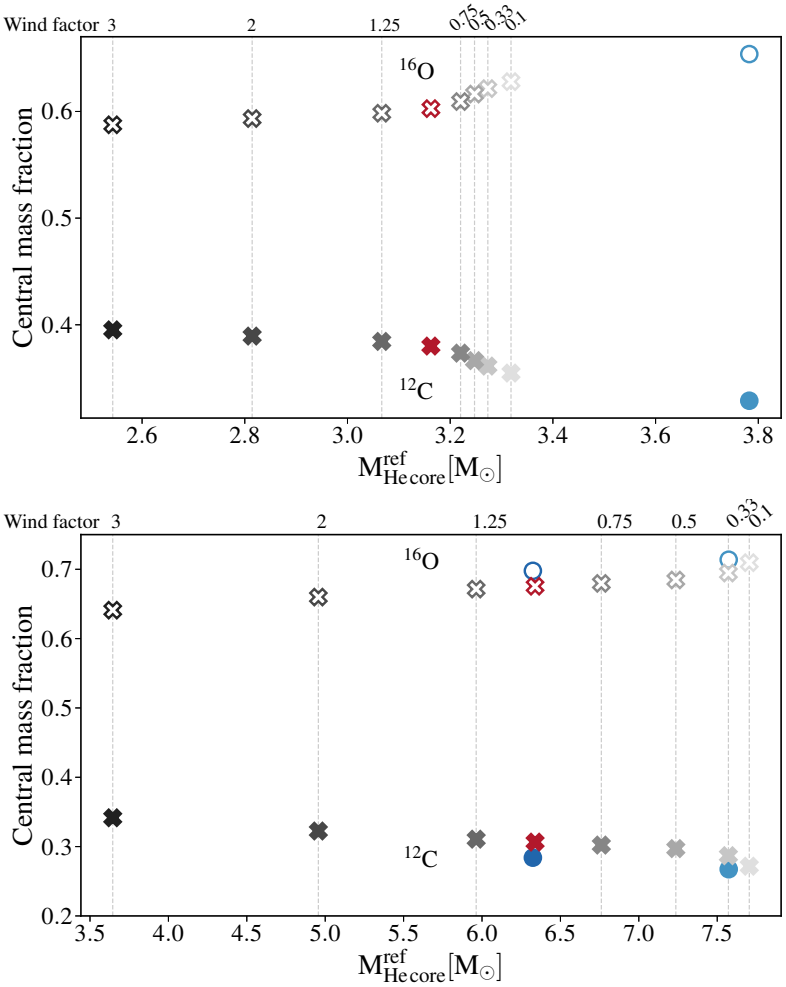

Fig. B.9: Impact of binary-stripped star wind variations on the central mass fractions at the moment of core helium depletion. Open and filled crosses indicate the central mass fractions of ^{12}C and ^{16}O, respectively. Grey crosses show variations for binary-stripped star models when we decrease the strength of the winds after Roche-lobe overflow by a constant factor indicated on top of the vertical lines. For reference, we show a single (light blue) and binary-stripped (red) star model with the same initial mass of 11 $M_\odot$ (*top panel*) and 20 $M_\odot$ (*bottom panel*). In the bottom panel, we also compare the binary-stripped star models to a single star model with the same reference core mass of 6.3 $M_\odot$ with an initial mass of 16 $M_\odot$.

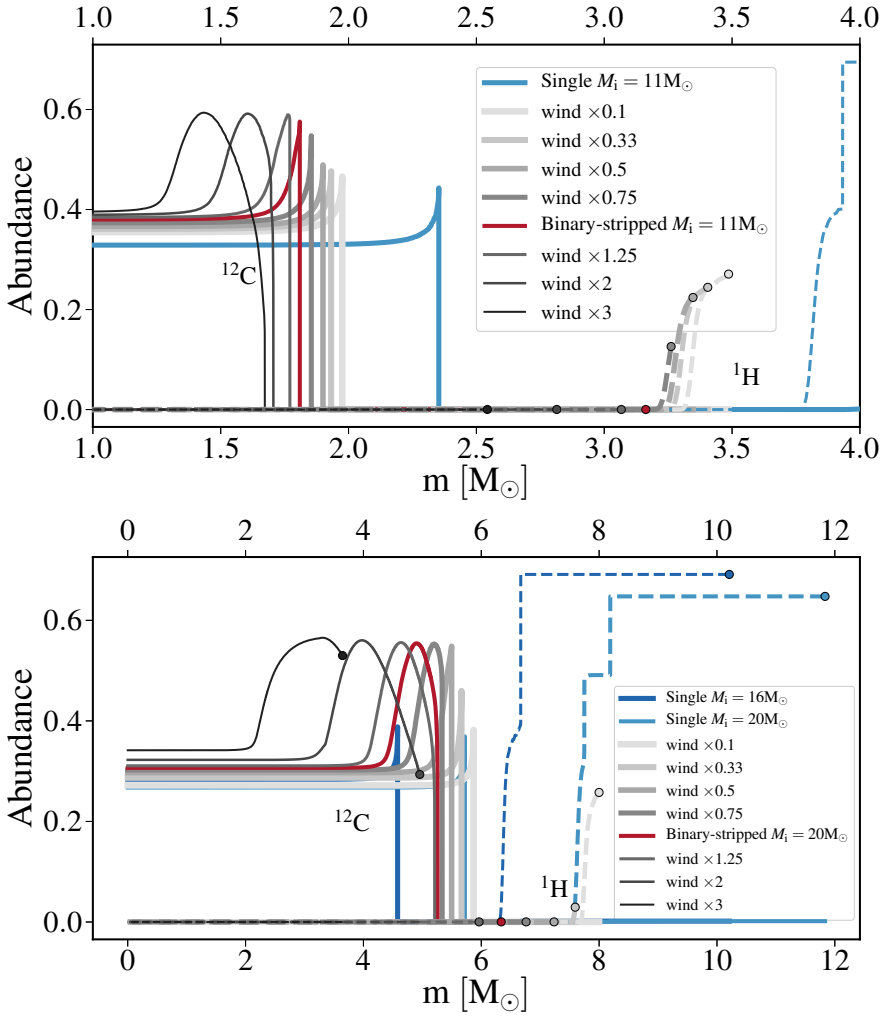

Fig. B.10: Impact of binary-stripped star wind variations on the composition profiles at the moment of core helium depletion as a function of the mass coordinate. We show our reference single (blue) and binary-stripped (red) star models with the same initial masses of 11 $M_\odot$ (*top panel*) and 20 $M_\odot$ (*bottom panel*). In gray, we show how the profiles of the binary-stripped star models change when we vary the wind mass loss rates by the factor indicated in the legend. Dashed and full lines indicate the mass fractions of ^{1}H and ^{12}C, respectively. The mass extent of the carbon-rich layer increases with higher wind mass loss rates. The surface of the stellar models is indicated with a colored circle. In the top panel, we limit the mass range for clarity, and do not show the entire hydrogen layer of the single star model.

& Couch 2020). They occur in both single and binary-stripped models. In this section, we discuss how these shell mergers arise and how the composition is modified. To this end, we focus on an example model, the single star model with an initial mass of 11 $M_\odot$.

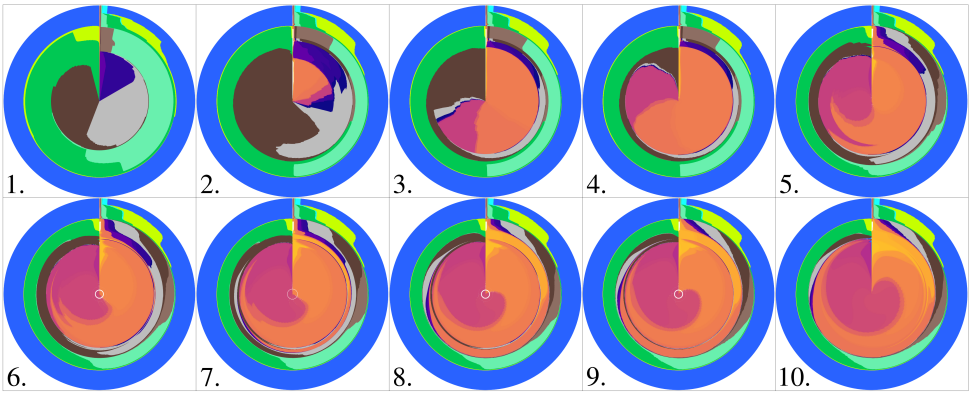

Fig. B.11: Evolution of the interior composition structure of an example single star model with an initial mass of 11 $M_\odot$ after core oxygen depletion. From diagram 1 to 3 core silicon burning occurs, leading to the creation of ^{54}Fe. The silicon-burning shell of the star merges with the oxygen-rich layers above between point 4 and 5, leading to the creation of ^{28}Si, ^{32}S, ^{36}Ar, ^{40}Ca, and ^{54}Fe in the oxygen-rich layer. From point 6 to 9, the outer layers of the silicon-rich region turn into iron-group elements.

In Fig. B.11, we show the evolution of the composition structure at selected points in the evolution. The star burns silicon in a convective core (labels 1 to 3 in Fig. B.11), before igniting silicon in a convective shell (label 4 in Fig. B.11). Shortly after the ignition of this shell, the burning shell moves upwards in mass coordinate. It then reaches the oxygen-rich region above and becomes mixed in (labels 4 to 5 in Fig. B.11). The merger leads to a more luminous and extended burning of silicon. Because silicon now burns in a different composition environment, different branching rates of the burning reactions occur. The ingestion of oxygen helps boost alpha-chain reactions and leads to an increased abundance of ^{28}Si, ^{32}S, ^{36}Ar, ^{40}Ca, and ^{54}Fe in the oxygen-rich layer. From point 6 to 9, the silicon-rich outer layers turn into iron-group elements.

B.6 Kippenhahn diagrams

For completeness, we show the Kippenhahn diagrams for our single and binary-stripped star models with initial masses of 11 $M_\odot$ in this section.

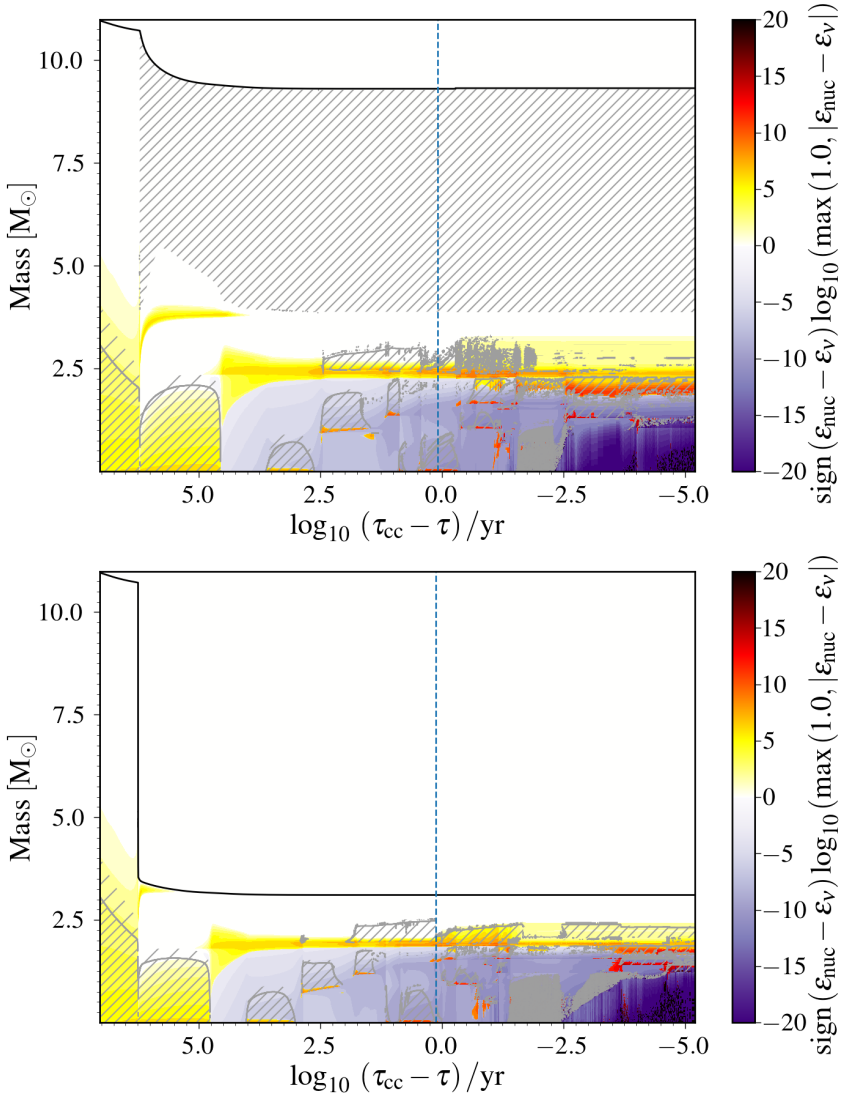

Fig. B.12: Kippenhahn diagrams: These figures show the evolution of the interior stellar structures of the single (top) and binary-stripped star (bottom) models with initial masses of 11 $M_\odot$ as a function of time until core collapse. Single and double hatching indicate overshooting and convection, respectively. The colors mark the difference between the specific energy generation rate $\epsilon_{\rm nuc}$ and the specific energy lost due to neutrino emission ϵ_ν. For each model, a blue vertical dashed line marks the moment when we switch to a nuclear network of 128 isotopes.

C

BINARY-STRIPPED STARS AS CORE-COLLAPSE SUPERNOVAE PROGENITORS

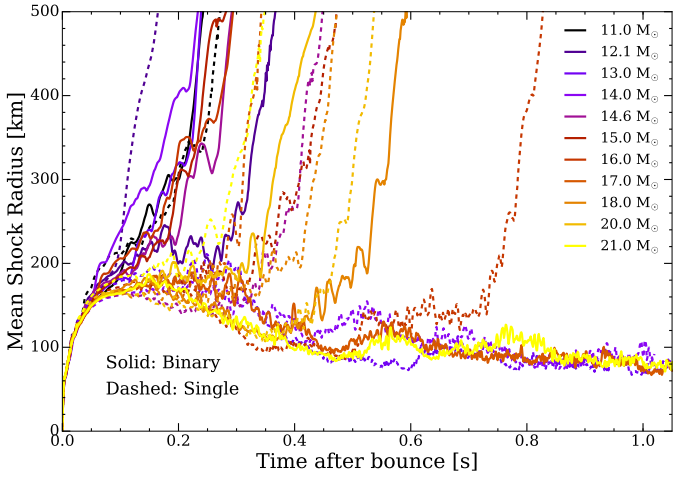

Fig. C.1: Mean shock radii (km) for the 11 pairs of models studied as a function of time after bounce (s). The single-star models are illustrated with solid lines, and the binary-stripped models with dashed lines. All but 4 models explode, and the explosions occur within 100-800 ms post-bounce. Note that even the non-exploding models feature a bump in the shock radii after 500 ms, corresponding to the accretion of the Si/O interface.

In the text, we highlighted the 14-$M_\odot$ progenitor as a case study of binary-stripped vs single star profile and explosion outcome, and discussed the various exceptions. Here, we illustrate the progenitor profile and explosion outcome of all models. In Fig. C.1, we plot the shock radii as function of time for all the models studied here. Only four models show no explosion, with all the other models evincing explosion within the first second post-bounce. Shock revival often corresponds to the presence of a sharp compositional interface located sufficiently deep within the star.

In Fig. C.2, we plot the density profiles for each of 11 pairs of single and binary-stripped models studied here. We highlight the location of the Si/O or equivalent density interface for each model as a vertical line. To identify the location of the relevant compositional interface, we look for a sharp density drop of a factor of several around 1.5-2 $M_\odot$, at a density of a few

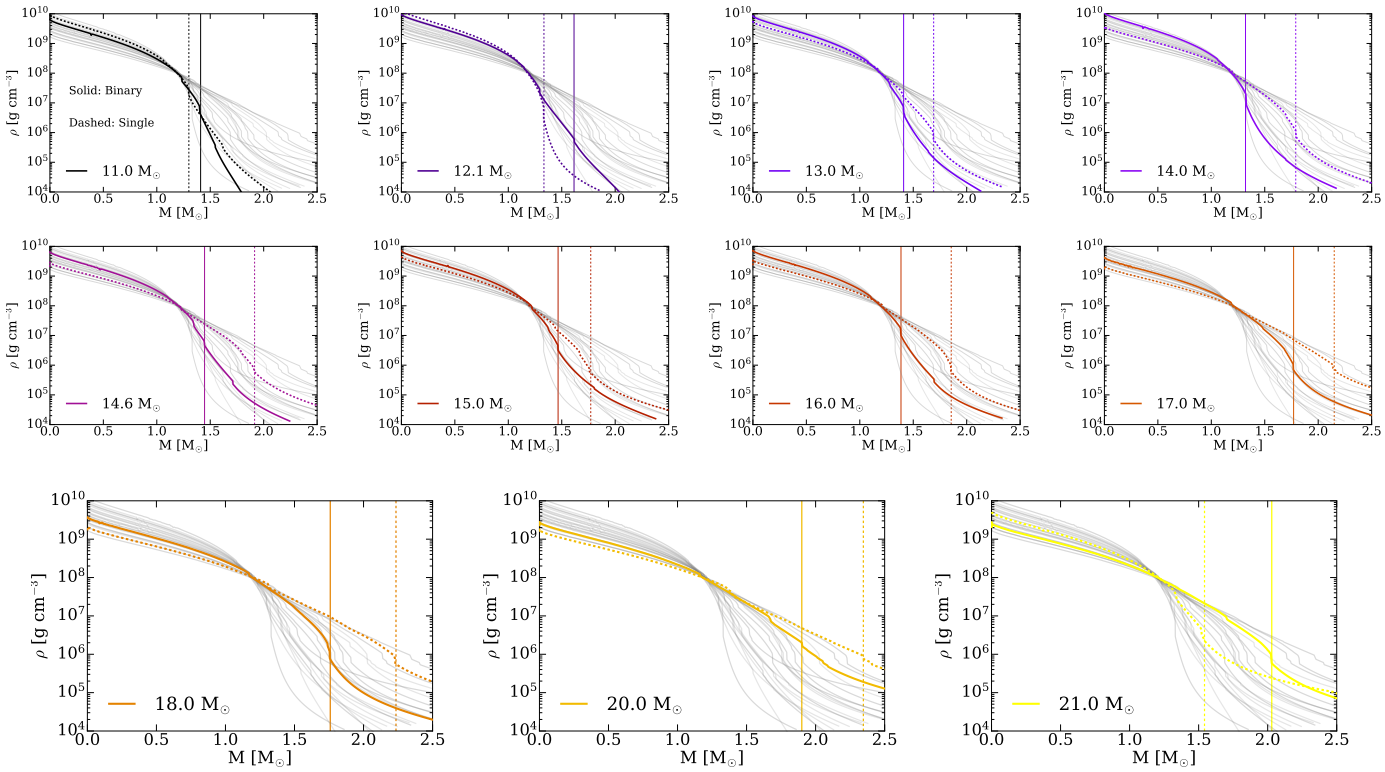

Fig. C.2: Density profiles for each of the 11 pairs of progenitors studied here. Dashed lines indicate single star progenitors and solid lines indicate binary-stripped. We overplot as vertical lines where the relevant density drops, indicative of a sharp Si/O interface, occur. Note that several models have multiple sharp interfaces – however, the interior Fe/Si interface is often irrelevant to explosion because it is accreted onto the PNS during core-collapse and lies interior to the post-bounce shock. In other cases where the relevant interface may be fragmented, we highlight the interface whose accretion occurs on timescales relevant to shock revival. Note the presence and strength of an interface is further complicated by limitations of mixing-length theory, particularly when nuclear burning occurs on similar timescales to convective turnover.

million g cm^{-3}. We then correlate these with the composition (e.g. top left panel of Fig. 4.1) to isolate which compositional boundary the interface corresponds to. When there are several "fragmented" interfaces in close proximity, we then check that the accretion of the chosen interface coincides with shock revival, or in the case of a failed explosion, a bump in the shock radii. We find that models with sharper interfaces, which may result from the merger of multiple shells, are preferentially explodable.

The cosmic carbon footprint of massive stars stripped in binary systems

D

D.1 Other physics choices

The EOS in MESA is blended from several sources; OPAL (Rogers & Nayfonov 2002), SCVH (Saumon et al. 1995), PTEH (Pols et al. 1995), HELM (Timmes & Swesty 2000), and PC (Potekhin & Chabrier 2010). Opacities are primarily from OPAL (Iglesias & Rogers 1993, 1996) with additional data from Buchler & Yueh (1976); Ferguson et al. (2005); Cassisi et al. (2007)

Nuclear reaction rates are a combination of rates from NACRE and JINA's REACLIB (Angulo et al. 1999; Cyburt et al. 2010), with additional weak reaction rates from Fuller et al. (1985); Oda et al. (1994); Langanke & Martínez-Pinedo (2000). Nuclear screening is computed with the prescription of Chugunov et al. (2007). Thermal neutrino loss rates are from Itoh et al. (1996). We compute the Roche lobe radii in binary systems using the fit from Eggleton (1983). The mass transfer rate in our Roche lobe overflowing binary systems is computed from the prescription of Ritter (1988).

D.2 Comparison to other works

D.2.1 Laplace et al. 2021

In Figure D.1 we compare the ^{12}C mass ejected in the supernova calculations presented in Figure 5.1 to the ^{12}C ejected when using progenitor models computed in Laplace et al. (2021). We took the models from Laplace et al. (2021) and exploded them with the same method as in Section 5.2. There are two primary differences between these sets of models; Laplace et al. (2021) was computed with MESA r10398, while this work uses MESA r11215; and Laplace et al. (2021) uses `mesa_128.net` after core oxygen depletion, while this work continues to use `approx21.net` after core oxygen depletion. For both sets of models we explode them with MESA r11215.

We can see that for both single and binary-stripped star models the amount of ^{12}C ejected in the supernovae is similar between both sets. The largest disagreement occurs for the binary-stripped stars at $M_{init} = 21\,M_{\odot}$. This is due to the carbon shell destroying more ^{12}C in the pre-supernova phase of the evolution. As this carbon shell acts before the switch to the larger

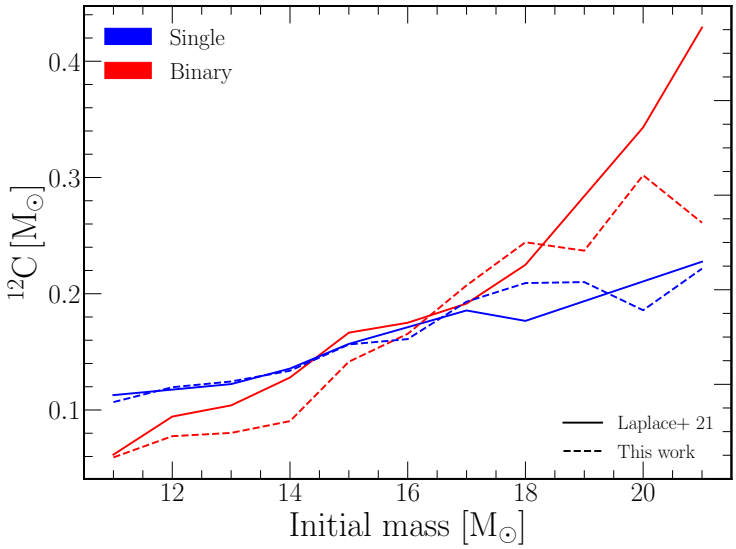

Fig. D.1: Total ^{12}C mass ejected during supernovae, comparing models from this work (dashed) with those from Laplace et al. (2021) (solid). In blue are plotted single-star models, while red represents binary-stripped models. The models of Laplace et al. (2021) were evolved with `mesa_128.net` after core oxygen depletion, and then exploded with the same method as in Section 5.2.

nuclear network this indicates the differences are due to changes in `MESA` between r10398 and r11215, rather than to differences in the nuclear network.

This indicates that it is reasonable, when considering the ^{12}C yields, to use a smaller but more computational efficient, nuclear network during the pre-supernova evolution. This is due to two reasons, first most of the ^{12}C that will be ejected is set by the evolution up to the end of core-carbon burning, which does not require large nuclear networks to compute. Secondly, the ^{12}C that is ejected in the supernova resides in/near the helium shell. Thus the total ^{12}C yield is insensitive to the structure of the inner core, which is sensitive to the choice of nuclear network (Farmer et al. 2016). This however may not be true for other isotopes, or for inferring neutron star masses which depend sensitively on pre-supernova structures.

D.2.2 Other core-collapse works

Figure D.2 shows a comparison between our core collapse yields and the results of Pignatari et al. (2016); Limongi & Chieffi (2018) and Griffith et al. (2021) for solar metallicity non-rotating single stars. Below $M_{init} \approx 20\,M_\odot$ there is a reasonable agreement between the different models, and software instruments, for the final core-collapse ^{12}C yield. Above this point the different models begin to diverge, most likely due to changes in the behavior of carbon shells in each set of models and choice of nuclear reaction rates. Differences in the choices for the treatment of stellar wind mass loss likely also plays a role. We note that the

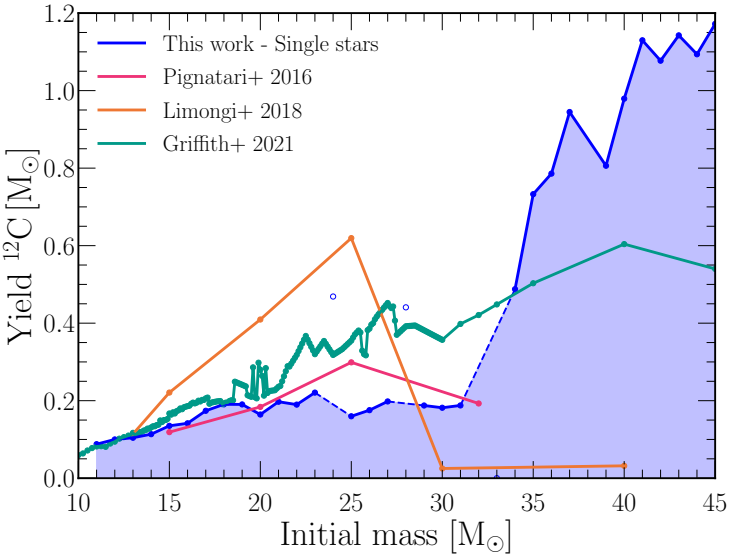

Fig. D.2: Comparison of nucleosynthetic ^{12}C yields for solar metallicity non-rotating single stars. In blue this work, magneta line (Pignatari et al. 2016) (delayed model), orange line (Limongi & Chieffi 2018), and teal line (Griffith et al. 2021). Dashed lines and empty circles have the same meaning as in Figure 5.1

spread in ^{12}C yields is of the order of the spread we find due to the differences in carbon shell burning (see section 5.4.1). Note the two open symbols, which indicate models in our grid where the mixing due to convective carbon shell burning destroyed less carbon. These two models are more consistent with the higher yields found by Limongi & Chieffi (2018) and Griffith et al. (2021).

D.3 Table of yields

In Table D.1 we show the total ^{12}C yields based on the source of the mass loss. Several of the models show anomalous carbon burning (see section 5.3.3), however the single $M_{init} = 33\,M_\odot$ star shows a slightly different behavior. Here the convection zone above the carbon-burning shell extended sufficiently far that the mixing region dredged down all the ^{12}C that existed in/near the helium shell. Thus by the time of core-collapse the star becomes depleted in ^{12}C.

We also provide the integrated yields for single and binary-stripped stars for different assumption with respect which stars explode successfully in Table D.2. The results are normalized to the assumption that all stars explode successfully. We can see that changing the assumption for the successful explosion has a large impact on the final ^{12}C yields, with the yields decreasing by 60–70%. The binary-stripped models show no differences between the different envelope assumptions as the final helium core mass cut and cut on initial masses are equivalent.

Table D.1: ^{12}C yields in solar masses broken down by mass-loss type for both single stars and the primary star in the binary. $M_{He,final}$ is the final helium core mass at core-collapse.

Initial mass [$M_\odot$]	Single [$M_\odot$]				Binary [$M_\odot$]				
	$M_{He,final}$	M_{Winds}	M_{CC}	M_{Total}	$M_{He,final}$	M_{RLOF}	M_{Winds}	M_{CC}	M_{Total}
11	3.798	-0.001	0.088	0.087	3.191	-0.006	-0.001	0.055	0.051
12	4.297	-0.002	0.100	0.098	3.602	-0.007	-0.001	0.073	0.069
13	4.800	-0.002	0.104	0.102	4.014	-0.007	-0.002	0.074	0.071
14	5.308	-0.003	0.114	0.111	4.422	-0.007	-0.002	0.084	0.081
15	5.829	-0.004	0.135	0.132	4.832	-0.007	-0.002	0.134	0.132
16	6.359	-0.004	0.142	0.137	5.222	-0.008	-0.003	0.157	0.156
17	6.896	-0.005	0.174	0.169	5.608	-0.008	-0.003	0.198	0.198
18	7.414	-0.006	0.191	0.185	5.980	-0.008	-0.004	0.235	0.235
19	7.817	-0.007	0.190	0.184	6.243	-0.008	-0.004	0.226	0.227
20	8.275	-0.007	0.164	0.157	6.579	-0.009	-0.005	0.290	0.291
21	8.382	-0.007	0.197	0.190	6.793	-0.010	-0.005	0.249	0.251
22	7.943	-0.009	0.190	0.181	8.365	-0.011	-0.002	0.134	0.133
23	9.366	-0.009	0.221	0.212	8.246	-0.011	-0.004	0.233	0.234
24	9.856	-0.010	0.469[a]	0.458[a]	9.476	-0.008	-0.004	0.178	0.182
25	9.530	-0.011	0.160	0.149	9.403	-0.010	-0.004	0.250	0.256
26	9.995	-0.011	0.176	0.164	10.636	-0.010	-0.005	0.185	0.191
27	10.785	-0.013	0.198	0.185	10.283	-0.009	-0.005	0.187	0.196
28	11.154	-0.012	0.441[a]	0.429[a]	10.889	-0.009	-0.006	0.189	0.201
29	12.194	-0.014	0.188	0.173	11.085	-0.009	-0.010	0.613	0.631
30	12.449	-0.014	0.182	0.167	11.094	-0.010	-0.011	0.719	0.737
31	13.303	-0.015	0.188	0.173	13.131	-0.011	-0.007	0.167[a]	0.182[a]
32	14.238	-0.017	0.000[b]	0.000[b]	11.632	-0.010	0.012	0.949	0.997
33	15.031	-0.016	0.000[a]	−0.016[a]	11.969	-0.011	-0.013	0.866	0.890
34	14.870	-0.019	0.488	0.469	12.818	-0.010	-0.014	0.718	0.747
35	15.031	-0.021	0.733	0.712	13.252	-0.010	0.025	1.002	1.073
36	15.469	-0.021	0.786	0.764	11.650	-0.014	0.575	0.975	1.595
37	15.789	-0.005	0.945	0.939	13.159	-0.010	0.879	0.977	1.912
38	16.196	0.052	0.000[b]	0.000[b]	13.552	-0.010	0.962	1.008	2.029
39	16.576	0.120	0.806	0.926	13.948	-0.011	1.039	0.971	2.071
40	16.966	0.186	0.979	1.165	14.357	-0.011	1.112	1.063	2.240
41	17.311	0.277	1.130	1.407	14.776	-0.011	1.180	1.062	2.311
42	17.638	0.379	1.077	1.456	15.183	-0.012	1.253	1.021	2.346
43	17.999	0.458	1.143	1.600	15.599	-0.013	1.322	1.134	2.531
44	18.328	0.554	1.094	1.648	15.831	-0.013	1.434	1.069	2.585
45	18.621	0.667	1.172	1.839	16.279	-0.013	1.485	1.138	2.709

[a] Model shows anomalous carbon burning behavior (See section 5.3.3)

[b] Model did not reach core-collapse.

Table D.2: Impact of assumptions regarding black hole formation on the core-collapse IMF weighted yield predictions normalized to the default assumption that all stars explode successfully. We assume an IMF power-law exponent $\alpha = -2.3$. In case of BH formation we assume that the carbon-rich layers fall back onto the BH.

BH formation assumption	Normalized ^{12}C yields	
	Single stars	Binary-stripped stars
All stars explode successfully	1.0	1.0
BHs form from stars with initial masses $M_{init} > 22\,M_\odot$	0.41	0.34
BHs form from stars final core masses $M_{He,final} > 7\,M_\odot$	0.27	0.34

Bibliography

Abbott, B. P., Abbott, R., Abbott, T. D., et al. 2016, Physical Review Letters, 116, 061102

Abbott, B. P., Abbott, R., Abbott, T. D., et al. 2017a, The Astrophysical Journal, Letters, 848, L13, eprint: 1710.05834

Abbott, B. P., Abbott, R., Abbott, T. D., et al. 2017b, Physical Review Letters, 119, 161101

Abbott, B. P., Abbott, R., Abbott, T. D., et al. 2017c, The Astrophysical Journal, 848, L12, publisher: American Astronomical Society

Abbott, B. P., Abbott, R., Abbott, T. D., et al. 2019, The Astrophysical Journal, Letters, 882, L24, eprint: 1811.12940

Abt, H. A. 1983, Annual Review of Astronomy and Astrophysics, 21, 343

Adams, S. M., Kochanek, C. S., Beacom, J. F., et al. 2013, The Astrophysical Journal, 778, 164

Aerts, C., Thoul, A., Daszyńska, J., et al. 2003, Science, 300, 1926

Afsariardchi, N., & Matzner, C. D. 2018, The Astrophysical Journal, 856, 146

Aguilera-Dena, D. R., Langer, N., Antoniadis, J., et al. 2020, arXiv:2008.09132 [astro-ph]

Akerman, C. J., Carigi, L., Nissen, P. E., et al. 2004, Astronomy and Astrophysics, 414, 931, eprint: astro-ph/0310472

Akiyama, S., Wheeler, J. C., Meier, D. L., et al. 2003, The Astrophysical Journal, 584, 954

Aleo, P. D., Lock, S. J., Cox, D. J., et al. 2020, Astronomy and Computing, 33, 100424

Almeida, L. A., Sana, H., Taylor, W., et al. 2017, Astronomy and Astrophysics, 598, A84, eprint: 1610.03500

Amaro-Seoane, P., Audley, H., Babak, S., et al. 2017, arXiv e-prints, arXiv:1702.00786

Andrassy, R., Herwig, F., Woodward, P., et al. 2020, Monthly Notices of the Royal Astronomical Society, 491, 972

Angulo, C., Arnould, M., Rayet, M., et al. 1999, Nuclear Physics A, 656, 3

Arnett, D., Meakin, C., & Young, P. A. 2009, The Astrophysical Journal, 690, 1715

Arnett, W. D. 1979, The Astrophysical Journal, 230, L37

Arnett, W. D. 1982, The Astrophysical Journal, 253, 785

Arnett, W. D. 1987, The Astrophysical Journal, 319, 136

Arnett, W. D., Fryer, C., & Matheson, T. 2017, The Astrophysical Journal, 846, 33

Arnett, W. D., Meakin, C., Viallet, M., et al. 2015, The Astrophysical Journal, 809, 30, eprint: 1503.00342

Arnett, W. D., & Truran, J. W. 1969, The Astrophysical Journal, 157, 339

Asif, A., Barschke, M., Bastian-Querner, B., et al. 2021, arXiv e-prints, arXiv:2108.01493
Asplund, M., Grevesse, N., Sauval, A. J., et al. 2009, Annual Review of Astronomy and Astrophysics, 47, 481
Astropy Collaboration, Robitaille, T. P., Tollerud, E. J., et al. 2013, Astronomy & Astrophysics, 558, A33, eprint: 1307.6212
Astropy Collaboration, Price-Whelan, A. M., Sip\Hocz, B. M., et al. 2018, The Astronomical Journal, 156, 123, eprint: 1801.02634
Aufderheide, M. B., Baron, E., & Thielemann, F. K. 1991, The Astrophysical Journal, 370, 630
Baade, W., & Zwicky, F. 1934a, Proceedings of the National Academy of Science, 20, 259
Baade, W., & Zwicky, F. 1934b, Proceedings of the National Academy of Science, 20, 254
Bailyn, C. D., Jain, R. K., Coppi, P., et al. 1998, The Astrophysical Journal, 499, 367, eprint: astro-ph/9708032
Bazan, G., & Arnett, D. 1994, The Astrophysical Journal, Letters, 433, L41
Bazán, G., & Arnett, D. 1998, The Astrophysical Journal, 496, 316, eprint: astro-ph/9702239
Belczynski, K., Kalogera, V., Rasio, F. A., et al. 2008, The Astrophysical Journal, Supplement, 174, 223
Bellm, E. C., Kulkarni, S. R., Graham, M. J., et al. 2019, Publications of the Astronomical Society of the Pacific, 131, 018002
Bensby, T., & Feltzing, S. 2006, Monthly Notices of the Royal Astronomical Society, 367, 1181, eprint: astro-ph/0601130
Bersten, M. C., Benvenuto, O. G., Nomoto, K., et al. 2012, The Astrophysical Journal, 757, 31, eprint: 1207.5975
Bersten, M. C., Benvenuto, O. G., Folatelli, G., et al. 2014, The Astronomical Journal, 148, 68
Bersten, M. C., Folatelli, G., García, F., et al. 2018, Nature, 554, 497
Bertola, F. 1964, Annales d'Astrophysique, 27, 319
Bertola, F., Mammano, A., & Perinotto, M. 1965, Contributi dell'Osservatorio Astrofisica dell'Universita di Padova in Asiago, 174, 3
Bestenlehner, J. M., Gräfener, G., Vink, J. S., et al. 2014, Astronomy and Astrophysics, 570, A38
Bethe, H. A., & Wilson, J. R. 1985, The Astrophysical Journal, 295, 14
Bevan, A., Barlow, M. J., & Milisavljevic, D. 2017, Monthly Notices of the Royal Astronomical Society, 465, 4044, eprint: 1611.05006
Bhattacharya, D., & van den Heuvel, E. P. J. 1991, Physics Reports, 203, 1
Bianco, F. B., Modjaz, M., Hicken, M., et al. 2014, The Astrophysical Journal Supplement Series, 213, 19
Bionta, R. M., Blewitt, G., Bratton, C. B., et al. 1987, Physical Review Letters, 58, 1494
Bisnovatyi-Kogan, G. S., Popov, I. P., & Samokhin, A. A. 1976, Astrophysics and Space Science, 41, 287
Blinnikov, S. I., & Bartunov, O. S. 2011, Astrophysics Source Code Library, ascl:1108.013
Bonnet-Bidaud, J.-M., Praderie, F., & Whitfield, S. 2009, Journal of Astronomical History

and Heritage, 12, 39
Breivik, K., Coughlin, S. C., Zevin, M., et al. 2019, arXiv e-prints, arXiv:1911.00903
Bressan, A., Marigo, P., Girardi, L., et al. 2012, Monthly Notices of the Royal Astronomical Society, 427, 127
Brooker, E. S., Stangl, S. M., Mauney, C. M., et al. 2021, arXiv e-prints, arXiv:2103.12781, eprint: 2103.12781
Brott, I., de Mink, S. E., Cantiello, M., et al. 2011, Astronomy and Astrophysics, 530, A115
Brown, G. E., Heger, A., Langer, N., et al. 2001, New Astronomy, 6, 457
Brown, G. E., Lee, C.-H., & Bethe, H. A. 1999, New Astronomy, 4, 313
Brown, G. E., Weingartner, J. C., & Wijers, R. A. M. J. 1996, The Astrophysical Journal, 463, 297
Brown, J. M., & Woosley, S. E. 2013, The Astrophysical Journal, 769, 99, eprint: 1302.6973
Bruch, R. 2019, in The Extragalactic Explosive Universe: the New Era of Transient Surveys and Data-Driven Discovery, 10
Bruenn, S. W. 1987, Physical Review Letters, 59, 938
Buchler, J. R., & Yueh, W. R. 1976, The Astrophysical Journal, 210, 440
Burbidge, E. M., Burbidge, G. R., Fowler, W. A., et al. 1957, Reviews of Modern Physics, 29, 547
Burrows, A. 2013, Reviews of Modern Physics, 85, 245, eprint: 1210.4921
Burrows, A., Dessart, L., Livne, E., et al. 2007, The Astrophysical Journal, 664, 416
Burrows, A., & Goshy, J. 1993, The Astrophysical Journal, Letters, 416, L75
Burrows, A., & Lattimer, J. M. 1987, The Astrophysical Journal, 318, L63
Burrows, A., Radice, D., & Vartanyan, D. 2019a, Monthly Notices of the Royal Astronomical Society, 485, 3153, eprint: 1902.00547
Burrows, A., Radice, D., Vartanyan, D., et al. 2019b, Monthly Notices of the Royal Astronomical Society, 491, 2715, publisher: Oxford University Press (OUP)
Burrows, A., & Vartanyan, D. 2021, Nature, 589, 29, eprint: 2009.14157
Burrows, A., Vartanyan, D., Dolence, J. C., et al. 2018, Space Science Reviews, 214, 33
Burton, W. B., & Gordon, M. A. 1978, Astronomy and Astrophysics, 63, 7
Böhm-Vitense, E. 1958, Zeitschrift fur Astrophysik, 46, 108
Cameron, A. G. W. 1959, The Astrophysical Journal, 130, 429
Cano, Z. 2013, Monthly Notices of the Royal Astronomical Society, 434, 1098
Cano, Z., Wang, S.-Q., Dai, Z.-G., et al. 2017, Advances in Astronomy, 2017, 8929054
Cao, Y., Kasliwal, M. M., Arcavi, I., et al. 2013, The Astrophysical Journal, Letters, 775, L7
Carigi, L., Peimbert, M., Esteban, C., et al. 2005, The Astrophysical Journal, 623, 213, eprint: astro-ph/0408398
Carilli, C. L., & Walter, F. 2013, Annual Review of Astronomy and Astrophysics, 51, 105, eprint: 1301.0371
Cassisi, S., Potekhin, A. Y., Pietrinferni, A., et al. 2007, The Astrophysical Journal, 661, 1094
Cawthon, N., & Moere, A. V. 2007, in 2007 11th International Conference Information Visualization (IV '07), 637, iSSN: 1550-6037

Cescutti, G., Matteucci, F., McWilliam, A., et al. 2009, Astronomy and Astrophysics, 505, 605, eprint: 0907.4308
Chevalier, R. A. 1976, The Astrophysical Journal, 207, 872
Chieffi, A., & Limongi, M. 2020, The Astrophysical Journal, 890, 43, eprint: 1911.08988
Chini, R., Hoffmeister, V. H., Nasseri, A., et al. 2012, Monthly Notices of the Royal Astronomical Society, 424, 1925
Chugunov, A. I., Dewitt, H. E., & Yakovlev, D. G. 2007, Physical Review D, 76, 025028, eprint: 0707.3500
Claeys, J. S. W., de Mink, S. E., Pols, O. R., et al. 2011, Astronomy and Astrophysics, 528, A131
Colgate, S. A., & White, R. H. 1966, The Astrophysical Journal, 143, 626
Collaboration, G., Prusti, T., de Bruijne, J. H. J., et al. 2016, Astronomy and Astrophysics, 595, A1
Collins, C., Müller, B., & Heger, A. 2018, Monthly Notices of the Royal Astronomical Society, 473, 1695
Colpi, M., Holley-Bockelmann, K., Bogdanovic, T., et al. 2019, arXiv e-prints, arXiv:1903.06867
Couch, S. M., & Ott, C. D. 2013, The Astrophysical Journal Letters, 778, L7
Cox, J. P., & Giuli, R. T. 1961, The Astrophysical Journal, 133, 755
Cox, J. P., & Giuli, R. T. 1968, Principles of stellar structure, by J.P. Cox and R. T. Giuli. New York: Gordon and Breach, 1968
Cristini, A., Meakin, C., Hirschi, R., et al. 2017, Monthly Notices of the Royal Astronomical Society, 471, 279, eprint: 1610.05173
Cromartie, H. T., Fonseca, E., Ransom, S. M., et al. 2020, Nature Astronomy, 4, 72, eprint: 1904.06759
Crowther, P. A. 2007, Annual Review of Astronomy and Astrophysics, 45, 177
Curtis, S., Ebinger, K., Fröhlich, C., et al. 2019, The Astrophysical Journal, 870, 2, eprint: 1805.00498
Cyburt, R. H., Amthor, A. M., Ferguson, R., et al. 2010, The Astrophysical Journal, Supplement, 189, 240
Davis, A., Jones, S., & Herwig, F. 2019, Monthly Notices of the Royal Astronomical Society, 484, 3921, eprint: 1712.00114
De, K., Kasliwal, M. M., Ofek, E. O., et al. 2018, Science, 362, 201, eprint: 1810.05181
de Jager, C., Nieuwenhuijzen, H., & van der Hucht, K. A. 1988, Astronomy and Astrophysics Supplement Series, 72, 259
de Kool, M. 1990, The Astrophysical Journal, 358, 189
de Mink, S. E., Pols, O. R., & Hilditch, R. W. 2007, Astronomy and Astrophysics, 467, 1181
de Mink, S. E., Pols, O. R., Langer, N., et al. 2009, Astronomy and Astrophysics, 507, L1, eprint: 0910.1086
de Mink, S. E., Pols, O. R., & Yoon, S.-C. 2008, First Stars III, 990, 230
Dessart, L., Hillier, D. J., Li, C., et al. 2012, Monthly Notices of the Royal Astronomical

Society, 424, 2139
Dessart, L., Hillier, D. J., Livne, E., et al. 2011, Monthly Notices of the Royal Astronomical Society, 414, 2985, publisher: Oxford University Press (OUP)
Dessart, L., Hillier, D. J., Woosley, S., et al. 2015, Monthly Notices of the Royal Astronomical Society, 453, 2189
Dessart, L., Hillier, D. J., Woosley, S., et al. 2016, Monthly Notices of the Royal Astronomical Society, 458, 1618
Dessart, L., & John Hillier, D. 2020, Astronomy and Astrophysics, 642, A33, eprint: 2007.02243
Dessart, L., Yoon, S.-C., Aguilera-Dena, D. R., et al. 2020, arXiv:2008.07601 [astro-ph]
Dessart, L., Yoon, S.-C., Livne, E., et al. 2018, Astronomy and Astrophysics, 612, A61
Dewi, J. D. M., Podsiadlowski, P., & Sena, A. 2006, Monthly Notices of the Royal Astronomical Society, 368, 1742
Dewi, J. D. M., & Pols, O. R. 2003, Monthly Notices of the Royal Astronomical Society, 344, 629
Dewi, J. D. M., Pols, O. R., Savonije, G. J., et al. 2002, Monthly Notices of the Royal Astronomical Society, 331, 1027
Díaz-Rodríguez, M., Murphy, J. W., Williams, B. F., et al. 2021, Monthly Notices of the Royal Astronomical Society, 506, 781
Divine, N. 1965, The Astrophysical Journal, 142, 824
Dray, L. M., Tout, C. A., Karakas, A. I., et al. 2003, Monthly Notices of the Royal Astronomical Society, 338, 973
Drout, M. R., Massey, P., Meynet, G., et al. 2009, The Astrophysical Journal, 703, 441
Drout, M. R., Soderberg, A. M., Gal-Yam, A., et al. 2011, The Astrophysical Journal, 741, 97
Dudley, R. E., & Jeffery, C. S. 1990, Monthly Notices of the Royal Astronomical Society, 247, 400
Eddington, A. S. 1926, The Internal Constitution of the Stars (Cambridge: Cambridge University Press), publication Title: The Internal Constitution of the Stars
Eggleton, P. P. 1971, Monthly Notices of the Royal Astronomical Society, 151, 351
Eggleton, P. P. 1972, Monthly Notices of the Royal Astronomical Society, 156, 361
Eggleton, P. P. 1983, The Astrophysical Journal, 268, 368
Eggleton, P. P., Faulkner, J., & Flannery, B. P. 1973, Astronomy and Astrophysics, 23, 325
Eggleton, P. P., & Tokovinin, A. A. 2008, Monthly Notices of the Royal Astronomical Society, 389, 869
Ekström, S., Georgy, C., Eggenberger, P., et al. 2012, Astronomy and Astrophysics, 537, A146, eprint: 1110.5049
Eldridge, J. J., Fraser, M., Maund, J. R., et al. 2015, Monthly Notices of the Royal Astronomical Society, 446, 2689
Eldridge, J. J., Fraser, M., Smartt, S. J., et al. 2013, Monthly Notices of the Royal Astronomical Society, 436, 774
Eldridge, J. J., Izzard, R. G., & Tout, C. A. 2008, Monthly Notices of the Royal Astronomical

Society, 384, 1109, eprint: 0711.3079
Eldridge, J. J., & Maund, J. R. 2016, Monthly Notices of the Royal Astronomical Society, 461, L117
Eldridge, J. J., & Stanway, E. R. 2016, Monthly Notices of the Royal Astronomical Society, 462, 3302, eprint: 1602.03790
Eldridge, J. J., Stanway, E. R., Xiao, L., et al. 2017, Publications of the Astronomical Society of Australia, 34, e058
Eldridge, J. J., & Tout, C. A. 2004, Monthly Notices of the Royal Astronomical Society, 348, 201, eprint: astro-ph/0310255
Eldridge, J. J., & Tout, C. A. 2019, The Structure and Evolution of Stars, publication Title: The Structure and Evolution of Stars. Edited by J J Eldridge Christopher A Tout. Published by World Scientific Publishing Co. Pte. Ltd
Eldridge, J. J., & Vink, J. S. 2006, Astronomy and Astrophysics, 452, 295
Eldridge, J. J., Xiao, L., Stanway, E. R., et al. 2018, Publications of the Astronomical Society of Australia, 35
Ertl, T., Janka, H. T., Woosley, S. E., et al. 2016, The Astrophysical Journal, 818, 124, eprint: 1503.07522
Ertl, T., Woosley, S. E., Sukhbold, T., et al. 2020, The Astrophysical Journal, 890, 51, eprint: 1910.01641
Evans, C. J., Taylor, W. D., Hénault-Brunet, V., et al. 2011, Astronomy and Astrophysics, 530, A108
Evergreen, S., & Metzner, C. 2013, New Directions for Evaluation, 2013, 5
Eyer, L., Dubath, P., Mowlavi, N., et al. 2012, 282, 33, conference Name: From Interacting Binaries to Exoplanets: Essential Modeling Tools Place: eprint: arXiv:1201.5140
Falk, S. W., & Arnett, W. D. 1973, The Astrophysical Journal, 180, L65
Falk, S. W., & Arnett, W. D. 1977, The Astrophysical Journal Supplement Series, 33, 515
Faran, T., Goldfriend, T., Nakar, E., et al. 2019, The Astrophysical Journal, 879, 20
Farmer, R. 2020, rjfarmer/mesaplot
Farmer, R., & Bauer, E. B. 2018, rjfarmer/pyMesa: Add support for 10398
Farmer, R., Fields, C. E., Petermann, I., et al. 2016, The Astrophysical Journal Supplement Series, 227, 22
Farmer, R., Fields, C. E., & Timmes, F. X. 2015, The Astrophysical Journal, 807, 184
Farmer, R., Renzo, M., de Mink, S. E., et al. 2020, The Astrophysical Journal, Letters, 902, L36, eprint: 2006.06678
Farmer, R., Renzo, M., de Mink, S. E., et al. 2019, The Astrophysical Journal, 887, 53
Farr, W. M., Sravan, N., Cantrell, A., et al. 2011, The Astrophysical Journal, 741, 103, eprint: 1011.1459
Ferguson, J. W., Alexander, D. R., Allard, F., et al. 2005, The Astrophysical Journal, 623, 585, eprint: astro-ph/0502045
Fields, C. E., & Couch, S. M. 2020, The Astrophysical Journal, 901, 33
Fields, C. E., Timmes, F. X., Farmer, R., et al. 2018, The Astrophysical Journal Supplement

Series, 234, 19
Filippenko, A. V. 1997, Annual Review of Astronomy and Astrophysics, 35, 309
Fitzpatrick, E. L. 1988, The Astrophysical Journal, 335, 703
Foley, R. J., Smith, N., Ganeshalingam, M., et al. 2007, The Astrophysical Journal, Letters, 657, L105, eprint: astro-ph/0612711
Fowler, W. A., & Hoyle, F. 1964, The Astrophysical Journal Supplement Series, 9, 201
Fox, O. D., Azalee Bostroem, K., Van Dyk, S. D., et al. 2014, The Astrophysical Journal, 790, 17
Fragos, T., Andrews, J. J., Ramirez-Ruiz, E., et al. 2019, Astrophysical Journal, Letters, 883, L45
Fragos, T., Lehmer, B., Tremmel, M., et al. 2013, The Astrophysical Journal, 764, 41
Fraley, G. S. 1968, Astrophysics and Space Science, 2, 96
Franchini, M., Morossi, C., Di Marcantonio, P., et al. 2020, The Astrophysical Journal, 888, 55, eprint: 1911.13132
Fremling, C., Sollerman, J., Taddia, F., et al. 2014, Astronomy and Astrophysics, 565, A114
Frerking, M. A., Langer, W. D., & Wilson, R. W. 1982, The Astrophysical Journal, 262, 590
Fryer, C. L. 1999, The Astrophysical Journal, 522, 413, eprint: astro-ph/9902315
Fryer, C. L., Belczynski, K., Wiktorowicz, G., et al. 2012, The Astrophysical Journal, 749, 91
Fuller, G. M., Fowler, W. A., & Newman, M. J. 1985, The Astrophysical Journal, 293, 1
Fuller, J. 2017, Monthly Notices of the Royal Astronomical Society, 470, 1642
Fuller, J., & Ro, S. 2018, Monthly Notices of the Royal Astronomical Society, 476, 1853
Funkhouser, H. G. 1936, Osiris, 1, 260, publisher: [Saint Catherines Press, The University of Chicago Press, The History of Science Society]
Gezari, S., Jones, D. O., Sanders, N. E., et al. 2015, The Astrophysical Journal, 804, 28
Giacobbo, N., & Mapelli, M. 2018, Monthly Notices of the Royal Astronomical Society, 480, 2011
Gilkis, A., Vink, J. S., Eldridge, J. J., et al. 2019, Monthly Notices of the Royal Astronomical Society, 486, 4451
Glas, R., Just, O., Janka, H. T., et al. 2019, The Astrophysical Journal, 873, 45, eprint: 1809.10146
Gomez, S., Berger, E., Nicholl, M., et al. 2019, The Astrophysical Journal, 881, 87, eprint: 1904.07259
Grassberg, E. K., Imshennik, V. S., & Nadyozhin, D. K. 1971, Astrophysics and Space Science, 10, 28
Graur, O., Bianco, F. B., Huang, S., et al. 2017a, The Astrophysical Journal, 837, 120
Graur, O., Bianco, F. B., Modjaz, M., et al. 2017b, The Astrophysical Journal, 837, 121
Greiner, J., Mazzali, P. A., Kann, D. A., et al. 2015, Nature, 523, 189
Grevesse, N., & Sauval, A. J. 1998, ßr, 85, 161
Griffith, E. J., Sukhbold, T., Weinberg, D. H., et al. 2021, arXiv e-prints, arXiv:2103.09837, eprint: 2103.09837
Groh, J. H., Meynet, G., Georgy, C., et al. 2013, Astronomy and Astrophysics, 558, A131

Groh, J. H., Oliveira, A. S., & Steiner, J. E. 2008, Astronomy and Astrophysics, 485, 245
Groh, J. H., Ekström, S., Georgy, C., et al. 2019, Astronomy and Astrophysics, 627, A24, eprint: 1904.04009
Guillochon, J., Nicholl, M., Villar, V. A., et al. 2018, The Astrophysical Journal Supplement Series, 236, 6
Gullberg, B., Swinbank, A. M., Smail, I., et al. 2018, The Astrophysical Journal, 859, 12, eprint: 1804.03663
Götberg, Y., de Mink, S. E., Groh, J. H., et al. 2018, Astronomy and Astrophysics, 615, A78
Götberg, Y., de Mink, S. E., Groh, J. H., et al. 2019, Astronomy and Astrophysics, 629, A134
Götberg, Y., de Mink, S. E., McQuinn, M., et al. 2020a, Astronomy and Astrophysics, 634, A134
Götberg, Y., Korol, V., Lamberts, A., et al. 2020b, The Astrophysical Journal, 904, 56
Götberg, Y., Mink, D., E, S., et al. 2017, Astronomy and Astrophysics, 608, A11
Habets, G. M. H. J. 1986a, Astronomy and Astrophysics, 165, 95
Habets, G. M. H. J. 1986b, Astronomy and Astrophysics, 167, 61
Hachinger, S., Mazzali, P. A., Taubenberger, S., et al. 2012, Monthly Notices of the Royal Astronomical Society, 422, 70
Hamacher, D. W. 2014, Journal of Astronomical History and Heritage, 17, 161
Han, Z., Podsiadlowski, P., & Eggleton, P. P. 1994, Monthly Notices of the Royal Astronomical Society, 270, 121
Harrison, L., Reinecke, K., & Chang, R. 2015, in Proceedings of the 33rd Annual ACM Conference on Human Factors in Computing Systems, CHI '15 (New York, NY, USA: Association for Computing Machinery), 1187
Hassan, A., & Fluke, C. J. 2011, Publications of the Astronomical Society of Australia, 28, 150
Hayashi, C., Hōshi, R., & Sugimoto, D. 1962, Progress of Theoretical Physics Supplement, 22, 1
Heger, A., Fryer, C. L., Woosley, S. E., et al. 2003, The Astrophysical Journal, 591, 288
Henry, R. B. C., Edmunds, M. G., & Köppen, J. 2000, The Astrophysical Journal, 541, 660, eprint: astro-ph/0004299
Herald, D., McNaught, R. H., Morel, M., et al. 1987, International Astronomical Union Circular, 4317, 1
Herbst, E., & van Dishoeck, E. F. 2009, Annual Review of Astronomy and Astrophysics, 47, 427
Hertzsprung, E. 1909, Astronomische Nachrichten, 179, 373
Hertzsprung, E. 1911, Publikationen des Astrophysikalischen Observatoriums zu Potsdam, 63
Hewish, A., Bell, S. J., Pilkington, J. D. H., et al. 1968, Nature, 217, 709
Hillstrom, A. P., & Yantis, S. 1994, Perception & Psychophysics, 55, 399
Hiramatsu, D., Howell, D. A., Van Dyk, S. D., et al. 2021, Nature Astronomy
Hirata, K., Kajita, T., Koshiba, M., et al. 1987, Physical Review Letters, 58, 1490
Hirschi, R., Meynet, G., & Maeder, A. 2004, Astronomy and Astrophysics, 425, 649, eprint:

astro-ph/0406552
Hirschi, R., Meynet, G., & Maeder, A. 2005, Astronomy and Astrophysics, 433, 1013, eprint: astro-ph/0412454
Hix, W. R., & Thielemann, F.-K. 1996, The Astrophysical Journal, 460, 869
Hofmeister, E., Kippenhahn, R., & Weigert, A. 1964, Zeitschrift fur Astrophysik, 59, 242
Hopkins, P. F., Kereš, D., Oñorbe, J., et al. 2014, Monthly Notices of the Royal Astronomical Society, 445, 581
Hosseinzadeh, G., McCully, C., Zabludoff, A. I., et al. 2019, The Astrophysical Journal, Letters, 871, L9, eprint: 1901.03332
Hoyle, F., & Fowler, W. A. 1960, The Astrophysical Journal, 132, 565
Hsi, T.-T. 1957, Smithsonian Contributions to Astrophysics, 2, 109
Huang, F., Wang, X. F., Hosseinzadeh, G., et al. 2018, Monthly Notices of the Royal Astronomical Society, 475, 3959
Hunter, I., Dufton, P. L., Smartt, S. J., et al. 2007, Astronomy and Astrophysics, 466, 277, eprint: astro-ph/0609710
Hunter, I., Brott, I., Lennon, D. J., et al. 2008, The Astrophysical Journal, Letters, 676, L29, eprint: 0711.2267
Hunter, I., Brott, I., Langer, N., et al. 2009, Astronomy and Astrophysics, 496, 841, eprint: 0901.3853
Hunter, J. D. 2007, Computing in Science and Engineering, 9, 90
Hurley, J. R., Pols, O. R., & Tout, C. A. 2000, Monthly Notices of the Royal Astronomical Society, 315, 543
Hurley, J. R., Tout, C. A., & Pols, O. R. 2002, Monthly Notices of the Royal Astronomical Society, 329, 897
Hut, P. 1981, Astronomy and Astrophysics, 99, 126
Iglesias, C. A., & Rogers, F. J. 1993, The Astrophysical Journal, 412, 752
Iglesias, C. A., & Rogers, F. J. 1996, The Astrophysical Journal, 464, 943
Imshenik, V. S., & Nadezhin, D. K. 1965, Soviet Astronomy, 8, 664
Inserra, C. 2019, Nature Astronomy, 3, 697, arXiv: 1908.02314
Inserra, C., Smartt, S. J., Jerkstrand, A., et al. 2013, The Astrophysical Journal, 770, 128
Itoh, M., Kumagai, S., Shigeyama, T., et al. 1987, Nature, 330, 233
Itoh, N., Hayashi, H., Nishikawa, A., et al. 1996, The Astrophysical Journal, Supplement, 102, 411
Ivanova, N., Belczynski, K., Kalogera, V., et al. 2003, The Astrophysical Journal, 592, 475
Ivanova, N., Justham, S., Chen, X., et al. 2013, Astronomy and Astrophysics Review, 21, 59
Ivezic, Z., Axelrod, T., Brandt, W. N., et al. 2008, Serbian Astronomical Journal, 176, 1
Izzard, R. G., Dray, L. M., Karakas, A. I., et al. 2006, Astronomy and Astrophysics, 460, 565
Izzard, R. G., Tout, C. A., Karakas, A. I., et al. 2004, Monthly Notices of the Royal Astronomical Society, 350, 407
Janka, H.-T. 2012, Annual Review of Nuclear and Particle Science, 62, 407, eprint: 1206.2503
Janka, H.-T. 2017, The Astrophysical Journal, 837, 84, eprint: 1611.07562

Janka, H. T., Langanke, K., Marek, A., et al. 2007, Physics Reports, 442, 38
Janka, H.-T., Melson, T., & Summa, A. 2016, Annual Review of Nuclear and Particle Science, 66, 341, eprint: 1602.05576
Jerkstrand, A., Ergon, M., Smartt, S. J., et al. 2015, Astronomy and Astrophysics, 573, A12
Jiang, Y.-F., Cantiello, M., Bildsten, L., et al. 2015, The Astrophysical Journal, 813, 74
Jiang, Y.-F., Cantiello, M., Bildsten, L., et al. 2018, Nature, 561, 498
Jones, S., Hirschi, R., Nomoto, K., et al. 2013, The Astrophysical Journal, 772, 150, eprint: 1306.2030
Kalogera, V., Berry, C. P. L., Colpi, M., et al. 2019, Bulletin of the American Astronomical Society, 51, 242
Karakas, A. I., & Lugaro, M. 2016, The Astrophysical Journal, 825, 26, eprint: 1604.02178
Kasen, D., & Bildsten, L. 2010, The Astrophysical Journal, 717, 245
Kasen, D., Thomas, R. C., & Nugent, P. 2006, The Astrophysical Journal, 651, 366
Kasen, D., & Woosley, S. E. 2009, The Astrophysical Journal, 703, 2205
Khatami, D. K., & Kasen, D. N. 2019, The Astrophysical Journal, 878, 56
Khazov, D., Yaron, O., Gal-Yam, A., et al. 2016, The Astrophysical Journal, 818, 3
Kim, H.-J., Yoon, S.-C., & Koo, B.-C. 2015, The Astrophysical Journal, 809, 131
Kippenhahn, R., Ruschenplatt, G., & Thomas, H.-C. 1980, Astronomy and Astrophysics, 91, 175
Kippenhahn, R., & Weigert, A. 1967, Zeitschrift fur Astrophysik, 65, 251
Kippenhahn, R., Weigert, A., A., & Weiss, A., A. 2012, Stellar Structure and Evolution - NASA/ADS, Astronomy and Astrophysics Library (Springer-Verlag Berlin Heidelberg)
Kipper, T., & Klochkova, V. G. 2012, Baltic Astronomy, 21, 219
Kleiser, I., Fuller, J., & Kasen, D. 2018, Monthly Notices of the Royal Astronomical Society, 481, L141
Kleiser, I. K. W., & Kasen, D. 2014, Monthly Notices of the Royal Astronomical Society, 438, 318
Klencki, J., & Nelemans, G. 2018, arXiv e-prints, arXiv:1812.00012
Klencki, J., Nelemans, G., Istrate, A. G., et al. 2020, Astronomy and Astrophysics, 638, A55
Kluyver, T., Ragan-Kelley, B., Pérez, F., et al. 2016, in Positioning and Power in Academic Publishing: Players, Agents and Agendas: Proceedings of the 20th International Conference on Electronic Publishing, ed. F. Loizides & B. Schmidt (Amsterdam: IOS Press), 87
Kobayashi, C., Umeda, H., Nomoto, K., et al. 2006, The Astrophysical Journal, 653, 1145, eprint: astro-ph/0608688
Kobulnicky, H. A., Kiminki, D. C., Lundquist, M. J., et al. 2014, The Astrophysical Journal, Supplement, 213, 34, eprint: 1406.6655
Kochanek, C. S., Shappee, B. J., Stanek, K. Z., et al. 2017, Publications of the Astronomical Society of the Pacific, 129, 104502
Kopal, Z. 1956, Annales d'Astrophysique, 19, 298
Korkmaz, O. 2009, The Social Sciences, 4, 525
Kozyreva, A., Shingles, L., Mironov, A., et al. 2020, Monthly Notices of the Royal Astronomi-

cal Society, 499, 4312
Kruckow, M. U., Tauris, T. M., Langer, N., et al. 2018, Monthly Notices of the Royal Astronomical Society, 481, 1908
Kulkarni, S. R. 2012, arXiv e-prints, arXiv:1202.2381
Kunkel, W., Madore, B., Shelton, I., et al. 1987, International Astronomical Union Circular, 4316, 1
Kupfer, T., Korol, V., Shah, S., et al. 2018, Monthly Notices of the Royal Astronomical Society, 480, 302
Kuroda, T., Arcones, A., Takiwaki, T., et al. 2020, The Astrophysical Journal, 896, 102, eprint: 2003.02004
Kuroda, T., Kotake, K., Takiwaki, T., et al. 2018, Monthly Notices of the Royal Astronomical Society, 477, L80
Kurosu, M., & Kashimura, K. 1995, in Conference Companion on Human Factors in Computing Systems, CHI '95 (New York, NY, USA: Association for Computing Machinery), 292
Kushnir, D. 2015, arXiv e-prints, arXiv:1506.02655
Kushnir, D., & Katz, B. 2015, The Astrophysical Journal, 811, 97
Lamers, H. J. G. L. M., & Levesque, E. M. 2017, Understanding Stellar Evolution, publication Title: Understanding Stellar Evolution
Langanke, K., & Martínez-Pinedo, G. 2000, Nuclear Physics A, 673, 481, eprint: nucl-th/0001018
Langer, N. 1989a, Astronomy and Astrophysics, 220, 135
Langer, N. 1989b, Astronomy and Astrophysics, 210, 93
Langer, N. 1991a, Astronomy and Astrophysics, 252, 669
Langer, N. 1991b, Astronomy and Astrophysics, 248, 531
Langer, N. 2012, Annual Review of Astronomy and Astrophysics, 50, 107
Langer, N., & Henkel, C. 1995, ßr, 74, 343
Laplace, E., Götberg, Y., de Mink, S. E., et al. 2020, Astronomy and Astrophysics, 637, A6, eprint: 2003.01120
Laplace, E., Justham, S., Renzo, M., et al. 2021, arXiv e-prints, arXiv:2102.05036, eprint: 2102.05036
Lau, R. M., Eldridge, J. J., Hankins, M. J., et al. 2020, The Astrophysical Journal, 898, 74, eprint: 2006.08695
LeBlanc, J. M., & Wilson, J. R. 1970, The Astrophysical Journal, 161, 541
Lentz, E. J., Bruenn, S. W., Hix, W. R., et al. 2015, The Astrophysical Journal, Letters, 807, L31, eprint: 1505.05110
Leung, S.-C., & Nomoto, K. 2020, The Astrophysical Journal, 888, 80, eprint: 1901.10007
Lewis, J. L., & Sheppard, S. R. J. 2006, Landscape and Urban Planning, 77, 291
Li, A., & Draine, B. T. 2001, The Astrophysical Journal, 554, 778, eprint: astro-ph/0011319
Li, W., Leaman, J., Chornock, R., et al. 2011, Monthly Notices of the Royal Astronomical Society, 412, 1441

LIGO Scientific Collaboration and Virgo Collaboration, Abbott, B., Abbott, R., et al. 2019, Physical Review X, 9, 031040, publisher: American Physical Society
Limongi, M., & Chieffi, A. 2018, The Astrophysical Journal Supplement Series, 237, 13
Lusk, E. J., & Kersnick, M. 1979, Management Science, 25, 787, publisher: INFORMS
Lyman, J. D., Bersier, D., James, P. A., et al. 2016, Monthly Notices of the Royal Astronomical Society, 457, 328
Maeder, A. 1983, Astronomy and Astrophysics, 120, 113
Maeder, A. 1990, Astronomy and Astrophysics Supplement Series, 84, 139
Maeder, A. 1992, Astronomy and Astrophysics, 264, 105
Maeder, A., & Meynet, G. 2000, Annual Review of Astronomy and Astrophysics, 38, 143, eprint: arXiv:astro-ph/0004204
Maeder, A., Przybilla, N., Nieva, M.-F., et al. 2014, Astronomy and Astrophysics, 565, A39, eprint: 1404.1020
Maggiore, M., Van Den Broeck, C., Bartolo, N., et al. 2020, Journal of Cosmology and Astroparticle Physics, 2020, 050
Maíz Apellániz, J., Sota, A., Arias, J. I., et al. 2016, Astrophysical Journal, Supplement, 224, 4
Mandel, I., M ueller, B., Riley, J., et al. 2020, arXiv e-prints, 2007, arXiv:2007.03890
Mandel, I., & Müller, B. 2020, Monthly Notices of the Royal Astronomical Society, 499, 3214
Marchant, P., Renzo, M., Farmer, R., et al. 2019, The Astrophysical Journal, 882, 36
Marek, A., Dimmelmeier, H., Janka, H.-T., et al. 2006, Astronomy and Astrophysics, 445, 273, eprint: astro-ph/0502161
Martinez, L., Bersten, M. C., Anderson, J. P., et al. 2020, Astronomy and Astrophysics, 642, A143
Mason, B. D., Hartkopf, W. I., Gies, D. R., et al. 2009, The Astronomical Journal, 137, 3358, eprint: 0811.0492
Matheson, T., Filippenko, A. V., Ho, L. C., et al. 2000, The Astronomical Journal, 120, 1499
Matzner, C. D., Levin, Y., & Ro, S. 2013, The Astrophysical Journal, 779, 60
Maund, J. R., Smartt, S. J., Kudritzki, R. P., et al. 2004, Nature, 427, 129, eprint: astro-ph/0401090
Maury, A. C., & Pickering, E. C. 1897, Annals of Harvard College Observatory, 28, 1
McNeill, L. O., & Müller, B. 2020, Monthly Notices of the Royal Astronomical Society, 497, 4644
Meier, D. L., Epstein, R. I., Arnett, W. D., et al. 1976, The Astrophysical Journal, 204, 869
Melson, T., Janka, H.-T., Bollig, R., et al. 2015, The Astrophysical Journal, Letters, 808, L42, eprint: 1504.07631
Metzger, B. D., Giannios, D., Thompson, T. A., et al. 2011, Monthly Notices of the Royal Astronomical Society, 413, 2031
Metzger, B. D., Margalit, B., Kasen, D., et al. 2015, Monthly Notices of the Royal Astronomical Society, 454, 3311
Meynet, G., Ekström, S., & Maeder, A. 2006, Astronomy and Astrophysics, 447, 623, eprint: astro-ph/0510560

Meynet, G., & Maeder, A. 2000, Astronomy and Astrophysics, 361, 101, eprint: astro-ph/0006404
Minkowski, R. 1941, Publications of the Astronomical Society of the Pacific, 53, 224
Modjaz, M., Gutiérrez, C. P., & Arcavi, I. 2019, Nature Astronomy, 3, 717
Modjaz, M., Liu, Y. Q., Bianco, F. B., et al. 2016, The Astrophysical Journal, 832, 108
Modjaz, M., Li, W., Butler, N., et al. 2009, The Astrophysical Journal, 702, 226
Modjaz, M., Blondin, S., Kirshner, R. P., et al. 2014, The Astronomical Journal, 147, 99
Modjaz, M., Bianco, F. B., Siwek, M., et al. 2020, The Astrophysical Journal, 892, 153
Moe, M., & Di Stefano, R. 2017, The Astrophysical Journal Supplement Series, 230, 15
Mokiem, M. R., de Koter, A., Vink, J. S., et al. 2007, Astronomy and Astrophysics, 473, 603, eprint: 0708.2042
Moriya, T. J., Förster, F., Yoon, S.-C., et al. 2018, Monthly Notices of the Royal Astronomical Society, 476, 2840
Moriya, T. J., & Maeda, K. 2012, The Astrophysical Journal, 756, L22
Moriya, T. J., Suzuki, A., Takiwaki, T., et al. 2020, Monthly Notices of the Royal Astronomical Society, 497, 1619, eprint: 2007.04438
Morozova, V., Piro, A. L., Renzo, M., et al. 2016, The Astrophysical Journal, 829, 109, eprint: 1603.08530
Morozova, V., Piro, A. L., Renzo, M., et al. 2015, The Astrophysical Journal, 814, 63, eprint: 1505.06746
Murphey, C. T., Hogan, J. W., Fields, B. D., et al. 2021, Monthly Notices of the Royal Astronomical Society
Murphy, J. W., & Dolence, J. C. 2017, The Astrophysical Journal, 834, 183, eprint: 1507.08314
Murphy, L. J., Groh, J. H., Ekström, S., et al. 2021, Monthly Notices of the Royal Astronomical Society, 501, 2745, eprint: 2012.07420
Mösta, P., Ott, C. D., Radice, D., et al. 2015, Nature, 528, 376
Mösta, P., Richers, S., Ott, C. D., et al. 2014, The Astrophysical Journal, 785, L29
Müller, B. 2015, Monthly Notices of the Royal Astronomical Society, 453, 287, eprint: 1506.05139
Müller, B., Gay, D. W., Heger, A., et al. 2018, Monthly Notices of the Royal Astronomical Society, 479, 3675
Müller, B., Heger, A., Liptai, D., et al. 2016, Monthly Notices of the Royal Astronomical Society, 460, 742, eprint: 1602.05956
Müller, B., Tauris, T. M., Heger, A., et al. 2019, Monthly Notices of the Royal Astronomical Society, 484, 3307
Nagakura, H., Burrows, A., Radice, D., et al. 2019a, arXiv:1905.03786 [astro-ph]
Nagakura, H., Sumiyoshi, K., & Yamada, S. 2019b, The Astrophysical Journal, 878, 160, eprint: 1906.10143
Nakamura, K., Takiwaki, T., Kuroda, T., et al. 2015, Publications of the Astronomical Society of Japan, 67, 107, eprint: 1406.2415
Nakar, E., & Piro, A. L. 2014, The Astrophysical Journal, 788, 193

Nakar, E., & Sari, R. 2010, The Astrophysical Journal, 725, 904
Nandra, K., Barret, D., Barcons, X., et al. 2013, arXiv e-prints, arXiv:1306.2307
Neijssel, C. J., Vigna-Gómez, A., Stevenson, S., et al. 2019, Monthly Notices of the Royal Astronomical Society, 490, 3740, eprint: 1906.08136
Newell, R., Dale, A., & Winters, C. 2016, Cogent Social Sciences, 2, 1201885, publisher: Cogent OA _eprint: https://doi.org/10.1080/23311886.2016.1201885
Nicholl, M., Smartt, S. J., Jerkstrand, A., et al. 2015, Monthly Notices of the Royal Astronomical Society, 452, 3869
Nissen, P. E., Chen, Y. Q., Carigi, L., et al. 2014, Astronomy and Astrophysics, 568, A25, eprint: 1406.5218
Nomoto, K. 1982a, The Astrophysical Journal, 253, 798
Nomoto, K. 1982b, The Astrophysical Journal, 257, 780
Nomoto, K. 1984, The Astrophysical Journal, 277, 791
Nomoto, K., & Hashimoto, M. 1988, Physics Reports, 163, 13
Nomoto, K., Suzuki, T., Shigeyama, T., et al. 1993, Nature, 364, 507
Nomoto, K., Thielemann, F. K., & Yokoi, K. 1984, The Astrophysical Journal, 286, 644
Nomoto, K., Tominaga, N., Umeda, H., et al. 2006, Nuclear Physics A, 777, 424, eprint: astro-ph/0605725
Nugis, T., & Lamers, H. J. G. L. M. 2000, Astronomy and Astrophysics, 360, 227
O'Connor, E., & Ott, C. D. 2011, The Astrophysical Journal, 730, 70
O'Connor, E., & Ott, C. D. 2013, The Astrophysical Journal, 762, 126
O'Connor, E. P., & Couch, S. M. 2018, The Astrophysical Journal, 865, 81, eprint: 1807.07579
Oda, T., Hino, M., Muto, K., et al. 1994, Atomic Data and Nuclear Data Tables, 56, 231
Öpik, E. 1924, Publications of the Tartu Astrofizica Observatory, 25
Ott, C. D., Roberts, L. F., da Silva Schneider, A., et al. 2018, The Astrophysical Journal Letters, 855, L3
Ouchi, R., & Maeda, K. 2017, The Astrophysical Journal, 840, 90
Özel, F., Psaltis, D., Narayan, R., et al. 2010, The Astrophysical Journal, 725, 1918
Paczyński, B. 1967, Acta Astronomica, 17, 355
Paczyński, B. 1971, Annual Review of Astronomy and Astrophysics, 9, 183
Pastorello, A., Smartt, S. J., Mattila, S., et al. 2007, Nature, 447, 829, eprint: astro-ph/0703663
Pastorello, A., Mattila, S., Zampieri, L., et al. 2008, Monthly Notices of the Royal Astronomical Society, 389, 113, eprint: 0801.2277
Patton, R. A., & Sukhbold, T. 2020, Monthly Notices of the Royal Astronomical Society, 499, 2803, eprint: 2005.03055
Paxton, B., Bildsten, L., Dotter, A., et al. 2011, The Astrophysical Journal Supplement Series, 192, 3
Paxton, B., Cantiello, M., Arras, P., et al. 2013, The Astrophysical Journal Supplement Series, 208, 4
Paxton, B., Marchant, P., Schwab, J., et al. 2015, The Astrophysical Journal Supplement Series, 220, 15

Paxton, B., Schwab, J., Bauer, E. B., et al. 2018, The Astrophysical Journal Supplement Series, 234, 34
Paxton, B., Smolec, R., Schwab, J., et al. 2019, The Astrophysical Journal, Supplement, 243, 10, eprint: 1903.01426
Pejcha, O., & Thompson, T. A. 2012, The Astrophysical Journal, 746, 106, eprint: 1103.4864
Perets, H. B., Gal-Yam, A., Mazzali, P. A., et al. 2010, Nature, 465, 322
Perez, F., & Granger, B. E. 2007, Computing in Science and Engineering, 9, 21
Phillips, M., Matthews, J., McLean, B., et al. 1987, International Astronomical Union Circular, 4318, 1
Pignatari, M., Herwig, F., Hirschi, R., et al. 2016, The Astrophysical Journal, Supplement, 225, 24, eprint: 1307.6961
Pinto, P. A., & Woosley, S. E. 1988, The Astrophysical Journal, 329, 820
Piro, A. L., & Nakar, E. 2013, ApJ, 769, 67
Podsiadlowski, P. 1992, Publications of the Astronomical Society of the Pacific, 104, 717
Podsiadlowski, P., Hsu, J. J. L., Joss, P. C., et al. 1993, Nature, 364, 509
Podsiadlowski, P., Joss, P. C., & Hsu, J. J. L. 1992, The Astrophysical Journal, 391, 246
Podsiadlowski, P., Langer, N., Poelarends, A. J. T., et al. 2004, The Astrophysical Journal, 612, 1044
Podsiadlowski, P., Rappaport, S., & Han, Z. 2003, Monthly Notices of the Royal Astronomical Society, 341, 385
Poelarends, A. J. T., Herwig, F., Langer, N., et al. 2008, The Astrophysical Journal, 675, 614
Pols, O. R., & Dewi, J. D. M. 2002, Publications of the Astronomical Society of Australia, 19, 233
Pols, O. R., Schröder, K.-P., Hurley, J. R., et al. 1998, Monthly Notices of the Royal Astronomical Society, 298, 525
Pols, O. R., Tout, C. A., Eggleton, P. P., et al. 1995, Monthly Notices of the Royal Astronomical Society, 274, 964
Popov, D. V. 1993, The Astrophysical Journal, 414, 712
Potekhin, A. Y., & Chabrier, G. 2010, Contributions to Plasma Physics, 50, 82, eprint: 1001.0690
Prantzos, N., Abia, C., Limongi, M., et al. 2018, Monthly Notices of the Royal Astronomical Society, 476, 3432, eprint: 1802.02824
Predehl, P., Andritschke, R., Arefiev, V., et al. 2021, Astronomy and Astrophysics, 647, A1
Prentice, S. J., Ashall, C., James, P. A., et al. 2019, Monthly Notices of the Royal Astronomical Society, 485, 1559, eprint: 1812.03716
Prialnik, D. 2009, An Introduction to the Theory of Stellar Structure and Evolution, publication Title: An Introduction to the Theory of Stellar Structure and Evolution by Dina Prialnik. Cambridge University Press
Pursiainen, M., Childress, M., Smith, M., et al. 2018, Monthly Notices of the Royal Astronomical Society, 481, 894, eprint: 1803.04869
Quimby, R. M., Kulkarni, S. R., Kasliwal, M. M., et al. 2011, Nature, 474, 487

Radice, D., Burrows, A., Vartanyan, D., et al. 2017, The Astrophysical Journal, 850, 43, eprint: 1702.03927
Radice, D., Morozova, V., Burrows, A., et al. 2019, The Astrophysical Journal, 876, L9, eprint: 1812.07703
Raives, M. J., Couch, S. M., Greco, J. P., et al. 2018, Monthly Notices of the Royal Astronomical Society, 481, 3293, eprint: 1801.02626
Ramírez-Tannus, M. C., Backs, F., de Koter, A., et al. 2021, Astronomy and Astrophysics, 645, L10
Rauscher, T., Heger, A., Hoffman, R. D., et al. 2002, The Astrophysical Journal, 576, 323, eprint: astro-ph/0112478
Reitze, D., Adhikari, R. X., Ballmer, S., et al. 2019, in Bulletin of the American Astronomical Society, Vol. 51, 35
Renzini, A. 1987, Astronomy and Astrophysics, 188, 49
Renzo, M. 2015, Master's thesis, Università di Pisa, Italy
Renzo, M., Farmer, R. J., Justham, S., et al. 2020, Monthly Notices of the Royal Astronomical Society, 493, 4333, eprint: 2002.08200
Renzo, M., Ott, C. D., Shore, S. N., et al. 2017, Astronomy and Astrophysics, 603, A118
Ritter, C., Andrassy, R., Côté, B., et al. 2018, Monthly Notices of the Royal Astronomical Society, 474, L1, eprint: 1704.05985
Ritter, H. 1988, Astronomy and Astrophysics, 202, 93
Roberge, A., Fischer, D., Peterson, B., et al. 2021, 53, 332, conference Name: Bulletin of the American Astronomical Society
Roberts, L. F., Ott, C. D., Haas, R., et al. 2016, The Astrophysical Journal, 831, 98
Rogers, F. J., & Nayfonov, A. 2002, The Astrophysical Journal, 576, 1064
Romano, D., Franchini, M., Grisoni, V., et al. 2020, Astronomy and Astrophysics, 639, A37, eprint: 2005.05717
Romano, D., Matteucci, F., Zhang, Z. Y., et al. 2017, Monthly Notices of the Royal Astronomical Society, 470, 401, eprint: 1704.06701
Roming, P. W. A., Kennedy, T. E., Mason, K. O., et al. 2005, Space Science Reviews, 120, 95
Russell, H. N. 1914, Popular Astronomy, 22, 275
Ryder, S. D., Van Dyk, S. D., Fox, O. D., et al. 2018, The Astrophysical Journal, 856, 83
Sagan, C. 1973, Garden City
Sana, H., & Evans, C. J. 2011, in IAU Symposium, Vol. 272, Active OB Stars: Structure, Evolution, Mass Loss, and Critical Limits, ed. C. Neiner, G. Wade, G. Meynet, & G. Peters, 474, eprint: 1009.4197
Sana, H., Ramírez-Tannus, M. C., de Koter, A., et al. 2017, Astronomy and Astrophysics, 599, L9
Sana, H., de Mink, S. E., de Koter, A., et al. 2012, Science, 337, 444, eprint: 1207.6397
Sana, H., Le Bouquin, J. B., Lacour, S., et al. 2014, The Astrophysical Journal Supplement Series, 215, 15
Sander, A. A. C., & Vink, J. S. 2020, Monthly Notices of the Royal Astronomical Society,

499, 873, eprint: 2009.01849
Sarangi, A., Matsuura, M., & Micelotta, E. R. 2018, ßr, 214, 63
Sato, K., & Suzuki, H. 1987, Physical Review Letters, 58, 2722
Saumon, D., Chabrier, G., & van Horn, H. M. 1995, The Astrophysical Journal, Supplement, 99, 713
Sawada, R., & Maeda, K. 2019, The Astrophysical Journal, 886, 47, eprint: 1910.06972
Schaller, G., Schaerer, D., Meynet, G., et al. 1992, Astronomy and Astrophysics Supplement Series, 96, 269
Schawinski, K., Justham, S., Wolf, C., et al. 2008, Science, 321, 223, eprint: 0803.3596
Schneider, F. R. N., Podsiadlowski, P., & Müller, B. 2021, Astronomy and Astrophysics, 645, A5, eprint: 2008.08599
Schneider, F. R. N., Sana, H., Evans, C. J., et al. 2018, Science, 359, 69, eprint: 1801.03107
Schoenberner, D., & Drilling, J. S. 1983, The Astrophysical Journal, 268, 225
Schootemeijer, A., Götberg, Y., de Mink, S. E., et al. 2018, Astronomy and Astrophysics, 615, A30, eprint: 1803.02379
Schootemeijer, A., Langer, N., Grin, N. J., et al. 2019, Astronomy and Astrophysics, 625, A132, eprint: 1903.10423
Schwarzschild, M. 1958, Structure and evolution of the stars., publication Title: Princeton
Shappee, B., Prieto, J., Stanek, K. Z., et al. 2014, 223, 236.03, conference Name: American Astronomical Society Meeting Abstracts #223
Shi, Y. 2015, in Handbook of Archaeoastronomy and Ethnoastronomy, ed. C. L. Ruggles (New York, NY: Springer), 2031
Shibazaki, N., & Ebisuzaki, T. 1988, The Astrophysical Journal, 327, L9
Shiode, J. H., Quataert, E., & Arras, P. 2012, Monthly Notices of the Royal Astronomical Society, 423, 3397
Shivvers, I., Modjaz, M., Zheng, W., et al. 2017, Publications of the Astronomical Society of the Pacific, 129, 054201
Shivvers, I., Filippenko, A. V., Silverman, J. M., et al. 2019, Monthly Notices of the Royal Astronomical Society, 482, 1545, eprint: 1810.03650
Skinner, M. A., Dolence, J. C., Burrows, A., et al. 2019, The Astrophysical Journal, Supplement, 241, 7, eprint: 1806.07390
Smartt, S. J., Eldridge, J. J., Crockett, R. M., et al. 2009, Monthly Notices of the Royal Astronomical Society, 395, 1409
Smith, N. 2014, Annual Review of Astronomy and Astrophysics, 52, 487, eprint: 1402.1237
Smith, N., Li, W., Filippenko, A. V., et al. 2011, Monthly Notices of the Royal Astronomical Society, 412, 1522
Smith, T., & Guild, J. 1931, Transactions of the Optical Society, 33, 73
Soderberg, A. M., Berger, E., Page, K. L., et al. 2008, Nature, 453, 469
Soker, N., Grichener, A., & Gilkis, A. 2019, Monthly Notices of the Royal Astronomical Society, 484, 4972
Solomon, P. M., Rivolo, A. R., Barrett, J., et al. 1987, The Astrophysical Journal, 319, 730

Spera, M., Mapelli, M., Giacobbo, N., et al. 2019, Monthly Notices of the Royal Astronomical Society, 485, 889
Sravan, N., Marchant, P., & Kalogera, V. 2019, The Astrophysical Journal, 885, 130
Steiner, A. W., Hempel, M., & Fischer, T. 2013, The Astrophysical Journal, 774, 17, eprint: 1207.2184
Stevenson, S., Vigna-Gómez, A., Mandel, I., et al. 2017, Nature Communications, 8, 14906, eprint: 1704.01352
Stritzinger, M. D., Anderson, J. P., Contreras, C., et al. 2018, Astronomy and Astrophysics, Volume 609, id.A134, 609, A134
Sukhbold, T., & Adams, S. 2020, Monthly Notices of the Royal Astronomical Society, 492, 2578, eprint: 1905.00474
Sukhbold, T., Ertl, T., Woosley, S. E., et al. 2016, The Astrophysical Journal, 821, 38
Sukhbold, T., & Woosley, S. E. 2014, The Astrophysical Journal, 783, 10, eprint: 1311.6546
Sukhbold, T., Woosley, S. E., & Heger, A. 2018, The Astrophysical Journal, 860, 93
Summa, A., Hanke, F., Janka, H.-T., et al. 2016, The Astrophysical Journal, 825, 6, eprint: 1511.07871
Summa, A., Janka, H.-T., Melson, T., et al. 2018, The Astrophysical Journal, 852, 28
Sutherland, P. G., & Wheeler, J. C. 1984, The Astrophysical Journal, 280, 282
Suwa, Y., Tominaga, N., & Maeda, K. 2019, Monthly Notices of the Royal Astronomical Society, 483, 3607, eprint: 1704.04780
Taddia, F., Sollerman, J., Leloudas, G., et al. 2015, Astronomy & Astrophysics, Volume 574, id.A60, 31 pp., 574, A60
Taddia, F., Stritzinger, M. D., Bersten, M., et al. 2018, Astronomy and Astrophysics, 609, A136, eprint: 1707.07614
Takiwaki, T., Kotake, K., & Suwa, Y. 2012, The Astrophysical Journal, 749, 98
Tartaglia, L., Sand, D. J., Valenti, S., et al. 2018, The Astrophysical Journal, 853, 62
Tauris, T. M., & Dewi, J. D. M. 2001, Astronomy and Astrophysics, 369, 170
Tauris, T. M., Langer, N., Moriya, T. J., et al. 2013, The Astrophysical Journal, 778, L23
Tauris, T. M., Langer, N., & Podsiadlowski, P. 2015, Monthly Notices of the Royal Astronomical Society, 451, 2123
Tauris, T. M., Kramer, M., Freire, P. C. C., et al. 2017, The Astrophysical Journal, 846, 170
Tews, I., Lattimer, J. M., Ohnishi, A., et al. 2017, The Astrophysical Journal, 848, 105, eprint: 1611.07133
The LIGO Scientific Collaboration, the Virgo Collaboration, Abbott, R., et al. 2020, The Astrophysical Journal, 896, L44, eprint: 2006.12611
Thielemann, F. K., & Arnett, W. D. 1985, The Astrophysical Journal, 295, 604
Thielemann, F.-K., Nomoto, K., & Hashimoto, M.-A. 1996, The Astrophysical Journal, 460, 408
Thompson, T. A., Chang, P., & Quataert, E. 2004, The Astrophysical Journal, 611, 380
Timmes, F. X. 1999, The Astrophysical Journal Supplement Series, 124, 241, publisher: IOP Publishing

Timmes, F. X., Hoffman, R. D., & Woosley, S. E. 2000, The Astrophysical Journal Supplement Series, 129, 377, publisher: IOP Publishing
Timmes, F. X., & Swesty, F. D. 2000, The Astrophysical Journal, Supplement, 126, 501
Timmes, F. X., Woosley, S. E., & Weaver, T. A. 1996, The Astrophysical Journal, 457, 834
Toonen, S., Nelemans, G., & Portegies Zwart, S. 2012, Astronomy and Astrophysics, 546, A70
Tout, C. A., Pols, O. R., Eggleton, P. P., et al. 1996, Monthly Notices of the Royal Astronomical Society, 281, 257
Townsend, R. 2019, MESA SDK for Linux: 20190911
Tractinsky, N. 1997, in Proceedings of the ACM SIGCHI Conference on Human factors in computing systems, CHI '97 (New York, NY, USA: Association for Computing Machinery), 115
Tramper, F., Sana, H., & de Koter, A. 2016, The Astrophysical Journal, 833, 133
Treisman, A. 1988, The Quarterly Journal of Experimental Psychology Section A, 40, 201
Trimble, V., & Paczynski, B. 1973, Astronomy and Astrophysics, 22, 9
Tutukov, A., Yungelson, L., & Klayman, A. 1973, Nauchnye Informatsii, 27, 3
Ugliano, M., Janka, H.-T., Marek, A., et al. 2012, The Astrophysical Journal, 757, 69
Utrobin, V. P., Wongwathanarat, A., Janka, H. T., et al. 2021, The Astrophysical Journal, 914, 4, eprint: 2102.09686
Valkanova, N., Jorda, S., Tomitsch, M., et al. 2013, in Proceedings of the SIGCHI Conference on Human Factors in Computing Systems, CHI '13 (New York, NY, USA: Association for Computing Machinery), 3461
van den Heuvel, E. P. J., & Heise, J. 1972, Nature Physical Science, 239, 67
van den Heuvel, E. P. J., Portegies Zwart, S. F., & de Mink, S. E. 2017, Monthly Notices of the Royal Astronomical Society, 471, 4256
van der Velden, E. 2020, The Journal of Open Source Software, 5, 2004, eprint: 2003.01069
van der Walt, S., Colbert, S. C., & Varoquaux, G. 2011, Computing in Science and Engineering, 13, 22
Van Dyk, S. D., de Mink, S. E., & Zapartas, E. 2016, The Astrophysical Journal, 818, 75
Vartanyan, D., & Burrows, A. 2020, The Astrophysical Journal, 901, 108, eprint: 2007.07261
Vartanyan, D., Burrows, A., & Radice, D. 2019a, Monthly Notices of the Royal Astronomical Society, 489, 2227, eprint: 1906.08787
Vartanyan, D., Burrows, A., Radice, D., et al. 2018, Monthly Notices of the Royal Astronomical Society, 477, 3091
Vartanyan, D., Burrows, A., Radice, D., et al. 2019b, Monthly Notices of the Royal Astronomical Society, 482, 351
Vartanyan, D., Laplace, E., Renzo, M., et al. 2021, The Astrophysical Journal, 916, L5
Vaytet, N. M. H., Audit, E., Dubroca, B., et al. 2011, Journal of Quantitiative Spectroscopy and Radiative Transfer, 112, 1323, eprint: 1101.4955
Verbunt, F., & Zwaan, C. 1981, Astronomy and Astrophysics, Vol. 100, p. L7-L9 (1981), 100, L7

Vigna-Gómez, A., Neijssel, C. J., Stevenson, S., et al. 2018, Monthly Notices of the Royal Astronomical Society, 481, 4009
Villaseñor, J. I., Taylor, W. D., Evans, C. J., et al. 2021, arXiv e-prints, arXiv:2107.10170
Vink, J. S. 2017, Astronomy and Astrophysics, 607, L8
Vink, J. S., & de Koter, A. 2005, Astronomy and Astrophysics, 442, 587
Vink, J. S., de Koter, A., & Lamers, H. J. G. L. M. 2001, Astronomy and Astrophysics, 369, 574
Weaver, T. A., & Woosley, S. E. 1993, Physics Reports, 227, 65
Webbink, R. F. 1979, The Astrophysical Journal, 227, 178
Webbink, R. F. 1984, The Astrophysical Journal, 277, 355
Weingartner, J. C., & Draine, B. T. 2001, The Astrophysical Journal, 548, 296, eprint: astro-ph/0008146
Weisskopf, M. C., Brinkman, B., Canizares, C., et al. 2002, Publications of the Astronomical Society of the Pacific, 114, 1
Weisskopf, M. C., Tananbaum, H. D., Van Speybroeck, L. P., et al. 2000, 4012, 2, conference Name: X-Ray Optics, Instruments, and Missions III Place: eprint: arXiv:astro-ph/0004127
Wellstein, S., & Langer, N. 1999, Astronomy and Astrophysics, 350, 148, eprint: astro-ph/9904256
Wheeler, J. C., & Levreault, R. 1985, The Astrophysical Journal, 294, L17
Wheeler, J. C., Meier, D. L., & Wilson, J. R. 2002, The Astrophysical Journal, 568, 807
Wheeler, J. C., Yi, I., Höflich, P., et al. 2000, The Astrophysical Journal, 537, 810
Williams, B. F., Peterson, S., Murphy, J., et al. 2014, The Astrophysical Journal, 791, 105
Williamson, M., Modjaz, M., & Bianco, F. B. 2019, The Astrophysical Journal, 880, L22
Wilson, J. R. 1985, in Numerical Astrophysics, ed. J. M. Centrella, J. M. Leblanc, & R. L. Bowers, 422
Wolfire, M. G., Hollenbach, D., McKee, C. F., et al. 1995, The Astrophysical Journal, 443, 152
Wolfire, M. G., McKee, C. F., Hollenbach, D., et al. 2003, The Astrophysical Journal, 587, 278, eprint: astro-ph/0207098
Wollaeger, R. T., & van Rossum, D. R. 2014, The Astrophysical Journal Supplement Series, 214, 28
Woosley, S. E. 2019, The Astrophysical Journal, 878, 49, eprint: 1901.00215
Woosley, S. E., & Bloom, J. S. 2006, Annual Review of Astronomy & Astrophysics, vol. 44, Issue 1, pp.507-556, 44, 507
Woosley, S. E., & Heger, A. 2007, Physics Reports, 442, 269
Woosley, S. E., Heger, A., & Weaver, T. A. 2002, Reviews of Modern Physics, 74, 1015
Woosley, S. E., Langer, N., & Weaver, T. A. 1993a, The Astrophysical Journal, 411, 823
Woosley, S. E., Langer, N., & Weaver, T. A. 1995, The Astrophysical Journal, 448, 315
Woosley, S. E., Sukhbold, T., & Janka, H.-T. 2020, The Astrophysical Journal, 896, 56, publisher: American Astronomical Society
Woosley, S. E., Sukhbold, T., & Kasen, D. N. 2021, The Astrophysical Journal, 913, 145,

eprint: 2009.06868
Woosley, S. E., Timmes, F. X., & Weaver, T. A. 1993b, Journal of Physics G Nuclear Physics, 19, S183
Woosley, S. E., & Weaver, T. A. 1986, Annual Review of Astronomy and Astrophysics, 24, 205
Woosley, S. E., & Weaver, T. A. 1995, The Astrophysical Journal, Supplement, 101, 181
Xi, Z.-z., & Bo, S.-r. 1965, Acta Astronomica Sinica, 13, 1
Yadav, N., Müller, B., Janka, H. T., et al. 2020, The Astrophysical Journal, 890, 94
Yoon, S.-C. 2015, Publications of the Astronomical Society of Australia, 32, e015
Yoon, S.-C., Dessart, L., & Clocchiatti, A. 2017, The Astrophysical Journal, 840, 10
Yoon, S.-C., Gräfener, G., Vink, J. S., et al. 2012, Astronomy and Astrophysics, 544, L11
Yoon, S.-C., Woosley, S. E., & Langer, N. 2010, The Astrophysical Journal, 725, 940
Yoshida, T., Takiwaki, T., Kotake, K., et al. 2019, The Astrophysical Journal, 881, 16
Yoshida, T., Takiwaki, T., Kotake, K., et al. 2020, arXiv:2012.13261 [astro-ph]
Young, P. A., & Fryer, C. L. 2007, The Astrophysical Journal, 664, 1033, eprint: astro-ph/0612698
Zapartas, E., de Mink, S. E., Justham, S., et al. 2021a, Astronomy and Astrophysics, 645, A6, eprint: 2002.07230
Zapartas, E., de Mink, S. E., Van Dyk, S. D., et al. 2017, The Astrophysical Journal, 842, 125, eprint: 1705.07898
Zapartas, E., de Mink, S. E., Justham, S., et al. 2019, Astronomy and Astrophysics, 631, A5
Zapartas, E., Renzo, M., Fragos, T., et al. 2021b, arXiv e-prints, arXiv:2106.05228, eprint: 2106.05228
Zevin, M., Kremer, K., Siegel, D. M., et al. 2019, arXiv:1906.11299 [astro-ph]
Zhou, P., Vink, J., Li, G., et al. 2018, The Astrophysical Journal, 865, L6
Zinnecker, H., & Yorke, H. W. 2007, Annual Review of Astronomy and Astrophysics, 45, 481

Contribution from co-authors

Chapter 2: The expansion of stripped-envelope stars

E. Laplace, Y. Götberg, S. E. de Mink, S. Justham, and R. Farmer

Astronomy & Astrophysics, 2020, 637, A6

(Also referred to as Laplace et al. 2020)

Chapter 3: Different to the core: the pre-supernova structures of massive single and binary-stripped stars

E. Laplace, S. Justham, M. Renzo, Y. Götberg, R. Farmer, D. Vartanyan, and S. E. de Mink

Resubmitted to Astronomy & Astrophysics after making suggested revisions

(Also referred to as Laplace et al. 2021)

Chapter 4: Binary-stripped stars as core-collapse supernovae progenitors

D. Vartanyan, **E. Laplace**, M. Renzo, Y. Götberg, A. Burrows, and S. E. de Mink

The Astrophysical Journal Letters, 2021, 916, L5

EL computed the evolutionary models for this paper, which were used as input for the supernova simulations, and performed several tests. EL wrote Section 4.2.1 and parts of the introduction, provided data for Table 4.1, contributed extensively to the analysis and to the interpretation of the results, and helped improve the manuscript.
(Also referred to as Vartanyan et al. 2021)

Chapter 5: The cosmic carbon footprint of massive stars stripped in binary systems

R. Farmer, **E. Laplace**, S. E. de Mink, and S. Justham

Submitted to The Astrophysical Journal

EL's findings of the impact of binary stripping on the internal ^{12}C distribution (presented in Chapter 3) provided the direct motivation for the topic and scope of this paper. EL's provided the evolutionary models that were used for the initial calculations. EL further contributed to the analysis and to the interpretation of the results, and helped improve the manuscript.
(Also referred to as Farmer et al. submitted)

Chapter 6: TULIPS: a Tool for Understanding the Lives, Interiors, and Physics of Stars

E. Laplace

Received a positive review from Astronomy & Computing. Suggestions for minor revisions made by the referees have been accounted for in the version presented in this thesis.

(Also referred to as Laplace submitted)

Other publications

1. L. A. C. van Son; S. E. de Mink; F. S. Broekgaarden; M. Renzo; S. Justham; **E. Laplace**; J. Moran-Fraile; D. D. Hendriks; R. Farmer, *Polluting the pair-instability mass gap for binary black holes through super-Eddington accretion in isolated binaries*, 2020, The Astrophysical Journal, 897, 100

2. M. Renzo; S. E. de Mink; D. J. Lennon; I. Platais; R. P. van der Marel; **E. Laplace**; J. M. Bestenlehner; C. J. Evans; V. Hénault- Brunet; S. Justham; A. de Koter; N. Langer; F. Najarro; F. R. N. Schneider; J. S. Vink, *Space astrometry of the very massive* $\sim 150\,M_{\odot}$ *candidate runaway star VFTS682*, 2018, Monthly Notices of the Royal Astronomical Society: Letters, Volume 482, L102

3. **E. Laplace**; T. Mihara; Y. Moritani; M. Nakajima; T. Takagi; K. Makishima; A. Santangelo, *Possible regular phenomena in EXO 2030+375*, 2017, Astronomy & Astrophysics, 597, A124

4. K. A. Postnov; M. I. Gornostaev; D. Klochkov; **E. Laplace**; V. V. Lukin; N. I. Shakura, *On the dependence of the X-ray continuum variations with luminosity in accreting X-ray pulsars*, 2015, Monthly Notices of the Royal Astronomical Society 452, 1601

Nederlandse Samenvatting

Dit proefschrift, getiteld "Late levensloop, dood en het leven daarna van sterren die gestript zijn in dubbelstersystemen" bespreekt de invloed die massaverlies door massaoverdracht tussen dubbelsterren heeft op de levensloop en explosies van sterren met een hoge massa (zware sterren).

In dit proefschrift maken we gebruik van numerieke berekeningen om onderzoek te doen naar de structuur en levensloop van zware sterren die hun buitenste lagen overdragen aan een begeleidende ster. We maken gebruik van de ééndimensionale, opensourcecode voor de levensloop van sterren: Modules for Experiments in Stellar Astrophysics (`MESA`, Paxton et al. 2011, 2013, 2015, 2018, 2019). Deze code berekent numerieke uitwerkingen van de structuurvergelijkingen van sterren en bevat een module die de interacties tussen twee door de zwaartekracht gebonden sterren berekent. In hoofdstuk 4 gebruiken we de multidimensionale code FORNAX die de straling en hydrodynamica berekent (Skinner et al. 2019) om de implosies van de kern aan het eind van het leven van zware sterren en de creatie en propagatie van een schokgolf van een supernova consequent te volgen. In hoofdstuk7 presenteren we preliminaire berekeningen van lichtkrommen van supernova's met de ééndimensionale hydrodynamische code `SNEC` (Morozova et al. 2015, 2016).

In hoofdstuk 2 onderzoeken we de late levensloop van gestripte sterren in dubbelstersystemen (gestripte dubbelsterren) bij zonne- en lage metalliciteit, waarbij we focussen op hun expansie, wat van cruciaal belang is om te bepalen of ze weer zullen interacteren met hun begeleidende ster. Bij zonnemetalliciteit (Z=0.0142, Asplund et al. 2009), bereiken onze modellen radii van maar liefst $100\,R_\odot$ voor modellen met beginmassa's onder de $10\,M_\odot$ en radii van $4\,R_\odot$ voor modellen met beginmassa's van $15\,M_\odot$, en ze zijn allemaal waterstofarm. Bij lage metalliciteit (Z=0,001) behouden al onze modellen een waterstofrijk omhulsel, waardoor de sterren in staat zijn om uit te groeien tot gigantische afmetingen, waarbij ze radii van 400 en $600\,R_\odot$ bereiken. Dit betekent dat ze allemaal weer zullen interacteren met hun begeleidende ster. Bovendien ontdekken we dat alle gestripte dubbelsterren die we berekend hebben met een lage metalliciteit hun Rochelob overvloeien vóór ze exploderen, wat interessante consequenties kan hebben voor de geobserveerde supernova's. We laten zien dat de groei van gestripte dubbelsterren tot wel twee ordes van grootte wordt onderschat door populatiesynthesemodellen die de levensloop van gestripte dubbelsterren benaderen als pure heliumsterren. We bespreken de implicaties van onze bevindingen voor de hoeveelheid van zwaartekrachtgolfbronnen van fusies van dubbele neutronensterren en de afhankelijkheid van metalliciteit ervan.

Wegens dit minder grote – of niet-bestaande – waterstofrijke omhulsel hebben natuurlijk exploderende gestripte dubbelsterren heel andere kenmerkende eigenschappen dan sterren die hun omhulsel behouden. De supernova's die ze produceren missen de opvallende waterstoflijnen die kenmerkend zijn voor de grote waterstofrijke omhulsels van enkele sterren. Bovendien wordt de vorm van hun lichtkrommen beïnvloed door dit minder grote, of zelfs niet-bestaande omhulsel (zie sectie 1.2.3). Worden alleen de buitenste lagen van sterren beïnvloed door het strippen in een dubbelstersysteem? Wordt de kern eigenlijk wel beïnvloed door het massaverlies van het omhulsel? Zijn er systematische verschillen tussen de kernstructuren van enkele sterren en gestripte dubbelsterren?

Dit zijn de vragen die we bespreken in hoofdstuk 3, waar we een systematische vergelijking presenteren van de kernstructuren van enkele en gestripte sterren met identieke beginmassa's. In dit hoofdstuk laten we zien dat de gestripte sterren die we in dit proefschrift onderzoeken inderdaad andere kernstructuren produceren dan enkele sterren. Bij gelijke beginmassa's hebben de heliumkernen van gestripte sterren een kleinere massa en zijn ze compacter dan kernen van enkele sterren. Dit komt door twee factoren: 1) gestripte dubbelsterren kunnen, in tegenstelling tot enkele sterren, geen grotere heliumkern krijgen door het verbranden van een waterstofschil en 2) gestripte dubbelsterren raken sommige heliumlagen kwijt door winden. Het is opmerkelijk dat enkele en gestripte dubbelsterren, zelfs met gelijke kernmassa's, verschillende kernstructuren ontwikkelen. Hun dichtheid is verschillend, net als hun samenstelling. Gestripte dubbelsterren ontwikkelen een koolstofrijke laag om de zuurstofrijke kern heen die men niet aantreft bij de structuur van enkele sterren. Dit komt door verschillen tijdens de verbranding van de heliumkern. We laten zien dat dit verschil aanhoudt tot het begin van de kernimplosie en dat het leidt tot verschillende beginomstandigheden voor de explosie van de kernen van enkele en gestripte dubbelsterren.

In hoofdstuk 4 bouwen we voort op dit werk om te onderzoeken hoe dit verschil tussen de kernen van enkele en gestripte dubbelsterren de supernova-explosie beïnvloedt. Hiervoor berekenen we de kernimplosies van deze sterren in twee dimensies met de `FORNAX`-code. Over het algemeen ontdekken we dat gestripte dubbelsterren explosiever zijn dan enkele sterren. We laten zien dat geen enkele variabele de uitkomst van de explosie kan voorspellen, maar dat een combinatie van factoren kan leiden tot een succesvolle explosie.

Het opmerkelijkste verschil in samenstelling dat we in hoofdstuk 3 vonden was het ^{12}C-gehalte in enkele en gestripte dubbelsterren met een hoge massa. Bij de modellen die we hebben berekend, bleek dat gestripte dubbelsterren twee keer zoveel ^{12}C bevatten als enkele sterren. Dit is met name interessant vanwege de rol van ^{12}C als bouwsteen voor het leven. Wordt deze ^{12}C uiteindelijk uitgestoten tijdens de supernova-explosie of wordt het omgezet in andere isotopen tijdens de nucleosynthese van de supernova? Zijn zware gestripte dubbelsterren een grote bron van ^{12}C in het heelal? Is ^{12}C wellicht nog een kenmerk van explosies van gestripte dubbelsterren, mogelijk waarneembaar in restanten van supernova's? Deze vragen komen in hoofdstuk 5 aan bod en we ondervinden dat de gestripte dubbelsterren die we nabootsen inderdaad over het algemeen twee keer zoveel ^{12}C in het heelal produceren als enkele sterren door middel van hun winden en supernova-explosies. We ontdekken dat de

^{12}C die wordt uitgestoten tijdens supernova-explosies amper wordt aangetast door de schokgolf van de supernova en de nucleosynthese die dit achterlaat, voor de variëteit aan supernova energieën dat we berekenen. Dit komt doordat deze schokgolf drastisch afkoelt voordat het de koolstofrijke lagen bereikt en niet in staat is grote hoeveelheden ^{12}C te vernietigen.

Hoofdstuk 6 introduceert `TULIPS`: een gratis opensourcesoftware die het mogelijk maakt om de structuur en levensloop van sterren (dynamisch) weer te geven. `TULIPS` is ontwikkeld en toegepast voor het onderzoek dat in dit proefschrift is tentoongespreid (zie, bijvoorbeeld, de compositiediagrammen van hoofdstuk 3). Het is gebaseerd op de simulatieresultaten van ééndimensionale sterrenlevensloopsimulaties en is geoptimaliseerd om met `MESA` te gebruiken. `TULIPS` maakt gebruik van de intrinsieke bolvormige symmetrie van deze simulaties om de eigenschappen van sterren te visualiseren als de eigenschappen van cirkels. Verscheidene voorbeeldapplicaties van `TULIPS` worden tentoongespreid, waaronder een ster die op de zon lijkt, een $16\,M_\odot$ zware ster en een witte dwergster die waterstofrijk materiaal accreteert. Hoofdstuk 6 vergelijkt `TULIPS` met traditionele diagrammen, zoals het Hertzsprung-Russell-diagram en bespreekt de verschillen. `TULIPS` is niet bedoeld als vervanging van traditionele weergaves van de sterrenstructuur. In plaats daarvan biedt het een nieuw perspectief dat kan leiden tot een intuïtiever begrip van de onderzochte processen. `TULIPS` is ontworpen met het idee om de pracht van de natuurwetenschap die het leven en de opbouw van sterren bepaalt over te brengen op de sterrenkundegemeenschap. Daarnaast kan het ook worden toegepast voor educatieve doeleinden en om het grote publiek te bereiken.

Ten slotte werpen we in hoofdstuk 7 een blik op toekomstig onderzoek naar gestripte dubbelsterren, hun explosies en hun leven na de dood. We presenteren een inleidend onderzoek naar een methode om de explosie-eigenschappen van geobserveerde supernova's zonder omhulsel in te perken, gebaseerd op een grote verzameling vooraf berekende lichtkrommemodellen van supernova's. We bespreken de implicaties van onze voorlopige uitslagen en sluiten af met een vooruitzicht op middelen waarvoor observaties de mogelijkheid hebben om theorieën over de evolutie van gestripte dubbelsterren af te bakenen.

Acknowledgements

Voilà, ça y est. The end of a four-year adventure. And what an adventure it was! Every single letter in this manuscript owes its existence to the contributions, ideas, support, comments, and conversations with and of people who have been part of my journey. Even if your name is not mentioned here, I hope you know who you are, and how grateful I am.

First I would like to acknowledge my advisors and promotors.

Selma, I would like to thank you for hiring me as your PhD student and welcoming me in your group, even though I had a very different, observational background, and managed to unknowingly criticize your work in one of our first conversations. Working with you has been incredibly stimulating and, looking back, I am amazed how much I have learned and grown in these years. I am grateful for all your support, for your feedback, and your help. Thank you for connecting me to so many interesting people, for sending me to conferences all around the world, and for trusting me to mentor others. Thank you for encouraging me and for your investment in promoting women in science.

Stephen, you came to Amsterdam almost a year after I had started and yet you have had such a key influence on the content of this thesis that it feels like you were there from day one. I could always count on you and this has made all the difference. Your kindness and your readiness to help others inspire me and I feel lucky to have met you. Thank you for all our conversations about science, life, and animals. Thank you for sharing your incredibly vast knowledge, your intuition for physics, and your insights always humbly and carefully. Your insistence to be precise and to triple-check everything has greatly improved the quality of my research, for the long term. Thank you.

Lex, thank you for your enthusiasm, for always being interested in my research, and for our discussions. You only got involved toward the end of my PhD, yet I have found that you were always available when I needed your help. Thank you.

I have been very fortunate to work with excellent international collaborators around the world during my PhD. These experiences have been inspiring and have given more depth and breadth to my research. First, I would like to acknowledge Maryam Modjaz for inviting me to Heidelberg all these years ago. Thank you for the inspiring conversations and for teaching me about supernova classification and spectra! One of the fondest memories of my PhD is my two-month visit to the National Observatory in Japan. Takashi Moriya, thank you so much for inviting me to work with you and for hosting me. Returning to Japan was an incredible and lovely experience and I very much enjoyed our conversations and our work together. I am grateful for all I have learned about supernovae and their light-curves and will remember my time at your institute for the rest of my life.

Further, I would like to thank David Vartanyan and Adam Burrows for our collaboration. Working with you was a lot of fun and has made me appreciate the complexity and intricacies of multi-dimensional supernova simulations. David, thank you for all the times you got up

very early to make it to our meetings because of our time difference!
I would also like to acknowledge Tony Piro for helpful and stimulating discussions about supernova light-curves and for explaining the intricacies of the SNEC code to me. Sung-Chul Yoon, thank you very much for hosting me in Seoul. It was a great pleasure to visit your institute and to exchange with you and your group. I am grateful to have had the opportunity to discuss the properties of binary-stripped stars with you and I am already excited to learn about your next research! Moreover, I would like to thank JJ Eldridge, Iair Arcavi, Nathan Smith, Carles Badenes, Jose Groh, Jorick Vink, Raffaella Margutti, Jim Fuller, Maria Drout, and Andy Howell for interesting and inspiring discussion at various conferences and meetings, and for their patience with answering all of my questions.
I would also like to acknowledge all API staff members who have encouraged and helped me, and with whom I have had interesting science discussions. Ed van den Heuvel and Henny Lamers, thank you very much for your interest in my research, and for your encouraging words. These meant a lot to me, coming from you. In addition, I would like to thank all the members of the massive star community for the interesting and instructive exchanges of ideas. Alex, I would like to thank you in particular. Thank you for your kindness and for your support. Your advice and guidance played a large role in making my postdoc applications a success, and in helping me reach my objectives.

During my PhD, I was very fortunate to be part of a research group consisting of people who have been incredibly helpful, generous, and kind; who have had a major influence on the content of this thesis, and greatly improved its quality. Ylva, thank you for all your advice, feedback and generous help, and for teaching me the fundamentals of binary-stripped stars. You inspire me and I feel privileged for having had the chance to work with you. If someone can solve the mysteries around stripped stars, it is you! Mathieu, thank you for all our conversations and for your help. Working with you is like gaining access to unlimited knowledge and insights. Every time you gave me feedback my work has benefited from it. Our conversations in Frenglish have been always been precious moments to me. It is a pity that I had to cancel my trip to New York because of the pandemic! I hope we will have the occasion to see each other again soon. Rob, I am privileged to have worked with you during these years. Thank you for all the help with MESA, for your insights, and for being such a reliable and trustworthy person. I keep a fond memory of our travels together, in particular our stay in Argentina when we climbed a mountain followed by a stray dog. I will miss you and your sense of humor dearly. Manos, I have learned a lot from you and deeply appreciate that you taught me patiently and kindly the basics of binary stellar evolution when I started my PhD. You are a great teacher and scientist and I am still working to try and reach your level of understanding one day. Lieke, my little sister from the PhD, my friend. Thank you so much for your engagement throughout the years. Thank you for staying confident and enthusiastic about my research even when I was not. Our weekly conversations across the Atlantic were often the highlight of my week and have helped me to keep going during some of the lowest moments. I have no doubt you will produce some more great science in the coming years and

look forward to seeing it.
Thank you also to all the other members of the BinCosmos group throughout the years! Silvia, you are a role model for me. Thank you for always trusting in my abilities and for your encouragement and support. Floor, Walter, Athira, Karel, Javier, David, Floris, Loki, Tom, Kathy, and many others, working with you all was a privilege. Thank you for participating in the group and cookie meetings! Thank you for having made science fun for me.

Next I would like to thank the students I helped mentor, in particular Thomas and Carla, and all my students from the three stellar evolution classes I taught as a teaching assistant. Interacting with you, trying to solve problems together, and to explain stellar and supernova physics to you was a highlight of my PhD and a joyful experience. Even if I forget your names one day the feeling of motivation and purpose this gave me will stay in my heart forever. Ilse, thank you for your dedication and motivation for the TULIPS project! Working with you through github problems, python issues, and the complexity of programming on Windows systems was incredibly fun and I enjoyed every moment of it. My only regret is that we had to work online and only met in person when I was about to leave. I am excited to see what you will do next and I am confident that you will succeed greatly at whichever direction you will choose to take.

API is a special, warm, and lovely place and it is the people that are part of it that make it so. A few words for my paranymphs and those who could have been if there was room for more people. Ben, you are a deeply kind and lovely person and I feel that my life is more complete because I have you as my friend. Thank you for all our crazy adventures, for the accidental and intentional half marathons, for all the laughs and tears. I don't know how you do it but you always know what to say to cheer me up. Your optimism is contagious and you give the best advice. This thesis would not be the same without your help. Geert, when you are around, I can't help but start grinning in anticipation of your first joke, and my day immediately becomes a happier one. Sharing an office with you was the best and you really made my day when you surprised me during my second pandemic birthday. I remember the time in Japan with you, Kelly, and Marcella fondly as one of the most wonderful moments of my PhD. Vlad, my old friend. Thank you for encouraging me to come to Amsterdam! You were right, living there was one of the best times of my life. And a big part of what made it so is that I always had my Slovak brother to share happy moments with and who I could count on when I needed help, or to get home after a party. Eleanor, I remember all our conversations fondly and am grateful I could count on you when I needed to talk. Thank you for being such a lovely person and for our friendship. Dimitris, I still find it amazing how we became instant friends when we first met at the PhD interviews. You never fail to bring me chocolate when I really need it, you give the best hugs and what more can a friend ask for? I miss you already and can't wait to finally visit you in Greece one day :)

During my PhD, I got extremely lucky to share an office with amazing people who became my friends. Even during the worst lockdowns our virtual coffee meetings made me feel like we were still in the same room. Kelly, thank you for being one of the first people to make me feel welcome in Amsterdam, for all the fun memories (remember that night when the Oranje

Leeuwinnen made it to the finals!), and for being someone who cares. I will try my best to visit you in Australia! Inés, I've never met someone who brings as much energy to a party as you! Thank you for your enthusiasm for karaoke and our "not-so-secret" conversations in French / Spanish. Seeing you dance to your headphone music on your office chair at the edge of my screen never failed to cheer me up. Sarah, I remember all our interactions as fun and lovely moments. Thanks for sharing my passion for creative office improvements. I still believe building analog speakers to talk to each other from one end of the office to the other was one of our most brilliant ideas ever, even though it didn't work so well in practice. Jure, thank you for your quiet and kind presence and for the care you give to everything you do. Thank you also to Liam, Leon, David, Sebastian, Lieke, Kevin, Floris, and Iris, for making my time in the office so happy and fun!

There are many more APIs, who I cannot all list here, who have made life at the institute incredibly enjoyable by helping build the amazing API atmosphere in the first place, by their social engagement, and by enriching API with their presence.
Of course the first person who comes to mind is Martin, the soul of API. The conversations with you are always memorable and fun, and sometime made me wiser. Thank you for taking care of API and its members and for your refreshing honesty.
The people who keep API running are a lovely and incredibly helpful group of people. Susan, Milena, Renee, Wim, and Lucas, thank you all for all the help throughout the years!

A special thought also for my API friends from the bunch of avengers I have not mentioned yet: Vatsal, Deniz, Frank, Kenzie, Alex C., Arkadip, David, Annelotte, Claire, Lennart, Oliver, and Niloo. Thank you for all the game nights, movie nights, drinks, parties, and adventures! The memories of the time spend with you all will always stay in my heart!
I would also like to give a shout out to all the members of the API PhD & Postdoc councils throughout the years for their engagement and for helping make API a better place. In particular I want to thank my fellow council members Vlad, Jakob, Leon, Frank, and Atul for all the effort they put in and for all the fun that we had.
Toward the end of my PhD, I also had the chance to join the then newly formed API equity, inclusion, and diversity committee. Working with you all was a great and humbling learning experience, and an important motivation for me. Keep up the good work! Luna, I want to thank you in particular for your efforts in creating an inclusive API logo/sticker, it was rewarding to take part in this project with you.

Thank you also to my friends from outside of API, who have made my life one full of happy and special moments. A special thanks to my old friends from Strasbourg, in particular Camilla, Juliette C., and Grace, who came to visit me with Marina and Gautier! Also to Marcel from Tübingen! And to my sister Sara! Even though we don't see each other often, it is always a pleasure to spend time together and I feel lucky to have you as my friends. A big thank you to Juliette R. for the writing sessions and for the mutual encouragements and help for our theses! It played an important role in helping me complete this thesis. Neige, after our conversations I often feel my cheek because I smile and laugh so much. Thank you for all the support and for the fun, and for the time we spent together hiking! I can't wait to explore the

Canadian wilderness with you soon! David and Abel, you two make the worst jokes I've ever heard, but you have hearts of gold. It was incredible how we became friends in a matter of seconds and it made me very happy that we kept in touch during the lockdowns. I've enjoyed every single moment with you. My Davidito, exploring Washington together was amazing and I can't wait to go on an adventure with you again, who knows, maybe in Greece?? Lara, thank you for all your support, and for believing in me. The time spent with you has made me grow into a better person. I'm also grateful to my flatmates Wendy and Serena for the fun time spent together! And to my cousins Felix and Ellen for creating the Netherlands gang with me and for all the fun we had! Jacobine, thank you for the Dutch translation of my thesis summary! And Lieke, thank you for rereading it! Thanks also to Aya and Dita for staying in touch after all these years! It was incredible to be able to see you again in Tokyo! Playing escape games with you made me forget my worries during some of the hardest times.

Annie, it's simple, finishing my thesis in this manner would not have been possible without your help. Thank you for all the support you have given me, even when I was stressed and grumpy. And for introducing me to Marley, who is, in all objectivity, the most lovely cat in the Universe. You have the best sense of humor and you bring out the beauty in the world all around you. You encourage me to try and be the best version of myself even when it's hard. I am grateful every day for having you in my life.

Finally, I would like to thank my family. Mama, Papa, when I was eight years old, I told you I wanted to become an astrophysicist one day. It has taken 20 years, and if now this dream has come true it is because you gave me the means to realize it. Johanna, Marina, Marc, and Guillaume having you as my siblings is my greatest source of joy. Thank you! I love you.

Eva Laplace,
November 18, 2021.

Ph.D. thesis, Anton Pannekoek Institute, Universiteit van Amsterdam

ISBN: 978-94-6419-388-6

Cover design by A. Faber.

Le petit prince s'assit sur une pierre et leva les yeux vers le ciel:
- Je me demande, dit-il, si les étoiles sont éclairées afin que chacun puisse un jour retrouver la sienne.

The little prince sat down on a stone and looked up at the sky.
"I wonder," he said, "whether the stars are set alight in heaven so that one day each one of us may find their own again."

Antoine de Saint-Exupéry, *Le Petite Prince (1943).*